TECHNISCHE UNIVERSITÄT WIEN
Vienna University of Technology

Dissertation

Replicating liver tissue in terms of mechanical properties for anatomical models

carried out for the purpose of obtaining the degree of Doctor technicae (Dr. techn.), submitted at TU Wien, Faculty of Mechanical and Industrial Engineering, by

Sarah-Jane Estermann

Mat.Nr.: 01025629

under the supervision of

Dipl.-Ing. Dr. Andreas Reisinger
Karl Landsteiner University of Health Sciences; TU Wien

and

Univ.Prof. Dipl.-Ing. Dr. Dieter H. Pahr
Institute of Lightweight Design and Structural Biomechanics, E317

reviewed by

Prof. Dipl.-Ing. Dr.
Stéphane Avril
École des Mines de Saint-Étienne
Cours Fauriel 158, 42023 Saint-Étienne

Associate Prof. Priv.-Doz. Dipl.-Ing. Dr.
Stefan Scheiner
IMWS, TU Wien
Karlsplatz 13/202, 1040 Vienna

This work was supported by the NFB Science Call Dissertations 2017 (SC17-016), and the Austrian Center for Medical Innovation and Technology (ACMIT). The research center ACMIT is funded in the framework of COMET by BMVIT, BMDW, the Federal State of Lower Austria and Standortagentur Tirol.

I confirm, that going to press of this thesis needs the confirmation of the examination committee.

Affidavit

I declare in lieu of oath, that I wrote this thesis and performed the associated research myself, using only literature cited in this volume. If text passages from sources are used literally, they are marked as such.

I confirm that this work is original and has not been submitted elsewhere for any examination, nor is it currently under consideration for a thesis elsewhere.

Vienna, June, 2021

Signature

For Sally, Rudi,
and Amy

Kurzfassung

Realistische anatomische Modelle sind ein wichtiges Instrument in der Forschung und Lehre und werden in der Entwicklung neuer Medizinprodukte, im Anatomieunterricht und in der chirurgischen Ausbildung eingesetzt. Die Herstellung anatomischer Modelle mit realistischen mechanischen Eigenschaften ist jedoch aufgrund des inhärent komplexen mechanischen Verhaltens von Weichgeweben eine Herausforderung.

In dieser Dissertation wurden die mechanischen Eigenschaften von Weichgewebe ausführlich analysiert, mit dem Ziel haptische Eigenschaften in anatomischen Modellen besser abbilden zu können. Mit speziellem Fokus auf Leberparenchym, wurden verschiedene experimentelle und Datenanalysemethoden entwickelt, um nichtlineare und viskoelastische Eigenschaften zu charakterisieren. Dabei wurde frische menschliche Leber, frische Tierleber, Thiel-einbalsamierte menschliche Leber und verschiedene künstliche Ersatzmaterialien evaluiert.

Einerseits wurde die Palpation von Weichgewebe mittels Makroindentation nachgeahmt, um objektiv bewerten zu können, wie sich Materialien anfühlen. Diese Methode ermöglicht den effizienten Vergleich verschiedener Materialien hinsichtlich ihrer haptischen Eigenschaften. Zur Untersuchung des nichtlinearen elastischen Verhaltens wurden die Materialien langsam eingedrückt und Steifigkeiten für verschiedene Eindringbereiche definiert. Unter Berücksichtigung von Viskoelastizität wurde die Kraftrelaxation des Materials während eines Zeitraums konstanter Indentation gemessen. Die Abnahme von Kraft über Zeit wurde mittels rheologischem Model beschrieben und die frequenzabhängige Speichersteifigkeit, Verluststeifigkeit und Verlustfaktor wurden berechnet. Durch den Vergleich der resultierenden mechanischen Eigenschaften verschiedener künstlicher Materialien mit Lebergewebe, unter Verwendung des neu eingeführten "taktilen Ähnlichkeitsfehlers", wurde ein weiches Silikon gefunden, das hinsichtlich der getesteten Eigenschaften, Leber am ähnlichsten war.

Andererseits wurden Zugversuche mit ähnlichen Prüfprotokollen (Rampenbelastung und Spannungsrelaxation) durchgeführt, um Eigenschaften auf Materialebene zu definieren. Der Spannungs-Dehnungs-Verlauf in Belastung und Entlastung der Rampe wurden mit einem pseudohyperelastischen Veronda-Westmann Modell approximiert und es wurden dehnungsspezifische Elastizitätsmodule gefunden. Basierend auf Spannungsrelaxation, wurden die viskoelastischen Eigenschaften als Speichermodul, Verlustmodul und Verlustfaktor ausgedrückt. Zusätzlich wurden äquivalente viskoelastische Eigenschaften mit dynamischen zyklischen Tests gemessen, um Relaxation und zyklische Tests miteinander zu vergleichen. Die Ergebnisse zeigten, dass Spannungsrelaxation und zyklische Tests vergleichbare viskoelastische Ergebnisse ergaben, solange nichtlineares Verhalten berücksichtigt und Tests bei gleichem Dehnungsniveau durchgeführt wurden.

Mit diesen experimentellen Methoden wurden neue Erkenntnisse über die visko-

elastischen Zugeigenschaften von menschlicher und tierischer Leber gewonnen. Somit konnten Unterschiede zwischen menschlicher und tierischer Leber analysiert und durch ihre charakteristischen histologischen Morphologien erklärt werden. Darüber hinaus wurde festgestellt, dass die Thiel-Konservierung mit einer Versteifung des Gewebes und vermindertem viskosen Verhalten verbunden ist.

Testergebnisse der Makroindentation zeigten, dass durch die Kombination verschiedener Materialien, mechanische Eigenschaften adaptiert werden können, um Lebergewebe besser zu imitieren. Um solche Materialkombinationen zu entwerfen, wurde ein viskoelastisches Mori-Tanaka-Modell (vMTM) zur Homogenisierung viskoelastischer Eigenschaften von Materialien mit Matrix-Einschluss-Morphologien entwickelt. Zur Validierung des vMTM wurden Proben getestet, die aus Kombinationen zweier weicher Silikonen mit variierendem Volumenanteil bestanden, und mit den Modellvorhersagen verglichen. Für die Anwendung des vMTM wurden viskoelastische Materialeigenschaften verschiedener weicher Silikonelastomere als Eingangsößen definiert. Die dabei resultierenden homogenisierten Eigenschaften wurden mit Lebereigenschaften aus den Zugversuchen verglichen. Weiters, wurde untersucht inwiefern die homogenisierten Modelleigenschaften sich mit anderen Weichgeweben aus der Literatur decken.

Schließlich wurden dadurch geeignete Mikrostrukturen identifiziert, die sehr ähnliche viskoelastische Eigenschaften wie bestimmte biologische Weichgewebe aufweisen. In Zukunft, können diese Mikrostrukturen, dank kontinuierlicher Innovationen im Bereich 3D-Druck von weichen Materialien, hoffentlich durch additive Fertigung hergestellt werden.

Diese Dissertation bietet neue Einblicke in die mechanischen Eigenschaften des Leberparenchyms und präsentiert eine effiziente Strategie für das Materialdesign von realistischen anatomischen Modellen, basierend auf mikromechanischer Homogenisierung. Die Ergebnisse dieser Arbeit können somit dazu beitragen, dass realistischere anatomische Weichgewebemodelle produziert werden, zum Beispiel für Anwendungen in der medizinische Ausbildung.

Abstract

Realistic anatomical models are an important tool in research and education, used for aiding the development of new medical products and procedures, for teaching anatomy, and for surgical training. However, producing anatomical models, exhibiting accurate mechanical properties, is challenging due to the inherently complex mechanical behaviour of soft tissues.

In this dissertation, it was assessed which properties need be be considered, in the context of describing what soft tissues actually *feel* like. Focussing especially on liver parenchyma, different experimental and data analysis methods were developed, considering non-linear and viscoelastic properties of fresh human liver, fresh animal liver, Thiel embalmed human liver, and different tissue-mimicking artificial materials.

On the one hand, macroindentation, mimicking soft tissue palpation, was applied for objectively assessing what materials feel like, allowing easy comparison between different materials. For examining the non-linear elastic behaviour, the materials were slowly indented and stiffness was defined for different levels of indentation. Considering viscoelasticity, force relaxation of the material was measured during a period of constant indentation. The decline of force over time was described with rheological modelling and frequency-dependent storage stiffness, loss stiffness, and loss tangent were calculated. By comparing resulting mechanical properties of different artificial materials with liver tissue, using the newly introduced "tactile similarity error", a soft silicone elastomer was found that resembled liver best in terms of the tested properties.

On the other hand, tensile tests were conducted with similar testing protocols (ramp loading-unloading and stress relaxation) to define properties on a material level. The ramp loading-unloading stress-stretch data was analysed with a pseudo-hyperelastic Veronda-Westmann model and strain-specific tensile moduli were found. Viscoelastic properties were expressed in terms of storage modulus, loss modulus, and loss tangent, based on the stress relaxation data. Additionally, equivalent viscoelastic properties were measured with dynamic cyclic testing, in order to compare relaxation and cyclic testing. The results showed that stress relaxation and cyclic testing yielded comparable viscoelastic results, as long as non-linear behaviour was considered and tests were conducted at the same level of strain.

Based on these experimental methods, novel insight into tensile viscoelastic properties of fresh human, animal, and Thiel preserved liver was gained. Thus, differences between human and animal liver could be analysed and explained by their characteristic histological morphologies. Furthermore, Thiel preservation was found to be associated with tissue stiffening and decreased viscous behaviour.

Results from testing composite materials in macroindentation, revealed that combining different materials on a structural level is a promising strategy for fine-tuning mechanical properties to better match liver tissue. In order to design such composites,

a viscoelastic Mori-Tanaka model (vMTM) for homogenising effective properties of materials, exhibiting matrix-inclusion morphologies with soft viscoelastic phases, was developed. The vMTM was validated experimentally by testing samples, consisting of two soft silicones with varying inclusion volume fractions, for comparison with the vMTM predictions. Applying the developed vMTM, frequency dependent viscoelastic material properties of various soft silicone elastomers were then used as input quantities. The thereby resulting effective properties were compared to those of human and animal fresh liver from the tensile tests. Furthermore, it was assessed how well the effective properties matched other soft biological tissues, whose properties were previously reported in literature.

Finally, suitable microstructures of matrix-inclusion-type were identified, which exhibited very similar viscoelastic properties to certain soft biological tissues. These microstructures can hopefully be produced via additive manufacturing in future, thanks to recent developments in the field of soft material 3D printing.

The work, presented in this dissertation, provides new insight into the mechanical properties of liver parenchyma, based on rigorous experimental evaluation and computational analysis. Furthermore, microstructural material design for realistic anatomical models was presented, based on the viscoelastic Mori-Tanaka model. Therefore, the results of this dissertation can contribute to the production of more realistic soft tissue models, for instance for applications in medical education.

Acknowledgements

This work was carried out during my employment at the Karl Landsteiner University of Health Sciences and at the Austrian Center of Medical Innovation and Technology. I would like to thank the special people at the KL and ACMIT, without whom this dissertation would not have been possible. My deepest gratitude goes to my supervisors Dr. Andreas Reisinger and Prof. Dieter Pahr for their fruitful scientific discussions and constant support, but also their reassurance when things did not always go according to plan. Thank you to Dipl.-Ing. Nikolaus Dellantoni and Dr. Gernot Kronreif from ACMIT for providing valuable feedback and reminding me to always keep the overall goal in mind.

I would also like to thank Prof. Stéphane Avril and Prof. Stefan Scheiner for their time and effort for evaluating this dissertation.

Furthermore, I am grateful to Dr. Sophie Förster-Streffleur, Dr. Lena Hirtler, and Prof. Johannes Streicher for their valuable help in conducting experiments on human tissue and for providing me with interesting insights into human anatomy.

I would also like to thank all my fellow PhD students (especially Nedaa Amraish, Juan Diego Silva Henao, Othniel James Aryeetey, László Jaksa, and Alexandre Schmitt) for keeping research fun and always encouraging me to continue. Thank you, to our lab technician, Lukas Warnung, for all the help with conducting experiments and to our group secretaries, Christina Aaron and Maria Höpfner, for their administrative work.

My grateful acknowledgment is also owed to my funding sources, the Niederösterreichische Gesellschaft für Forschungsförderung (Science Call Dissertations 2017, SC17-016) and the TU Wien University Library for financial support through its Open Access Funding Program.

Finally, I am deeply grateful for the loving support from my friends and family. Thank you, Rubén and Johanna, for always believing in me and cheering me on along the way. Thank you so much, Mom, Dad, and Amy for giving me stability, love, and courage.

Publications

Peer reviewed journal publications

The contributions of **S.-J. Estermann** to the below listed publications included planning the studies and methodology, independently conducting the experiments, performing data analysis, and writing the manuscripts. As the head of the group and PhD supervisor, **D. H. Pahr** provided resources, infrastructure, project guidance, and reviewed manuscript drafts. **A. Reisinger** was responsible for overseeing the project progress as the primary supervisor, conceptualisation, and reviewing the manuscript drafts. **S. Förster-Streffleur**, **L. Hirtler**, and **J. Streicher** facilitated the experimental work, done with human tissue, by supplying fresh and preserved liver specimen and aiding in sample preparation.

S.-J. Estermann, D. H. Pahr, and A. Reisinger. Quantifying tactile properties of liver tissue, silicone elastomers, and a 3D printed polymer for manufacturing realistic organ models. *Journal of the Mechanical Behavior of Biomedical Materials* 104, 103630, April 2020.

S.-J. Estermann, D. H. Pahr, and A. Reisinger. Hyperelastic and viscoelastic characterisation of hepatic tissue under uniaxial tension in time and frequency domain. *Journal of the Mechanical Behavior of Biomedical Materials* 112, 104038, December 2020.

S.-J. Estermann, S. Förster-Streffleur, L. Hirtler, J. Streicher, D. H. Pahr, and A. Reisinger. Comparison of Thiel preserved, fresh human, and animal liver tissue in terms of mechanical properties. *Annals of Anatomy* 236, 151717, July 2021

S.-J. Estermann, D. H. Pahr, and A. Reisinger. Material design of soft biological tissue replicas using viscoelastic micromechanical modelling. currently under review in *Journal of the Mechanical Behavior of Biomedical Materials*.

Conference contributions

S.-J. Estermann, C. Müller-Guttenbrunn,D. H. Pahr, and A. Reisinger. Comparison of tactile properties of liver tissue and potential 3D printing materials via macroindentation. poster presentation at 11. Kongress der Deutschen Gesellschaft fr Biomechanik (DGfB), Berlin. April 03-05, 2019

S.-J. Estermann, C. Müller-Guttenbrunn, D. H. Pahr, and A. Reisinger. Macroindentation of liver tissue and 3D printing materials for comparison of tactile properties. oral presentation at 25th Congress of the European Society of Biomechanics, Vienna. July 07-10, 2019; in: Book of Abstracts of the 25th Congress of the European Society of Biomechanics, TU Verlag, (2019), ISBN: 978-3-903024-96-0; p. 230.

S.-J. Estermann, S. Förster-Streffleur, L. Hirtler, J. Streicher, D. H. Pahr, and A. Reisinger. Reisinger. Viscoelastic Properties of Human Liver Tissue: Influence of Thiel Preservation and Comparison with Animal Tissue. accepted for oral presentation at 26th Congress of the European Society of Biomechanics, Milan. July 11-14, 2021.

Contents

List of Figures

List of Tables

Nomenclature

Abbreviations

AM	additive manufacturing
DAQ	data acquisition module
DIC	digital image correlation
DMA	dynamic mechanical analysis
LVDT	linear variable differential transformer
MW	Maxwell
NaCl	sodium chloride
RMSE	root mean square error
RVE	representative volume element
SU	Shore units
vMTM	viscoelastic Mori-Tanaka model

Latin symbols

$\mathbb{A}_r$	concentration tensor of phase r (matrix $r = \mathrm{m}$, inclusion $r = \mathrm{i}$)
$\mathbf{b}$	left Cauchy-Green deformation tensor
c	model parameter in Veronda-Westmann model
$\mathbb{C}_{\mathrm{eff}}$	effective stiffness tensor
$\mathbb{C}_r$	stiffness tensor of phase r (matrix $r = \mathrm{m}$, inclusion $r = \mathrm{i}$)
$\mathbb{C}^*_{\mathrm{eff}}$	effective complex stiffness tensor
$\mathbb{C}^*_r$	complex stiffness tensor of phase r (matrix $r = \mathrm{m}$, inclusion $r = \mathrm{i}$)
$\mathbf{C}$	right Cauchy-Green deformation tensor
d	displacement
E^*	complex modulus
E'	storage modulus
E''	loss modulus
E_i	elastic modulus of spring element ($i = 1, 2, ...N$)
E_∞	longterm modulus
E_{I}	small strain modulus
E_{II}	large strain modulus
E_{III}	unloading modulus
F	force
$\mathbf{F}$	deformation tensor
f_r	volume fraction of phase r (matrix $r = \mathrm{m}$, inclusion $r = \mathrm{i}$)
H	Shore hardness
h	indentation height

I_i	strain invariants ($i = 1, 2, 3$)
$\mathbb{I}$	4th order unity tensor
$\mathbb{J}$	volumetric part of 4th order unity tensor
$\mathbb{K}$	deviatoric part of 4th order unity tensor
k	equivalent spring stiffness
k'	storage stiffness
k''	loss stiffness
k_∞	longterm spring stiffness
k_r	bulk modulus of matrix of phase r (matrix $r = \mathrm{m}$, inclusion $r = \mathrm{i}$)
l	gauge length
n	number of samples
$\mathbf{n}$	normal vector to a surface
$\mathbb{P}_{\mathrm{i,m}}$	Hill tensor of inclusion i embedded in matrix m
p	probability, p-value from t-test
Q	tactile similarity error
S	contact stiffness
$\mathbf{S}$	2nd Piola-Kirchoff stress tensor
t	time
$\mathbf{t}$	surface traction
u	displacement
V	volume
W_{dis}	dissipated energy
W_{st}	stored energy
$\mathbf{x}$	location vector

Greek symbols

α	level of significance
β	model parameter in Veronda-Westmann model
δ	phase shift
$\tan\delta$	loss tangent
ε	uniaxial strain
$\boldsymbol{\varepsilon}$	2nd order strain tensor
$\boldsymbol{\varepsilon}_r$	microscopic 2nd order strain tensor in phase r
$\mathbf{E}$	macroscopic 2nd order strain tensor
λ	stretch ratio
λ_i	principle stretches ($i = 1, 2, 3$)
μ_r	shear modulus of phase r (matrix $r = \mathrm{m}$, inclusion $r = \mathrm{i}$
μ_r^*	complex shear modulus of phase r (matrix $r = \mathrm{m}$, inclusion $r = \mathrm{i}$
μ_i	viscoelastic damping of dashpot elements ($i = 1, 2, ...N$)
ν	Poisson's ratio
σ	uniaxial stress
$\boldsymbol{\sigma}$	2nd order stress tensor
$\boldsymbol{\sigma}_r$	microscopic 2nd order stress tensor in phase r
$\boldsymbol{\Sigma}$	macroscopic 2nd order stress tensor
τ_i	relaxation times ($i = 1, 2, ...N$)
ψ	strain energy function
ω	angular frequency

Chapter 1

Introduction

1.1 Anatomical Models

Anatomical models are an important tool in the context of education, research, and medical instrument development. Depending on the application of the model, different requirements have to be met.

For instance, models with highly accurate anatomical features are necessary when teaching general anatomy or visible pathologies. These types of models demand high morphological resolution and need to *look* realistic. Therefore, such models are often made of hard plastics and are optically similar to the real organ, but exhibit unrealistic mechanical properties. Additive manufacturing has become popular for producing anatomically detailed models out of relatively hard polymers, that can either be standardised for medical instrument development and education [Salmi et al., 2013, Cai et al., 2018, Ye et al., 2020], or patient-specific for pre-operative planning [Starosolski et al., 2014, Anderson et al., 2016, Cherkasskiy et al., 2017, Mukherjee et al., 2017, Vukicevic et al., 2017]. Figure 1.1a depicts the anterior view of a 3D printed knee joint model, produced with the mulitmaterial printer Objet500 Connex3 (Stratasys Ltd., Eden Prairie, Minnesota), based on MRI imaging (Open knee(s): virtual biomechanical representations of the knee joint, SimTK). The ligaments and cartilage were printed with a more flexible material than the bone.

Other applications of anatomical models, however, require accurate mechanical properties. For instance, when practicing surgical procedures on artificial models it is important that the models *feel* realistic to the touch and behave appropriately during cutting and suturing. Regarding models of soft biological tissues, silicones or hydrogels (e.g. gelatine or alginate) are typically considered as tissue-mimicking materials in terms of mechanical properties [Madsen et al., 2005, Wang et al., 2014, Leibinger et al., 2016, Ismail et al., 2017]. These soft models are generally produced by moulding, with newer approaches using 3D printed moulds [Adams et al., 2017, Tejo-Otero et al., 2020]. Moulding, however, can turn into a very complicated procedure, especially when considering hollow organs. Figure 1.1b depicts a complex model of the pelvic region for surgical training of radical prostatectomy (ACMIT Gmbh, Wiener Neustadt, Austria).

Attempts have been made to combine the anatomical accuracy, provided by additive manufacturing, with realistic mechanical properties, by directly printing soft materials. However, even relatively soft commercially available 3D printing materials, are still quite different to actual tissues regarding haptics [Zein et al., 2013, Yoo et al.,

2017]. Therefore, progress in direct silicone 3D printing has been made, including a prostate model by Qiu et al. [2018] and a variety of organ models that can be acquired, ready-to-use, from Lazarus 3D (Houston, TX, USA) [Rundstedt et al., 2017]. However, recreating soft tissue mechanical properties is very challenging, due to their typically non-linear and viscoelastic behaviour. Thus, rigorous mechanical characterisation of the tissues, as well as the artificial materials, is necessary. To address this complex mechanical behaviour, microstructured multi-materials have been additively manufactured [Wang et al., 2016, Maier et al., 2019, Tarantino et al., 2019, Kwon et al., 2020], introducing new possibilities in material design.

With the difficulties, described in the context of producing anatomical models out of artificial materials, real biological tissues and organs are still widely used in medical education, surgical training, and development of medical devices [Yokoyama et al., 2003, Tang et al., 2005, Hildebrand et al., 2007, Laird et al., 2011]. Figure 1.1c, for instance, depicts a laparoscopic training system, consisting of the abdominal cavity of a mannequin which contains an externally perfused porcine liver [Liu et al., 2018]. Actual biological tissues—either from human donors or from animals—are presumably anatomically and mechanically similar to the *in vivo* situation. Nevertheless, the use of animal tissues is connected to major ethical issues, and possible differences between humans and animals, regarding mechanical properties and anatomy, must still be considered.

When using human cadavers for research and education, availability issues and the specific source of human cadavers are also reason for ethical concern [Halperin, 2007, Jones and Whitaker, 2011, Habicht et al., 2018]. In most western European countries, human cadavers, used for anatomy teaching, stem exclusively from voluntary donation programmes, where the donor gives informed consent during their lifetime for the use of their body in research and education [Habicht et al., 2018]. However, according to Habicht et al. [2018], unclaimed bodies are still the major source of cadavers for anatomical education, considering countries around the whole world. It is therefore important to further develop body donation programmes worldwide and enforce ethical standards in the cadaver procurement.

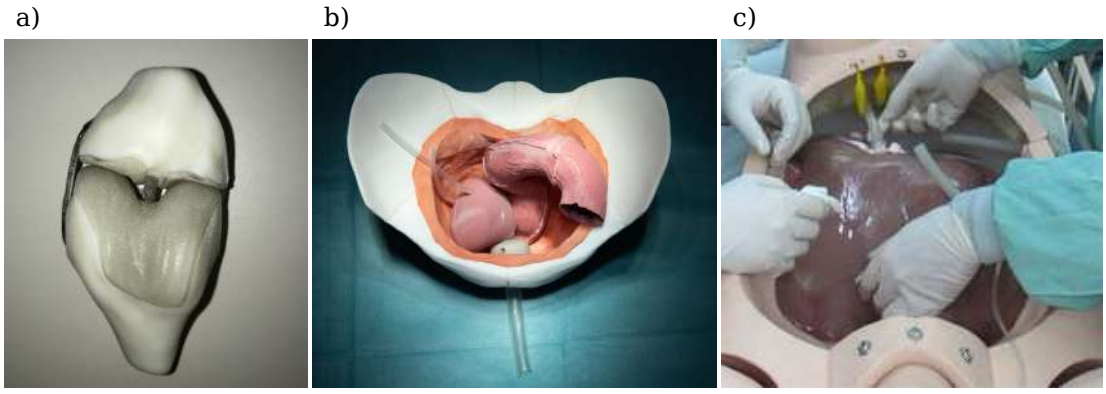

Figure 1.1: Examples of anatomical models for research and surgical training: (a) 3D printed multi-material knee joint model with ligaments and cartilage printed in a softer material than the bone; (b) Pelvic model for surgical training of radical prostatectomy (courtesy of ACMIT Gmbh); (c) Laparoscopic training system containing porcine liver (reprinted by permission from Springer Nature: Liu et al. [2018])

Human bodies, used for research and education, are normally not recently deceased, but preserved to prevent decay. For instance, human cadavers are routinely embalmed using formalin, which heavily alters mechanical tissue properties, making formalin cadavers unsuitable for surgical training [Hayashi et al., 2016]. Thus, for obtaining more realistic mechanical properties during embalming, newer strategies, such as the Thiel method [Thiel, 1992], were developed. Walter Thiel introduced his method for "the preservation of the whole corpse with natural color", aiming at conserving the pliant and elastic nature of soft biological tissues [Thiel, 1992]. However, a certain change in mechanical properties during Thiel preservation is still to be expected and remains to be quantified.

In order to avoid physical models all together, efforts have been made to develop virtual models of anatomical features. These models are predominantly used for surgical training, especially in the context of teleoperation and laparoscopy [Panait et al., 2006, Tsujita et al., 2013, Chen et al., 2020], or patient-specific preoperative planning [Reitinger et al., 2006]. While the former requires accurate mechanical properties to be incorporated into the model, using tactile feedback, the latter requires high morphological precision but not necessarily tactile feedback.

Figure 1.2 gives an overview of various options for creating anatomical models, concerning production, properties, and applications. In the context of models that require mechanical accuracy, meaningful mechanical properties and methods for experimentally measuring these need to be defined. For real feeling models, it is important to first ascertain which mechanical properties are actually significant in the context of tactile perception. Furthermore, it would be convenient if the material properties of artificial microstructural materials could be predicted, based on their structural morphology, in order to estimate similarity to biological tissues efficiently.

In this dissertation, it was attempted to characterise a certain organ rigorously in terms of mechanical properties, in order to facilitate the development of a mechanically accurate anatomical model for pre-surgical training.

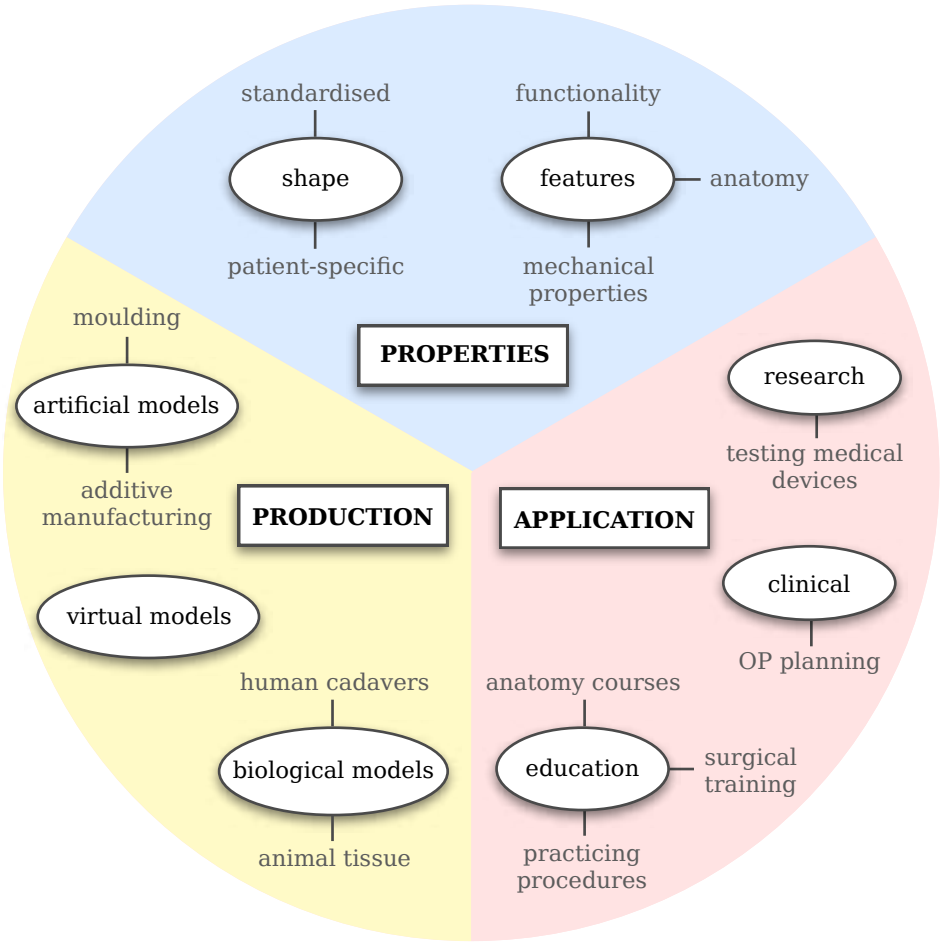

Figure 1.2: Anatomical models must meet different requirements concerning their properties (e.g. patient-specific or standardised, accurate mechanical properties, etc.), depending on their application (e.g. in research, clinical, or educational applications).These models are produced either out of artificial materials, biological materials, or exist only virtually.

1.2 The liver

In the context of anatomical models of soft tissues, challenges in replicating mechanical properties stem from non-linear and viscoelastic behaviour of the tissues. Liver tissue, specifically, is investigated in the following chapters since it exhibits behaviour, typical for other soft tissues. Furthermore liver models have important applications in surgical training systems, especially for laparoscopic procedures. Today, common procedures, such as cholecystectomy and hepatectomy, are widely done laparoscopically as opposed to open surgery approaches [Alli et al., 2017, Yoshida et al., 2019]. Appropriate training systems are a prerequisite for learning laparoscopic surgery which is connected to a unique set of challenges [Liu et al., 2018].

The liver, the largest gland in the human body, is located in the upper right abdomen below the diaphragm and above the stomach (Fig. 1.3). The main functions of the liver include detoxification of metabolites, regulation of glycogen storage, production of hormones and digestive fluids (e.g. bile for lipid digestion), and storage of blood [Jungermann, 1995].

Concerning vascularisation, the portal vein provides around two thirds of the liver's blood supply, delivering nutrient-rich blood, drained from lower abdominal organs (e.g. stomach, intestines, pancreas, and spleen). The remaining blood supply is covered by the hepatic arteries which carry oxygen-rich blood from the abdominal aorta [Lautt, 2009]. See Figure 1.3 for an overview of the liver anatomy and main blood vessels. Branching off the portal vein and the main hepatic arteries, smaller blood vessels lead to the functional units of the liver parenchyma tissue, called lobules (Figure 1.4). The liver lobules are 1–2 mm wide structures with approximately hexagonal cross-sections. They consist of cells (mainly hepatocytes and sinusoids), a central vein, and so-called portal triads at the edges (one portal venule, one hepatic arteriole, and one bile duct) [Crawford and Lui, 2010]. Bile is secreted by the hepatocytes and transported towards a nearby portal triad's bile duct from where it is passed to the gallbladder for storage. Blood from the portal venules and hepatic arterioles moves in the opposite way of bile, through the sinusoids towards the centre of the lobule. The sinusoids form a network of specialised vasculature and are surrounded by porous endothelial lining, which allows the passage of nutrients and oxygen to the surrounding hepatocytes [Braet and Wisse, 2002]. The pores, found in the sinusoidal endothelial lining, are referred to as fenestrae and their size varies between species [Wood, 1962, Higashi et al., 2002]. Finally, the blood, drained into the central vein, is collected by the hepatic veins and removed from the liver into the inferior vena cava [Sasse et al., 1992].

From an engineering point of view, liver parenchyma is a microstructured fluid-filled material, indicating that its mechanical behaviour is likely viscoelastic and non-linear. Hepatic parenchyma is often treated as isotropic and incompressible. Even though, these assumptions may be simplifications of the actual material properties, there is experimental evidence that liver parenchyma may indeed be isotropic [Chatelin et al., 2011, Pervin et al., 2011, Nguyen et al., 2012] and nearly incompressible [Chui et al., 2004].

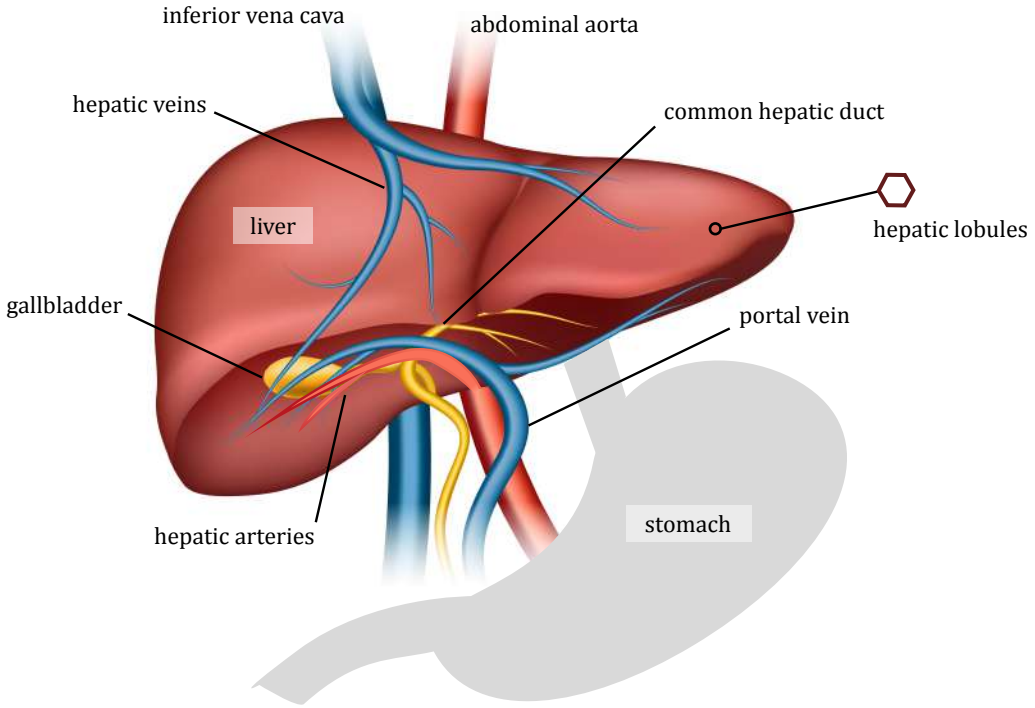

Figure 1.3: Human liver anatomy and blood supply; liver parenchyma consists of functional units called hepatic lobules (adapted from www.freepik.com).

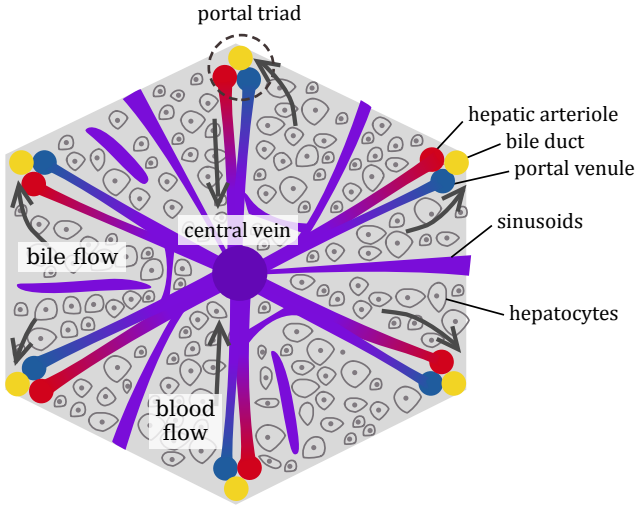

Figure 1.4: Schematic overview of the cross-section of a hepatic lobule: bile is produced in the hepatocytes and transported towards the bile ducts of the portal triads; blood is supplied by the portal venules and hepatic arterioles (branches of portal vein and hepatic artery) and flows through the sinusoids towards the central vein of the lobule.

1.3 Mechanical properties of liver tissue

Mechanical properties of hepatic parenchyma have been evaluated in tension [Brunon et al., 2010, Kemper et al., 2010, Lu et al., 2014, Duong et al., 2015, Dunford et al., 2018, Karimi and Shojaei, 2018], compression [Tamura et al., 2002, Kiss et al., 2004, Roan and Vemaganti, 2007, Ocal et al., 2010], shear [Nicolle et al., 2010, Tan et al., 2013, Wex et al., 2013, Ayyildiz et al., 2014, Capilnasiu et al., 2020], indentation [Ottensmeyer et al., 2004, Kerdok et al., 2006, Samur et al., 2007, Lu and Untaroiu, 2012, Li et al., 2019], and using elastography-based methods [Sandrin et al., 2003, Chatelin et al., 2011, Fang and Sidhu, 2020]. Typical mechanical behaviour of liver tissue thereby included non-linear stress-strain curves, hysteresis for loading and unloading, strain rate dependent behaviour, stress relaxation, and creep.

1.3.1 Hyperelasticity

Stress-strain curves of hepatic tissue, e.g. resulting from tensile tests, were found to be non-linear, exhibiting the toe-heel shape, typical for biological tissues [Fung, 1993, Chen et al., 1996]: For very small strains the stress-strain curve is approximately linear in the "toe" region, followed by the highly non-linear "heel" region for larger strains. Finally, when strains exceed the heel, another nearly linear region of high stiffness can be observed (see Figure 1.5). Therefore, different moduli must generally be given, depending on the level of strain. Furthermore, hyperelastic approaches can be utilized to approximate this non-linear behaviour, as has been done previously for liver tissue [Chui et al., 2004, Gao and Desai, 2010, Umale et al., 2013, Fu and Chui, 2014].

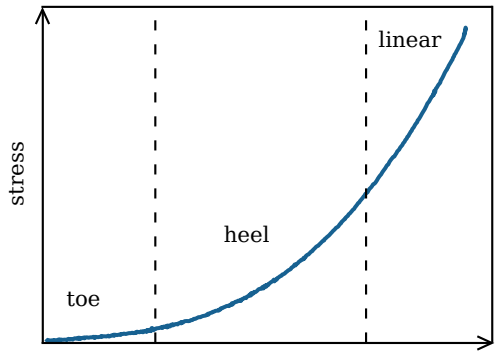

Figure 1.5: Typical non-linear behaviour of biological tissues during mechanical loading: Low stiffness nearly linear range in the toe region, non-linear heel region, and high stiffness nearly linear region.

Uniaxial tension of incompressible material

Hyperelasticity is based on the existence of the *strain energy function* Ψ for relating stress and strain of a non-linear elastic material. The 2nd Piola-Kirchhoff stress tensor $\mathbf{S}$ for an incompressible hyperelastic material, can be expressed, using the derivative of the strain energy function in respect to the components of the right Cauchy-Green deformation tensor $\mathbf{C}$ and the hydrostatic pressure p [Holzapfel, 2000],

$$\mathbf{S} = -p\,\mathbf{C}^{-1} + 2\frac{\partial \Psi}{\partial \mathbf{C}}\,. \tag{1.1}$$

The right Cauchy-Green deformation tensor is composed of the 2nd order gradient of deformation tensor $\mathbf{F}$, according to

$$\mathbf{C} = \mathbf{F}^{\mathrm{T}}\mathbf{F}\,, \tag{1.2}$$

while the left Cauchy-Green deformation tensor $\mathbf{b}$ is defined as

$$\mathbf{b} = \mathbf{F}\mathbf{F}^{\mathrm{T}}\,. \tag{1.3}$$

The gradient of deformation $\mathbf{F}$ describes the deformation of the material and is the derivative of a deformed state $\mathbf{x}$ in respect to the undeformed reference state $\mathbf{X}$. For uniaxial tension in x_1-direction of an incompressible material $\mathbf{F}$ is

$$\mathbf{F} = \frac{\partial \mathbf{x}}{\partial \mathbf{X}} = \begin{pmatrix} \lambda_1 & 0 & 0 \\ 0 & \lambda_2 & 0 \\ 0 & 0 & \lambda_3 \end{pmatrix} = \begin{pmatrix} \lambda & 0 & 0 \\ 0 & 1/\sqrt{\lambda} & 0 \\ 0 & 0 & 1/\sqrt{\lambda} \end{pmatrix} \tag{1.4}$$

with $\lambda_1 = \lambda$, $\lambda_2 = \lambda_3 = 1/\sqrt{\lambda}$ being the principle stretch ratios and its determinant $J = \det(\mathbf{F}) = 1$. Therefore, the right and left Cauchy-Green deformation tensor result in

$$\mathbf{C} = \mathbf{b} = \begin{pmatrix} \lambda^2 & 0 & 0 \\ 0 & 1/\lambda & 0 \\ 0 & 0 & 1/\lambda \end{pmatrix} \tag{1.5}$$

for uniaxial tension of an incompressible hyperelastic material.

The strain energy function is a function of strain invariants in an isotropic material, $\Psi = \Psi(I_1, I_2, I_3)$, and its derivative in Eq. 1.1 can be written as

$$\frac{\partial \Psi}{\partial \mathbf{C}} = \frac{\partial \Psi}{\partial I_1}\frac{\partial I_1}{\partial \mathbf{C}} + \frac{\partial \Psi}{\partial I_2}\frac{\partial I_2}{\partial \mathbf{C}} + \frac{\partial \Psi}{\partial I_3}\frac{\partial I_3}{\partial \mathbf{C}}\,. \tag{1.6}$$

The strain invariants for isotropic material are calculated as the eigenvalues of the right Cauchy-Green deformation tensor and their respective derivatives result in [Holzapfel, 2000]

$$I_1 = \mathrm{tr}(\mathbf{C})\,, \quad \frac{\partial I_1}{\partial \mathbf{C}} = \mathbf{I}\,, \tag{1.7}$$

$$I_1 = \frac{1}{2}\left[(\mathrm{tr}(\mathbf{C}))^2 + \mathrm{tr}(\mathbf{C}^2)\right], \quad \frac{\partial I_2}{\partial \mathbf{C}} = I_1\mathbf{I} - \mathbf{C}\,, \tag{1.8}$$

and

$$I_1 = \det(\mathbf{C})\,, \quad \frac{\partial I_1}{\partial \mathbf{C}} = I_3\mathbf{C}^{-1}\,. \tag{1.9}$$

Inserting Eqs 1.7 – 1.9 into Eq. 1.6 and then into Eq. 1.1, yields

$$\mathbf{S} = -p\mathbf{C}^{-1} + 2\Big[\Big(\frac{\partial \Psi}{\partial I_1} + I_1\frac{\partial \Psi}{\partial I_2}\Big)\mathbf{I} - \frac{\partial \Psi}{\partial I_2}\mathbf{C} + I_3\frac{\partial \Psi}{\partial I_3}\mathbf{C}^{-1}\Big]\,. \tag{1.10}$$

Next, the Cauchy stress tensor is calculated, based on its definition $\boldsymbol{\sigma} = \frac{1}{J}\mathbf{F}\mathbf{S}\mathbf{F}^{\mathrm{T}}$, using Eqs. 1.10, 1.2, and 1.3,

$$\boldsymbol{\sigma} = -p\mathbf{I} + 2\Big[\Big(\frac{\partial \Psi}{\partial I_1} + I_1\frac{\partial \Psi}{\partial I_2}\Big)\mathbf{b} - \frac{\partial \Psi}{\partial I_2}\mathbf{b}^2 + I_3\frac{\partial \Psi}{\partial I_3}\mathbf{I}\Big]\,, \tag{1.11}$$

with $J = 1$ for incompressible material. Subsequently, the strain invariants under uniaxial tension,

$$I_1 = \lambda^2 + \frac{2}{\lambda}\,, \tag{1.12}$$

$$I_2 = 2\lambda + \frac{2}{\lambda^2}\,, \tag{1.13}$$

and

$$I_3 = 1\,, \tag{1.14}$$

are inserted into 1.11. A solution for the hydrostatic pressure p is found, using the boundary conditions for uniaxial tension ($\sigma_1 = \sigma$, $\sigma_2 = \sigma_3 = 0$), finally yielding the Cauchy stress in loading direction as

$$\sigma = 2\Big(\lambda^2 - \frac{1}{\lambda}\Big)\Big(\frac{\partial \Psi}{\partial I_1} + \frac{1}{\lambda}\frac{\partial \Psi}{\partial I_2}\Big)\,, \tag{1.15}$$

depending on the strain energy function. Thus, the next step is to find the strain energy function $\Psi(I_1, I_2, I_3)$, suitable for representing the behaviour of the hyperelastic material.

Strain energy function for hepatic tissue

The strain energy function $\Psi(I_1, I_2, I_3)$ in Eq. 1.15 must be selected, based on thermodynamic, symmetry, and energy considerations. Historically, different strain energy functions were first proposed for modelling the hyperelastic behaviour of soft rubbers [Mooney, 1940, Treloar, 1943, Rivlin and Rideal, 1948, Yeoh, 1993]. Since then, however, the same models and improved approaches have been applied to soft biological tissues as well (overview given by [Chagnon et al., 2017]).

Hyperelasticity of liver tissue has been modelled using various strain energy functions, as can be seen in Table 1.1. In general, the strain energy functions can be classified as polynomial (e.g. Neo-Hookean, Mooney-Rivlin, Ogden, Yeoh), exponential (e.g. Fung-Demiray), or polynomial combined with exponential (e.g. Veronda-Westmann). According to Chui et al. [2004], who tested a variety of hyperelastic models for uniaxial tension and compression of hepatic tissue, the Mooney-Rivlin model had the lowest root mean square error, compared to the experimental data, however, only if 9 constants were used. The advantage of exponential models, as opposed to polynomial ones, is their small number of required fitting parameters. Combining polynomial and exponential approaches, yields models that have only a small number of fitting parameters, while still agreeing well with experimental liver data [Chui et al., 2004, Marchesseau et al., 2017]. An example of such a combined model is the Veronda-Westmann model, initially suggested by Veronda and Westmann [1970] for feline skin.

Figure 1.6 depicts different hyperelastic models (Neo-Hookean, 2-element Mooney-Rivlin, Veronda-Westmann, and 3-element Yeoh), applied to the stress-stretch loading part of bovine liver sample under uniaxial tension (see Appendix 3.8.1 [Estermann et al., 2020b]). Both, the Yeoh and Veronda-Westmann strain energy functions matched the experimental data very well, with coefficients of determination of $r^2 = 0.9998$ and $r^2 = 0.9980$, respectively. However, the Veronda-Westmann model requires only two fitting parameters, compared to three parameters, needed for the Yeoh model.

Table 1.1: Hyperelastic models with corresponding strain energy functions (for uniaxial tension and incompressibility) that have previously been used for liver tissue in the given references.

Material model	Strain energy function	Material constants	Reference
Neo-Hookean	$\Psi = c_1(I_1 - 3)$	c_1	Chui et al. [2004], Fu and Chui [2014]
Mooney-Rivlin	$\Psi = \sum_{i+j>0}^{N} c_{ij}(I_1 - 3)^i(I_2 - 3)^j$	c_{ij}	Umale et al. [2013], Fu and Chui [2014] Chui et al. [2004]
Ogden*	$\Psi = \sum_{i=1}^{N} \frac{2c_i}{\alpha_i^2}(\lambda^{\alpha_i} + 2\lambda^{-\alpha_i/2} - 3)$	c_i, α_i	Gao and Desai [2010], Umale et al. [2013]
Yeoh	$\Psi = \sum_{i=1}^{N} c_i(I_1 - 3)^i$	c_i	Nafo and Al-Mayah [2021]
Fung-Demiray	$\Psi = \frac{c_1}{c_2}\left(e^{c_2(I_1-3)} - 1\right)$	c_1, c_2	Chui et al. [2004]
Veronda-Westmann	$\Psi = c\left(\mathrm{e}^{\beta(I_1-3)} - 1\right) - c\frac{\beta}{2}(I_2 - 3)$	c, β	Chui et al. [2004], Roan and Vemaganti [2011]

* The strain energy function of the Ogden model depends on the principle stretches, instead of the strain invariants. Thus, the given relation can not be directly inserted into Eq. 1.15.

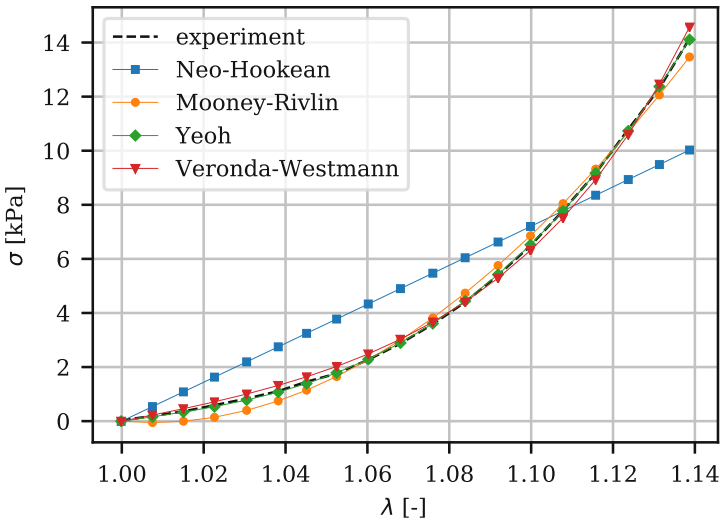

Figure 1.6: True stress-stretch curve of a bovine liver sample during loading sequence (dashed line), fitted with different hyperelastic models [Estermann et al., 2020b].

1.3.2 Pseudohyperelasticity

Hyperelastic models match liver behaviour under uniaxial conditions well, considering loading (see Table 1.1). However, experiments, that include not only the loading stress-strain behaviour but also the unloading part, exhibit hysteresis (Figure 1.7), which is an indication of energy dissipation. Purely hyperelastic approaches assume completely elastic material, meaning that loading and unloading would occur along the same curve. Thus, pseudohyperelastic modelling was suggested by Fung et al. [1979] for describing the hysteresis, observed in preconditioned cyclic tension of rabbit arteries. The loading and unloading parts of the stress-strain curve are thereby treated separately with two distinct hyperelastic models, yielding two sets of material parameters for their characteristic loading and unloading behaviour (Figure 1.7). Fung et al. [1979] pointed out that pseudohyperelasticity can not be considered to be an intrinsic material property, but rather a convenient method for describing the complex mechanical behaviour of soft tissues under specific loading conditions.

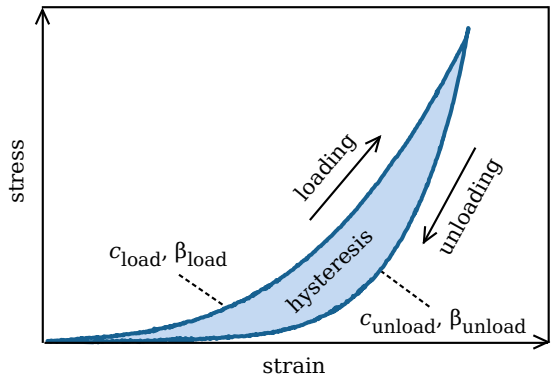

Figure 1.7: Hysteresis between loading and unloading, signifying energy dissipation, observed for liver tissue. According to the pseudoelastic model, the loading and unloading parts are modelled with different characteristic parameters (e.g. c_{laod}, β_{load} and c_{unlaod}, β_{unload} for the Veronda-Westmann model).

1.3.3 Viscoelasticity

Viscoelastic materials respond to applied strains with time dependent stresses, due to the composition of their internal structure. When a viscoelastic material is deformed, the applied work, causing the deformation, is partially dissipated as heat and partially stored as elastic energy. Thus, in a ramp loading-unloading sequence, the stress-strain curve of the unloading part follows a different path, compared to the loading part (Figure 1.7). For characterising viscoelastic properties, different testing modalities can be applied.

- During repeated cyclic loading-unloading, for instance in form of a sinusoidal strain, the stress-strain relation reaches a steady state after a certain number of cycles. Plotted over time, the stress response is also sinusoidal with the same frequency as the applied strain, but lagging behind by a phase δ (Figure 1.8a). Since the phase lag is dependent on the excitation frequency, sine waves of different frequencies are applied, which is referred to as dynamic mechanical analysis (*DMA*).

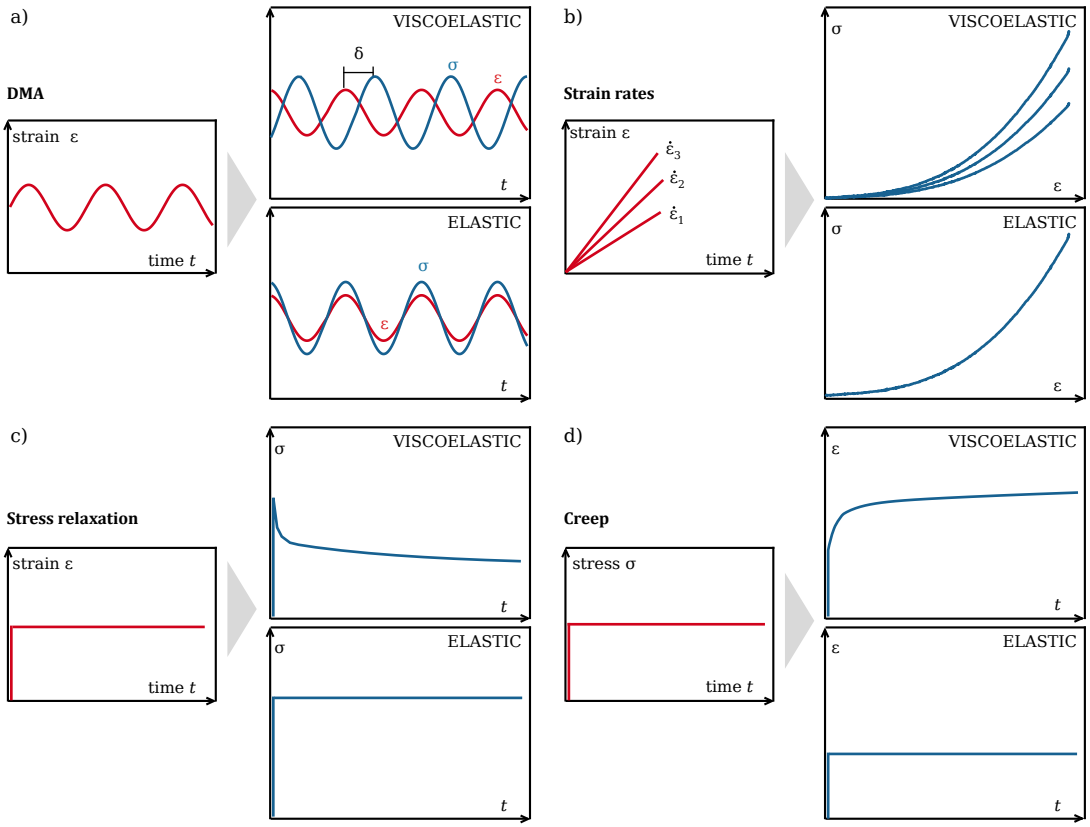

Figure 1.8: Typical behaviour of viscoelastic material, compared to the elastic material response, during different loading conditions: (a) Dynamic sinusoidal strain; (b) Ramp tests with different strain rates; (c) Constant strain, causing stress relaxation; (d) Constant stress, causing creep.

- Another typical characteristic of viscoelastic materials, is that their stress response varies, depending on the applied *strain rate*. For instance, the viscoelastic material might become stiffer in response to faster strain rates (Figure 1.8b).
- Furthermore, if the applied strain is held constant for a period of time, a decline in stress can be observed, referred to as *stress relaxation* (Figure 1.8c).
- Likewise, if stress is applied and held constant, strain increases over time, referred to as *creep* (see Figure 1.8d).

Linear viscoelasticity is generally measured, utilizing dynamic cyclic tests (dynamic mechanical analysis), different strain rates, stress relaxation, or creep [Findley et al., 1989, Lakes, 1998, Gutierrez-Lemini, 2014]. In this context, *linear viscoelasticity* means that the viscoelastic properties are not dependent on the magnitude of loading up to a certain limit of linear viscoelasticity. Special focus is placed on the methods DMA and stress relaxation in this dissertation.

Dynamic mechanical analysis

Dynamic mechanical analysis (DMA) is the gold standard in assessing viscoelastic properties, since the relevant properties can be directly extracted from the experimental data, without requiring any additional models. A linear viscoelastic material,

subjected to a uniaxial sinusoidal tensile strain $\varepsilon(t)$

$$\varepsilon(t) = \varepsilon_{\mathrm{A}} \sin(\omega t)\,, \tag{1.16}$$

with the amplitude ε_{A} and angular frequency ω, provokes a sinusoidal stress response $\sigma(t)$ with amplitude σ_{A} of the same frequency, but phase shifted by δ,

$$\sigma(t) = \sigma_{\mathrm{A}} \sin(\omega t + \delta)\,, \tag{1.17}$$

which can alternatively be written as

$$\sigma_{\mathrm{A}} \sin(\omega t + \delta) = \sigma_{\mathrm{A}} \sin(\omega t)\cos(\delta) + \sigma_{\mathrm{A}} \cos(\omega t)\sin(\delta)\,. \tag{1.18}$$

The first term in Eq. 1.18 is in phase with the applied strain, while the second term is out of phase. Now, the *storage modulus* E' and *loss modulus* E'' are introduced as a measure of the in phase (E') and out of phase (E'') contributions to the stress response [Kelly, 2015] as

$$E' = \frac{\sigma_{\mathrm{A}}}{\varepsilon_{\mathrm{A}}} \cos(\delta) \tag{1.19}$$

and

$$E'' = \frac{\sigma_{\mathrm{A}}}{\varepsilon_{\mathrm{A}}} \sin(\delta)\,, \tag{1.20}$$

yielding the stress response,

$$\sigma(t) = \varepsilon_{\mathrm{A}} E' \sin(\omega t) + \varepsilon_{\mathrm{A}} E'' \cos(\omega t)\,. \tag{1.21}$$

Figure 1.9a plots the stress and strain relation of a viscoelastic material, exposed to steady state sinusoidal cyclic loading. For a completely elastic material there is no phase lag between stress and strain, $\delta = 0$: The storage modulus reduces to the Young's modulus $E' = \frac{\sigma_{\mathrm{A}}}{\varepsilon_{\mathrm{A}}}$, while the loss modulus disappears $E'' = 0$, and the stress response in Eq. 1.21 is completely in phase with the applied strain. In Figure 1.9a, loading and unloading would occur along the same straight line, without hysteresis. For a completely viscous fluid, the phase lag becomes $\delta = 90°$: The storage modulus disappears $E' = 0$, leaving only the loss modulus as $E'' = \frac{\sigma_{\mathrm{A}}}{\varepsilon_{\mathrm{A}}}$, and the stress response is completely out of phase. A viscoelastic material has a phase lag between $0 - 90°$ and is dependent on the excitatory frequency ω. Typically, the phase lag is expressed as the *loss tangent*

$$\tan\delta(\omega) = \frac{E''(\omega)}{E'(\omega)}\,. \tag{1.22}$$

The time dependent stress and strain functions in Eqs. 1.16 and 1.17 can also be written as complex exponential functions [Jalocha et al., 2015] with

$$\varepsilon^* = \varepsilon_{\mathrm{A}} e^{i\omega t} \tag{1.23}$$

and

$$\sigma^* = \sigma_{\mathrm{A}} e^{i\omega t + \delta} \tag{1.24}$$

For the harmonic oscillation of the linear viscoelastic material, the frequency dependent *complex modulus* $E^*(\omega)$ connects the strain and stress functions [Jalocha et al., 2015], according to

$$E^*(\omega) = \frac{\sigma^*}{\varepsilon^*}\,. \tag{1.25}$$

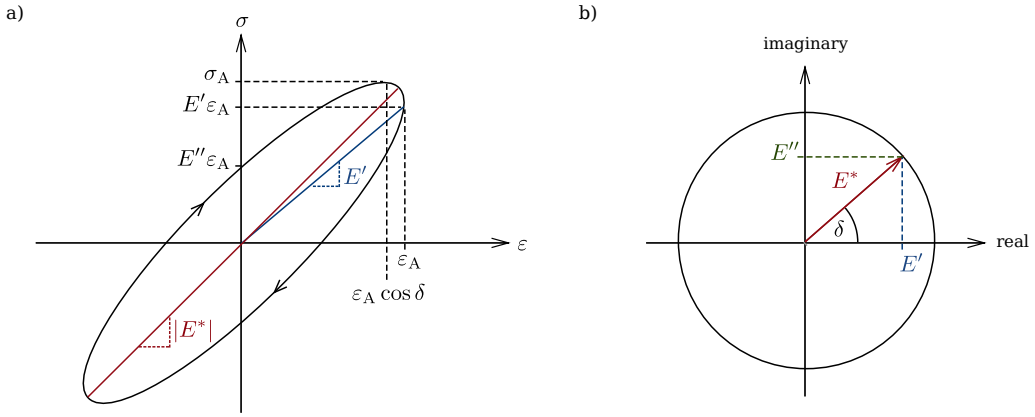

Figure 1.9: (a) Hysteresis loop for one cycle of sinusoidal loading during steady state cyclic testing; (b) Complex modulus E^*, plotted with its real and imaginary components (storage E' and loss E'' modulus).

Inserting the strain and stress functions, as given in Eqs. 1.23 and 1.24, into 1.25 yields the complex modulus as,

$$\begin{aligned} E^*(\omega) &= \frac{\sigma_A e^{i\omega t+\delta}}{\varepsilon_A e^{i\omega t}} = \frac{\sigma_A}{\varepsilon_A} e^{i\delta} \\ &= \frac{\sigma_A}{\varepsilon_A}\cos\delta + i\frac{\sigma_A}{\varepsilon_A}\sin\delta\,, \end{aligned} \tag{1.26}$$

using Euler's formula. Finally, the complex modulus (plotted in Figure 1.9b) can be written as a complex quantity with its components being the storage modulus $E'(\omega)$, according to Eq. 1.19, as real part and the loss modulus $E''(\omega)$, according to Eq. 1.20, as imaginary part,

$$E^*(\omega) = E'(\omega) + iE''(\omega)\,. \tag{1.27}$$

Besides, $E'(\omega)$, $E''(\omega)$, and $\tan\delta(\omega)$, the absolute value of the complex modulus

$$|E^*(\omega)| = \sqrt{E'(\omega)^2 + E''(\omega)^2} \tag{1.28}$$

is also a commonly used viscoelastic material property.

Stress relaxation

Stress relaxation is observed when a viscoelastic material is strained with a constant strain ε_0 and is characterised by a decline in stress over a period of time $\sigma(t)$. If a tensile strain is applied instantaneously at $t = 0$, as a step function, the corresponding stress immediately rises to $\sigma(0)$ and then decreases. In this case, stress and strain are related by the relaxation function $E(t)$,

$$\sigma(t) = E(t)\varepsilon_0\,. \tag{1.29}$$

The relaxation function $E(t)$ is typically defined, using rheological models, consisting of elastic spring elements with modulus E_i and viscous dashpot elements with viscosity μ_i, arranged in parallel and serial configurations. The most simple rheological models are the Maxwell and Kelvin models (Figure 1.10a–b), which consist of one spring

E and one dashpot μ in series (Maxwell) and parallel (Kelvin), or the Zener model which is a combination of the two (Figure 1.10c). Furthermore, the Zener model can be extended by adding N more parallel Maxwell branches, yielding the generalised Maxwell model (Figure 1.10d).

In parallel configurations, the strain is the same in all branches and stresses are added up, while for elements in series, the strains are added up and the stresses of the individual elements are the same. For instance, considering the Zener model, the the overall strain ε and stress σ, expressed in terms of the model components (one Maxwell element MW, parallel to the long-term spring element E_∞) as

$$\varepsilon = \varepsilon_\infty = \varepsilon_{\mathrm{MW}} \tag{1.30}$$

and

$$\sigma = \sigma_\infty + \sigma_{\mathrm{MW}}\,. \tag{1.31}$$

Stress is related linearly to strain in the individual spring elements ($\sigma_{\mathrm{spring}} = E_i\varepsilon_{\mathrm{spring}}$) and related linearly to strain rate in dashpot elements ($\sigma_{\mathrm{dashpot}} = \mu_i\dot{\varepsilon}_{\mathrm{dashpot}}$). In order to insert the dashpot strain into Eq. 1.30, which occurs as a time derivative, Laplace transformation is applied. In general, the Laplace transform of the function $f(t)$ of time t to $\bar{f}(s)$ of the complex variable s, is calculated with

$$\bar{f}(s) = \int_0^\infty f(t)e^{-st}\mathrm{d}t\,. \tag{1.32}$$

Stress of a spring element, accordingly, transforms to $\bar{\sigma}(s)_{\mathrm{spring}} = E_i\bar{\varepsilon}_{\mathrm{spring}}(s)$ and stress of a dashpot element transforms to $\bar{\sigma}(s)_{\mathrm{dashpot}} = s\mu\bar{\varepsilon}_{\mathrm{dashpot}}$ in the Laplace domain. Setting the Laplace variable $s = i\omega$ (Laplace transform becomes equivalent to Fourier transform), Eq. 1.30 can now be written as

$$\bar{\varepsilon}(i\omega) = \frac{\bar{\sigma}_\infty(i\omega)}{E_\infty} = \frac{\bar{\sigma}_{\mathrm{MW}}(i\omega)}{E_1} + \frac{\bar{\sigma}_{\mathrm{MW}}(i\omega)}{i\omega\mu_1}\,. \tag{1.33}$$

Next, $\bar{\sigma}_{\mathrm{MW}}(i\omega)$ from Eq. 1.31 is written in Laplace domain as

$$\bar{\sigma}_{\mathrm{MW}}(i\omega) = \bar{\sigma}(i\omega) - E_\infty\bar{\varepsilon}(i\omega)\,, \tag{1.34}$$

and inserted into Eq. 1.33. Reorganising in terms of the ratio between stress and strain $\bar{\sigma}/\bar{\varepsilon}$, yields the complex modulus $E^* = E' + iE''$, consisting of the real part E' and imaginary part E'' [Lakes, 1998]:

$$\frac{\bar{\sigma}(i\omega)}{\bar{\varepsilon}(i\omega)} = E^*(\omega) = E_\infty + \frac{E_1^2\omega^2\mu_1^2}{E_1^2+\omega^2\mu_1^2} + i\frac{E_1^2\omega\mu_1}{E_1^2+\omega^2\mu_1^2}\,. \tag{1.35}$$

Storage and loss stiffness $E'(\omega)$ and $E''(\omega)$, utilizing relaxation times $\tau_1 = \mu_1/E_1$, for the Zener model are finally given by

$$E'(\omega) = E_\infty + \frac{E_1\omega^2\tau_1^2}{1+\omega^2\tau_1^2} \tag{1.36}$$

and

$$E''(\omega) = \frac{E_1\omega\tau_1}{1+\omega^2\tau_1^2} \tag{1.37}$$

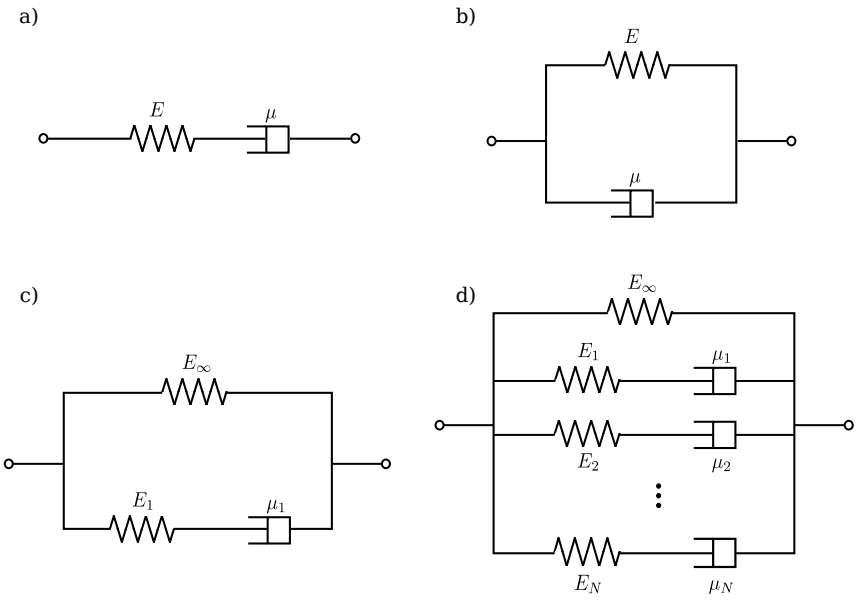

Figure 1.10: Common rheological models, used for describing material viscoelastic behaviour: (a) Maxwell model; (b) Kelvin model; (c) Zener model; (d) Generalised Maxwell model.

with the ratio between the two yielding the loss tangent

$$\tan\delta(\omega) = \frac{E''(\omega)}{E'(\omega)}\,. \tag{1.38}$$

Now considering the generalised Maxwell model with N Maxwell branches instead of one, storage modulus an loss modulus, can be calculated in an equivalent way, yielding

$$E'(\omega) = E_\infty + \sum_{i=1}^{N} \frac{E_i\omega^2\tau_i^2}{1+\omega^2\tau_i^2} \tag{1.39}$$

and

$$E''(\omega) = \sum_{i=1}^{N} \frac{E_i\omega\tau_i}{1+\omega^2\tau_i^2}\,. \tag{1.40}$$

In time domain, the relaxation function of the generalised Maxwell model $E(t)$ corresponds to a Prony series function with N elements [Findley et al., 1989],

$$E(t) = E_\infty + \sum_{i=1}^{N} E_i e^{-\frac{t}{\tau_i}}\,, \tag{1.41}$$

which can be fitted to experimental data of stress relaxation for identifying the rheological model parameters E_∞, E_i, and τ_i. The obtained rheological model parameters can subsequently be used for computing the viscoelastic properties E', E'', and $\tan\delta$ (Eq. 1.39, Eq. 1.40, and Eq. 1.38).

Creep, expressed as strain in terms of a function of time, is usually evaluated analogously to stress relaxation, based on a suitable rheological model (Figure 1.10). Similar to stress relaxation, creep methods have been utilized predominantly in shear

[Kobayashi et al., 2017], compression [Kiss et al., 2004], or indentation [Kerdok et al., 2006], as opposed to tension, concerning the viscoelasticity of liver tissue.

Strain rate approaches have been applied to evaluate liver viscoelasticity in tension [Kemper et al., 2010, Lu et al., 2014, Dunford et al., 2018]. However, these studies do not report linear viscoelastic properties (such as E', E'', and $\tan\delta$), but instead, how failure stress and strain depend on the variation of strain rate.

In this dissertation, stress relaxation and DMA are applied in indentation and tension, in order to evaluate linear viscoelastic properties. In case of DMA, viscoelastic properties $E'(\omega)$, $E''(\omega)$, $E^*(\omega)$, and $\tan\delta(\omega)$ are typically measured for different frequencies ω. When using rheological models for the interpretation of stress relaxation tests, the viscoelastic properties $E'(\omega)$, $E''(\omega)$, $E^*(\omega)$, and $\tan\delta(\omega)$ are calculated for different ω. The comparison between viscoelastic properties, measured with the two methods, is interesting: On the one hand, the above described stress relaxation approach includes certain assumptions and simplifications, but is experimentally convenient for soft biological tissue in tension. On the other hand, DMA is the gold standard in viscoelastic testing, but is connected to experimental difficulties [Estermann et al., 2020b].

1.4 Mechanical testing of liver tissue

In this dissertation, liver tissue was tested with two different test setups: On the one hand, *macroindentation* was conducted to mimic tissue manual palpation, and on the other hand *tensile tests* were conducted to extract pseudoelastic and viscoelastic properties on the material level. However, there are many challenges associated with handling liver tissue during mechanical testing.

1.4.1 Challenges

Cutting uniform samples out of the whole liver is difficult, since the tissue is highly deformable and the overall thickness of the organ is not constant (Figure 1.11a). Liver parenchyma is highly vascularised, and if homogenous samples are required, large blood vessels need to be avoided during sample production (Figure 1.11b). Previously, authors have attempted to use frozen livers for extracting mechanical test specimen [Tamura et al., 2002]. However, studies have shown that liver tensile mechanical properties are influenced by freeze-thaw cycles [Ocal et al., 2010, Nguyen et al., 2012, Lu et al., 2014]. Concerning compression and shear, the influence of freezing seems to become negligible for liver [Tamura et al., 2002, Wex et al., 2014]. Furthermore, non-frozen cooled storage up to one week before sample preparation does not seem to alter liver mechanical properties [Duong et al., 2015], as opposed to other soft tissues, such as spleen or kidney [Nguyen et al., 2012, Duong et al., 2015]. The reason why liver properties are more robust against prolonged storage, compared to other soft biological tissues, is the extremely low content of elastin in liver [Neuman and Logan, 1950]. Elastin autolysis seems to be the main reason for the deterioration of mechanical properties in elastin-rich organs [Nguyen et al., 2012].

Besides sample preparation, fixation of liver samples in mechanical testing machine is also challenging. For tensile tests, especially if the tissue is to be tested with large strains until failure [Kemper et al., 2010], care must be taken to avoid slippage or destruction at the interface between tissue and clamp. For compression and indentation

tests, unclear boundary conditions between compression plate or indenter and tissue could cause problems in evaluating the data.

Furthermore, measured displacements, during tensile testing, should not be based on the cross-head displacement of the machine alone, due to clamping effects and stiffness of the testing machine. Instead, it is recommendable to utilise optical measuring systems, such as digital image correlation (DIC) [Gao and Desai, 2010].

Finally, it should also be noted that *in vitro* testing neglects perfusion, which most likely plays a significant role in such a highly vascularised and perfused tissue as liver [Kerdok et al., 2006]. However, the scope of this dissertation was to assess possible tissue replica materials and, therefore, the required material properties were not extracted *in vivo*.

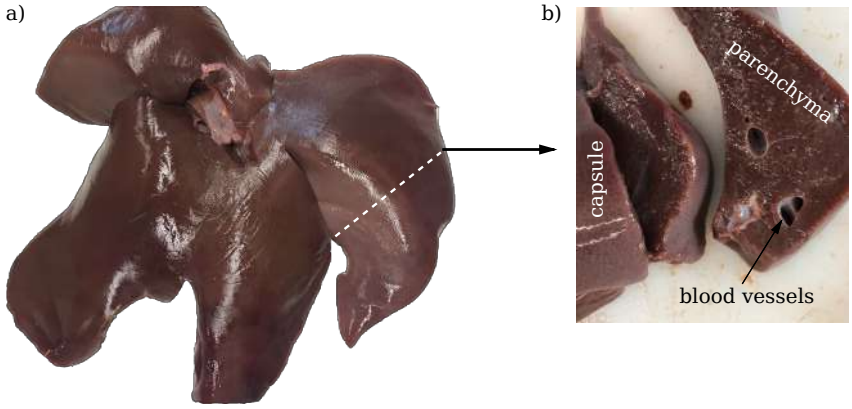

Figure 1.11: (a) Whole porcine liver covered in hepatic capsule tissue; (b) Inner structure, consisting of soft parenchyma tissue, revealed after cutting the liver open.

1.4.2 Indentation

Indentation typically relates the displacement h of an indenter tip, moving into a sample, with the corresponding reaction force $F(h)$ exerted by the material (see Figure 1.12a). The starting point, relative to which h is measured, is the undeformed reference state ($h = 0$ and $F(h) = F_0$). Based on resulting force-displacement curves or force-time curves (for constant displacement), different structural mechanical properties can be extracted.

For identifying properties on a material level, force must be converted to stress and displacement to strain, which requires assumptions, concerning the contact area and interaction between sample and indenter. Selecting the appropriate contact model is not a trivial problem, since indenter shape, surface roughness, and adhesion between the sample and indenter can be incorporated into the model. Frequently used models for indentation of soft biological tissue include the Oliver-Pharr model [Oliver and Pharr, 1992] or the Hertzian model [Hertz, 1882, Fischer-Cripps, 1999].

Indentation-based strategies have previously been applied for mechanical testing of liver tissue. For instance, scale-dependant mechanical properties of liver parenchyma were evaluated, utilizing nanoindentation and macroindentation [Evans et al., 2013, Wu et al., 2020]. Macroindentation differs from nanoindentation in that the utilized, usually spherical, indenters are much larger, with diameters in the range of a few millimetres. Previously, macroindentation has been used for simulating prostate palpation

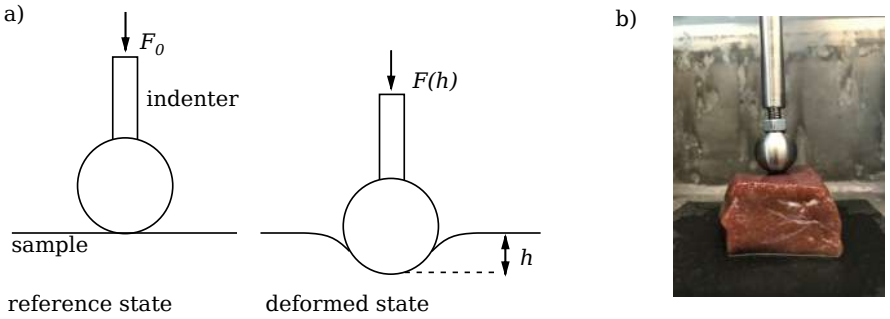

Figure 1.12: (a) Schematic overview of the indentation test; (b) Porcine liver sample, tested under macroindentation

to identify tissue abnormalities [Carson et al., 2011, Ahn et al., 2012, Palacio-Torralba et al., 2015] and in the context of developing virtual surgical training systems with haptic feedback [Lim et al., 2009, Takács et al., 2017]. Figure 1.12b depicts a porcine liver sample, exposed to macroindentation.

It should be noted, that indentation-based methods are susceptible to substrate effects, stemming from the surface under the sample. To address this issue, the sample must be sufficiently thick, in relation to the indentation depth. According to Carson et al. [2011], prostate tissue can be indented with a macroindenter up to 30% sample thickness, without measuring substrate effects. Furthermore, inhomogeneities within the sample can influence the measurement. Therefore, samples should be homogeneous, considering the size scale of the indenter.

In general, macroindentation is a good method for *comparing* materials with each other, that were tested with the same procedure on samples of the same geometry [Zhao et al., 2020]. Due to the method being relatively simple, it can be applied to samples of various sizes and shapes and allows testing biological tissues under different environmental conditions (e.g. perfused or wet liver [Ottensmeyer et al., 2004, Kerdok et al., 2006, Li et al., 2019]). For quantitatively *describing* mechanical properties of soft tissues on a material level, tensile testing avoids some of the challenges of indentation.

1.4.3 Tensile testing

In tensile testing, a sample is generally fixed between two clamps, securing it to a mechanical testing machine, and then exposed to uniaxial displacement (or force) by movement of the machine cross-head (Figure 1.13). The responding force F (or displacement) is measured and related to the subscribed quantity. Since the machine displacement, u_{M}, contains contributions from the machine stiffness and clamping effects (e.g. sample slippage), displacements, u_{T}, must be measured in the tissue, preferably with non-contact methods. Digital image correlation is a practical method for measuring displacements in soft tissues: A measuring length is defined with marker pairs on the tissue sample, ensuring sufficient distance from the clamps to exclude non-uniform displacements. The movement of these markers is tracked during testing by a camera system, recording the current length l between the marker pairs. Relating the change in length, in regard to the original measuring length l_0, gives the tissue displacement $u_{\mathrm{T}} = l - l_0$. Generally, more than one marker pair is applied, in order to verify whether displacements were, indeed, uniform along the sample width. See Figure 1.13a for an overview of the measured and applied quantities and Figure 1.13b

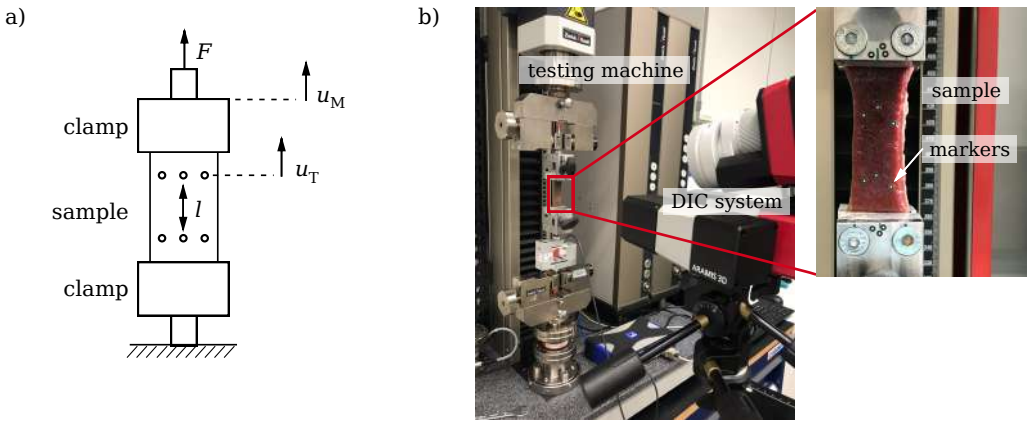

Figure 1.13: (a) Schematic overview of the tensile test with sticky markers placed on the clamped sample for measuring tissue displacements; (b) Porcine liver sample in the testing machine with the digital image correlation (DIC) system for measuring tissue displacements based on marker movement.

for an actual tensile test on a porcine liver specimen.

In soft tissue testing, tensile specimen are normally produced in shape of dogbones or strips with constant width and thickness. Dogbone-shaped samples are recommended for failure tests to ensure sample breakage in the measuring length, instead of in the clamp region. However, the extremely compliant nature of liver tissue, makes the cutting of dogbone samples very difficult [Kemper et al., 2010]. Tensile tests, aiming at measuring stiffness or linear viscoelastic properties, can be conducted on strip-shaped samples, since failure is usually not desired.

Previously, tensile failure stress and failure strain, at different strain rates, were evaluated for liver parenchyma [Santago et al., 2009, Kemper et al., 2010, Nguyen et al., 2012, Lu et al., 2014, Duong et al., 2015, Dunford et al., 2018] and the liver capsule [Brunon et al., 2010]. Furthermore, uniaxial large strains were applied to liver tissue for identifying hyperelastic material parameters [Chui et al., 2004, Gao and Desai, 2010, Nguyen et al., 2012, Fu and Chui, 2014, Zhao et al., 2020]. However, concerning liver viscoelastic properties, tensile tests have hardly been used in DMA, stress relaxation, and creep methods [Chen et al., 2011].

In this dissertation, macroindentation and tensile testing were conducted on liver tissue and artificial materials, applying ramp loading-unloading sequences, stress relaxation, and DMA, in order to extract elastic and viscoelastic properties.

1.5 Micromechanical model

In order to replicate tissue mechanical properties with artificial materials, a combination of different materials, in terms of composites, allows fine-tuning the effective mechanical properties. Based on micromechanical models, the resulting properties of composite materials can be predicted, depending on their microstructure, enabling efficient material design for mimicking biological tissues.

In the context of continuum micromechanics, materials are considered as heterogenous on a *microscale*, but homogenous for a sufficiently large volume of material which is referred to as the *macroscale*. Homogenisation describes the modelling step for upscaling position-dependent quantities on the microscale to macroscopic average quan-

tities, thereby replacing the heterogenous material with an equivalent homogenous material.

Heterogenous materials typically exhibit microstructures that are too complex to describe in their entirety. Instead, homogenous *phases* are defined on the microscale, representing the constituents of the heterogenous material. For instance, the later-described Mori-Tanaka model is applicable to matrix-inclusion-morphologies, where one phase is embedded as ellipsoidal inclusions in a matrix of another phase. Phases are characterised by their homogenous mechanical properties (e.g. stiffness tensors), characteristic shape (e.g. spherical inclusions), spatial distribution, and volume fractions.

Material phases are defined in *representative volume elements* (RVEs), which means that properties given for the RVE are representative of the contained material in terms of mechanical properties (Figure 1.14). For this to hold true, the characteristic length of the RVE must be much larger than the characteristic length of the encompassed inclusions [Zaoui, 2002],

$$l_{\mathrm{RVE}} \gg l_{\mathrm{inclusion}} \,. \tag{1.42}$$

According to Drugan and Willis [1996], a factor of at least 3 between RVE size and inclusion is sufficient. Furthermore, the characteristic length of the RVE must be much smaller than the characteristic length of the overall geometry of a structure, composed of RVE material,

$$l_{\mathrm{RVE}} \ll L_{\mathrm{structure}} \,, \tag{1.43}$$

and with that, much smaller than the fluctuations of loading acting on such a structure. In particular, l_{RVE} must be at least $5-10$ times smaller than $L_{\mathrm{structure}}$ [Kohlhauser and Hellmich, 2013]. Heterogenous materials that contain inhomogeneities on multiple size scales, can be treated within the same framework, using multi-step homogenisation.

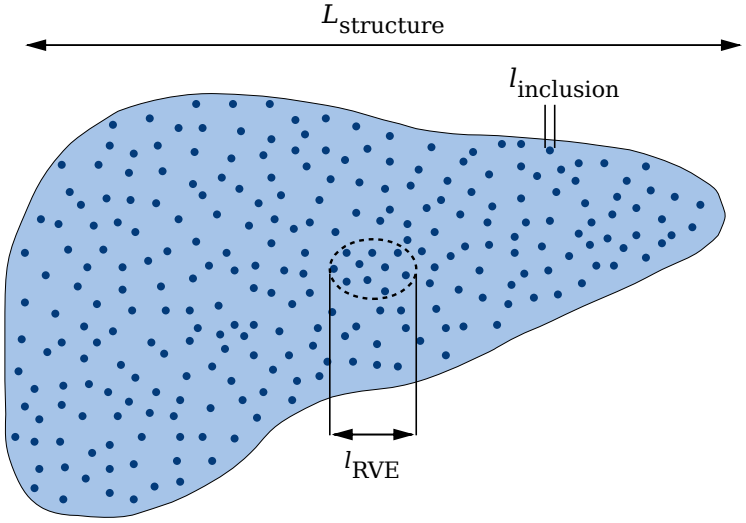

Figure 1.14: Defining the size of a representative volume element (RVE) l_{RVE} entails taking the size of the inhomogeneities $l_{\mathrm{inclusion}}$, as well as the overall size of the structure $L_{\mathrm{structure}}$, which is built up of the inhomogeneous material, into account.

1.5.1 Mean field homogenisation

Mean field homogenisation can be used to compute mechanical properties of composite materials, based on average stress and strain fields in the individual material phases. The most simple forms of mean field homogenisation are the Voigt [Voigt, 1887] and Reuss [Reuss, 1929] models, while more sophisticated formulations, such as the Mori-Tanaka model [Mori and Tanaka, 1973] or self-consistent scheme [Hill, 1965a], are founded on the Eshelby inclusion problem [Eshelby, 1957].

An RVE of composite material, defined according to the previous section (Eqs. 1.42 and 1.43), consists of individual homogenous material phases r of volume fraction f_r. On the microscale level, the second order stress tensor $\boldsymbol{\sigma}(\mathbf{x})$ and strain tensor $\boldsymbol{\varepsilon}(\mathbf{x})$ are dependent on their position $\mathbf{x}$ within the RVE (see Figure 1.15). Averaging $\boldsymbol{\sigma}(\mathbf{x})$ and $\boldsymbol{\varepsilon}(\mathbf{x})$ over the volume of the RVE, V_{RVE}, yields the homogenous average strain $\langle\boldsymbol{\varepsilon}\rangle$ and stress $\langle\boldsymbol{\sigma}\rangle$ on the scale of the RVE, according to

$$\langle\boldsymbol{\varepsilon}\rangle = \frac{1}{V_{\mathrm{RVE}}}\int_{V_{\mathrm{RVE}}} \boldsymbol{\varepsilon}(\mathbf{x})\mathrm{d}V = \sum_r f_r\boldsymbol{\varepsilon}_r\,, \tag{1.44}$$

and

$$\langle\boldsymbol{\sigma}\rangle = \frac{1}{V_{\mathrm{RVE}}}\int_{V_{\mathrm{RVE}}} \boldsymbol{\sigma}(\mathbf{x})\mathrm{d}V = \sum_r f_r\boldsymbol{\sigma}_r\,, \tag{1.45}$$

with $\boldsymbol{\varepsilon}_r$ and $\boldsymbol{\sigma}_r$ being the average strain and stress fields in each phase r [Zaoui, 2002].

If the *homogenous strain boundary condition* is applied, the displacements $\mathbf{u}(\mathbf{x})$ at the RVE boundary $\partial V_{\mathrm{RVE}}$,

$$\forall\mathbf{x}\in\partial V_{\mathrm{RVE}}:\ \mathbf{u}(\mathbf{x}) = \mathbf{E}\cdot\mathbf{x}\,, \tag{1.46}$$

produce the homogenous strain field $\mathbf{E}$. It can be shown, based on Eq. 1.46 and Eq. 1.44, that the homogenous strain tensor $\mathbf{E}$ is equal to the strain average of the RVE,

$$\mathbf{E} = \langle\boldsymbol{\varepsilon}\rangle\,, \tag{1.47}$$

which is referred to as strain average theorem [Aboudi et al., 2013]. It should be noted that for deriving Eq. 1.47, perfect bonding between the individual phases, signifying continuous displacements at the interfaces, was assumed [Aboudi et al., 2013].

Instead, if surface tractions $\mathbf{t}$ are prescribed at the boundary of the RVE, the *homogenous stress boundary condition* reads as

$$\forall\mathbf{x}\in\partial V_{\mathrm{RVE}}:\ \mathbf{t}(\mathbf{x}) = \boldsymbol{\Sigma}\cdot\mathbf{n}\,, \tag{1.48}$$

with surface normal $\mathbf{n}$ to the boundary and the homogenous stress tensor $\boldsymbol{\Sigma}$. Similarly, the stress average theorem can be derived, based on Eq. 1.48 and Eq. 1.45, showing that the homogenous stress tensor $\boldsymbol{\Sigma}$ is equal to the stress average of the RVE,

$$\boldsymbol{\Sigma} = \langle\boldsymbol{\sigma}\rangle\,. \tag{1.49}$$

For deriving Eq. 1.49, continuous tractions at the phase interfaces were assumed. Furthermore, the equilibrium relation

$$\forall\mathbf{x}\in V_{\mathrm{RVE}}:\ \mathrm{div}\,\boldsymbol{\sigma}(\mathbf{x}) = 0\,. \tag{1.50}$$

was utilized, meaning that the stress tensor $\boldsymbol{\sigma}(\mathbf{x})$ inside the RVE was free of divergence, which is only valid for absence of body forces [Aboudi et al., 2013].

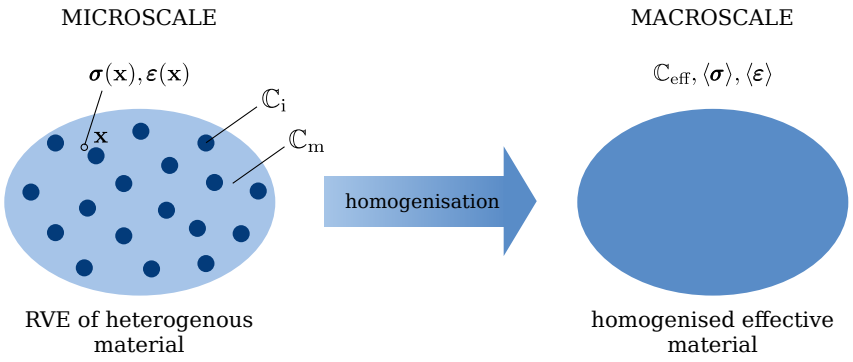

Figure 1.15: Stresses $\boldsymbol{\sigma}(\mathbf{x})$ and strains $\boldsymbol{\varepsilon}(\mathbf{x})$ in the heterogenous material depend on their position vector $\mathbf{x}$, while stresses $\langle\boldsymbol{\sigma}\rangle$ and strains $\langle\boldsymbol{\varepsilon}\rangle$ are averaged in the homogenised equivalent material with effective mechanical properties $\mathbb{C}_{\text{eff}}$.

In the context of mean field approaches, the average strain $\boldsymbol{\varepsilon}_r$ and stress $\boldsymbol{\sigma}_r$ of each phase is related to the macroscopic strain $\mathbf{E}$ and stress $\boldsymbol{\Sigma}$ via the 4th order strain concentration tensor $\mathbb{A}_r$ and stress concentration tensor $\mathbb{B}_r$,

$$\boldsymbol{\varepsilon}_r = \mathbb{A}_r : \mathbf{E}\,. \tag{1.51}$$

and

$$\boldsymbol{\sigma}_r = \mathbb{B}_r : \boldsymbol{\Sigma}\,. \tag{1.52}$$

If the considered RVE consists of linear elastic phases, stress $\boldsymbol{\sigma}_r$ and strain $\boldsymbol{\varepsilon}_r$ within the phases r are related via their 4th order phase stiffness tensor $\mathbb{C}_r$,

$$\boldsymbol{\sigma}_r = \mathbb{C}_r : \boldsymbol{\varepsilon}_r\,. \tag{1.53}$$

Now, inserting Eq. 1.51 into Eq. 1.53, and subsequently into the stress average, Eq. 1.45, yields

$$\boldsymbol{\Sigma} = \sum_r f_r \mathbb{C}_r : \mathbb{A}_r : \mathbf{E}\,, \tag{1.54}$$

and, introducing the effective stiffness tensor $\mathbb{C}_{\text{eff}}$ ($\boldsymbol{\Sigma} = \mathbb{C}_{\text{eff}} : \mathbf{E}$),

$$\mathbb{C}_{\text{eff}} = \sum_r f_r \mathbb{C}_r : \mathbb{A}_r\,. \tag{1.55}$$

The strain concentration tensors $\mathbb{A}_r$, associated with the individual phases r, can then be calculated based on the analytical solution for a single ellipsoidal inclusion, embedded in an infinite medium (assuming perfect bonding), which is referred to as the dilute case [Eshelby, 1957]. For higher inclusion volume fractions, the dilute case can be extended to the non-dilute case, using for instance the Mori-Tanaka model for matrix-inclusion morphologies [Mori and Tanaka, 1973, Benveniste, 1987] or the self-consistent scheme for polycrystalline materials [Hill, 1965a]. Finally, the resulting effective stiffness tensor $\mathbb{C}_{\text{eff}}$ is dependent on the phase volume fractions f_r, mechanical properties $\mathbb{C}_r$, characteristic shapes (spheres, ellipsoids, fibres, disks, etc.), and the interactions between the phases (e.g matrix-inclusion or polycrystalline).

For the Mori-Tanaka model, the effective stiffness tensor of a material, consisting of one inclusion phase i in a matrix phase m, results in [Hill, 1965b, Laws, 1975, Hellmich et al., 2004],

$$\mathbb{C}_{\text{eff}} = \left\{ f_{\text{m}}\mathbb{C}_{\text{m}} + f_{\text{i}}\mathbb{C}_{\text{i}} : [\mathbb{I} + \mathbb{P}_{\text{i,m}} : (\mathbb{C}_{\text{i}} - \mathbb{C}_{\text{m}})]^{-1} \right\} : \left\{ f_{\text{m}}\mathbb{I} + f_{\text{i}}[\mathbb{I} + \mathbb{P}_{\text{i,m}} : (\mathbb{C}_{\text{i}} - \mathbb{C}_{\text{m}})]^{-1} \right\}^{-1}, \tag{1.56}$$

with volume fractions, f_i and f_m, stiffness tensors, $\mathbb{C}_\mathrm{i}$ and $\mathbb{C}_\mathrm{m}$, and fourth order unity tensor $\mathbb{I}$. The Hill tensor $\mathbb{P}_{\mathrm{i,m}}$ describes the interaction between inclusion phase i, embedded in a fictitious unbounded homogenous matrix with stiffness $\mathbb{C}_\mathrm{m}$, and depends only on the characteristic shape of the inclusions and the matrix stiffness. It should be noted that $\mathbb{P}_{\mathrm{i,m}}$ is only defined for ellipsoidal inhomogeneities, including extreme cases of ellipsoids, such as fibres and spheres. In case of spherical inclusions, the Hill tensor can be calculated analytically, resulting in [Eshelby, 1957, Parnell, 2016]

$$\mathbb{P}_{\mathrm{i,m}} = \frac{1}{3k_\mathrm{m} + 4\mu_\mathrm{m}}\mathbb{J} + \frac{3k_\mathrm{m} + 6\mu_\mathrm{m}}{5\mu_\mathrm{m}(3k_\mathrm{m} + 4\mu_\mathrm{m})}\mathbb{K}\,, \tag{1.57}$$

with k_m and μ_m being the bulk and shear modulus of the matrix material, and $\mathbb{J}$ and $\mathbb{K}$ being the volumetric and deviatoric part of the unity tensor $\mathbb{I}$ ($J_{ijkl} = \frac{1}{3}\delta_{ij}\delta_{kl}$ with Kronecker delta δ_{ij} and $\mathbb{K} = \mathbb{I} - \mathbb{J}$.)

1.5.2 Correspondence principle

The elastic-viscoelastic correspondence principle allows extending the relations, derived in the previous section for linear elastic material phases, to linear viscoelastic phases, using the Laplace-Carson transform [Hashin, 1970]. In the homogenous viscoelastic phases r, the stress response $\boldsymbol{\sigma}_r(t)$ is dependent on the strain history with a fading-memory effect. Mathematically, stress at time t can be expressed, using the Boltzmann superposition principle [Hashin, 1965]

$$\boldsymbol{\sigma}_r(t) = \int_{-\infty}^{t} \mathbb{C}_r(t - t') : \frac{\partial \boldsymbol{\varepsilon}_r(t')}{\partial t'}\mathrm{d}t'\,, \tag{1.58}$$

with t' being the times at which strain changes occurred. For harmonic excitation, the strain tensor can be written as

$$\boldsymbol{\varepsilon}_r(t) = \boldsymbol{\varepsilon}_\mathrm{c} e^{i\omega t}\,, \tag{1.59}$$

with the time independent tensor $\boldsymbol{\varepsilon}_\mathrm{c}$, which can have real and complex components, and angular frequency ω. Inserting Eq. 1.59 into Eq. 1.58, yields

$$\boldsymbol{\sigma}_r(t) = i\omega \int_{-\infty}^{t} \mathbb{C}_r(t - t') : \boldsymbol{\varepsilon}_\mathrm{c} e^{i\omega t'}\mathrm{d}t'\,. \tag{1.60}$$

The subsequent change of variable, $t - t' = v$, turns Eq. 1.60 into [Hashin, 1970]

$$\boldsymbol{\sigma}_r(t) = i\omega e^{i\omega t} \int_{0}^{\infty} \mathbb{C}_r(v) : \boldsymbol{\varepsilon}_\mathrm{c} e^{-i\omega v}\mathrm{d}v\,. \tag{1.61}$$

Remembering the definition of the Laplace-Carson transform, $f^\mathrm{LC}(p)$, of a function $f(t)$,

$$f^\mathrm{LC}(p) = p \int_{0}^{\infty} f(t) e^{-pt}\mathrm{d}t\,, \tag{1.62}$$

and comparing with Eq. 1.61, yields a relation of stress and strain for the linear viscoelastic material (with $p = i\omega$), that is formally equivalent to the linear elastic material (Eq. 1.53):

$$\boldsymbol{\sigma}_r(t) = \mathbb{C}_r^\mathrm{LC} : \boldsymbol{\varepsilon}_r(t)\,. \tag{1.63}$$

For harmonic excitation, the transform variable $p = i\omega$ and the Laplace-Carson transformed stiffness tensor $\mathbb{C}_r^{\mathrm{LC}}(\omega)$ can be written in terms of the Laplace transformed stiffness tensor $\mathbb{C}_r^{\mathrm{L}}(\omega)$ as

$$\mathbb{C}_r^{\mathrm{LC}}(\omega) = i\omega\mathbb{C}_r^{\mathrm{L}}(\omega) = \mathbb{C}_r^*(\omega)\,, \tag{1.64}$$

resulting in the complex frequency-dependent stiffness tensor $\mathbb{C}_r^*(\omega)$, whose components consist of complex material properties [Lakes, 1998, Tschoegl et al., 2002, Andreasen et al., 2014]. For instance, a linear viscoelastic isotropic material has the complex stiffness tensor (written in Kelvin notation),

$$\mathbb{C}_{\mathrm{r}}^*(\omega) = \frac{E_{\mathrm{r}}^*}{(1+\nu_{\mathrm{r}}^*)(1-2\nu_{\mathrm{r}}^*)} \begin{pmatrix} 1-\nu_{\mathrm{r}}^* & \nu_{\mathrm{r}}^* & \nu_{\mathrm{r}}^* & 0 & 0 & 0 \\ \nu_{\mathrm{r}}^* & 1-\nu_{\mathrm{r}}^* & \nu_{\mathrm{r}}^* & 0 & 0 & 0 \\ \nu_{\mathrm{r}}^* & \nu_{\mathrm{r}}^* & 1-\nu_{\mathrm{r}}^* & 0 & 0 & 0 \\ 0 & 0 & 0 & 1-2\nu_{\mathrm{r}}^* & 0 & 0 \\ 0 & 0 & 0 & 0 & 1-2\nu_{\mathrm{r}}^* & 0 \\ 0 & 0 & 0 & 0 & 0 & 1-2\nu_{\mathrm{r}}^* \end{pmatrix}, \tag{1.65}$$

with the complex frequency-dependent tensile modulus $E_{\mathrm{r}}^* = E_{\mathrm{r}}^*(\omega)$ and Poisson's ratio $\nu_{\mathrm{r}}^* = \nu_{\mathrm{r}}^*(\omega)$ of the phases.

Applying homogenous displacements at the RVE boundary (according to Eq. 1.46) yields an analogous relation to Eq. 1.63 for relating the macroscopic homogenous stress and strain:

$$\boldsymbol{\Sigma}(t) = \mathbb{C}_{\mathrm{eff}}^*(\omega) : \mathbf{E}(t)\,, \tag{1.66}$$

introducing the macroscopic complex stiffness tensor $\mathbb{C}_{\mathrm{eff}}^*(\omega)$. Now, inserting complex phase stiffness tensors $\mathbb{C}_r^*(\omega)$ into relations derived in section 1.5.1, yields the equivalent expressions for the effective complex stiffness tensor

$$\mathbb{C}_{\mathrm{eff}}^*(\omega) = \sum_r f_r \mathbb{C}_r^*(\omega) : \mathbb{A}_r \tag{1.67}$$

and for the Mori-Tanaka model for the inclusion-matrix morphology,

$$\begin{aligned} \mathbb{C}_{\mathrm{eff}}^*(\omega) = \Big\{ f_{\mathrm{m}}\mathbb{C}_{\mathrm{m}}^*(\omega) + f_{\mathrm{i}}\mathbb{C}_{\mathrm{i}}^*(\omega) : [\mathbb{I} + \mathbb{P}_{\mathrm{i,m}} : (\mathbb{C}_{\mathrm{i}}^*(\omega) - \mathbb{C}_{\mathrm{m}}^*(\omega))]^{-1} \Big\} : \\ \Big\{ f_{\mathrm{m}}\mathbb{I} + f_{\mathrm{i}}[\mathbb{I} + \mathbb{P}_{\mathrm{i,m}} : (\mathbb{C}_{\mathrm{i}}^*(\omega) - \mathbb{C}_{\mathrm{m}}^*(\omega))]^{-1} \Big\}^{-1}. \end{aligned} \tag{1.68}$$

The homogenised complex tensor $\mathbb{C}_{\mathrm{eff}}^*(\omega)$ can be calculated for various material combinations, for instance to simulate composites with different inclusion volume fractions and complex stiffness tensors. For spherical inclusions, Eq. 1.68 consists of completely analytical expressions. Therefore, extremely fast estimation of composite viscoelastic properties is possible.

1.6 Objectives

The main objective of this dissertation is to define materials that are suitable for creating soft tissue anatomical models with realistic mechanical properties, concentrating specifically on liver tissue.

To achieve this, rigorous examination of liver mechanical properties is required, using various methods in the context of non-linear and viscoelastic behaviour. Macroindentation can be applied for assessing structural properties, while tensile testing yields

material properties. Besides animal liver, human liver (fresh and Thiel preserved) must also be characterised with some of the developed methods.

Furthermore, a variety of artificial alternatives to biological liver tissue, such as silicones and 3D printed polymers, need to be tested, in order to identify which artificial materials best mimic liver tissue. Combining different materials by creating composites is proposed, in order to adapt their effective mechanical properties and improve similarity to liver.

Finally, a micromechanical model is required for computing effective viscoelastic properties of the composites, in order to predict how well, resulting mechanical properties would correspond to liver and other soft biological tissues. The micromechanical model can be used as a design tool for creating tissue-mimicking microstructures, using artificial materials as input.

1.7 Dissertation outline

The outline of this dissertation is as follows. First, a general introduction and research motivations are given in the current chapter (Chapter 1), presenting relevant background information on anatomical models, liver anatomy and biomechanics, and micromechanical modelling. Next, the subsequent four chapters (Chapters 2–5) consist of scientific papers, containing the original research of this dissertation and how the objectives introduced in Chapter 1 were addressed.

- Chapter 2 deals with tactile properties of porcine and bovine liver tissue, in comparison with, potentially tissue-mimicking, artificial materials. One main question of this study was, which mechanical properties play a key role in the tactile perception of soft tissue. For this reason, macroindentation experiments, with the indenter simulating a finger, were conducted on liver tissues and the different substitute materials. Elastic, viscoelastic, and hardness properties were extracted and a method for comparing materials with each other was found by introducing the "tactile similarity error". The lowest tactile similarity error, signifying good agreement between an artificial material and liver tactile properties, was found for a super-soft silicone elastomer. However, the results also indicated that combining different materials could be a more promising strategy for representing liver parenchyma than using bulk materials alone.

- Chapter 3 is focussed on the viscoelastic characterisation of liver tissue on a material level, while in the previous chapter properties were evaluated on a structural level. Tensile tests were conducted on bovine and porcine hepatic parenchyma under different loading conditions (ramp loading and unloading, stress relaxation, and dynamic cyclic strains). Pseudohyperelastic modelling was utilised for the ramp loading and unloading data. Viscoelasticity was evaluated, based on complex frequency dependent tensile moduli for stress relaxation, as well as for dynamic cyclic data. The complex moduli, stemming from the different test methods were compared with each other, asking whether results from the more simple stress relaxation tests could approximate the results from dynamic cyclic testing. The aim of this study was to find simple methods for assessing liver linear viscoelasticity on a material level, using tensile tests. It was found that complex moduli from stress relaxation were similar to the results of dynamic

cyclic testing, but that it was crucial to heed the elastic non-linear behaviour of liver and conduct all tests at the same level of strain.

- Chapter 4 applies some of the methods, developed in the previous chapter, to human fresh and Thiel preserved hepatic parenchyma. Resulting pseudohyperelastic and viscoelastic properties were compared to results from the previous chapter for porcine and bovine tissue. It was investigated to what extent Thiel preservation influences the properties of fresh human liver and how human and animal liver differ from each other, in the context of elastic and viscoelastic mechanical properties. The main question was which biological substitute material (Thiel embalmed human tissue or animal derived fresh tissue) best represents fresh human parenchyma tissue. The results showed that finding a perfect substitute depends on which mechanical properties are important for the application. For instance, concerning elastic properties, bovine fresh liver was most similar to human fresh liver, while, considering viscoelastic properties, Thiel preserved liver was more suitable.

- Chapter 5 combines results from all the previous chapters, with the aim of designing artificial microstructure materials that exhibit similar effective viscoelastic properties as soft biological tissues. A viscoelastic Mori-Tanaka model (vMTM) was utilized for homogenising viscoelastic properties (e.g. complex moduli) of matrix-inclusion-type composites, consisting of different soft viscoelastic silicone elastomers. The input properties for the phases (matrix and inclusions) were found by conducting stress relaxation compression testing on selected silicones, whose properties had seemed promising in Chapter 2. Composite samples, using the respective silicones, were also tested to validate the model predictions experimentally. Furthermore, additional highly viscous silicones were considered in the vMTM, with their viscoelastic properties taken from literature. Finally, the effective viscoelastic properties, predicted by the vMTM for various silicone combinations, were compared to the corresponding properties of soft biological tissues (e.g. the viscoelastic properties found for liver in Chapters 4 and 5). This strategy allowed designing suitable composite materials, concerning material choice and inclusion volume fractions, to match the viscoelastic properties of soft biological tissues.

Finally, the last chapter is dedicated to summarising main findings, concluding remarks, and suggestions for future research (Chapter 6).

Chapter 2

Tactile properties of liver tissue

From the manuscript:

Quantifying tactile properties of liver tissue, silicone elastomers, and a 3D printed polymer for manufacturing realistic organ models

S.-J. Estermann, D. H. Pahr, A. Reisinger

Published in: *J. Mech. Behav. Biomed. Mater. 104:103630, April 2020*

Abstract

In order to produce anatomical models that feel realistic to the touch, artificial materials need to be found that mimic tactile properties of biological tissues. The aim of this study was to provide a guideline for identifying materials that feel similar to biological tissues, based on a quantifiable and reproducible measure. For this, a testing procedure was developed to identify mechanical properties that contribute to tactility. Bovine and porcine liver tissues were compared to different silicone elastomers and a soft 3D printed polymer. Macroindentation was chosen to simulate the palpation of material cubes with loading occurring during actual finger and material interaction. Elastic behaviour was considered by conducting quasistatic loading and unloading for extracting contact stiffness S and equivalent spring stiffness k. Viscoelasticity was quantified by means of force relaxation for calculating loss tangent $\tan\delta$ based on a Prony series approach. Furthermore, Shore 00 hardness H was measured with a hand-held durometer. For assessing how well materials mimicked liver in terms of tactile properties, a mean error of all measured properties was introduced, referred to as tactile similarity error Q. The 3D printed polymer exhibited the highest error ($Q = 100 - 150\%$), while the material with the lowest error – thus representing liver best – was a super-soft silicone elastomer (nominal hardness of 30 Shore Units) with $Q = 50\%$. In conclusion, a suitable material was found that best represented liver. However, the relatively high tactile similarity error, even for the best material tested, indicates that there is still room for improvement concerning material choice.

Keywords: tactile properties; liver; silicone; additive manufacturing; Macroindentation

2.1 Introduction

Artificial models are desirable substitutes for real biological tissues and organs for applications in research, medical training, and teaching. Ethical concerns and availability issues related to organs derived from human donors or animals promote the use of phantoms [Leibinger et al., 2016]. However, accurately mimicking tissue mechanical properties is a challenge, resulting in organ models that are frequently made of hard plastics exhibiting mechanical properties vastly different compared to actual tissues. These hard models may be useful in the context of visualising and explaining certain anatomical features, but are unsuitable for practising surgeries or testing medical devices, as realistic cutting, suturing, and dissecting is not possible. Furthermore, the training of manual palpation for distinguishing healthy from pathological tissue requires models with accurate tactile properties.

Liver tissue, in particular, is interesting to study regarding tactile properties: Accurate hepatic models would contribute to improved surgical planning and training of procedures such as laparoscopic cholecystectomy [Tang et al., 2005] and partial resection of the liver [Reitinger et al., 2006]. On organ level, liver – the largest gland in the human body – consists of very soft parenchyma, a network of blood vessels and bile ducts, as well as a tough capsule. Hepatic parenchyma tissue is homogeneous and isotropic [Chatelin et al., 2011] and one of the softest tissues in the human body with an elastic modulus of around 0.6 kPa [Yeh et al., 2001]. The liver capsule, however, is much stiffer, ranging at around 10 – 40 MPa, depending on applied strain rate and tissue origin [Snedeker et al., 2005, Hollenstein et al., 2006, Brunon et al., 2010]. Apart from elastic characteristics [Chen et al., 1996, Barnes et al., 2007, Brunon et al., 2010], liver tissue also exhibits viscoelasticity [Kiss et al., 2004, Snedeker et al., 2005, DeWall et al., 2012] as do many other biological tissues, such as cartilage [Lamela et al., 2013, Espino et al., 2014], brain [Fallenstein et al., 1969, Budday et al., 2017], and prostate [Zhang et al., 2008].
Instead of using human derived liver in research and education, animal tissue is often preferred due to its easier availability. However, mechanical properties can vary between human and animal tissues. While failure strain of porcine and human liver parenchyma is very similar, failure stress is significantly higher for porcine tissue [Kemper et al., 2010]. This difference is attributed to the distinct structure of porcine liver parenchyma: The functional tissue units in porcine liver are separated by interlobular collagenous septa, unlike in human liver. When comparing human and bovine parenchyma, Kemper et al. [2010] found no significant difference regarding failure stress and strain, owed to the structural similarity of human and bovine parenchyma. Thus, porcine as well as bovine liver tissue can be considered as a reasonably accurate models for human hepatic tissue. Ethical aspects, however, are still a compelling reason for using artificial substitutes for human liver instead of biological animal models. Furthermore, mechanical properties of artificial tissue mimicking materials can be more accurately controlled and adjusted depending on model requirements. For example, specific mechanical conditions, such as pathological stiffening of the liver tissue, could be recreated with artificial materials.

In order to mimic liver tissue, potential materials include soft compliant substances

such as silicones, gelatine, or hydrogels. Silicone elastomer appears to be a promising candidate, due to its versatility, covering a large range of Young's modulus and hardness, as well as relatively good preservability. Furthermore, silicone has been considered for experimental additive manufacturing processes [O'Bryan et al., 2017, Qiu et al., 2017, Pusch et al., 2018], an excellent method for controlling material structure, both on a macroscopic and microscopic level. On a macroscopic level, additive manufacturing allows anatomically accurate models that can be reliably reproduced in a standardised fashion or patient/pathology specific based on medical imaging [Rengier et al., 2010]. Structural control on a microscopic level enables tuning of material properties, such as increasing damping behaviour by adapting the microstructure [Andreasen et al., 2014].

While silicone 3D printing is still in its infancy, some commercially available additive manufacturing systems working with photopolymers are capable of producing flexible materials. The multimaterial printer Objet500 Connex3 (Stratasys Ltd., Eden Prairie, Minnesota), for instance, has previously been used for liver [Zein et al., 2013] as well as cardiovascular models [Izzo et al., 2016]. The utilized material is branded as TangoPlus and is described as "rubber-like" by the manufacturer. TangoPlus, being the softest material available on this system (nominal Shore A hardness of 26 – 28), combined with the structural controllability provided by additive manufacturing, is considered as a potential tissue mimicking material.

Tactile properties are not straightforwardly defined due to the complexity of the human sensing experience. The large variety of mechanoreceptors involved in tactile sensing allows the registration of many different properties during haption: Temperature, roughness, and wetness for instance, but also bulk properties such as hardness and viscoelasticity [Dargahi and Najarian, 2004]. Thus, when assessing mechanical material properties that determine tactile perception, elastic as well as viscoelastic considerations are necessary [Klatzky et al., 2013]. Experimental evaluation of this time-dependant behaviour can be performed in two ways: dynamic mechanical analysis (DMA), and force relaxation or creep testing. In DMA, a viscoelastic material is cyclically loaded yielding a mechanical response that is separated by the phase angle δ while the frequency of the displacement and force signals is the same, given linear viscoelasticity. Force relaxation registers the force decline over time when displacement is kept constant and creep is the change in displacement when a constant force is applied [Findley et al., 1989]. However, the results of both experimental approaches – DMA and relaxation/creep – are equivalent to one another.

Macroindentation on soft biological tissues has previously been used as material characterisation method for measuring stiffness in the context of optimising tactile feedback in teleoperation systems [Lim et al., 2009, Takács et al., 2016] and instrumented palpation for distinguishing pathological from healthy tissues [Carson et al., 2011, Palacio-Torralba et al., 2015]. Ahn et al. [2012] proposed a method that simulates palpation of prostate tissue for identifying tissue abnormalities with a round-tip indenter performing a sweeping motion on tissue phantoms containing inclusions. Carson et al. [2011] indented *ex vivo* human prostate samples quasistatically with a spherical indenter perpendicular to the surface, finding that healthy tissue had a lower stiffness compared to cancerous tissue. Ottensmeyer et al. [2004] conducted creep testing on whole pig livers with a flat faced punch indenter for characterising the influence of perfusion on viscoelasticity based on strain-time curves. Macroindentation was conducted on soft silicone elastomer by Chen et al. [2013], extracting stiffness according

to the Oliver-Pharr method from a quasistatic loading-unloading sequence as well as assessing viscoelasticity via cyclic testing. According to Chen et al. [2013], the tested silicone behaved highly elastic with negligible viscosity.

Overall tactile similarity of materials can be rated by subjective human palpation [Cheung et al., 2014, Lozoya, 2016, Takács et al., 2017]. However, in order to assess the suitability of a tissue mimicking material in a quantifiable and objective way, it would be greatly beneficial if the different measured properties were combined in an overall score describing tactile accuracy. Similar research has been conducted regarding the structural similarity of native bone and bone grafts, based on medical imaging and mechanical testing [Falvo D'Urso Labate et al., 2016]. The authors introduced a weighted average of differences of bone and graft properties related to graft suitability.

No study to our knowledge has combined different measured properties that describe tactility in terms of an overall tactile similarity error. We address this issue by extracting elastic properties from quasistatic macroindentation and viscoelastic properties from force relaxation, as well as measuring Shore hardness of porcine and bovine liver, different silicone elastomers, and a commercially available 3D printed soft polymer. The combined discrepancy concerning elasticity, viscoelasticity, and Shore hardness of synthetic materials compared to liver properties is introduced as tactile similarity error for assessing how well an artificial material mimics liver in terms of tactile properties.

2.2 Materials & methods

2.2.1 Sample preparation

Nine whole porcine livers and one bovine liver were obtained from animals slaughtered less than 24 hours prior to purchase. Whole livers were stored at 4° C submerged in 0.9% NaCl saline solution until cube-shaped samples ($30 \times 30 \times 30$ mm) were cut with a sharp knife and a surgical blade, avoiding large blood vessels and bile ducts. Between 1 and 4 samples were extracted from each porcine liver. The bovine liver being much larger than porcine liver yielded 18 samples from one single organ. Porcine samples ($n = 18$) consisted of parenchyma covered with capsule tissue at the top and bottom surface of the cube, while bovine samples ($n = 18$) only exhibited capsule at the top surface (see Fig. 2.1a) due to the larger thickness of the organ. Cut samples were kept hydrated at all times by wrapping them in saline solution soaked cloth before testing. The samples were never frozen and testing was conducted immediately after sample preparation at room temperature (approximately 23° C).

Concerning artificial tissue-mimicking materials, three inherently soft silicones, a slightly harder silicone, and a 3D printed photopolymer were selected. Furthermore, the soft silicones were used for producing layered samples, combining two types of silicone, and the harder silicone was softened by adding silicone oil in different volume fractions. By selecting a variety of materials we aimed at potentially covering a wide range of material properties for consideration as hepatic models.

Silicone samples were cast in a 3D printed mould made of polylactic acid and air bubbles were removed by degassing in a vacuum desiccator. Super-soft two-component Room-Temperature-Vulcanising (RTV) silicone elastomers of three different nominal Shore 00 hardness values (Ecoflex 00-30, Ecoflex 00-20, and Ecoflex 00-10 by Smooth-On Inc., Macungie, Pennsylvania) were chosen due to them being marketed as tissue

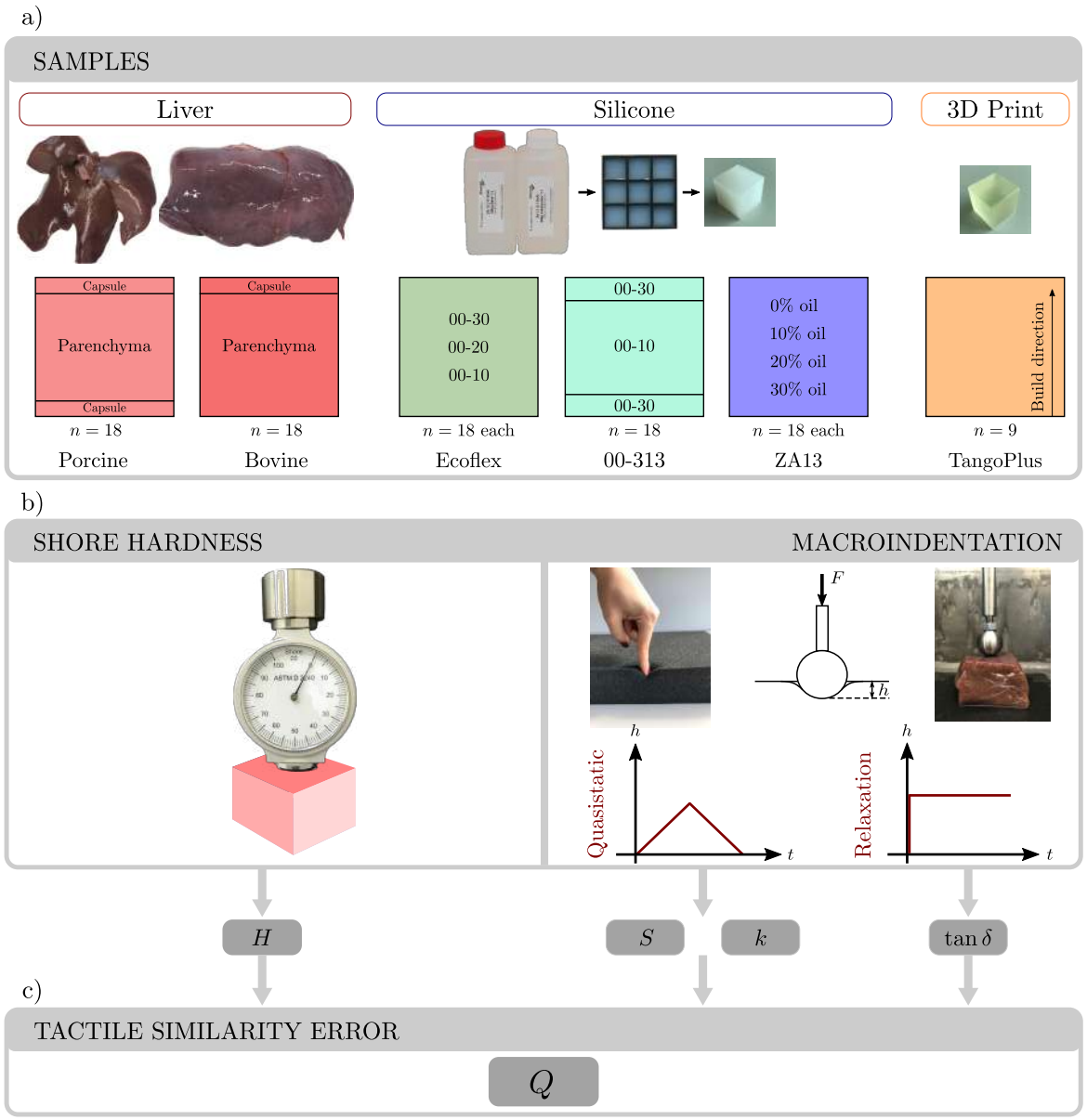

Figure 2.1: Experimental overview with (a) schematic description of the tested samples (porcine and bovine liver, super-soft Ecoflex silicones, layered samples 00-313, ZA13 silicone with different silicone oil concentrations, and TangoPlus; b) testing procedure consisting of shore hardness measurement H and macroindentation with the extracted parameters (k, S, and $\tan\delta$), and (c) calculation of the tactile similarity error Q based on the measured properties

mimicking by the manufacturer. Additionally, samples were produced that consisted of a 20 mm layer of 00-10 silicone sandwiched between two 5 mm layers of 00-30, referred to as "00-313" samples. Furthermore, a slightly harder Shore A two-component RTV silicone (ZA13 Mould WT45, Polymerschmiede GmbH, Mönchengladbach, Germany) was selected, aiming at reducing its hardness by adding silicone oil in different volume fractions (0%, 10%, 20%, and 30%), thus providing flexibility of adapting material properties. Silicone samples were left to fully harden for 48 hours before mechanical testing and their sample number was $n = 18$ for each silicone type. Schematic overview of the samples is represented in Fig. 2.1a.

The Objet500 Connex3, a polyjet multimaterial printer (Stratasys Ltd., Eden Prairie, Minnesota), was utilized for producing $n = 9$ samples of TangoPlus, the softest material available on this system. TangoPlus is described as rubber-like by the manufacturer and has previously been used for hepatic and cardiovascular models [Zein et al., 2013, Izzo et al., 2016]. Mechanical testing of TangoPlus was conducted 48 hours after additive manufacturing (AM) was completed. Pretests were conducted to assess the influence of printing layer orientation: Macroindentation showed no significant difference for samples indented parallel versus perpendicular to the printing direction. Subsequently, results for TangoPlus are reported for indentation occurring orthogonal to the layer orientation (Fig. 2.1a).

Dimensions and weight of all samples were measured before mechanical testing.

2.2.2 Mechanical testing

Shore hardness Utilizing an analogue durometer (ZwickRoell GmbH & Co. KG, Ulm, Germany), the Shore 00 hardness H given in Shore Units (SU) according to the ASTM D2240-00 standard was recorded 3 times for each sample (excluding 00-10 which was too soft for the Shore 00 hardness scale). Shore hardness is widely used for characterising silicone elastomers and other synthetic materials by providing a straightforward method for comparing materials.

Macroindentation Concerning more elaborate mechanical testing, a large spherical indenter was chosen to mimic the shape of an adult index finger for indenting the tested materials at loads comparable to those applied when a surface is touched. The indenter consisted of a 15 mm diameter steel sphere attached to a 140 mm long and 8 mm diameter steel rod (see Fig. 2.1b), which in turn was screwed into the bottom end of the S-type load cell (S2M/100N, Hottinger Baldwin Messtechnik GmbH, Darmstadt, Germany). A second steel rod, screwed into the top end of the load cell was mounted in the upper clamp of the LTM5 electrodynamic testing machine (ZwickRoell GmbH & Co. KG, Ulm, Germany). Reaction force F of the material during the indentation was measured with the 100 N single axis load cell which was connected to the universal data acquisition module QuantumX MX840B (Hottinger Baldwin Messtechnik GmbH, Darmstadt, Germany). Linear displacement of the testing machine h and force were measured at a frequency of 100 Hz. The samples were placed on sandpaper to avoid slipping while indentation occurred. In Fig. 2.1b a porcine liver sample during testing is depicted with a schematic description of the measured quantities. Liver samples were kept well hydrated by wetting with saline solution throughout the experiment. Testing was conducted without preconditioning as would be the case in human palpation or during surgical manipulation, as suggested by Brown et al. [2003].

According to Nicholson et al. [2003], who researched tactile properties in the context of spinal palpation done by manual therapists, elasticity and viscosity are two properties that contribute to the overall perception of spinal stiffness. Therefore, it is important to quantify elastic as well as viscous properties of biological tissues when describing what they feel like. For this, two types of experiments were conducted: quasistatic ramp loading and force relaxation.

Quasistatic ramp loading The first set of experiments consisted of quasistatic loading and unloading for obtaining an elastic material response, conducted on 9 samples of each material. After placing the sample centrally on the testing platform, the indenter tip was lowered until a small force of 0.1 N was recorded signifying contact between surface and indenter. The loading protocol was based on mimicking a human finger palpating the material: loading up to 5 N conducted in a quasistatic fashion at 5 mm/min and subsequent immediate unloading at the same speed. The upper limit of loading was defined in terms of a force instead of a displacement, given that mechanoreceptors in the fingertip translate mechanical forces into excitatory electrical signals [Abraira and Ginty, 2013]. 5 N was chosen as peak force due to estimations concerning the magnitude of forces when surfaces are touched for evaluating material properties.

Two different mechanical properties were extracted from the measured data due to the non-linearity of the force-displacement curves (see Fig. 2.2a). First, the equivalent spring stiffness k quantifies stiffness in terms of an equivalent linear elastic material. Second, contact stiffness S characterises the purely elastic material response during unloading, excluding any plastic effects which may occur during loading. Thus, a combined evaluation of S and k yields a good characterisation of elastic behaviour.

Equivalent spring stiffness k was calculated by dividing force $F(h_{\max})$ (in N) by displacement $h_{\max}$ (in mm) at the point of maximum indentation (see Fig. 2.2a):

$$k = \frac{F(h_{\max})}{h_{\max}}. \tag{2.1}$$

Contact stiffness S, analogously to the Oliver-Pharr stiffness [Oliver and Pharr, 1992, Carson et al., 2011], is here defined as

$$S = \frac{\mathrm{d}F}{\mathrm{d}h}(h_{\max})\,, \tag{2.2}$$

the ratio of the change in force to the change in displacement during the initial phase of unloading, as depicted in Fig. 2.2a. Force depending on displacement $F(h)$ was approximated by fitting the power law function

$$F(h) = c_1 h^{c_2} + c_3\,, \tag{2.3}$$

through the unloading part of the force-displacement curve with c_1, c_2, and c_3 being fit parameters. Non-linear least squares method was implemented with a Levenberg-Marquardt algorithm for curve fitting [Marquardt, 1963], the initial parameters for starting optimisation being $c_1 = 1$, $c_2 = 1$, and $c_3 = 0$. For evaluating goodness of fit, the root-mean-square error (RMSE) of fit values compared to experimental values was calculated.

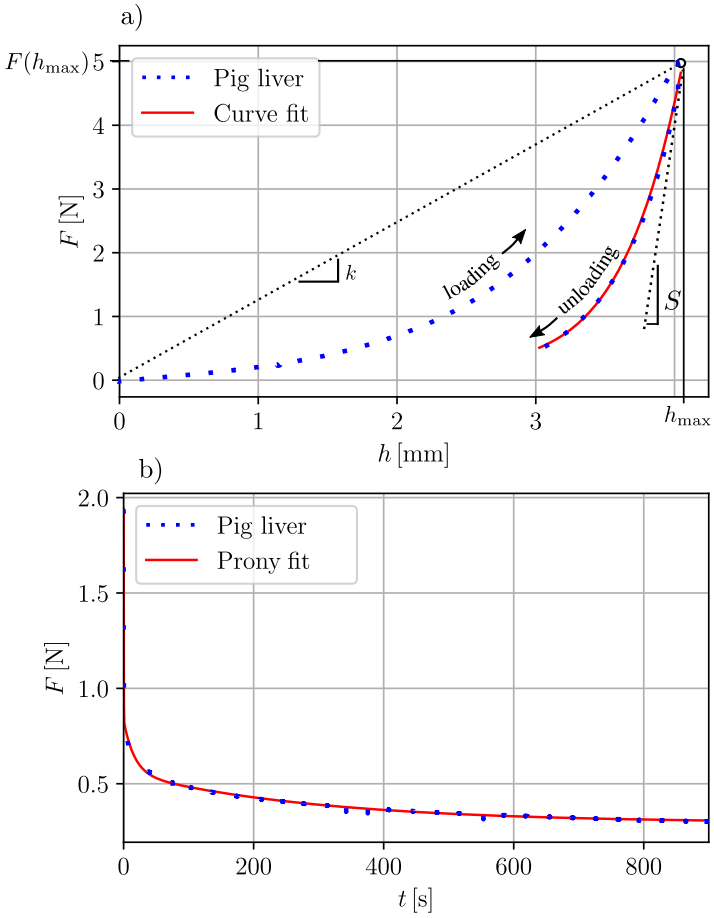

Figure 2.2: Typical porcine sample curves for (a) force-displacement of quasistatic test, depicting measured data (dotted line) and curve fitted to the unloading part (solid line), with contact stiffness S and spring stiffness k; and (b) measured relaxation force plotted over time (dotted line) and the corresponding Prony series fitted curve (solid line)

Force relaxation In a separate set of experiments, force relaxation via macroindentation was performed in order to evaluate viscoelastic properties in terms of the loss tangent $\tan\delta$. For each material, 9 samples (which were not the same samples as the ones exposed to quasistatic loading except for TangoPlus) were tested. In the case of TangoPlus, quasistatic testing was performed an hour prior to force relaxation on the same set of samples, due to restricted sample availability. However, deformations being in the non-damaging range allowed this procedure.

Contact of sample and indenter was established at a registered force of 0.05 N and the test was started subsequently. Step-like loading was applied rapidly, reaching the target indentation of 5 mm in under 0.1 s, followed by a period of holding the displacement for 900 s while recording force relaxation (see Fig. 2.2b).

In the idealised case of the instant application of a step displacement h_0, the force F over time t is related to h_0 through the transfer function of force relaxation $k(t)$ according to

$$F(t) = k(t)h_0\,. \tag{2.4}$$

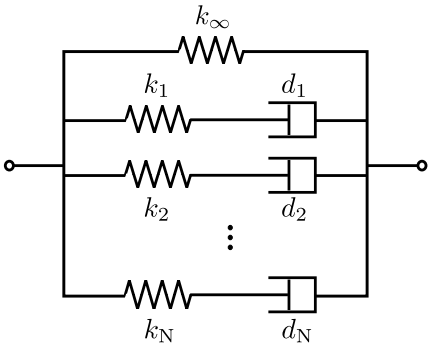

Figure 2.3: Generalised Maxwell model, consisting of a spring representing long-term stiffness k_∞ and N parallel Maxwell elements with spring stiffness k_1, k_2, ... k_N and respective dashpot viscosities d_1, d_2, ... d_N

Utilizing Prony series, $k(t)$ can be approximated as

$$k(t) = k_\infty + \sum_{i=1}^{N} k_i e^{-\frac{t}{\tau_i}}\,, \tag{2.5}$$

with k_∞ being the long term stiffness, k_i the Prony series coefficients, and τ_i the relaxation times, while N determines the number of Prony terms [Gutierrez-Lemini, 2014]. The corresponding rheological model is the generalised Maxwell model described in Fig. 2.3, consisting of the spring k_∞, parallel to N Maxwell elements with spring stiffness k_i and dashpot viscosities d_i [Findley et al., 1989].

Expressing k_∞ in Eq. 2.5 in terms of the initial stiffness k_0 exhibited at the starting point of the holding phase by

$$k_\infty = k_0 - \sum_{i=1}^{N} k_i\,, \tag{2.6}$$

yields

$$k(t) = k_0 - \sum_{i=1}^{N} k_i(1 - e^{-\frac{t}{\tau_i}})\,. \tag{2.7}$$

$N = 3$ Prony elements were chosen as suggested by Ocal et al. [2010] and as supported by the considerations described in 2.8.1. k_0 was calculated directly from the measured data as the material stiffness at the instance of applying the hold displacement. k_1, k_2, and k_3, as well as d_1, d_2, and d_3 result from fitting Eq. 2.7 to the experimental data of the relaxation curve using non-linear least squares method with a trust-region algorithm; fit parameters are thereby limited to positive values. Storage and loss stiffness k' and k'' of the generalised Maxwell model, as described by Gutierrez-Lemini [2014], are given by

$$k' = k_\infty + \sum_{i=1}^{N} \frac{k_i \omega^2 \tau_i^2}{1 + \omega^2 \tau_i^2} \tag{2.8}$$

and

$$k'' = \sum_{i=1}^{N} \frac{k_i \omega \tau_i}{1 + \omega^2 \tau_i^2}\,, \tag{2.9}$$

where ω is the frequency and $\tau_i = d_i/k_i$ are relaxation times, with the ratio k''/k' yielding the loss tangent $\tan\delta$ depending on ω:

$$\tan\delta = \frac{k''}{k'} = \sum_{i=1}^{N} \frac{\omega d_i k_i^2}{k_\infty(k_i^2 + \omega^2 d_i^2) + \omega^2 k_i d_i^2} \,. \tag{2.10}$$

Estimation of poking frequency when a material is probed by humans, suggested the calculation of $\tan\delta$ for 1 Hz in Eq. 2.10. The loss tangent is independent of sample or indenter geometry and, therefore, can be considered a material property as well as a structural one [Wilcox et al., 2014].

2.2.3 Data analysis

We propose a standardised tactile similarity error Q, simplifying the comparison of all 4 measured properties (S, k, H, and $\tan\delta$) of the artificial materials to liver tissue with a single score. Thereby, Q unifies considerations of tissue similarity in terms of surface hardness H, viscoelasticity and elasticity. Elastic behaviour is represented by equivalent spring stiffness k as well as contact stiffness S due to the non-linearity of the indentation curves. Viscoelasticity is characterised by the loss tangent $\tan\delta$. The relative importance of these contributors to tactile behaviour is prescribed through weighting factors in Q.

For identifying Q, the relative changes D_k, D_S, D_H, and $D_{\tan\delta}$ between the mean values of the measured properties k, S, H, and $\tan\delta$ of each synthetic material and the respective properties of bovine or porcine liver were calculated. For instance, material m exhibits the relative change in spring stiffness in regard to liver l

$$D_k = \frac{\overline{k}_m - \overline{k}_l}{\overline{k}_l} \,, \tag{2.11}$$

where $\overline{k}_m$ and $\overline{k}_l$ are the mean values of spring stiffness for the material and liver, respectively. Analogously, D_S, D_H, and $D_{\tan\delta}$ were calculated for all tested materials, in respect to both porcine and bovine liver. Next, the mean of the relative differences is reported according to

$$Q = w_k|D_k| + w_S|D_S| + w_H|D_H| + w_{\tan\delta}|D_{\tan\delta}| \,. \tag{2.12}$$

and referred to as tactile similarity error Q of material m in regard to liver l. The weighting factors $w_k, w_S, w_H, w_{\tan\delta}$ assign relative importance to the different properties and it holds that

$$w_k + w_S + w_H + w_{\tan\delta} = 1 \,. \tag{2.13}$$

For the subsequently reported results, all properties were weighted with the same importance, yielding $w_k = w_S = w_H = w_{\tan\delta} = 0.25$. Introducing Q allows straightforward conclusions based on one single value about the artificial material's ability to mimic liver tissue in terms of tactile properties.

2.3 Results

Samples varied in thickness depending on the material. Thickness of porcine and bovine samples were 27.6 ± 2.7 mm and 28.6 ± 2.7 mm, respectively, as cutting accurately shaped samples was challenging due to the very soft nature of the tissues.

Silicone samples were averagely 30.0 ± 1.1 mm in thickness, while the 3D printed TangoPlus could be produced with a very precise thickness of 30 ± 0.1 mm.

Fitting the power law function Eq. 2.3 to the unloading sequence of the quasistatic indentation resulted in an average RMSE of 0.0253 ± 0.0228 N compared to the experimental values. Concerning relaxation curves, the Prony series approximation yielded an average RMSE of 0.0158 ± 0.0225 N.

Resulting mean values and standard deviations for H, k, S, and $\tan\delta$ for 1 Hz are plotted as barplots in Fig. 2.4a – d and written in Tab. 2.1.
Porcine tissue hardness was 30.52 ± 1.52 SU (Shore Units) while mean H of bovine tissue was nearly 17% lower. The 3D printed polymer was more than twice as hard with $H = 76.22 \pm 0.20$ SU. ZA13-based silicone exhibited a hardness varying with the volume fraction of added silicone oil from around 65 SU (0% oil) to 40 SU (30% oil). While shore hardness for 00-30 and 00-20 was about 5 – 10 SU lower than their nominal values of 30 and 20 SU, 00-10 was too soft to even be measured on the Shore 00 scale at all.

Spring stiffness of liver tissue was on the low end of the scale with 0.97 ± 0.215 N/mm for porcine and 0.63 ± 0.067 N/mm for bovine liver; these values were well exceeded by TangoPlus (mean $k = 2.51$ N/mm) and the ZA13 silicones, while 00-30 and 00-20 were comparable to liver with 0.86 ± 0.014 N/mm and 0.53 ± 0.010 N/mm.

TangoPlus was characterised by the highest mean contact stiffness of 5.50 N/mm after liver (10.18 N/mm and 7.22 N/mm on average for porcine and bovine tissue), while S for all other measured materials was well below liver.

Porcine and bovine liver exhibited a pronounced loss tangent (mean value of 0.231 and 0.191 for porcine and bovine tissue). However, TangoPlus featured damping – in the context of loss tangent – to the highest extend with a $\tan\delta$ of 0.531 ± 0.036. All ZA13-based silicones, as well as 00-30 silicone, hardly exhibited damping with very low mean values of $\tan\delta$ in the range of around 0.03 – 0.06. Concerning 00-10 and the layered silicone, damping was in the range of liver with 0.280 ± 0.014 and 0.202 ± 0.027, respectively.

Fig. 2.5a and b depict the relative changes in properties in comparison to porcine liver and bovine liver, alongside the overall tactile similarity error Q for each material. A relative change smaller than 0 indicates that the property in question was lower than liver (i.e. softer, more compliant, less viscous), while positive values signify properties exceeding liver. D_H and D_k closest to zero was found for 00-30 in regard to porcine tissue (-0.17 and -0.12, respectively). When comparing to bovine tissue, absolute value of D_H was smallest for 00-30 (-0.01) while D_k was closer to zero for 00-20 than for 00-30 (-0.10 and 0.37, respectively). Regarding contact stiffness, D_S of all materials was < 0 for porcine and bovine liver. Excellent agreement between synthetic material and liver was found in regard to damping of the layered sample 00-313 ($D_{\tan\delta} = -0.13$ and $D_{\tan\delta} = 0.06$ for porcine and bovine tissue).

Tactile similarity errors Q exceeded 100% for the materials TangoPlus, ZA13 0%, ZA13 10%, and ZA13 20%, when compared to bovine liver, while the resulting Q of 00-20 and 00-30 was around 50%. When regarding porcine liver, the tactile similarity errors were generally slightly lower. The material with the lowest Q, 00-30, exhibited nearly the same error for porcine as for bovine tissue. Overall, Q of the tested materials varied between around 0.5 – 1.5.

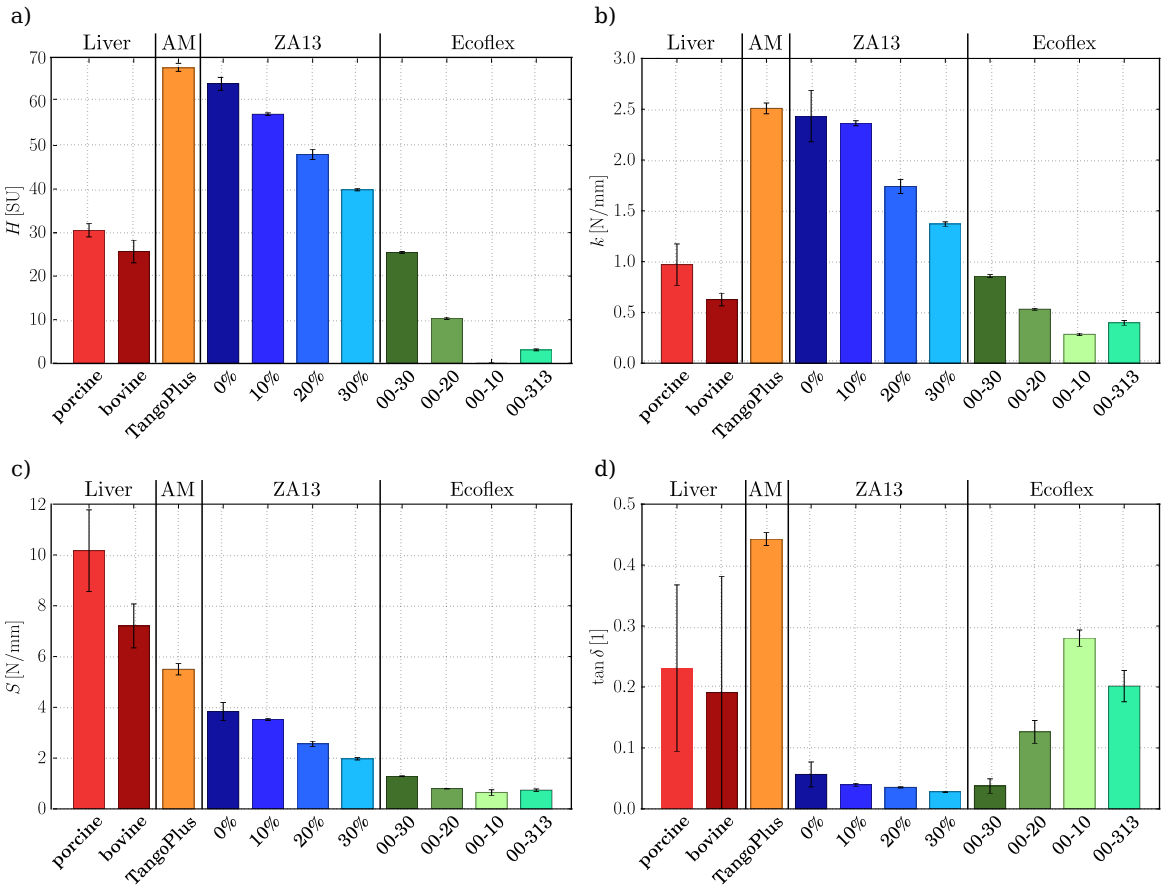

Figure 2.4: Mean values and standard deviations measured for all materials (porcine and bovine liver, the additive manufactured (AM) material TangoPlus, ZA13 with 0%, 10%, 20%, 30% silicone oil, 00-30, 00-20, 00-10, and layered silicone) for (a) Shore 00 hardness, (b) spring stiffness k, (c) contact stiffness S, and d) loss tangent $\tan\delta$ at 1 Hz

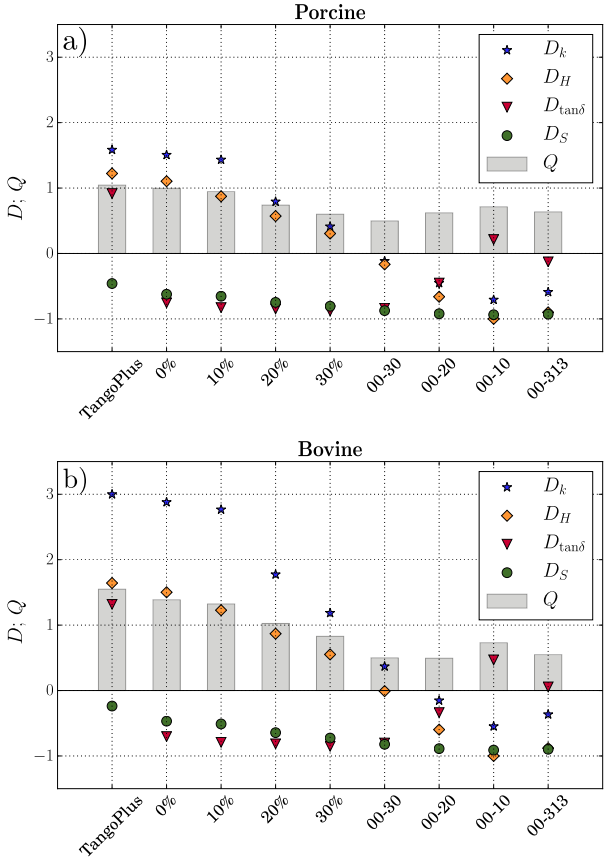

Figure 2.5: Relative changes of mechanical properties D_k, D_H, $D_{\tan\delta}$, and D_S (denoted by star, diamond, triangle, and circle symbol, respectively) and the tactile similarity error Q (grey bars) in reference to (a) porcine liver and (b) bovine liver. The lower Q, the more a material feels like liver.

2.4 Discussion

The objective of this study was to find a method for comparing biological tissues with tissue-mimicking materials in terms of tactility for improving material selection in anatomical models. Elastic as well as viscoelastic considerations were included to accurately describe tactile properties. The discrepancy between liver tissue and mimetic materials concerning Shore hardness, spring stiffness, contact stiffness, and loss tangent was expressed in terms of an overall tactile similarity error Q.

The advantage of Q is that tactile properties of different materials can be compared with each other according to one single value instead of comparing all 4 measured properties (H, k, S, and $\tan\delta$) of the two materials separately. The weighting factors w_H, w_k, w_S, and $w_{\tan\delta}$ in Q were equal in the current study. Depending on the application of the tissue mimicking material, the importance of a certain property can be emphasised by adjusting the weighting factors in favour of the preferred property. Optimising the weighting factors would require a separate study based on voluntary participants' ratings of tactile material properties. For other researchers dealing with biomimicry in terms of tactility, it would be recommendable to follow the here presented procedure for comparing their desired biological tissues with potential substitute materials. Material selection should then be based on which material exhibits the lowest tactile similarity error, while weighting factors can be adjusted depending on the application.

In this study, animal tissues were used instead of human tissue for comparison with artificial materials. As discussed previously, animal tissue differs from human tissue in respect to mechanical properties [Kemper et al., 2010]. Nevertheless, porcine models are widely used in surgical training and have been shown to be useful in the field of laparoscopic cholecystectomy by Tang et al. [2005]. Thus, even if considering animal tissue as a model for human tissue in the current study is justifiable, it would be beneficial to additionally test human liver with the reported method in future research.

Concerning the measured properties, the objective was to find parameters that influence tactility and specifically play a role in biological tissues. Motivated by the fact that a palpable difference exists between healthy and fibrotic liver tissue and that Shore hardness correlates with the degree of liver fibrosis [Yoon et al., 2017], Shore 00 hardness was measured. Furthermore, according to Nicholson et al. [2003], viscoelasticity is a crucial aspect when determining spinal pathologies trough manual palpation alongside purely elastic considerations. Thus, elastic as well as viscoelastic parameters were measured in the current study. Elastic properties were identified as the equivalent spring stiffness which treats the material as an ideally elastic spring, as well as the contact stiffness which describes the elastic stiffness during initial unloading. In combination, these two values should give an impression of the sample's, in general complex, elastic behaviour. The loss tangent, representing damping, was utilized as a measure for viscoelasticity. A more detailed discussion of the resulting tactile properties is presented as follows: Shore hardness, elastic behaviour, viscoelastic behaviour, and tactile similarity error.

Shore hardness Previously Yoon et al. [2017] measured Shore hardness of 22.59 ± 43.57 on excised samples of healthy human liver, agreeing well with the here presented values for bovine liver (25.67 ± 2.61 SU). Porcine hepatic hardness of the current study (30.52 ± 1.52 SU) appears to be similar to fibrotic human liver hardness measured by Yoon et al. [2017]. Porcine liver was slightly harder compared to bovine liver, but both were represented best by 00-30 silicone in this regard, see Fig. 2.5. All other Ecoflex silicones were too soft. TangoPlus as well as ZA13 silicone with 0% and 10% oil were about twice as hard compared to hepatic tissue.

Elastic behaviour TangoPlus was around 150% stiffer than liver in terms of spring stiffness, thus contributing to the fact that the polymer was the worst material for representing the tactile properties of liver in the current study (highest overall tactile similarity error). The super-soft Ecoflex silicones 00-30, 00-20, as well as the layered samples 00-313 more accurately mimic tissue regarding spring stiffness.

Concerning contact stiffness, all tested ZA13-based and Ecoflex silicone elastomers exhibited S less than half of liver. Even though contact stiffness of TangoPlus was sightly increased compared to the other synthetic materials, S of liver was still around 1.5 – 2 times higher.

Viscoelastic behaviour Both porcine and bovine liver exhibited hysteresis in the quasistatic test (see Fig. 2.2a for a typical porcine liver curve). This additionally supported the idea that further viscoelastic characterisation of the materials was essential, as was done by calculating $\tan\delta$.

The results of curve fitting Prony series to the force relaxation data were marginally dependant on the duration of the experiment. Shorter hold times of around 100 s

yielded higher root-mean-square errors on average for the fitted data compared to relaxation times of 900 s (approximately 0.02 N and 0.016 N, respectively). The resulting $\tan\delta$ only changed slightly by 1 % when hold time was increased from 400 s to 900 s. Thus, calculation of $\tan\delta$ based on 900 s hold time was valid.

The loss tangent of canine liver was found to be around 0.25 at 1 Hz by Kiss et al. [2004] who applied a modified (fractional) Kelvin-Voigt model to cyclic compression data, agreeing well with the current results. DeWall et al. [2012], who utilized dynamic compression of human hepatic tissue, found $\tan\delta$ in the same range (0.2 – 0.3) for non-fibrotic specimens. A loss tangent of around 0.3 at 1 Hz was extracted from Qiu et al. [2017] for human prostate tissue under cyclic compressive loading. The authors also interpreted storage and loss modulus for assessing how well a 3D printed silicone model represented the tissue; thus supporting the parameters chosen to measure tactile properties in the current study. Lim et al. [2009] obtained values of $\tan\delta$, between 0.6 – 0.7 at 1 Hz for human liver applying sinusoidal deformation with a flat-faced cylindrical indenter – nearly 3 times higher than the current values for porcine and bovine liver. These relatively high results could either stem from variation between human and porcine/bovine tissue, or the difference in choice of model and experimental setup.

Regarding the layered silicone 00-313 (consisting of 00-30 and 00-10), porcine and bovine liver tissue were best represented in terms of loss tangent by this material in our present study.

Tactile similarity error Concerning the overall tactile similarity error, Q of 00-313 layered silicone was relatively low (0.636 for porcine and 0.550 for bovine tissue) and with that lower than Q of pure 00-10 silicone. This indicates that combining different elastomers in order to tune tactile properties is a feasible approach.

The least suitable materials were TangoPlus, ZA13 0%, and ZA13 10% with mean $Q = 1.0$ regarding similarity to porcine liver and $Q = 1.0 - 1.5$ regarding bovine liver. TangoPlus has previously been used in models for surgical simulation [Zein et al., 2013, Izzo et al., 2016, Yoo et al., 2017]. For example, Yoo et al. [2017] developed a TangoPlus cardiac model as a training system for congenital heart surgery. The majority of the surgeons, participating in the training course, reported that the consistency and elasticity of the material was different to the actual tissue and that a weakness of the model was that the material could not be sutured and cut in a realistic way. Even though the model was overall rated as useful, the authors conclude that the utilized material was not completely satisfactory.

In the current study, no material exhibited a tactile similarity error lower than 50%, signifying that the ideal material for mimicking liver has not been found yet. However, 00-30 and 00-20 silicone elastomers are deemed reasonably suitable for substituting liver tissue in terms of tactile properties based on the current results.

2.5 Limitations

The following limitations should be considered: First, the loss tangent $\tan\delta$ was measured for one specific indentation depth h_0 only, while the effect of varying h_0 was not considered in the current study.

Second, the biggest limitation concerning the tactile similarity error, is that the weighting factors of each mechanical property could be quantified more rigorously.

In the current study all properties were weighted equally. Further investigation via palpation done by voluntary participants could rank the different properties in terms of their influence on tactility.

Next, a limitation concerning the experimental conditions, is that the *in vitro* model differs from *in vivo* conditions in certain aspects [Mattei and Ahluwalia, 2016]. For example, the tissue was non-perfused and not tested at body temperature. However, failure properties of bovine liver parenchyma do not change when tested at room temperature or body temperature according to Santago et al. [2009]. Perfusion, on the other hand, does influence the mechanical properties: Non-perfused liver is slightly stiffer and more viscous compared to perfused liver [Kerdok et al., 2006]. However, according to Kerdok et al. [2006] this effect does not play a role for initial loading while repeated loading causes significant tissue changes.

2.6 Conclusions

The here presented method provides insight into mechanical properties on a structural level that contribute to how a material feels to the touch and a means of comparing materials in this regard. The material found to resemble both porcine and bovine liver tissue the most was a silicone elastomer with a nominal Shore 00 hardness of 30. However, there is still room for improvement, for instance by adapting the material microstructure to enhance damping behaviour. Additive manufacturing of silicones and other soft polymers could be utilized for producing more versatile materials, potentially simulating liver tissue more accurately.

The described method is easily applicable to other biological tissues and could be a useful tool for validating tactile fidelity of any tissue mimicking material.

2.7 Acknowledgements

The research was funded by the NFB Science Call Dissertations 2017 (SC17-016), and the Austrian Center for Medical Innovation and Technology (ACMIT). The research center ACMIT is funded in the framework of COMET – Competence Centers for Excellent Technologies – by BMVIT, BMDW, as well as the Federal State of Lower Austria and Standortagentur Tirol. This study was partially supported by the Austrian Research Promoting Agency (FFG): M3dRES Project nr. 858060.

2.8 Appendix

2.8.1 Consideration of number of Prony series terms

Calculation of root-mean-square error (RMSE) when fitting Eq. 2.7 to the experimental relaxation curve utilizing 1, 2, 3, or 4 Prony terms, indicated how well the predicted values match the experimental ones. Evidently, the choice of a 3-element approach was supported by the comparison of RMSE for the varying element numbers seen in Fig. 2.6.

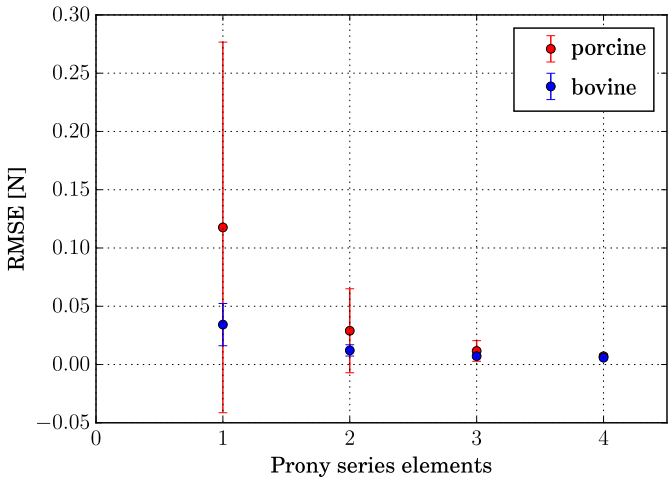

Figure 2.6: RMSE and standard deviation for 1-, 2-, 3-, and 4-element Prony series for porcine and bovine liver tissue

2.8.2 Tactile material properties

Table 2.1: Mean mechanical properties and standard deviations based on quasistatic and force relaxation testing; specifically Shore 00 hardness H, spring stiffness k, contact stiffness S, and loss tangent $\tan\delta$ for 1 Hz.

Material	H [SU]	k [N/mm]	S [N/mm]	$\tan\delta$ [1]
TangoPlus	67.22 ± 0.20	2.51 ± 0.056	5.50 ± 0.234	0.531 ± 0.036
0%	64.22 ± 1.54	2.43 ± 0.269	3.83 ± 0.381	0.057 ± 0.022
10%	57.18 ± 0.31	2.36 ± 0.026	3.53 ± 0.047	0.040 ± 0.003
20%	47.96 ± 1.20	1.74 ± 0.073	2.57 ± 0.108	0.035 ± 0.001
30%	39.83 ± 0.24	1.37 ± 0.022	1.97 ± 0.049	0.028 ± 0.001
pig	30.52 ± 1.52	0.97 ± 0.215	10.18 ± 1.718	0.231 ± 0.145
cow	25.67 ± 2.61	0.63 ± 0.067	7.22 ± 0.918	0.191 ± 0.202
00-30	25.44 ± 0.22	0.86 ± 0.014	1.29 ± 0.016	0.038 ± 0.012
00-20	10.33 ± 0.27	0.53 ± 0.010	0.80 ± 0.017	0.127 ± 0.020
00-10	n.a.	0.28 ± 0.014	0.65 ± 0.114	0.280 ± 0.014
00-313	3.06 ± 0.21	0.40 ± 0.024	0.74 ± 0.050	0.202 ± 0.027

Chapter 3

Hyperelasticity and viscoelasticity of liver

From the manuscript:

Hyperelastic and viscoelastic characterisation of hepatic tissue under uniaxial tension in time and frequency domain

S.-J. Estermann, D. H. Pahr, A. Reisinger

Published in: *J. Mech. Behav. Biomed. Mater. 112:104038, December 2020*

Abstract

In order to create accurate anatomical models for medical training and research, mechanical properties of biological tissues need to be studied. However, non-linear and viscoelastic behaviour of most soft biological tissues complicates the evaluation of their mechanical properties. In the current study, a method for measuring hyperelasticity and viscoelasticity of bovine and porcine hepatic parenchyma in tension is presented. First, non-linear stress-stretch curves, resulting from ramp loading and unloading, were interpreted based on a hyperelastic framework, using a Veronda-Westmann strain energy function. Strain-specific elastic moduli, such as initial stiffness E_I, were thereupon defined in certain parts of the stress-stretch curves. Furthermore, dissipated and stored energy density were calculated. Next, the viscoelastic nature of liver tissue was examined with two different methods: stress relaxation and dynamic cyclic testing. Both tests yielded dissipated and stored energy density, as well as loss tangent ($\tan\delta$), storage modulus (E'), and loss modulus (E''). In tension, stress relaxation was experimentally more convenient than dynamic cyclic testing. Thus we considered whether relaxation could be used for approximating the results of the cyclic tests.
Regarding the resulting elastic moduli, initial stiffness was similar for porcine and bovine liver ($E_\mathrm{I} = 30$ kPa), while porcine liver was stiffer for higher strains. Comparing stress relaxation with dynamic cyclic testing, $\tan\delta$ of porcine and bovine liver

was the same for both methods ($\tan\delta = 0.05 - 0.25$ *at 1 Hz). Storage and loss moduli matched well for bovine, but not as well for porcine tissue.*
In conclusion, the utilized Veronda-Westmann model was appropriate for representing the hyperelasticity of liver tissue, seen in ramp tests. Concerning viscoelasticity, both chosen testing methods—stress relaxation and DMA—yielded comparable results for E', E'', *and* $\tan\delta$, *as long as elasticity non-linearities were heeded.*
The here presented method provides novel insight into the tensile viscoelastic properties of hepatic tissue and provides guidelines for convenient evaluation of soft tissue mechanical properties.

Keywords: hepatic tissue; tensile testing; viscoelasticity; hyperelasticity; stress relaxation; dynamic mechanical analysis

3.1 Introduction

Surgical training requires scenarios that are as life-like as possible. However, before practising on real *in vivo* patients, teaching models are necessary. The use of fresh human tissue is limited due to ethical concerns, availability, and safety issues. Thus, models usually consist of preserved human cadavers, animal organs or artificial materials.

Especially, the increasing trend towards minimally invasive methods in general surgery calls for improved laparoscopic training systems [Alli et al., 2017, Armijo et al., 2018, Chen et al., 2020]. Cholecystectomy and hepatectomy, for instance, are common surgical procedures that are widely being performed laparoscopically and require corresponding training systems which must include the liver [Alli et al., 2017, Yoshida et al., 2019]. In this context, porcine and bovine liver models are deemed useful for laparoscopic training [Hildebrand et al., 2007, Laird et al., 2011, Liu et al., 2018]. Furthermore, liver models are important for risk analysis in crash tests, due to the high susceptibility of the liver to injury during vehicular crashes [Yoganandan et al., 2000, Kemper et al., 2010]. Another application for hepatic models is in practising palpation to distinguish fibrotic from healthy tissue and identifying tumours in open surgery approaches [Hata et al., 2011]. It is therefore important to accurately measure liver mechanical properties in order to manufacture realistic models.

In general, characterising mechanical properties of soft tissue can be challenging due to potentially non-linear and viscoelastic material behaviour, as well as the need for measuring small loads, resulting from the low stiffness (with the Young's modulus typically < 1 MPa [Akhtar et al., 2011]).

Hepatic tissue is difficult to handle in experimental setups and has predominantly been studied in compression [Tamura et al., 2002, Kiss et al., 2004, Ocal et al., 2010, DeWall et al., 2012, Jing et al., 2016] and shear [Liu and Bilston, 2002, Nicolle et al., 2010, Wex et al., 2013, Zhu et al., 2013, Capilnasiu et al., 2020], regarding elastic as well as viscoelastic tissue properties. Tensile tests on hepatic parenchyma have been conducted for evaluating failure properties [Brunon et al., 2010, Kemper et al., 2010, Lu et al., 2014, Duong et al., 2015, Dunford et al., 2018]; thus, illuminating the effect of large strains ($> 10\%$ [Marchesseau et al., 2017]) on the tissue, as experienced in the context of trauma. However, it is also interesting to study liver under small strains relevant for tactile properties.

Ramp tests of hepatic tissue result in non-linear stress-strain curves [Chen et al.,

1996], suggesting the use of hyperelastic modelling [Chui et al., 2004, Gao et al., 2010, Umale et al., 2013]. However, a purely hyperelastic approach neglects viscoelastic behaviour which plays an important role in liver tissue [Liu and Bilston, 2000]. As a partial solution to this problem, the idea of pseudoelasticity was introduced by Fung [1993] for interpreting loading-unloading curves exhibiting hysteresis (which is an indicator for viscoelasticity), utilizing a hyperelastic framework: Loading and unloading is thereby modelled separately, yielding two distinct stets of hyperelastic parameters. Another approach to analysing non-linear behaviour is to define certain strain ranges, where elastic moduli can be calculated [Fung, 1967]. For example, characteristic low-strain and high-strain elastic moduli were determined for liver capsule [Hollenstein et al., 2006, Karimi and Shojaei, 2018] and for kidney capsule [Snedeker et al., 2005] in uniaxial tension.

However, these methods are only descriptive of what is observed but fail to describe the constitutive effect of viscoelasticity itself. To study viscoelasticity in a more rigorous manner, the most common methods are: testing at different strain rates, stress relaxation (under constant strain), creep (under constant stress), and dynamic cyclic testing (oscillating stress and strain) which is also known as dynamic mechanical analysis (DMA). The results of these various testing methods can be compared with each other. For example, Bartolini et al. [2018] compared viscoelastic properties from indentation at different oscillatory frequencies with indentation at different strain rates for a soft silicone polymer – thus connecting frequency domain and time domain experimental data. Following this train of thought, viscoelastic properties, extracted from relaxation experiments, could be compared with the same type of properties found in dynamic cyclic tests.

Regarding stress relaxation of hepatic tissue, experiments have been conducted under compression [Taylor et al., 2002], shear [Liu and Bilston, 2000, 2002], tension [Chen et al., 2011] and indentation [Mattice et al., 2006, Estermann et al., 2020a]. DMA has been done on liver tissue in compressive and shear conditions [Kiss et al., 2004, Capilnasiu et al., 2020]. However, the authors are not aware of publications on liver parenchyma exposed to tensile oscillatory strain for assessing tissue viscoelastic properties. This may be due to experimental difficulties connected to tensile testing of extremely soft materials; with DMA being more complex than other testing methods, such as stress relaxation or creep. Thus, the question arises whether simple relaxation data could be utilized instead of DMA for hepatic tissue in tension. Viscoelastic properties, which are usually extracted directly from dynamic cyclic tests (e.g. loss tangent, storage modulus, and loss modulus), can be calculated based on relaxation data via transformation from time domain to frequency domain [Ocal et al., 2010].

The current study aims at a comprehensive characterisation of hepatic tensile mechanical properties, meaning that non-linear as well as viscoelastic behaviour must be taken into account. For this reason, different types of tests were conducted on porcine and bovine hepatic parenchyma tissue. First, ramp loading and unloading was done, yielding hysteresis and non-linear behaviour. These curves were interpreted with a pseudoelastic model and elastic moduli, defined at specific strain levels, were calculated. Furthermore, based on energy considerations, the ratio of dissipated to stored energy density was evaluated.

Next, two different methods of viscoelastic characterisation – force relaxation and DMA – were utilized for extracting loss tangent ($\tan\delta$), storage modulus (E'), and loss modulus (E''). These properties stemming from the two testing methods were finally

compared with each other, addressing the question whether a simplified viscoelastic evaluation via stress relaxation (assuming an ideal step-displacement) is justified for hepatic tissue in tension. In addition to the above mentioned viscoelastic properties, dissipated and stored energy density were calculated for relaxation and DMA, yielding results that are specific for each testing method.

3.2 Materials & methods

3.2.1 Tensile test specimen

Hepatic samples were taken from eight porcine, and two bovine livers, obtained from a local butchery about 24 h after slaughtering and prepared for testing immediately upon arrival in the laboratory (Figure 3.1a and b). Between slaughtering and sample preparation, whole livers were stored at 4° C in sealed plastic bags. Dunford et al. [2018] recommended storage of liver in large blocks as opposed to small cut samples. Rectangular tensile test specimen were extracted with their long axis orientated parallel to the diaphragmatic and the visceral surface of the organs: First a rectangular block (measuring around $75 \times 50 \times 30$ mm) was cut out of a relatively homogeneous region of the liver (Figure 3.1c). After removing the capsule, the block was placed in a 5 mm thick 3D printed cutting guide and a long knife was used for extracting thin rectangular slices by cutting parallel to the guide (Figure 3.1d). Next, a 75×20 mm stencil was placed on the liver slice and samples were obtained by cutting around the stencil (Figure 3.1e). The resulting samples consisted of parenchyma tissue, without the Glisson's capsule, free of large blood vessels and bile ducts, to ensure relative homogeneity (Figure 3.1f). Sample thickness was chosen as 5 mm due to the fact that samples of under 2.5 mm thickness exhibited dehydration at the sand paper contact area when being clamped in the mechanical testing machine, while significantly thicker samples were difficult to mount and clamp. The total numbers of porcine samples was $n = 36$, as was for the bovine samples whose total number was also $n = 36$. All samples were kept well hydrated by submerging them in 0.9% saline solution. Mechanical testing was conducted immediately after sample preparation at room temperature (approximately 23° C), thus the tissues were never frozen.

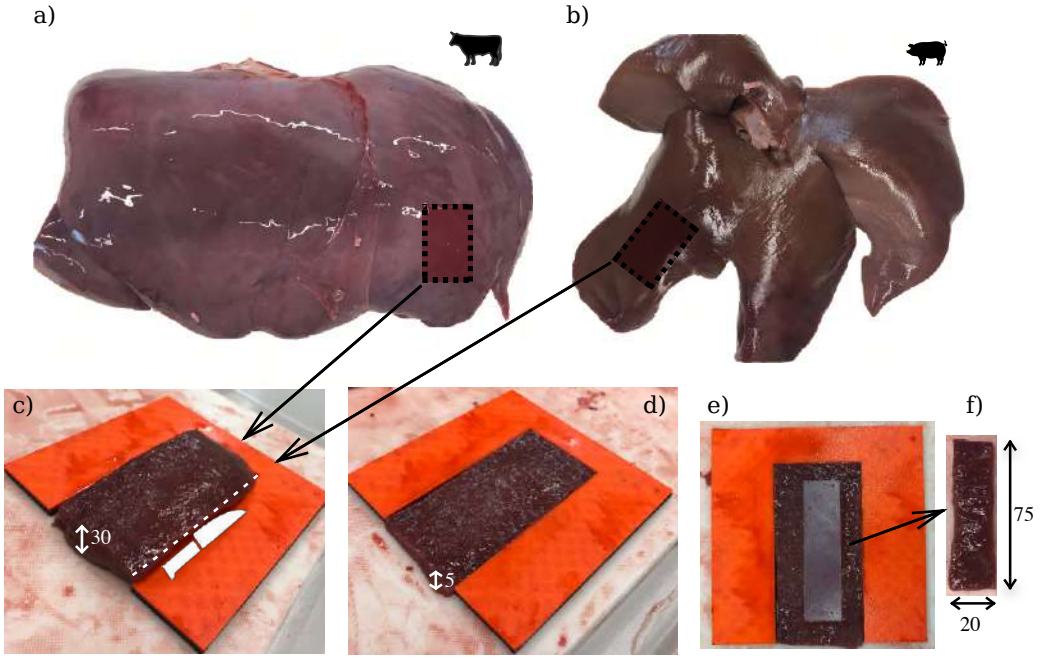

Figure 3.1: Sample preparation: (a) and (b) Whole bovine and porcine organs; (c) Block of hepatic tissue is placed in the 3D printed cutting guide; (d) Cutting along the surface of the cutting guide yields a thin tissue layer; (e) Rectangular stencil is placed on the tissue layer; (f) Sample that is cut from the tissue layer ($75 \times 20 \times 5$ mm).

3.2.2 Mechanical testing

Tensile testing was conducted on a ZwickiLine testing machine (ZwickRoell GmbH & Co. KG, Ulm, Germany) which allows axial forces F up to 2.5 kN and a machine displacement u_{M} of up to 113 cm. In soft tissue testing, the resulting forces are very small and thus an additional load cell for measuring F, with a measuring range up to 100 N and accuracy of 0.02% (S2M/100N, Hottinger Baldwin Messtechnik GmbH, Darmstadt, Germany) was connected to the universal data acquisition module (DAQ) QuantumX MX840B (Hottinger Baldwin Messtechnik GmbH, Darmstadt, Germany). The load cell was gripped by the lower machine clamp.

Custom-built tissue clamps enabled manual fine-tuning of the gripping force with a screw. One tissue clamp was secured in the upper machine clamp and the other one inserted above the external load cell. The tissue clamping surface was covered with sand paper (grit P80) to prevent sample slippage during tension.

For the evaluation of the dynamic cyclic tests, extremely small phase shifts between force and displacement of a few milliseconds need to be measured, requiring perfectly synchronous measurements. Thus, a linear variable differential transformer (LVDT) position sensor (Hottinger Baldwin Messtechnik GmbH, Darmstadt, Germany) was also connected to the same DAQ, for measuring displacement u_{LVDT} at exactly the same time as the load cell measurement.

The LVDT displacement, however, does not only describe tissue displacement, but also includes contributions stemming from machine and setup stiffness as well as clamping of the sample. For this reason, a specific measuring length l was defined with point markers on the sample whose change in length was recorded optically by

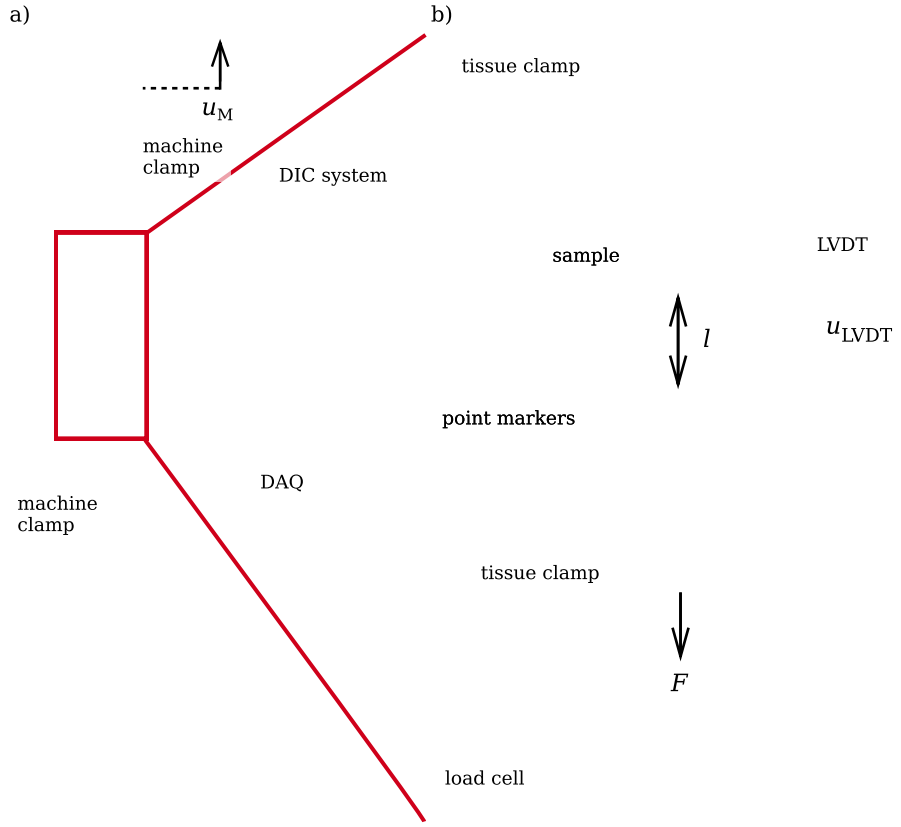

Figure 3.2: Overview of the mechanical test setup: (a) Complete setup with the machine displacement u_M, upper and lower machine clamps, digital image correlation (DIC) system, and data acquisition module (DAQ) – connected to the load cell and displacement sensor (LVDT) in (b); furthermore in (b), hepatic sample clamped with the tissue clamps, point markers to measure the length l, the tensile force F, and the displacement of the LVDT u_{LVDT}.

the digital image correlation (DIC) system ARAMIS (GOM GmbH, Braunschweig, Germany). To certify uniform displacement within the sample, three marker pairs were arranged along the width of the sample and length l was reported as the average of the three distances. Actual tissue strains were based on these DIC displacements, while the temporal information, needed for the dynamic cyclic tests was extracted from the LVDT measurement.

An overview of the mechanical test setup and the measured properties (force F, machine displacement u_M, position sensor displacement u_{LVDT}, and sample measuring length l) are depicted in Figure 3.2. A mounting procedure of the samples in the testing machine, similar to the one described by Manoogian et al. [2009] and Kemper et al. [2010], was followed: First the top tissue clamp was removed from the testing machine and the sample was placed on the sand paper surface of the clamp and aligned. Used sand paper was always replaced by a new layer for each sample. Next, the sample was inserted in the testing machine, attached to the top clamp with its bottom end hanging freely. At this stage, each sample was allowed to hang under its own weight (around 0.08 N) for approximately 3 minutes to ensure an equal small preloading of the tissue. Finally the bottom clamp was carefully closed, the sticky markers for DIC were applied, and sample cross-section was measured with an analogue calliper at three locations along the measuring length. The initial cross-section A_0 was taken as

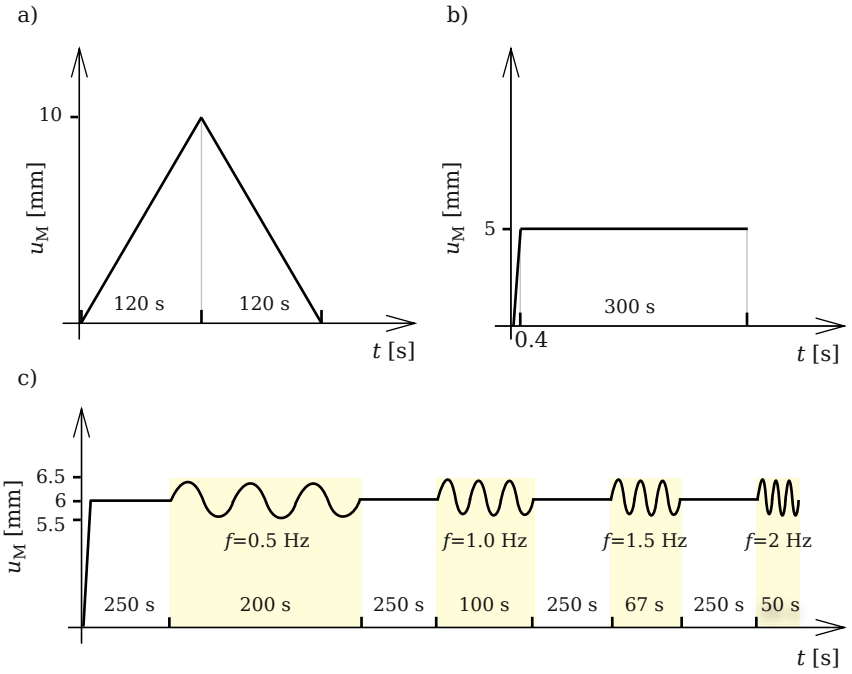

Figure 3.3: Overview of the mechancial testing protocols with u_M being the machine displacement and t the time: (a) Ramp loading and unloading sequence; (b) holding phase for relaxation; (c) Dynamic cyclic testing (100 cycles for each frequency).

the average of these three measurements. The initial length l_0 was defined based on a single DIC image taken before starting mechanical loading.

Each sample was exposed to one of the following mechanical tests: ramp test, stress relaxation, or dynamic cyclic test (Figure 3.3). All 36 samples of the porcine and bovine tissue were divided among the three testing methods, resulting in 12 samples per test and tissue type.

Ramp test Upon starting extension of the samples, a trigger signal was sent from the testing machine to the DIC system, prompting both measurements to start. The cross-head of the testing machine was displaced by $u_M = 10$ mm (resulting in a maximum engineering tissue strain of $0.10 - 0.14$) at a speed of 5 mm/min (corresponding to a strain rate of 0.001 s^{-1}) and then moved back to its initial position at the same speed (see Figure 3.3a). Due to the highly strain rate dependant behaviour of soft biological tissues, evaluation of elastic properties requires *quasistatic* strain rates [Fung, 1967, Miller and Chinzei, 1997]. A similar strain rate was utilized as the rate reported for hepatic capsule in tension by Brunon et al. [2010] who considers 0.001 s^{-1} to be quasistatic. Force F, from the 100 N load cell, and lengths l between the markers, from DIC for calculating strains, were both recorded at a measuring rate of 10 Hz.

Stress relaxation A cross-head displacement of $u_M = 5$ mm (0.06 tissue strain based on DIC measurement) was applied within 0.4 s and held for 300 s (see Figure 3.3b). Force F and lengths l between the markers were both recorded at a rate of

10 Hz by the 100 N load cell and DIC, respectively.

Dynamic cyclic test After capturing a single image with the DIC system for defining the initial length between the markers l_0, a cross-head displacement of $u_M = 6$ mm (0.08 tissue strain) was applied and then held for 250 s to allow best possible relaxation. Next, sinusoidal displacements of ±0.5 mm (±0.006 tissue strain) were applied at $f = 0.5$, $f = 1.0$, $f = 1.5$, and $f = 2.0$ Hz for 100 cycles at each frequency. Low frequencies were chosen to avoid inertia effects [Nicolle and Palierne, 2010, Chatelin et al., 2011] and to represent tactile palpation of the material [Estermann et al., 2020a]. Samples were allowed to relax at $u_M = 6$ mm for 250 s between each tested frequency to enable comparison of the frequency-dependant tissue response. See Figure 3.3c for an overview of the testing procedure.

The chosen strain level ensured that samples were not compressed but stayed in tension throughout the test. Lengths between markers l were recorded by the DIC system (at 10 Hz for $f = 0.5$ Hz and at 20 Hz for the other frequencies). Pretests showed that phase shifts between stress and strain were expected to be around 15 ms for liver. Thus, in order to resolve such small phase shifts, measuring of force and displacement must be perfectly synchronised. For this reason, u_{LVDT} from the LVDT was utilized alongside F from the load cell, both being controlled by the same data acquisition module and software at a sampling frequency of 100 Hz. The LVDT position sensor yielded the actual occurrence time of the displacement without delay, while DIC provided the accurate displacement (and strain) amplitude.

3.2.3 Data analysis

Uniaxial tissue stretch λ (in direction of the main sample axis) is expressed as the ratio between deformed length l and the initial length l_0 as

$$\lambda = \frac{l}{l_0} = \varepsilon + 1\,, \tag{3.1}$$

with ε being engineering strain. Cauchy (true) stress σ_T – assuming incompressibility of hepatic tissue [Chui et al., 2004] – and engineering stress σ_E were calculated based on the measured tensile force F and initial cross-section A_0 as

$$\sigma_T = \frac{F}{A_0}\lambda \tag{3.2}$$

and

$$\sigma_E = \frac{F}{A_0}\,. \tag{3.3}$$

Ramp test Hepatic parenchyma tissue is viscoelastic, exhibiting hysteresis, even during extremely slow loading and unloading cycles. Thus, a purely hyperelastic treatment of the material is not valid, as this would completely ignore viscoelasticity. The so-called pseudoelastic approach – introduced by Fung [1993] – allows the separate evaluation of the loading and unloading branch with two distinct sets of characteristic hyperelastic parameters.

In order to establish a stress-strain relation, in terms of a hyperelastic model, the strain energy function Ψ is introduced. For an isotropic material, $\Psi = \Psi(I_1, I_2, I_3)$ depends on the strain invariants I_1, I_2, and I_3. The strain invariants are calculated

based on the finite deformation applied to the material. In the following sections, liver tissue is modelled as incompressible ($\nu = 0.5$), as is often done for soft tissues [Fung, 1967, Miller and Chinzei, 1997, Gao et al., 2010, Roan and Vemaganti, 2011]. The Poisson's ratio of $\nu = 0.434 \pm 0.16$ for hepatic parenchyma in tension, reported by Chui et al. [2004], furthermore supports the assumption of incompressibility.

Thermodynamic, symmetry, and energy considerations enable the choice of strain energy function $\Psi(I_1, I_2, I_3)$. Based on the comparison of different hyperelastic models presented in 3.8.1, $\Psi(I_1, I_2, I_3)$ suggested by Veronda and Westmann [1970] for feline skin was utilized:

$$\Psi = c_1\left[\mathrm{e}^{\beta(I_1-3)} - 1\right] + c_2(I_2 - 3) + g(I_3)\,, \tag{3.4}$$

with c_1, c_2, and β being the model parameters, and $g(I_3)$ being a function of tissue compressibility. After inserting the strain invariants $I_1 = \lambda^2 + \frac{2}{\lambda}$, $I_2 = 2\lambda + \frac{1}{\lambda^2}$, and $I_3 = 1$ for uniaxial tension of an incompressible material into Eq. 3.4 and further simplifying with $g(I_3) = g(1) = 0$, $c_2 = -c_1\frac{\beta}{2}$, and $c_1 = c$, the strain energy function results in

$$\Psi = c\left[\mathrm{e}^{\beta(I_1-3)} - 1\right] - c\frac{\beta}{2}(I_2 - 3)\,, \tag{3.5}$$

leaving the two material parameters c and β to be determined.

In case of incompressibility, the uniaxial Cauchy stress σ_T can be expressed in terms of the strain invariants I_1 and I_2, according to Holzapfel [2000], as

$$\sigma_\mathrm{T} = 2\left(\lambda^2 - \frac{1}{\lambda}\right)\left(\frac{\partial\Psi}{\partial I_1} + \frac{1}{\lambda}\frac{\partial\Psi}{\partial I_2}\right), \tag{3.6}$$

Using Eqs. 3.5 and 3.6, the stress of the Veronda-Westmann model can thus be written as

$$\sigma_\mathrm{VW} = 2\left(\lambda^2 - \frac{1}{\lambda}\right)c\beta\left(\mathrm{e}^{\beta(I_1-3)} - \frac{1}{2\lambda}\right). \tag{3.7}$$

To now obtain material parameters for the loading and unloading part of the tensile ramp experiments, Eq. 3.7 was fit to the experimental true stress with non-linear least squares method, utilizing a Levenberg-Marquardt algorithm [Marquardt, 1963], for loading and unloading curves separately. Thus, the resulting fitting parameters were c_load and β_load (for loading) as well as c_unload and β_unload (for unloading). The coefficient of determination r^2 was calculated in order to evaluate how well the model data corresponded to the experimental data. See Figure 3.4 for a typical experimental stress-stretch curve alongside the corresponding hyperelastic model.

In addition to the above described hyperelastic approach, a second type of data evaluation was applied, that is more descriptive of the stress-stretch curve shape. For each loading-unloading sequence, three characteristic elastic moduli were defined: E_I as the initial elasticity, E_II for the highest stretch during loading, and E_III for the first stretch during unloading. E_I, E_II, and E_III were calculated based on the slope of tangent of σ_VW for the corresponding stretch ranges (see Figure 3.4).

Furthermore, the ramp tests were interpreted, based on energy considerations: For stretching the material, mechanical work is required in the loading phase, which is partly dissipated and partly stored as elastic strain energy. During the following unloading phase, part of the stored energy is recovered elastically while another part is dissipated. The ratio between the dissipated energy density W_dis and the recovered (or stored) energy density W_st is referred to as *relative dissipation*, $W_\mathrm{dis}/W_\mathrm{st}$, and can be calculated based on the stress-stretch curves. Thereby, W_dis is the area between the

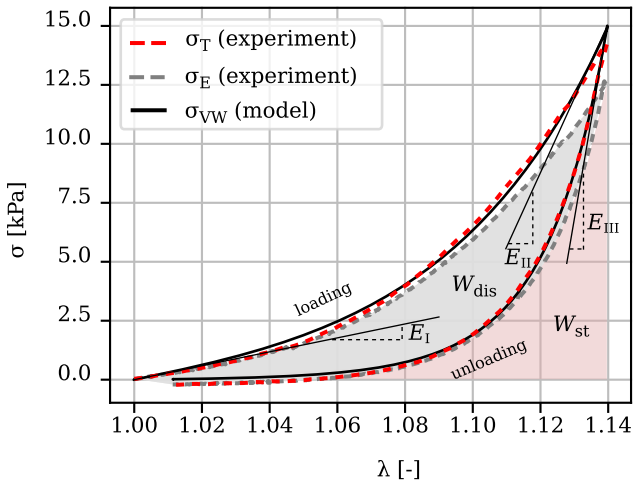

Figure 3.4: Typical stress-stretch curve of a bovine ramp test with the measured true stress σ_{T} (dashed red line), the corresponding Veronda-Westmann curve fit σ_{VW} (solid black line), and the calculated elastic moduli (E_{I}, E_{II}, and E_{III}). The engineering stress σ_{E} (dashed grey line) is used to calculate the dissipated energy density W_{dis} and stored energy density W_{st}.

loading and unloading curve and W_{st} is the area under the unloading curve (see Figure 3.4). Due to energy considerations, engineering stress σ_{E} with the stretch ratio λ as its energy conjugate [Shergold et al., 2006] were used for these calculations(Figure 3.4).

Stress relaxation Assuming a step displacement, where the holding phase is reached instantaneously, stress σ and the constant strain ε_0 are connected via the time-dependant relaxation function $E(t)$ according to

$$\sigma(t) = E(t)\varepsilon_0 \,. \tag{3.8}$$

The relaxation function can be approximated in terms of Prony series,

$$E(t) = E_\infty + \sum_{i=1}^{N} E_i e^{-\frac{t}{\tau_i}} \,, \tag{3.9}$$

which correspond to the generalised Maxwell model depicted in Figure 3.5, with the longterm elastic modulus E_∞, the elastic moduli of the springs E_i, and the character-

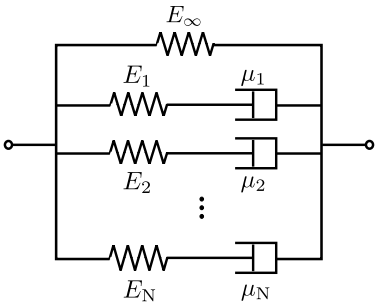

Figure 3.5: Generalised Maxwell model, consisting of the longterm elastic modulus E_∞ and the N parallel Maxwell branches with springs E_1, E_2, ... E_N and dashpots μ_1, μ_2, ... μ_N.

istic relaxation times τ_i (which are related to the dashpot viscosities μ_i via $\tau_i = \mu_i/E_i$) [Findley et al., 1989]. Replacing E_∞ by

$$E_\infty = E_0 - \sum_{i=1}^{N} E_i \,, \tag{3.10}$$

in Eq. 3.9, expresses the relaxation function in terms of the initial elasticity E_0 (the ratio between stress and strain at the beginning of the holding phase) according to

$$E(t) = E_0 - \sum_{i=1}^{N} E_i(1 - e^{-\frac{t}{\tau_i}}) \,. \tag{3.11}$$

After inserting Eq. 3.11, Eq. 3.8 was utilized to approximate the experimental stress relaxation, applying a non-linear least squares method, implemented with a trust region reflective algorithm, which limited fitting parameters to positive values. Thereby, the curve fit was performed over the complete holding time of 300 s, as discussed below and in 3.8.2. Furthermore, based on considerations presented in 3.8.2, $N = 3$ was chosen for further calculations, as was also done by Ocal et al. [2010] for compression and Estermann et al. [2020a] for indentation of hepatic tissue in the context of relaxation within the same magnitude of holding times.

Obtained, model parameters E_i and τ_i were then utilized to calculated the storage and loss moduli E' and E'' according to Gutierrez-Lemini [2014] with

$$E' = E_\infty + \sum_{i=1}^{N} \frac{E_i \omega^2 \tau_i^2}{1 + \omega^2 \tau_i^2} \tag{3.12}$$

and

$$E'' = \sum_{i=1}^{N} \frac{E_i \omega \tau_i}{1 + \omega^2 \tau_i^2} \,, \tag{3.13}$$

where ω is the angular frequency. The ratio of loss modulus to storage modulus

$$\frac{E''}{E'} = \tan\delta = \sum_{i=1}^{N} \frac{\omega \mu_i E_i^2}{E_\infty(E_i^2 + \omega^2 \mu_i^2) + \omega^2 E_i \mu_i^2} \tag{3.14}$$

is called *loss tangent* $\tan\delta$, which is a characteristic viscoelastic property that describes the frequency-dependant material damping behaviour.

Concerning the Prony series curve fit, the question arises, whether holding duration influences the resulting viscoelastic properties. The reason for this being the following: Data was sampled equidistantly throughout the holding phase of 300 s. Thus, the portion of rapid stress decline at the beginning of the stress-time curve is emphasised less in the curve fit, in contrast to the portion of nearly constant stress in the middle and end part of the curve, where many more data points are available. Further examination of the influence of holding time is described in 3.8.2, showing that $\tan\delta$ is fairly consistent throughout the tested time span. Thus, if not further specified, $\tan\delta$ is reported for a holding time of 300 s in the following sections.

Additionally to the frequency-dependant damping behaviour, expressed by $\tan\delta$ and the dynamic moduli E' and E'', relative dissipation $\frac{W_{\text{dis}}}{W_{\text{st}}}$ is calculated for the

performed experiment. The work density, necessary for initially reaching ε_0 during the fast ramp loading, can be expressed as

$$W_0 = \frac{1}{2} E_0 \varepsilon_0^2 \,, \tag{3.15}$$

with $E_0 = E_\infty + E_1 + E_2 + E_3$ (Eq. 3.10) referring to the parallel springs in Figure 3.5. After waiting for the holding period to pass and the viscosities to dissipate, the only spring contributing to the stress response is the long-term stiffness E_∞, signifying work, which can be elastically recovered if the material were unloaded at this point,

$$W_{\mathrm{st}} = \frac{1}{2} E_\infty \varepsilon_0^2 \,. \tag{3.16}$$

Thus, the dissipated energy density, being the difference between W_0 and W_∞, can be expressed as

$$W_{\mathrm{dis}} = \frac{1}{2} (E_1 + E_2 + E_3) \varepsilon_0^2 \,. \tag{3.17}$$

Finally, the relative dissipation $W_{\mathrm{dis}}/W_{\mathrm{st}}$ results in

$$\frac{W_{\mathrm{dis}}}{W_{\mathrm{st}}} = \frac{E_1 + E_2 + E_3}{E_\infty} \,. \tag{3.18}$$

Dynamic cyclic test The analysis of dynamic cyclic tests consists of finding $\tan\delta$, E', and E'' from sinusoidal data. For a linear viscoelastic material exposed to a sinusoidal displacement

$$u(t) = u_{\mathrm{A}} \sin(\omega t) \tag{3.19}$$

with the displacement amplitude u_{A}, angular frequency ω, and time t, the responding force is also sinusoidal with the same frequency and amplitude F_{A} but shifted by a phase δ (Figure 3.6a)

$$F(t) = F_{\mathrm{A}} \sin(\omega t + \delta) \,. \tag{3.20}$$

Due to the fact that phase shifts are expected to be in the range of a few milliseconds, special attention needs to be taken concerning the synchronicity of the force and displacement measurement. Thus, the loss tangent $\tan\delta$ was based on LVDT displacements. Non-linear least squares method was utilized to fit Eq. 3.19 and Eq. 3.20 to F and u_{LVDT}, yielding the fitting parameters F_{A}, u_{A}, ω, and δ. This method was applied to the last 30 cycles of each frequency test, leaving the first 70 cycles for preconditioning the material to a steady state oscillation.

Furthermore, after utilizing u_{LVDT} for calculating $\tan\delta$, storage and loss modulus E' and E'' were calculated using strains ε based on the DIC measurement with

$$E' = \frac{\sigma_{\mathrm{A}}}{\varepsilon_{\mathrm{A}}} \cos\delta \tag{3.21}$$

and

$$E'' = \frac{\sigma_{\mathrm{A}}}{\varepsilon_{\mathrm{A}}} \sin\delta \,, \tag{3.22}$$

with ε_{A} being the amplitude of engineering strain and σ_{A} being the amplitude of true stress. Description of the measured quantities can be found in Figure 3.6.

In order to describe the loss factor in terms of energy dissipation, $\tan\delta$ can be written as the ratio between dissipated and maximum stored energy density [Roylance, 2001]:

$$2\pi \tan\delta = \frac{W_{\text{dis}}}{W_{\text{st}}}\,. \tag{3.23}$$

Thus, the relative dissipation $W_{\text{dis}}/W_{\text{st}}$ per cycle is calculated, base on the obtained $\tan\delta$. In case of linear viscoelasticity, it is assumed that the energy dissipation stems from viscous effects only and not plastic behaviour.

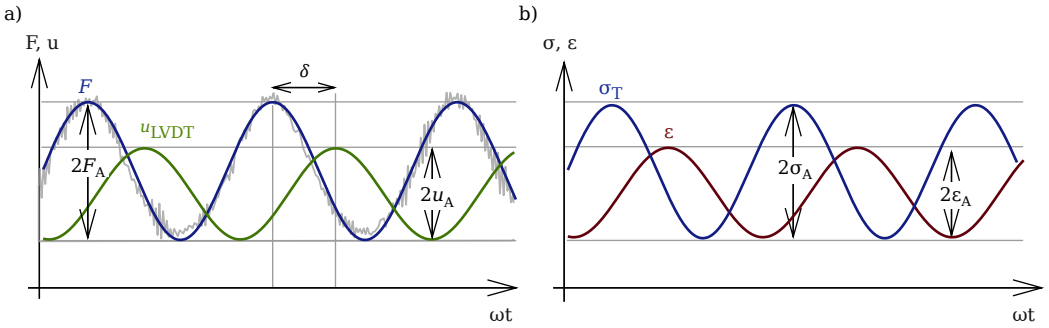

Figure 3.6: Schematic overview of the analysis of the dynamic tests: (a) LVDT displacement and load cell force are utilized to identify the phase shift δ due to their perfect measuring synchonicity; (b) Accurate signal amplitudes, ε_{A} and σ_{A}, are extracted from the strain, based on the DIC measurement, and the true stress, based on the load cell force.

3.2.4 Statistical analysis

Mean values and standard deviations were calculated over 12 bovine and 12 porcine samples for every result:

- from ramp tests, the pseudoelastic parameters (c_{load}, β_{load}, c_{unload}, β_{unload}), elastic moduli (E_{I}, E_{II}, E_{III}), and $W_{\text{dis}}/W_{\text{st}}$
- from relaxation, the Prony parameters (E_0, E_i, τ_i for $i = 1, 2, 3$), viscoelastic properties (E', E'', $\tan\delta$), and $W_{\text{dis}}/W_{\text{st}}$
- and from DMA at 4 frequencies, viscoelastic properties (E', E'', $\tan\delta$), and $W_{\text{dis}}/W_{\text{st}}$.

For comparing the two methods of viscoelastic characterisation, the resulting viscoelastic properties $\tan\delta$, E', and E'' of relaxation and DMA were checked for normal distribution (Shapiro-Wilk test). Then, given normality, Welch's t-tests were performed to identify significant differences ($\alpha = 0.05$) between the measured properties for $\tan\delta$, E', and E'' at $f = 0.5$, $f = 1.0$, $f = 1.5$, and $f = 2.0$ Hz, depending on the experimental modality without the requirement of homogenous variances.

3.3 Results

Ramp test The average values and standard deviations of true stress and stretch resulting from the loading-unloading sequence were plotted for all samples of the two tissue types in Figure 3.7a. The characteristic mean stress-stretch-curves of porcine

and bovine tissue are visibly different from each other with the average maximum stress for porcine tissue being 19.15 kPa and for bovine tissue 10.69 kPa. The maximum average strain applied to the samples was 11 % on average. The experimental curves – exhibiting non-linearity and hysteresis – were interpreted with a pseudoelastic Veronda-Westmann model with the resulting parameters for the loading and unloading part given in Table 3.2. The coefficient of determination being around 0.998 for bovine as well as porcine tissue, signifies an excellent agreement between experimental data and model. Parameters c_{load} and c_{unload} can be interpreted as shear-like moduli with β_{load} and β_{unload} being dimensionless exponential parameters [Limbert, 2019]. The initial zero-strain shear-like modulus c_{load} was higher for bovine tissue (0.542 ± 0.190 kPa) than for porcine tissue (0.353 ± 0.237 kPa).

Based on the pseudoelastic model, elastic moduli at different strain values were calculated (Table 3.2). While, the initial stiffness E_{I} was nearly the same for porcine and bovine tissue, the average elastic moduli for larger strains E_{II} and unloading E_{III} were more than twice as high for porcine liver. For the ramp loading and unloading sequence, the ratio between dissipated and stored energy density was calculated and results are given in Table 3.2. The relative energy dissipation being around $W_{\text{dis}}/W_{\text{st}} = 1.1$ for both tissue types, signifies that a similar amount of energy was dissipated due to viscosity and plasticity as stored elastically.

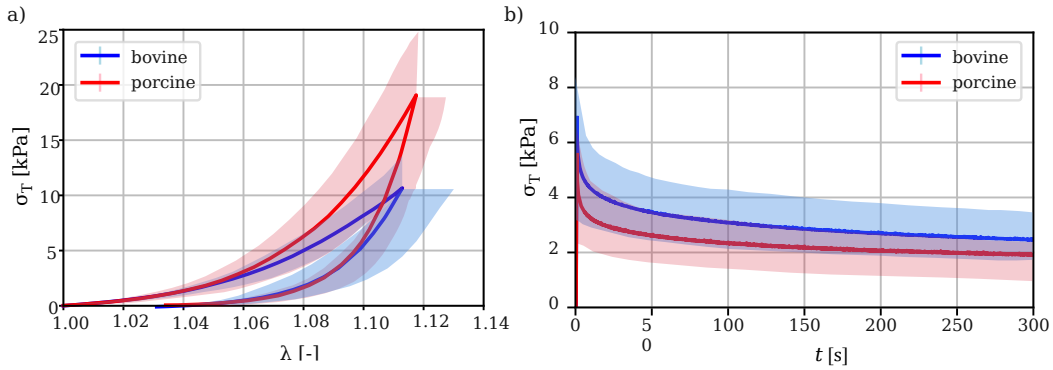

Figure 3.7: (a) Mean true stress σ_{T} plotted over the mean stretch λ for the ramp tests with the shaded areas being the standard deviations of stress and stretch ($n = 12$ for bovine and $n = 12$ for porcine); (b) Mean true stress σ_{T} plotted over time t for the relaxation tests, with the shaded area being the standard deviation of stress ($n = 12$ for bovine and $n = 12$ for porcine).

Stress relaxation Characteristic stress relaxation curves were plotted in Figure 3.7b for bovine and porcine tissue by averaging the true stress of all tested samples for each time instance. Prony series were fit to these experimental curves, yielding the model parameters given in Table 3.1. The resulting relaxation times represent 3 orders of magnitude with average $\tau_1 = 0.58$ s, $\tau_2 = 11.07$ s, and $\tau_3 = 140.48$ s for bovine tissue and average $\tau_1 = 0.34$ s, $\tau_2 = 7.33$ s, and $\tau_3 = 115.80$ s for porcine tissue. Relaxation times were shorter for porcine tissue compared to bovine tissue for each time scale. Relative dissipation for bovine and porcine tissue was $W_{\text{dis}}/W_{\text{st}} > 2$ (Table 3.1), meaning that more than twice as much energy was dissipated during relaxation than stored elastically in the material. Porcine hepatic tissue exhibited $W_{\text{dis}}/W_{\text{st}}$ around 20% higher than bovine tissue which is also mirrored in the trend that porcine $\tan\delta$ is higher than bovine $\tan\delta$ (Figure 3.8). Thus, the relaxation results indicate that porcine hepatic tissue exhibits a higher viscous contribution than bovine tissue.

Table 3.1: Results of the stress relaxation tests for bovine and porcine tissue, given as mean values and standard deviations: parameters of the Prony series fit ($N = 3$) E_0, E_1, τ_1, E_2, τ_2, E_3, and τ_3, the resulting root-mean-square error RMSE, and the relative dissipation $W_{\mathrm{dis}}/W_{\mathrm{st}}$.

Tissue	E_0 [kPa]	E_1 [kPa]	τ_1 [s]	E_2 [kPa]	τ_2 [s]	E_3 [kPa]	τ_3 [s]	RMSE [kPa]	$W_{\mathrm{dis}}/W_{\mathrm{st}}$ [-]
Bovine	117.96 ± 30.24	33.92 ± 8.85	0.58 ± 0.15	20.16 ± 5.67	11.07 ± 0.83	26.61 ± 6.81	140.48 ± 6.84	0.03 ± 0.01	2.17 ± 0.14
Porcine	129.89 ± 64.91	44.19 ± 20.34	0.34 ± 0.19	22.08 ± 12.04	7.33 ± 2.04	24.98 ± 13.83	115.80 ± 22.29	0.04 ± 0.01	2.64 ± 0.71

Table 3.2: Results of the ramp tests for bovine and porcine tissue, given as mean values and standard deviations: parameters of the pseudoelastic Veronda-Westmann model c_{load}, β_{load}, c_{unload}, and β_{unload}, the coefficient of determination r^2, elastic moduli E_{I}, E_{II}, and E_{III}, and relative dissipation $W_{\mathrm{dis}}/W_{\mathrm{st}}$.

Tissue	c_{load} [kPa]	β_{load} [-]	c_{unload} [kPa]	β_{unload} [-]	r^2 [-]	E_{I} [kPa]	E_{II} [kPa]	E_{III} [kPa]	$W_{\mathrm{dis}}/W_{\mathrm{st}}$ [-]
Bovine	0.542 ± 0.190	21.76 ± 8.953	0.013 ± 0.007	85.13 ± 23.97	0.998	32.00 ± 11.18	283.9 ± 92.94	689.6 ± 221.5	1.129 ± 0.177
Porcine	0.353 ± 0.237	35.11 ± 15.39	0.009 ± 0.008	101.50 ± 26.54	0.998	29.77 ± 14.79	669.9 ± 299.7	1428.4 ± 512.9	1.052 ± 0.285

Dynamic cyclic test For identifying the phase shift δ between force and displacement, sine curves were fit to the experimental force data F and the displacement of the position sensor u_{LVDT}. Due to the noisiness of the force readings for the two higher frequencies and due to the fact that the force level of bovine samples was even lower than porcine samples, the analysis for bovine tissue at $f = 1.5$ Hz and $f = 2.0$ Hz was not possible in the current setup. Dynamic viscoelastic properties are thus given for $f = 0.5$, $f = 1.0$, $f = 1.5$, and $f = 2.0$ Hz for porcine tissue and for $f = 0.5$ and $f = 1.0$ Hz for bovine tissue in the following sections. Due to the pre-stress and the small oscillatory amplitudes, samples were under tension throughout the whole experiment.

Table 3.3 lists the relative dissipation $W_{\mathrm{dis}}/W_{\mathrm{st}}$ depending on the tested frequency for both tissue types, showing that on average $W_{\mathrm{dis}}/W_{\mathrm{st}} = 0.64$ for bovine and $W_{\mathrm{dis}}/W_{\mathrm{st}} = 0.66$ for porcine liver. $W_{\mathrm{dis}}/W_{\mathrm{st}} < 1$ means that more energy was recovered elastically than dissipated due to viscosity for each cycle.

Furthermore, given in Table 3.3, are the mean values and standard deviations of the viscoelastic properties $\tan\delta$, E', and E'' found for bovine and porcine hepatic tissue in the dynamic tests.

Comparison of the viscoelastic parameters Loss tangent, storage modulus and loss modulus were extracted from relaxation, as well as DMA tests. Figures 3.8 – 3.10 depict the frequency dependence of $\tan\delta$, E', and E'' as was calculated based on the generalised Maxwell model for relaxation and measured in DMA. Porcine and bovine loss tangents correspond very well for the different testing methods throughout the examined frequency range (Figures 3.8a and b). When regarding the porcine storage modulus (Figure 3.9a), however, a discrepancy between relaxation ($E' = 100$ kPa) and dynamic cyclic testing ($E' = 500$ kPa) becomes apparent for all tested frequencies. Bovine tissue, on the other hand, yielded storage moduli that matched well for the testing methods (Figure 3.9b). A similar trend can be observed, concerning E'': While for porcine tissue, the dynamic loss modulus was more than two times higher than that found in relaxation (Figure 3.10a), bovine tissue exhibited E'' relatively independent of the testing method (Figure 3.10b).

Regarding a given frequency, for instance 1 Hz, the loss tangent $\tan\delta$ was not significantly different depending on the type of test for porcine ($p = 0.3$) or bovine tissue ($p = 0.07$). The viscoelastic moduli E' and E'' found in dynamic tests, however, were significantly higher than the relaxation E' and E'' for porcine tissue at 1 Hz

Table 3.3: Relative dissipation $W_{\mathrm{dis}}/W_{\mathrm{st}}$, loss tangent $\tan\delta$, storage modulus E', and loss modulus E'' for the tested frequencies of bovine and porcine tissue.

		$f = 0.5$ Hz	$f = 1.0$ Hz	$f = 1.5$ Hz	$f = 2.0$ Hz
Bovine	$W_{\mathrm{dis}}/W_{\mathrm{st}}$ [-]	0.603 ± 0.183	0.683 ± 0.335	n.a.	n.a.
	$\tan\delta$ [-]	0.096 ± 0.029	0.121 ± 0.067	n.a.	n.a.
	E' [kPa]	172.9 ± 88.74	158.4 ± 83.34	n.a.	n.a.
	E'' [kPa]	17.08 ± 9.975	17.55 ± 9.565	n.a.	n.a.
Porcine	$W_{\mathrm{dis}}/W_{\mathrm{st}}$ [-]	0.611 ± 0.086	0.662 ± 0.283	0.696 ± 0.241	0.675 ± 0.254
	$\tan\delta$ [-]	0.097 ± 0.012	0.114 ± 0.061	0.117 ± 0.017	0.102 ± 0.046
	E' [kPa]	527.2 ± 172.2	488.3 ± 163.9	556.3 ± 205.6	509.8 ± 163.5
	E'' [kPa]	50.76 ± 16.75	52.23 ± 28.91	64.59 ± 25.49	48.00 ± 20.31

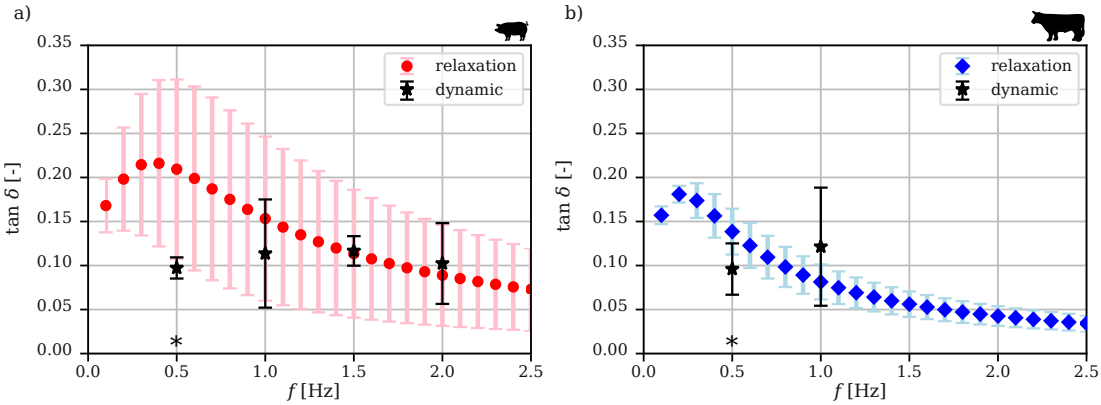

Figure 3.8: Loss tangent $\tan\delta$ and standard deviation measured in dynamic cyclic tests for different frequencies plotted alongside $\tan\delta$, based on relaxation data, calculated for different frequencies with the generalised Maxwell model for a) porcine hepatic tissue ($n = 12$ for relaxation and $n = 12$ for dynamic) and b) bovine tissue ($n = 12$ for relaxation and $n = 12$ for dynamic), asterisks marking frequencies at which the properties found in the two testing methods were significantly different ($\alpha = 0.05$).

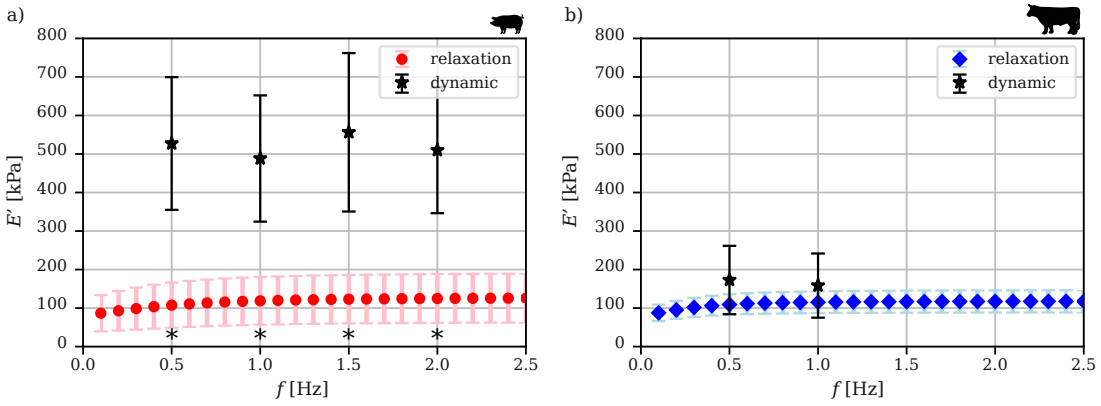

Figure 3.9: Storage modulus E' and standard deviation measured in dynamic cyclic tests for different frequencies plotted alongside E', based on relaxation data, calculated for different frequencies with the generalised Maxwell model for (a) porcine hepatic tissue ($n = 12$ for relaxation and $n = 12$ for dynamic) and (b) bovine tissue ($n = 12$ for relaxation and $n = 12$ for dynamic), asterisks marking frequencies at which the properties found in the two testing methods were significantly different ($\alpha = 0.05$).

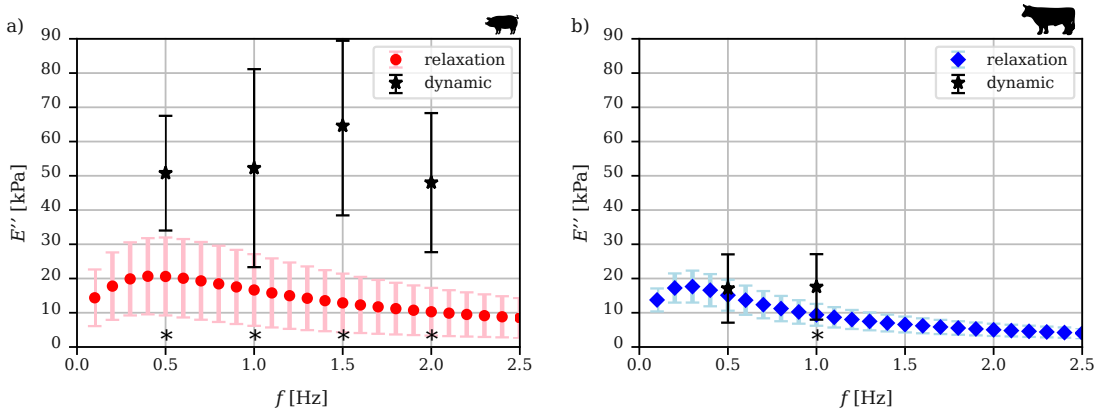

Figure 3.10: Loss modulus E'' and standard deviation measured in dynamic cyclic tests for different frequencies plotted alongside E'', based on relaxation data, calculated for different frequencies with the generalised Maxwell model for (a) porcine hepatic tissue ($n = 12$ for relaxation and $n = 12$ for dynamic) and (b) bovine tissue ($n = 12$ for relaxation and $n = 12$ for dynamic), with asterisks marking frequencies at which the properties found in the two testing methods were significantly different ($\alpha = 0.05$).

($p = 0.000006$ and $p = 0.002$). For bovine tissue at 1 Hz, only E'' was significantly different depending the testing method ($p = 0.01$), while E' was statistically the same for relaxation and cyclic testing ($p = 0.1$).

3.4 Discussion

For evaluating liver mechanical properties, different tests were performed in tension on bovine and porcine hepatic parenchyma samples. In order to describe non-linear as well as viscoelastic behaviour, mechanical testing consisted of ramp loading and unloading, stress relaxation, and DMA. In the following section, the resulting properties from the different tests are discussed and finally the two viscoelastic testing methods (stress relaxation and DMA) are compared with each other.

Ramp test The ramp stress-stretch curves were interpreted based on a hyperelastic modelling approach, utilizing a Veronda-Westmann strain energy function.

Chui et al. [2004] examined different strain energy functions for hyperelastic modelling of combined compression and elongation of porcine liver parenchyma at a much faster strain rate of approximately $0.03\,\mathrm{s}^{-1}$ than the current study ($0.001\,\mathrm{s}^{-1}$), however without modeling unloading. The Veronda-Westmann model thereby yielded average parameters of $c = 0.07$ kPa and $\beta = 4.5$, which are lower than the current results ($c_{\mathrm{load}} = 0.35$ kPa and $\beta_{\mathrm{load}} = 35.1$ for porcine tissue). The differing model parameters could be attributed to the higher strain rate, used by Chui et al. [2004]. Interestingly, it is counterintuitive that the stiffness would be lower for higher strain rates. The results furthermore differ when comparing the magnitude of stress found for similar strains, with Chui et al. [2004] obtaining much smaller stresses than stresses measured in in the current study. Other publications [Lu et al., 2014, Dunford et al., 2018] reported similar stress magnitudes as found in the current study, even though strain rates were also higher with $0.01\,\mathrm{s}^{-1}$. This discrepancy between stress response found in Chui et al. [2004] and other publications could be explained by differences in sample

fixation strategies during testing: For example, Chui et al. [2004] glued the samples to movable plates while Lu et al. [2014], Dunford et al. [2018], and the here-presented study utilized tissue clamps. Another difference is that Chui et al. [2004] reported stretch based on the machine displacement, while the other mentioned studies utilized optical measurement.

The current loading curves of the ramp tests were nearly linear for small strains up to 3% (see Figure3.7a), which is similar to behaviour reported by Hollenstein et al. [2006] and Snedeker et al. [2005], who calculated initial stiffness up to 2% and 5% for hepatic and renal capsule tissue, which means that a single modulus E_{I} can describe tensile behaviour of liver up to a strain of 3% with sufficient accuracy. Furthermore, it can be observed that the parenchyma is much softer than the capsule when comparing average $E_{\mathrm{I}} = 30$ kPa for bovine and porcine tissue, found in the current study, with the values reported for capsule of around 1100 kPa [Hollenstein et al., 2006]. This huge difference shows that for complete liver characterisation, capsule as well as parenchyma need be examined.

While E_{I} was the same for porcine and bovine tissue, stiffness differences between the two tissues only became apparent for higher strains in E_{II} and E_{III}. This could be due to histological differences of the tissues: Porcine hepatic tissue exhibits a higher content of collagen than bovine tissue [Neuman and Logan, 1950], which is the main structural protein in healthy liver due to elastin content being very low [Kanta, 2016]. While elastin mainly contributes to the the initial stiffness in the initial linear region of the stress-stretch curve, collagen characterises the tissue stiffness for higher strains [Duong et al., 2015]. Thus, the higher stiffness in E_{II} and E_{III} of porcine liver could be explained by its higher collagen content compared to bovine liver.

Regarding the comparison of animal and human hepatic tissue, Kemper et al. [2010] tested human liver parenchyma in uniaxial tension at different strain rates, showing that failure stress and stretch were very similar to bovine but significantly different to porcine hepatic tissue by comparing their results with Santago et al. [2009] for bovine and with Uehara [1995] for porcine tissue. Thus, it would be interesting to further investigate the similarity between the tissue types, not only for failure properties but also for stiffness in sub-failure strain ranges. Concerning its collagen distribution, human liver corresponds better to bovine than porcine liver [Zhang, 1999, Eurell and Frappier, 2006, Lowe and Anderson, 2015], which might lead to similar stiffness of human and bovine tissue, especially in terms of E_{II} and E_{III}. This, however, still remains to be shown in future research.

The resulting relative dissipation of around 1 for porcine and bovine tissue indicated that liver tissue is highly viscoelastic, which motivated the detailed analysis via relaxation and dynamic cyclic testing.

Stress relaxation In order to quantify the viscous properties of liver tissue that already became visible as hysteresis and, with that, energy dissipation in the ramp tests, stress relaxation experiments were performed.

The stress decline over time was modelled with a 3-element Prony series and viscoelastic properties $\tan\delta$, E', and E'' were calculated in the frequency domain. Resulting mean $\tan\delta = 0.07 - 0.22$ for porcine and mean $\tan\delta = 0.05 - 0.17$ for bovine tissue corresponded very well to previously published values. For instance, the loss tangent has previously been reported to be in a range of $0.20 - 0.25$ for dynamic compression of canine liver [Kiss et al., 2004], dynamic shear of porcine and murine liver

[Wex et al., 2014, Zhang et al., 2017], and indentation relaxation of porcine and bovine liver [Estermann et al., 2020a].

Average storage and loss moduli for porcine as well as bovine hepatic tissue of around $E' = 100$ kPa and $E'' = 5-20$ kPa found in the current study match the values reported by Ocal et al. [2010] for bovine liver in compression (average $E' = 75$ kPa and $E'' = 10$ kPa after 48 h preservation for comparable frequencies) well.

Furthermore, the absolute value of the complex modulus $|E^*| = \sqrt{E'^2 + E''^2} = 10 - 40$ kPa was reported by Zhang et al. [2007] for compression tests on bovine liver, which is lower than the $|E^*| = 100$ kPa of the current study. However, Zhang et al. [2007] refrigerated the cut samples over night in saline solution before testing, which could have lead to a decrease in stiffness [Dunford et al., 2018].

Kiss et al. [2004] reported $E' = 50$ kPa and $E'' = 10$ kPa for $f = 1.0$ Hz in dynamic compression of canine liver, with E' being lower than the current values and E'' matching very well. The lower stiffness concerning the storage modulus could be associated with differences between canine and bovine/porcine liver or differences between compression and tension.

For all conducted experiments, the relative dissipation was calculated, yielding the highest values of $W_{\mathrm{dis}}/W_{\mathrm{st}}$ for relaxation, compared to ramp testing and DMA. $W_{\mathrm{dis}}/W_{\mathrm{st}}$ describes tissue behaviour in a specific experimental framework and is not understood as material property. Differences in relative dissipation are caused by inherent differences in the loading methods and cannot be compared directly between the methods. For instance, relative dissipation of stress relaxation is not frequency-dependant and describes viscoelasticity in a temporal sense. Relative dissipation of DMA, on the other hand, was calculated depending on the frequency. However, $W_{\mathrm{dis}}/W_{\mathrm{st}}$ can be used as a straight-forward parameter for comparing materials that were tested with the same method.

Dynamic cyclic testing Additionally to stress relaxation, DMA was conducted as the gold standard in terms of measuring viscoelastic properties. The large strain ramp tests yielded notable hyperelastic behaviour in their stress-stretch plots. However, due to the fact that the strain amplitudes used for DMA were very small (0.6%), linear elastic behaviour was assumed for the given prestrain level (8%) for the DMA tests in the range of the amplitude.

The sinusoidal stress and strain curves directly yielded the viscoelastic properties $\tan\delta$, E', and E'' for different frequencies ($f = 0.5$, $f = 1.0$, $f = 1.5$, and $f = 2.0$ Hz for porcine tissue and $f = 0.5$ and $f = 1.0$ Hz for bovine tissue). No clear trend, concerning the influence of frequency on the measured properties, could be observed (Figures 3.8 – 3.10). A much larger range of frequencies is necessary to accurately evaluate the frequency-dependant behaviour, for example using a shear rheometer [Zhu et al., 2013, Wex et al., 2014, Zhang et al., 2017]. Nevertheless, the here-presented method proved feasible for probing a few distinct frequencies of interest.

The tensile dynamic loss tangent of the current study matches $\tan\delta$ for compression, shear, and indentation found in literature [Kiss et al., 2004, Wex et al., 2014, Zhang et al., 2017, Estermann et al., 2020a]. However, no other studies conducted in tension were found, for comparing the current results of tensile storage E' and loss moduli E'' directly.

As discussed above, storage and loss moduli from compressive experiments corresponded to the current results for E' and E'' agreeably well for stress relaxation of

bovine tissue. Furthermore, bovine tissue yielded similar results in DMA as in stress relaxation. However, results based on DMA for porcine tissue were higher than previously published results for E' and E'' in compression [Kiss et al., 2004, Zhang et al., 2007, Ocal et al., 2010]. This discrepancy could mean that there is a larger difference between tensile and compressive properties for porcine tissue than for canine [Kiss et al., 2004] and bovine liver [Zhang et al., 2007, Ocal et al., 2010].

Experiments, concerning viscoelasticity of human liver, by Lim et al. [2009] yielded average $\tan\delta = 0.6$ for 1 Hz. However, these results were obtained via dynamic indentation on the whole intact organ, including contributions from the capsule and under different boundary conditions. Thus, to compare $\tan\delta$, E', and E'' of human hepatic tissue to the current results, human liver needs to be tested with the same or similar method.

Concerning relative dissipation, $W_{\text{dis}}/W_{\text{st}}$ was calculated for each tested frequency. When comparing $W_{\text{dis}}/W_{\text{st}}$ between porcine and bovine tissue, no significant difference can be observed between the tissue types. Thus, based on the here-presented dynamic results alone, it can not be concluded which tissue type is more viscous.

Comparison of the viscoelastic parameters Hysteresis found in the ramp stress-stretch curves, motivated further examination of liver viscoelastic behaviour. Thus, stress relaxation and DMA were conducted for extracting storage and loss moduli, as well as loss tangent. While DMA is the gold standard, concerning the evaluation of these viscoelastic properties, it is connected to experimental difficulties. The following section should answer the question whether relaxation experiments can yield comparable results to DMA.

Stress relaxation experiments, consisting of a single holding phase, were easier to conduct compared to the dynamic tests: For example, in DMA the temporal stress and strain resolution was of essence as phase shifts of approximately 15 ms had to be measured, thus demanding an additional LVDT position sensor. The DIC system which yields the accurate magnitude of strains does not necessarily coincide perfectly in a temporal sense with the displacement of the machine.

Usually, DMA is conducted on rheometers designed specifically for this type of experiment. However, the current setup consisted of a universal testing machine. Even though only limited testing frequencies and no temperature variations were possible, we were able to conduct the experiments without using a rheometer.

Ocal et al. [2010] also calculated storage and loss moduli based on relaxation data as well as on dynamic cyclic testing for bovine hepatic tissue, finding a good agreement between the two testing methods. However their experiments were conducted in compression.

Concerning both porcine and bovine tissue, $\tan\delta$ was statistically indiscernible depending on the testing method in the current study (Figure 3.8). Big differences in testing method, however, became visible for porcine liver when regarding E' and E'' (Figures 3.9a and 3.10a), while agreement for E' and E'' of bovine tissue was good (Figures 3.9b and 3.10b). Stress relaxation was conducted at 6% tissue strain while dynamic cyclic testing was done at a strain level of 8%. This difference in strain seems to be irrelevant for bovine tissue, which can be explained by the fairly linear behaviour in terms of elasticity in Figure 3.7a; not however for porcine tissue which exhibits a more pronounced non-linear stress relation for $6 - 8\%$ strain. This means that the difference between testing methods in porcine storage and loss moduli could

be explained by the non-linear elastic behaviour found in the tested strain range, while loss tangent $\tan\delta$ was unaffected by the difference in strain level.

In conclusion, the comparison of stress relaxation and DMA results is feasible as long as elasticity non-linearities are kept in mind. The results showed that $\tan\delta$ is quite robust in terms of slight variations of strain level between relaxation and DMA, while E' and E'' are more severely affected. The here presented viscoelastic investigation is novel in its application to hepatic parenchyma and provides a guideline for evaluation of soft tissues mechanical properties in tension.

3.5 Limitations

Following limitations of this study should be pointed out:

- Concerning the force relaxation experiments, a perfect step displacement was assumed where the tissue is stretched instantaneously. A more sophisticated modelling approach, as suggested for example by Oyen [2005], would include the influence of the finite ramp time.

- The methods for evaluating $\tan\delta$, E', and E'' are valid for linear viscoelastic materials, meaning that the viscoelastic properties are independent of strain up to the limit of linear viscoelasticity. The limit of linear viscoelasticity reported for liver in literature is based on oscillatory shear experiments at different compressive preloads [Liu and Bilston, 2000, Tan et al., 2013, Wex et al., 2013, Ayyildiz et al., 2014]. For example, Ayyildiz et al. [2014] found a linear shear strain limit of 1% at a prestrain of 5% for bovine liver. In the current study, DMA was performed at 8% prestrain, which was as low as possibly achievable with the given setup, while still avoiding compression of the sample throughout the whole test. Even though, the prestrain was higher than the limit for linear elasticity of 3% found in the ramp tests, the amplitude of oscillation (0.6%) was small enough to assume linear behaviour at the given prestrain level. However, we did not perform amplitude sweep experiments in tension to verify the linear viscoelastic limit.

- Given the long duration of the experiments (4 minutes for ramp tests, 5 minutes for relaxation, and 23 minutes for DMA), tissue dehydration can not be ruled out completely. Wetting the samples during testing was not possible, as water drops on the point markers would have impeded the DIC measurement. Nicolle and Palierne [2010] found an increase in stiffness and damping behaviour due to dehydration in kidney tissue after a few minutes of dynamic shear testing.

- Furthermore, it should be noted that the tissue was not perfused, thus poroelastic behaviour was not modelled in the current study. According to [Kerdok et al., 2006] excised unperfused samples are stiffer and more viscous, compared to *in vivo* conditions.

3.6 Conclusion

Hepatic parenchyma tissue is non-linear and viscoelastic. Thus, for comprehensively describing liver mechanical properties, both aspects must be considered. First, the

non-linear behaviour of porcine and bovine hepatic tissue was analysed via ramp tests and interpreted in the framework of a pseudoelastic Veronda-Westmann model for extracting strain-specific elastic moduli. Next, a method was presented to measure viscoelastic properties ($\tan\delta$, E'', and E'') in tension utilizing stress relaxation, as well as DMA. For each testing method, considerations of dissipated and stored energy were presented.

DMA is the gold standard for examining linear viscoelastic properties, but is associated with many experimental difficulties (e.g. the necessity of an extremely high temporal resolution of stress and strain measurement). We were able to answer the question whether loss tangent, storage modulus, and loss modulus, based on the relaxation experiments, could approximate the dynamic viscoelastic properties, affirmatively. However, special attention must be paid to the strain level at which the experiments are conducted when comparing the two methods, in order to avoid differing properties due to non-linearities.

The interesting discrepancies that were found regarding mechanical properties of bovine and porcine tissue call for further investigation on human hepatic tissue.

3.7 Acknowledgements

The research was funded by the NFB Science Call Dissertations 2017 (SC17-016), and the Austrian Center for Medical Innovation and Technology (funded in the framework of COMET by BMVIT, BMDW, the Federal State of Lower Austria and Standortagentur Tyrol). The authors acknowledge TU Wien University Library for financial support through its Open Access Funding Programme.

3.8 Appendix

3.8.1 Ramp test: Hyperelastic models

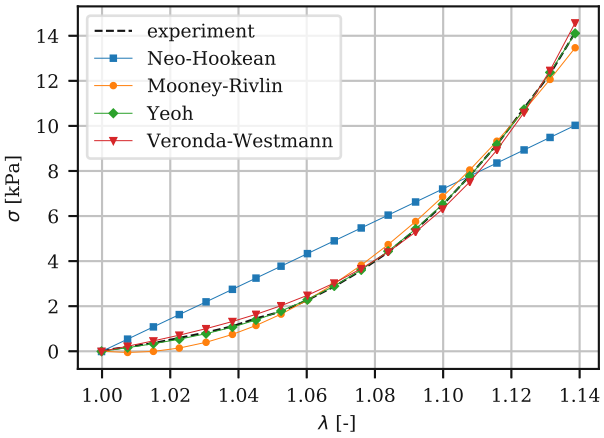

Figure 3.11: True stress-stretch curve of one bovine loading sequence fitted with different hyperelastic models

For selecting an appropriate hyperelastic model to represent the experimental ramp stress-stretch data, four different models varying in complexity were tested (Neo-

Table 3.4: Overview of material models with corresponding true stress expressions and model parameters, and the corresponding coefficient of determination r^2 for a typical bovine hepatic sample

Material model	**Stress expression**	**Model parameters**	r^2
Neo-Hookean	$\sigma_{\mathrm{NH}} = 2\left(\lambda^2 - \frac{1}{\lambda}\right)c_1$	c_1	0.9054
Mooney-Rivlin	$\sigma_{\mathrm{MR}} = 2\left(\lambda^2 - \frac{1}{\lambda}\right)\left(c_1 + c_2\frac{1}{\lambda}\right)$	c_1, c_2	0.9954
Veronda-Westmann	$\sigma_{\mathrm{VW}} = 2\left(\lambda^2 - \frac{1}{\lambda}\right)c\beta\left(\mathrm{e}^{\beta(I_1-3)} - \frac{1}{2\lambda}\right)$	c, β	0.9980
Yeoh	$\sigma_{\mathrm{Y}} = 2\left(\lambda^2 - \frac{1}{\lambda}\right)(c_1 + 2c_2(I_1-3) + 3c_3(I_1-3)^2)$	c_1, c_2, c_3	0.9998

Hookean, Mooney-Rivlin, Veronda-Westmann, and Yeoh). All four models have previously been used to describe hepatic tissue [Chui et al., 2004, Hollenstein et al., 2006, Umale et al., 2013]. Table 3.4 summarises the models, applied in a hyperelastic framework for an isotropic, incompressible material under uniaxial tension with I_1 being the first strain invariant. The resulting stress-stretch curves for the different models and the experimental data are plotted in Figure 3.11 for a bovine hepatic sample during extension. The coefficients of determination ranged from $r^2 = 0.9054$ for the Neo-Hookean model to $r^2 = 0.9998$ for the Yeoh model (see Table 3.4). The standard deviation of r^2 of each model was about 0.0005, when calculated for all samples in loading and unloading. Thus the curves depicted in Figure 3.11 are considered representative of the other samples.

The Yeoh model exhibited the highest coefficient of determination, however also has the largest number of fitting parameters. The Veronda-Westmann model also provided excellent correlation with the experimental data ($r^2 = 0.9980$) and has only two fitting parameters. Furthermore, the Veronda-Westmann model was originally developed specifically for soft tissues [Veronda and Westmann, 1970]. Thus, the Veronda-Westmann model was chosen for further calculations.

Detailed description of the different models and derivations of the equations can be found elsewhere; for example in Holzapfel [2000] or Martins et al. [2006].

3.8.2 Stress relaxation: Influence of Prony series elements and holding time

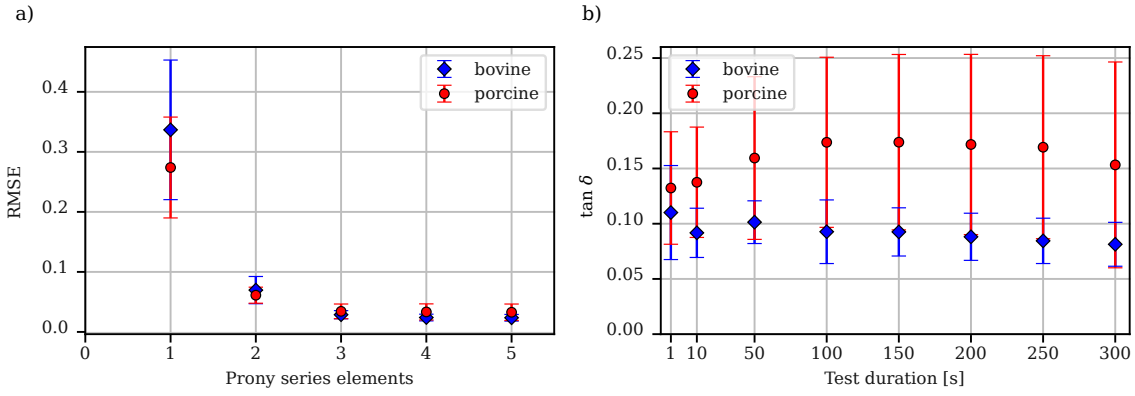

Figure 3.12: (a) Root-mean-square (RSME) and standard deviation of curve fitting Prony series with different numbers of elements to the 300 s of stress relaxation of bovine and porcine tissue ($f = 1$ Hz); (b) Loss tangent $\tan\delta$ plotted for varying relaxation durations ($N = 3$, $f = 1$ Hz).

Concerning the choice of how many terms are necessary in Eq. 3.11 to accurately

represent the experimental stress relaxation, the root-mean-square error (RMSE) – which describes the goodness of fit – was plotted for $N = \{1, 2, 3, 4, 5\}$ in Figure 3.12a. After reaching an average level of 0.03 kPa for $N = 3$, the RMSE did not decrease significantly when the number of terms was increased to $N = \{4, 5\}$. Compared to $N = 3$, the RSME was about ten times higher for $N = 1$ and two times higher for $N = 2$. Thus, the three element Prony series approach was selected.

When fitting the Prony series to the experimental data, the duration of the holding time could influences the resulting viscoelastic properties. Thus, the loss tangent was examined by calculating $\tan\delta$ for cut-off times ranging from $10 - 300$ s. The behaviour of $\tan\delta$ depending on changes in test duration, can be seen in Figure 3.12b. Even though the loss factors, calculated for different holding times, were statistically not distinguishable from each other, the influence of the finite ramp time may not be negligible for very short holding times [Liu and Bilston, 2002]. For further investigation, $\tan\delta$ is reported for 300 s.

Chapter 4

Human, animal, and Thiel preserved liver

From the manuscript:

Comparison of Thiel preserved, fresh human, and animal liver tissue in terms of mechanical properties

S.-J. Estermann, S. Förster-Streffleur, L. Hirtler, J. Streicher, D. H. Pahr, A. Reisinger

Published in: *Ann. Anat. 236, 151717, July 2021*

Abstract

In medical training and research fresh human tissue is often replaced by preserved human or fresh animal tissue, due to availability and ethical reasons. Newer preservation approaches, such as the Thiel method, promise more realistic mechanical properties than conventional formaldehyde fixation. Concerning animal substitute material, porcine and bovine tissue is often chosen, as it is easily obtainable and certain similarity to human tissue is assumed. However, it has not been thoroughly investigated how Thiel preservation changes non-linear and viscoelastic behaviour of soft organ tissues. Furthermore, differences in these properties between animal tissue and human tissue have not been previously corroborated. We conducted ramp and relaxation tensile tests on fresh human and Thiel preserved liver tissue, extracting strain-specific elastic moduli, and viscoelastic properties. The results for fresh human liver were then compared to corresponding results for Thiel preserved liver, as well as previously published results for porcine and bovine liver. Our results showed that Thiel preservation seems to be associated with increased stiffness as well as decreased viscoelastic damping behaviour. Porcine liver tissue was stiffer than human liver with similar viscoelastic properties. Bovine liver exhibited similar stiffness as human liver, however lower viscoelastic damping. The differences between human and animal liver tissue, concerning their mechanical properties, can be explained by their characteristic histology.

Changes in mechanical properties due to Thiel preservation might stem from altered protein cross-linking and dehydration. The results illustrate that appropriate materials for medical training systems must be selected based on which mechanical properties are relevant for the respective application.

Keywords: human liver tissue; mechanical properties; Thiel preservation; porcine and bovine liver; viscoelasticity

4.1 Introduction

In the course of a physician's education, anatomical study on human cadavers is very common. Practicing on fresh human tissue is connected with ethical concerns, risk of infection, and availability issues. To circumvent some of these problems, alternatives to fresh human tissue include embalmed or fresh-frozen human tissue, animal derived tissue, or artificial substitute materials.

Throughout history, various embalming techniques have been developed to prevent the decomposition of fresh tissues. Amongst the more recent strategies, the so-called Thiel method — described by its creator as "the preservation of the whole corpse with natural color" — aims at more realistic material properties, compared to previously utilized embalming techniques [Thiel, 1992]. In brief, Thiel's method involves first injecting the body with two infusion solutions and then storing it in an immersion solution for approximately $6 - 8$ months. The fluids contain chlorocresol solution, various salts for fixation, boric acid for disinfection, and ethylene glycol for preservation of elasticity, alongside very low levels of formaldehyde and other components [Thiel, 1992, 2002, Ottone et al., 2016]. Thiel preserved cadavers are becoming increasingly popular in medical training and research due to their low toxicity and pliant nature [Giger et al., 2008, Hölzle et al., 2012, Eisma et al., 2013, Usami et al., 2018].

Studies on how well Thiel preserved tissue really represents the mechanical properties of fresh tissue have been conducted on tendons [Fessel et al., 2011, Hohmann et al., 2019] and a variety of other animal tissues [Ling et al., 2016]. For instance, Fessel et al. [2011] found significantly altered mechanical properties of human and rat tendons in tensile tests due to Thiel preservation. Ling et al. [2016] concluded, based on optical coherence elastography, that stiffness increased during Thiel preservation for chicken breast, chicken tendon, porcine liver, and porcine fat.

Besides preserved human cadavers, animals have also been used for surgical training [Yokoyama et al., 2003, Tang et al., 2005, Laird et al., 2011]. However, the question whether animal mechanical properties are comparable to those of human tissue remains to be answered. Furthermore, ethical concerns, connected to using animals for medical education, call for appropriate synthetic materials or virtual models to be used instead. Thus, for answering the question of mechanical fidelity and also for developing artificial training systems, accurate knowledge of the actual tissue properties is essential.

Hepatic tissue, in particular, is interesting to study because the liver is an integral part of many surgical training models. For instance, common procedures such as cholecystectomy and hepatectomy are nowadays widely done laparoscopically [Alli et al., 2017, Yoshida et al., 2019] and require appropriate training systems due to the unique challenges connected to laparoscopic approaches in comparison to open surgery [Liu et al., 2018].

When comparing mechanical properties of animal liver with fresh human liver,

Kemper et al. [2010] found that bovine liver was more similar to human than porcine tissue in terms of failure stress. Failure strain was the same for human, porcine, and bovine hepatic tissue. This difference may be attributed to the distinct structural composition of the various parenchyma tissues; bovine liver thereby being more similar to human liver than porcine liver [Zhang, 1999, Eurell and Frappier, 2006, Lowe and Anderson, 2015].

The above mentioned studies compared mechanical properties of animal, human fresh, and Thiel preserved tissue, concentrating on tissue elasticity and failure properties. However, viscoelasticity also plays an important role in soft tissue tactile properties [Klatzky et al., 2013]. Viscoelastic properties are usually assessed in dynamic mechanical analysis, relaxation, and creep tests. Recently, a method was published by Estermann et al. [2020b] for measuring tensile liver properties, concerning hyperelasticity and viscoelasticity, demonstrating that stress relaxation is an appropriate method for quantifying storage modulus, loss modulus, and loss tangent for bovine and porcine hepatic tissue. In the current study the reported method was applied to human fresh and human Thiel preserved liver tissue for identifying the effect of Thiel preservation, as well as illuminating the difference between human and animal tissues in terms of hyperelastic and viscoelastic material behaviour. We aimed at answering the question which substitute tissue (Thiel preserved, porcine fresh, or bovine fresh) best represents fresh human liver tissue.

4.2 Materials & methods

4.2.1 Tensile test specimen

Mechanical testing was conducted on fresh unpreserved human liver, as well as Thiel embalmed human liver samples. Results from testing porcine and bovine fresh hepatic tissue with the identical testing method were taken from Estermann et al. [2020b].

One whole human liver (Figure 4.1a), provided by the Medical University Vienna, was obtained from a body donor, deceased 5 days prior to sample preparation (female, 76-years old). The cause of death was myocardial infarction and arteriosclerosis, with the liver exhibiting no visible pathological conditions.

The Thiel embalmed human liver was extracted from a body donor, preserved at the Karl Landsteiner University of Health Sciences. Embalming of the entire body of the donor was performed according to Thiel [1992] 24 h after death, employing the im-

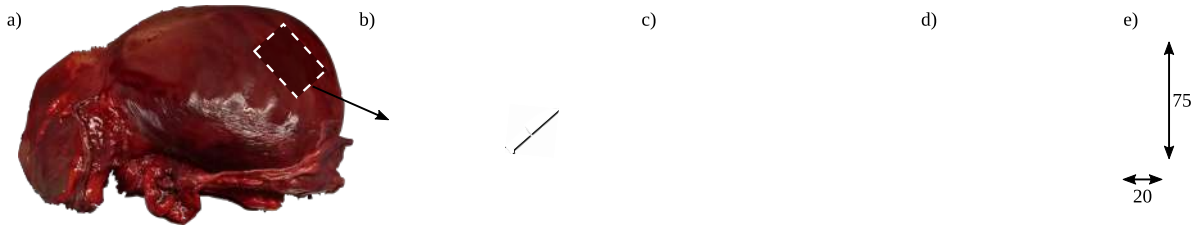

Figure 4.1: Sample preparation: (a) Whole human liver; (b) Block of hepatic tissue was cut out of the whole organ and placed in the 3D printed cutting guide; (c) Thin tissue layer was extracted from the block, following the surface of the cutting guide; (d) Rectangular stencil was placed on the tissue layer; (f) Sample was cut from the tissue layer ($75 \times 20 \times 5$ mm).

proved preservation fluids as published in 2002 by Thiel [2002]. The injections with the central-nervous-system-solution as well as intraluminal infusions of the digestive and respiratory system were dispensable for the present study and thus omitted. During the time between death and initiating preservation, the body was stored at 6°.

Concerning the handling of human tissues, experiments were conducted in accordance with the Committee of Scientific Integrity and Ethics of the Karl Landsteiner University and the Medical University Vienna. All human tissue was obtained from donors who gave informed consent before death for their bodies to be used for scientific purposes.

Samples for tensile testing of human fresh and preserved liver were prepared according to the method published by Estermann et al. [2020b], at the Medical University Vienna and University Hospital St. Pölten, respectively. In brief, rectangular tensile testing specimen (about $75 \times 20 \times 5$ mm) were extracted from the whole organs using surgical blades and 3D printed cutting guides, thereby making sure that the samples were extracted with their long axis oriented parallel to the diaphragmatic and the visceral surface of the organs. The Glisson's capsule was removed before sample preparation, thus yielding samples that consisted predominantly of parenchyma tissue. Large blood vessels and bile ducts were avoided as far as possible to ensure relatively homogenous samples. See Figure 4.1 for an overview of the sample preparation. The test specimen were stored in 0.9% NaCl saline solution after extracting them from the whole organ and transported to the mechanical testing facility within approximately one hour. Mechanical testing took place immediately upon arrival of the samples in the laboratory at room temperature.

The animal tissues (one bovine and six porcine whole livers) were acquired from a local butchery about 24 h after the animals' death and samples were prepared and tested immediately upon arrival in the biomechanics laboratory.

Human liver tissue is not easily obtainable for biomechanical studies, thus the numbers of organs were limited to one fresh human and one Thiel preserved human liver. It was therefore crucial to extract as many samples as possible from each liver. However, the number of samples per liver is limited by the size of the organ, with human and porcine livers being much smaller than bovine livers. As a consequence, the number of samples was $n = 13$ for the fresh and $n = 8$ for the Thiel preserved tissues, while the total number was $n = 24$ for porcine and $n = 24$ for bovine samples (see Figure 4.2a and Table 4.1).

Table 4.1: Number of samples n tested for fresh human and preserved human tissue, as well as porcine and bovine tissue from Estermann et al. [2020b].

	n ramp test	n relaxation	# Organs
Human fresh	8	5	1
Human Thiel	4	4	1
Porcine fresh	12	12	1
Bovine fresh	12	12	6

4.2.2 Mechanical testing

Mechanical testing aims at relating force and displacement, whereas one is prescribed and the other is measured as a response. For this, a mechanical testing machine (ZwickiLine Z2.5 by ZwickRoell GmbH & Co. KG, Ulm, Germany) was utilized for tensile testing (Figure 4.2b). The liver samples were secured in the machine by clamping them with custom-made tissue clamps allowing manual fine-tuning of the clamping force (Figure 4.2c). Due to the fact that in soft tissue testing the resulting forces are only in the range of a few Newtons, an additional load cell, with a measuring range up to 100 N (S2M/100N, Hottinger Baldwin Messtechnik GmbH, Darmstadt, Germany) was mounted below the lower clamp and connected to a universal data acquisition (DAQ) module (QuantumX MX840B by Hottinger Baldwin Messtechnik GmbH, Darmstadt, Germany). To measure the actual displacements within the sample, resulting from the displacement of the testing machine u_{M}, a measuring length l was defined on the gauge length of the samples using black and white sticky markers. Three marker pairs were arranged along the width of the sample to ascertain whether the displacements were uniform along the sample width, with l being the average of these three distances. The change of length was recorded throughout the test with a digital image correlation (DIC) system (Aramis by GOM GmbH Braunschweig, Germany).

The surfaces of the top and bottom tissue clamps were covered with sandpaper (grit P80) to avoid slippage of the samples during testing. Furthermore, due to the oily nature of the Thiel tissue, additional adhesive (Super Glue, UHU GmbH & Co. KG, Bühl, Germany) was used to attach the samples to the clamps. To mount the samples in the testing machine, a procedure similar to the one described by Manoogian et al. [2009] and Kemper et al. [2010], was followed. First the upper clamp was removed from the testing machine and the sample was aligned and clamped therein. Next the top clamp was placed back in the testing machine with the sample allowed to hang freely for approximately three minutes under its own weight (approximately 8 g), enabling a small consistent preloading of each sample. After carefully closing the bottom clamp, the sticky markers for measuring with image correlation were applied and the cross-section was measured with calipers at three locations along the measuring length. The initial cross-section A_0, needed for further data analysis, was calculated as the average of the three measurements, while the initial length l_0 was defined based on a single DIC image taken before starting the test as the average of the distance between the three marker pairs.

To obtain results that are independent of the sample geometry, the change in length l was expressed in terms of the stretch ratio λ with

$$\lambda = \frac{l}{l_0} \tag{4.1}$$

and forces F were converted to true stresses σ_{T} (assuming incompressibility for liver parenchyma [Chui et al., 2004]) with

$$\sigma_{\mathrm{T}} = \frac{F}{A_0}\lambda\,. \tag{4.2}$$

Reported tissue strains were calculated with

$$\varepsilon = \lambda - 1\,. \tag{4.3}$$

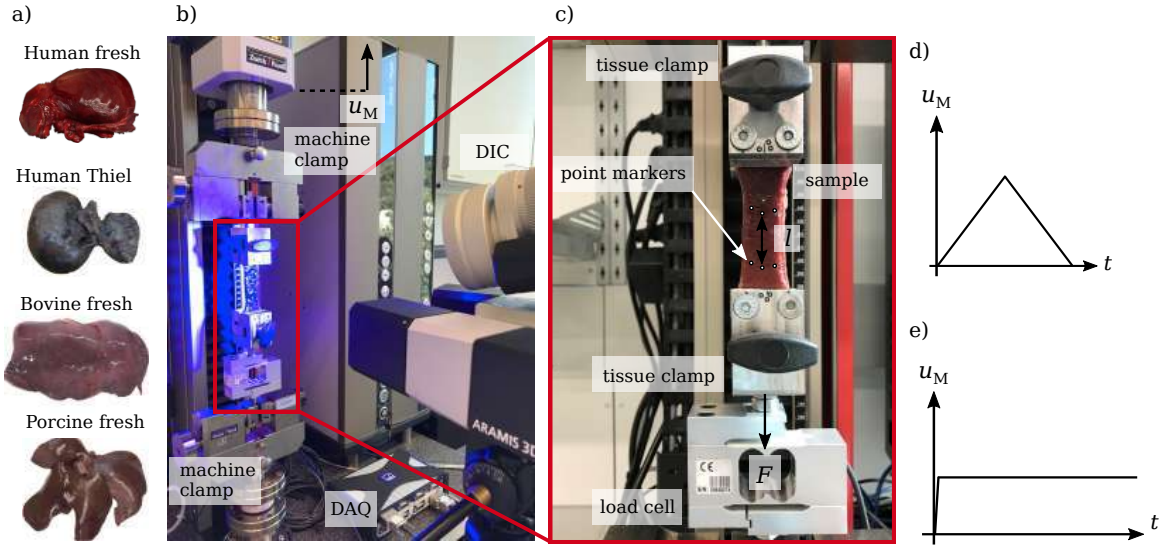

Figure 4.2: (a) The different examined organs (human fresh, human Thiel preserved, bovine fresh and porcine fresh liver); (b) Overview of the complete test setup with the machine displacement u_M, upper and lower machine clamps, digital image correlation system (DIC), and data acquisition module (DAQ) which is connected to the load cell; (c) Liver sample clamped with the tissue clamps, point markers to measure the distance between the markers as length l and the tensile force F; and loading protocol for (d) ramp test and (e) relaxation.

Each sample was exposed to one of the following two mechanical testing methods: ramp test or stress relaxation (Figure 4.2d–e). See Table 4.1 for a summery of examined tissues and testing methods.

Ramp test A trigger signal was sent from the testing machine to the DIC system, initiating the measurement of force and displacement. The cross-head of the testing machine was moved up by a machine displacement of $u_M = 10$ mm (corresponding to tissue strain of $\varepsilon = 0.12$) at a speed of 5 mm/min (corresponding to a strain rate of $\dot{\varepsilon} = 0.06$ min^{-1}) and then moved back to its initial position at the same speed. Force F (from the 100 N load cell) and change in length (from DIC) were both recorded at a rate of 10 Hz.

Stress relaxation Again, a trigger signal, emitted from the testing machine, prompted the image correlation system to start measuring upon initiating the displacement. For this test, a machine displacement of $u_M = 5$ mm ($\varepsilon = 0.06$) was applied rapidly within 0.4 s and then held for 5 min. Force F and change in length were both recorded at a rate of 10 Hz.

4.2.3 Data analysis

Ramp test For an ideally elastic material loading and unloading would not lead to hysteresis in its stress-stretch plot. However, due to the viscoelastic nature of hepatic parenchyma tissue, even extremely slow ramp loading followed directly by unloading results in hysteresis, meaning that energy was dissipated during the cycle. Modeling, based on a purely hyperelastic approach, would neglect this viscoelastic behaviour.

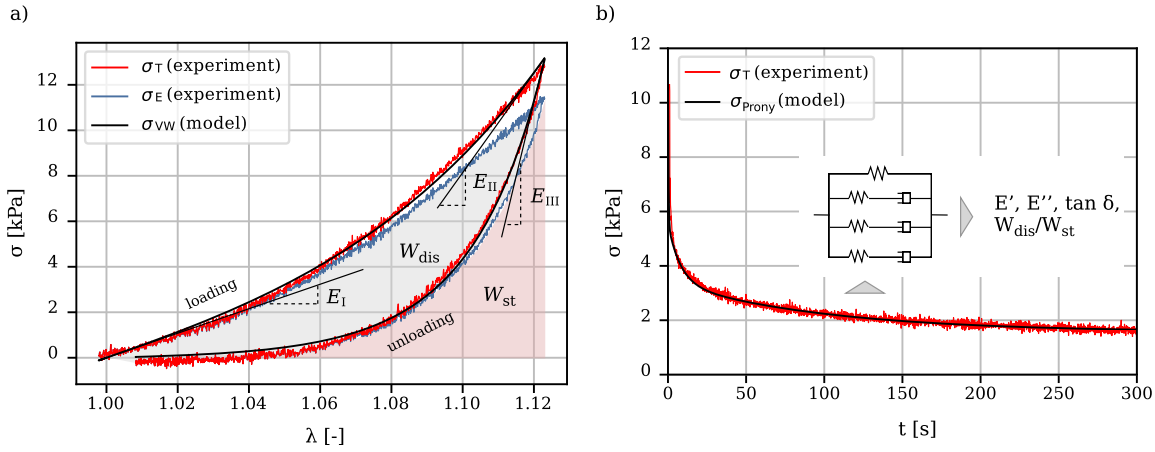

Figure 4.3: (a) Typical stress-stretch curve of fresh human sample in uniaxial tension with the experimental true stress (red line), the experimental engineering stress (blue line), the Veronda-Westmann curve fit (black line), the calculated elastic moduli (E_{I}, E_{II}, and E_{III}), and relative dissipation $W_{\mathrm{dis}}/W_{\mathrm{st}}$; (b) Typical relaxation curve with the Prony series fit, based on a rheological model, which yields E', E'', $\tan\delta$, and $W_{\mathrm{dis}}/W_{\mathrm{st}}$.

Thus, the loading and unloading branches were evaluated separately, as suggested by Fung [1993], yielding two distinct sets of characteristic hyperelastic parameters.

In a hyperelastic model, a strain-energy function is required for establishing a relation between stress and stretch. Based on thermodynamic, symmetry, and energy considerations, an appropriate strain-energy function is chosen. In the current study the strain-energy function for an isotropic material in uniaxial tension, suggested by Veronda and Westmann [1970] for feline skin, was utilized. Following the explanation given e.g. in Martins et al. [2006], the expression of true stress according to the Veronda-Westmann model results in

$$\sigma_{\mathrm{VW}} = 2\left(\lambda^2 - \frac{1}{\lambda}\right) c\beta \left(\mathrm{e}^{\beta(\lambda^2+\frac{2}{\lambda}-3)} - \frac{1}{2\lambda}\right), \tag{4.4}$$

with c and β being the model parameters.

Based on the considerations, described above, Eq. 4.4 was fit to the experimental true stress with a Levenberg-Marquardt algorithm [Marquardt, 1963] for the loading and unloading part of the stress-stretch curves separately (see Figure 4.3a). Thus, the resulting fitting parameters were c_{load} and β_{load} for the loading branch and c_{unload} and β_{unload} for the unloading branch. For evaluating how well the model data corresponded to the experimental data, the coefficient of determination r^2 was calculated.

Next, for identifying characteristic stiffness, elastic moduli E_{I}, E_{II}, and E_{III} were defined as the slope of the stress-stretch curve at specific points: E_{I} for the initial part of the curve, E_{II} for large stretches up to the maximum point of the curve, and E_{III} for initial unloading (see Figure 4.3a).

Furthermore, the ratio of dissipated to stored energy density was calculated based on the stress-stretch curves and referred to as relative dissipation $W_{\mathrm{dis}}/W_{\mathrm{st}}$. In the case of the ramp tests, the dissipated energy density W_{dis} is the area between the loading and unloading curve, while the stored energy density W_{st} is the area under the unloading curve [Estermann et al., 2020b]. Regarding relative dissipation, stress is expressed as engineering stress $\sigma_{\mathrm{E}} = F/A_0$, due to this definition of stress being

the work conjugate of stretch λ. The relative dissipation is understood as a means for comparing different materials that were evaluated with the same mechanical testing method and not as an intrinsic material property.

Stress relaxation For analysing the stress relaxation data, a step displacement was assumed, meaning that the the holding phase was reached instantaneously. In brief, the relaxation function which connects stress σ and strain ε_0 of the holding phase was modeled with a three element Prony series, resulting in

$$\sigma(t)_{\text{Prony}} = \left(E_0 - \sum_{i=1}^{3} E_i(1 - e^{-\frac{t}{\tau_i}})\right)\varepsilon_0\,, \tag{4.5}$$

with the initial elastic modulus E_0 (the ratio between stress and strain at the beginning of the holding phase). Each Prony series term consists of its elastic moduli E_i and characteristic relaxation time τ_i [Findley et al., 1989], which corresponds to the generalised Maxwell rheological model (see Figure 4.3b).

Eq. 4.5 was used to approximate the experimental stress relaxation over the entire holding time of 300 s, using non-linear least squares method with parameters limited to positive values. Goodness of fit was evaluated based on the root-mean-square error (RMSE).

Having obtained model parameters E_i and τ_i, the storage and loss moduli E' and E'' were calculated with

$$E' = E_0 + \sum_{i=1}^{3}\left(\frac{E_i\omega^2\tau_i^2}{1+\omega^2\tau_i^2} - E_i\right) \tag{4.6}$$

and

$$E'' = \sum_{i=1}^{3}\frac{E_i\omega\tau_i}{1+\omega^2\tau_i^2}\,, \tag{4.7}$$

where ω is the angular frequency. The ratio of loss modulus to storage modulus

$$\frac{E''}{E'} = \tan\delta = \sum_{i=1}^{3}\frac{\omega\tau_i E_i}{E_0 - E_i + E_0\omega^2\tau_i^2} \tag{4.8}$$

is called loss tangent $\tan\delta$, which is a characteristic viscoelastic property that describes the frequency-dependent material damping behaviour [Estermann et al., 2020b]. The viscoelastic properties, E', E'' and $\tan\delta$, were calculated for a frequency f of 1 Hz ($\omega = 2\pi$ rad/s), a frequency deemed relevant for assessment of tactile material properties [Caldiran et al., 2018].

As explained above for the ramp tests, relative dissipation $W_{\text{dis}}/W_{\text{st}}$ was also calculated for the relaxation tests according to

$$\frac{W_{\text{dis}}}{W_{\text{st}}} = \frac{E_1 + E_2 + E_3}{E_0 - (E_1 + E_2 + E_3)}\,, \tag{4.9}$$

with E_0, E_1, E_2, and E_3 being the Prony series elastic moduli [Estermann et al., 2020b].

4.2.4 Statistical analysis

First mean values and standard deviations were calculated for all obtained results (c_{load}, β_{load}, c_{unload}, β_{unload}, $W_{\text{dis}}/W_{\text{st}}$, E_{I}, E_{II}, E_{III}, E', E'', and $\tan\delta$). The resulting mechanical properties were then checked for normal distribution using a Shapiro-Wilk test ($\alpha = 0.05$). Next, given normality, Welch's t-tests were performed, without the requirement of homogenous variances, for comparing each property pairwise between tissue origins (fresh human, Thiel preserved human, fresh porcine, and fresh bovine). Furthermore, the Welch's t-test takes the unequal sample sizes of the compared groups into account. Due to the repetition of t-tests, Bonferroni correction is required to adjust the level of significance $\alpha = 0.05$ for multiple tests: For each individual comparison the corrected level of significance $\alpha' = \alpha/4$ is used. A p-value $p < 0.0125$ signifies that two tissues are significantly different regarding a certain property.

4.3 Results

In the following section, results from ramp tests, concerning pseudoelastic behaviour, as well as from stress relaxation, concerning viscoelastic properties, are presented for fresh and preserved hepatic tissue of different species.

Ramp test Figure 4.4a displays the average stress-stretch curves of the tested liver tissues. Characteristic tensile behaviour can be observed for the different tissues with varying maximum stresses and strains. Human Thiel preserved liver exhibited the highest maximum stress and bovine fresh liver the lowest. Concerning maximum stretch, the mean values ranged from 1.113 for bovine tissue to 1.135 for Thiel preserved tissue. All four mean curves showed hysteresis between their loading and unloading part. Thus loading and unloading was modeled separately with a Veronda-Westmann pseudoelastic model, yielding the parameters written in Table 4.2 for human fresh and Thiel preserved liver as well as porcine and bovine fresh liver. The fitted curves matched the experimental data very well, as can be seen in the coefficient of determination $r^2 = 0.998$ for all tissues.

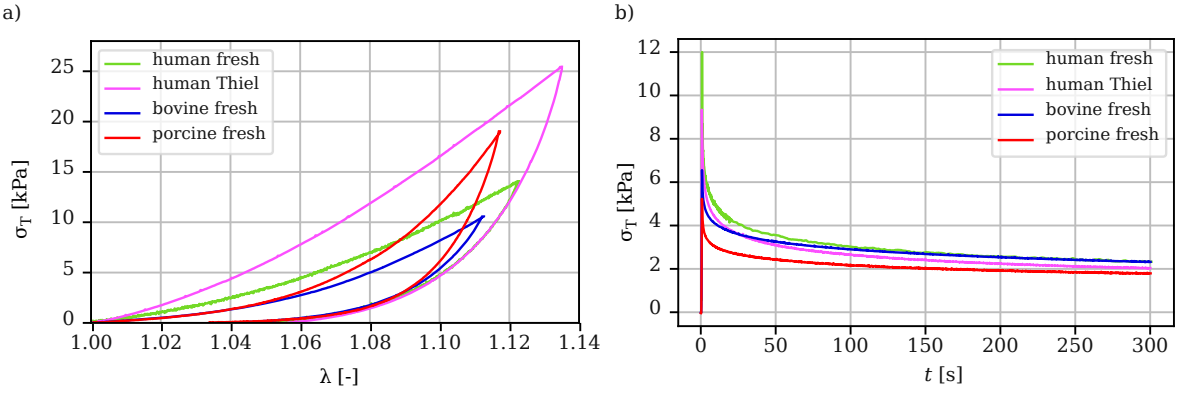

Figure 4.4: Characteristic curves of the different hepatic parenchyma tissues for (a) the ramp tests, based on averaged values of stress and stretch for all tested samples, and (b) for stress relaxation, based on averaged values of stress. Results for bovine and porcine tissue were taken from Estermann et al. [2020b].

Based on the true stress and stretch values resulting from the ramp tests, elastic moduli were defined in specific regions of the curve. Results for low strain stiffness E_{I}, high strain stiffness E_{II}, and unloading stiffness E_{III} are plotted in Figure 4.5a–c for the different liver tissues, expressed as mean values and standard deviations. It can be observed that the initial stiffness E_{I} is around an order of magnitude smaller than E_{II} and E_{III} for the animal tissues (porcine, and bovine). For the human tissues, however, E_{II} is only around $3.5 - 4.5$ times higher than E_{I}, which can also be seen in the more linear curve for human fresh and Thiel in Figure 4.4a, compared to the other tissues.

Energy density considerations yielded the resulting relative dissipation $W_{\mathrm{dis}}/W_{\mathrm{st}}$, plotted in Figure 4.5d for the tissue of preserved and fresh human liver and of fresh porcine and bovine liver. It can be observed that the relative dissipation varies between $1 - 2$, meaning that more more energy was dissipated than stored elastically in the ramp tests. Similar results were thereby obtained for the human tissues — fresh and preserved — while the two animal tissues were also similar to each other, but significantly lower.

Table 4.2: Parameters (given as mean values and standard deviations) of the pseudo-elastic Veronda-Westmann model and the respective coefficient of determination r^2 for the tested fresh and Thiel preserved human tissue with fresh bovine and porcine tissue taken from Estermann et al. [2020b].

Tissue	c_{load}	β_{load}	c_{unload}	β_{unload}	r^2
human fresh	2.389 ± 0.444	8.668 ± 2.668	0.026 ± 0.034	75.45 ± 29.42	0.998
human Thiel	8.281 ± 5.597	6.431 ± 3.065	0.025 ± 0.012	64.95 ± 13.91	0.998
bovine fresh	0.542 ± 0.190	21.76 ± 8.953	0.013 ± 0.007	85.13 ± 23.97	0.998
porcine fresh	0.353 ± 0.237	35.11 ± 15.39	0.009 ± 0.008	101.50 ± 26.54	0.998

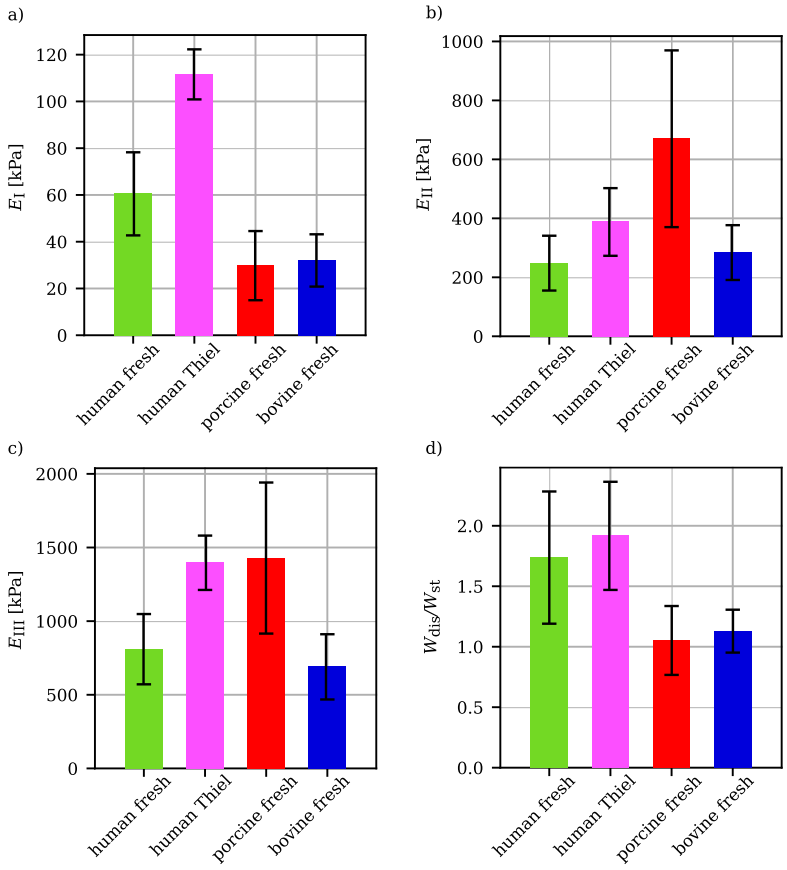

Figure 4.5: Results of the ramp tests for human fresh and Thiel preserved tissue with porcine and bovine fresh tissue from Estermann et al. [2020b] for (a) E_{I}, (b) E_{II}, (c) E_{III}, and (d) $W_{\mathrm{dis}}/W_{\mathrm{st}}$ expressed as mean values and standard deviations.

Stress relaxation Hysteresis, observed in the ramp tests (Figure 4.4a), indicated that further investigation into the viscoelastic tissue behaviour was necessary. Thus, stress relaxation tests were conducted to obtain viscoelastic material properties. Figure 4.4b depicts characteristic average stress relaxation curves of all the tested livers. Modeling these curves with the above described Prony series approach, yielded the parameters listed in Table 4.3.

Mean values and standard deviations of the resulting viscoelastic mechanical properties E', E'', and $\tan\delta$ were plotted in Figure 4.6a–c for the human tissues and animal tissues.

Relative dissipation $W_{\text{dis}}/W_{\text{st}}$ was evaluated for the relaxation tests based on the Prony series parameters and plotted for the different tissues in Figure 4.6d. Concerning the relaxation experiments, $W_{\text{dis}}/W_{\text{st}}$ was also > 1, as was obtained for the ramp tests, meaning that more energy was dissipated than stored elastically after relaxation.

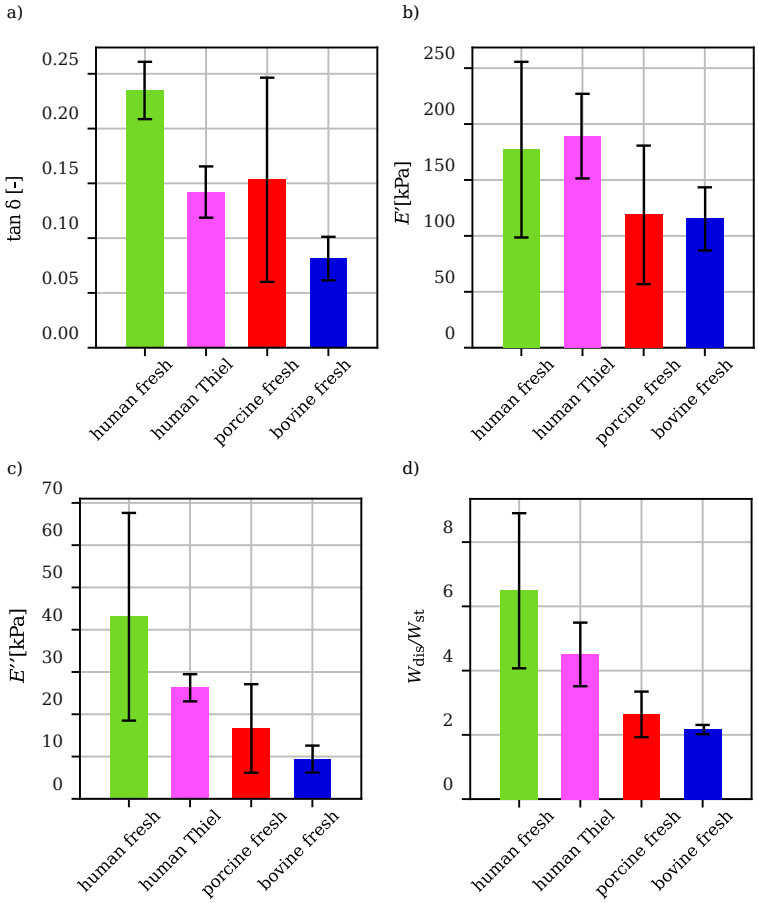

Figure 4.6: Results of the stress relaxation tests for human fresh and Thiel preserved tissue with porcine and bovine fresh tissue from Estermann et al. [2020b] for (a) $\tan\delta$, (b) E', (c) E'' calculated for 1 Hz, and (d) $W_{\text{dis}}/W_{\text{st}}$ expressed as mean values and standard deviations.

Table 4.3: Parameters of the Prony series fit ($N = 3$) of the relaxation tests E_0, E_1, τ_1, E_2, τ_2, E_3 and τ_3, and the resulting root-mean-square error RMSE with values for porcine and bovine fresh tissue from Estermann et al. [2020b].

Tissue	E_0 [kPa]	E_1 [kPa]	τ_1 [s]	E_2 [kPa]	τ_2 [s]	E_3 [kPa]	τ_3 [s]	RMSE [kPa]
human fresh	222.9 ± 85.12	103.7 ± 43.18	0.207 ± 0.09	45.27 ± 14.16	7.042 ± 1.008	35.64 ± 12.17	98.68 ± 5.646	0.16 ± 0.04
human Thiel	197.8 ± 42.89	84.42 ± 14.91	0.461 ± 0.082	41.73 ± 10.07	8.423 ± 2.050	33.82 ± 9.0367	104.0 ± 36.69	0.05 ± 0.01
bovine fresh	117.96 ± 30.24	33.92 ± 8.85	0.58 ± 0.15	20.16 ± 5.67	11.07 ± 0.83	26.61 ± 6.81	140.48 ± 6.84	0.03 ± 0.01
porcine fresh	129.89 ± 64.91	44.19 ± 20.34	0.34 ± 0.19	22.08 ± 12.04	7.33 ± 2.04	24.98 ± 13.83	115.80 ± 22.29	0.04 ± 0.01

Statistical analysis In order to identify significant differences between the tested liver tissues, p-values were calculated in pairwise t-tests. Tables 4.4 and 4.5 reveal which materials were significantly different ($p < 0.0125$) from one another, concerning certain mechanical properties. For example, human fresh hepatic tissue differs significantly from human Thiel preserved tissue in terms of E_{I}, E_{III}, and $\tan\delta$. Tissues that are the most similar, based on the number of different properties, were porcine fresh and Thiel preserved human tissue, as well as porcine and bovine fresh tissue.

Table 4.4: Properties that are significantly different ($p < 0.0125$), depending on the liver tissue origin, listed for the ramp test.

	human fresh	**human Thiel**	**porcine fresh**	**bovine fresh**
human fresh		E_{I}, E_{III}	E_{I}, E_{II}, E_{III}, $\frac{W_{\mathrm{dis}}}{W_{\mathrm{st}}}$	E_{I}, $\frac{W_{\mathrm{dis}}}{W_{\mathrm{st}}}$
human Thiel	E_{I}, E_{III}		E_{I}, $\frac{W_{\mathrm{dis}}}{W_{\mathrm{st}}}$	E_{I}, E_{III}, $\frac{W_{\mathrm{dis}}}{W_{\mathrm{st}}}$
porcine fresh	E_{I}, E_{II}, E_{III}, $\frac{W_{\mathrm{dis}}}{W_{\mathrm{st}}}$	E_{I}, $\frac{W_{\mathrm{dis}}}{W_{\mathrm{st}}}$		E_{II}, E_{III}
bovine fresh	E_{I}, $\frac{W_{\mathrm{dis}}}{W_{\mathrm{st}}}$	E_{I}, E_{III}, $\frac{W_{\mathrm{dis}}}{W_{\mathrm{st}}}$	E_{II}, E_{III}	

Table 4.5: Properties that are significantly different ($p < 0.0125$), depending on the liver tissue origin, listed for stress relaxation.

	human fresh	**human Thiel**	**porcine fresh**	**bovine fresh**
human fresh		$\tan\delta$	$\frac{W_{\mathrm{dis}}}{W_{\mathrm{st}}}$	$\tan\delta$, $\frac{W_{\mathrm{dis}}}{W_{\mathrm{st}}}$
human Thiel	$\tan\delta$			E'', $\tan\delta$
porcine fresh	$\frac{W_{\mathrm{dis}}}{W_{\mathrm{st}}}$			
bovine fresh	$\tan\delta$, $\frac{W_{\mathrm{dis}}}{W_{\mathrm{st}}}$	E'', $\tan\delta$		

4.4 Discussion

The mechanical properties of different liver tissues, commonly used in surgical training, were studied. Tensile ramp and stress relaxation tests were conducted on fresh human, Thiel preserved human, fresh bovine, and fresh porcine hepatic parenchyma, yielding hyperelastic and viscoelastic behaviour. The resulting mechanical properties were used for illuminating the effects of Thiel preservation and investigating the differences between human and animal tissue.

Concerning the loading part of the ramp tests, the stress response to the applied strains was comparable to curves previously published for human liver stretched until failure [Kemper et al., 2010, Untaroiu et al., 2015]. The differences in maximum mean stretch observed for the different tissues (Figure 4.4a) in the current study, could stem from variations in sample clamping and also from inhomogeneities in the measuring length. The ramp tests exhibited hysteresis between loading and unloading and non-linear behaviour for the examined range of stretch for fresh human, bovine, and porcine liver and for preserved human liver (Figure 4.4a). These results called for a more extensive evaluation of viscoelastic behaviour via stress relaxation. All tested tissues exhibited pronounced relaxation throughout the entire holding time of 300 s (Figure 4.4b).

Relative dissipation $W_{\text{dis}}/W_{\text{st}}$ provides indications on the shape of the mean curves, resulting from a specific type of mechanical test. For example, high relative dissipation in the ramp test means that the area between loading and unloading (dissipation) is large, signifying a high extent of hysteresis. Resulting $W_{\text{dis}}/W_{\text{st}}$ of the ramp test was very similar for fresh and preserved human tissue, while porcine and bovine tissue also exhibited similar $W_{\text{dis}}/W_{\text{st}}$, however lower than the two human tissues. Analogously, for the relaxation tests $W_{\text{dis}}/W_{\text{st}}$ characterises the relaxation curve shape via its dependence on the Prony series spring elements. Again, human fresh and human Thiel tissue were similar regarding relative dissipation, while $W_{\text{dis}}/W_{\text{st}}$ of the animal tissues was lower. In summary, the results indicate that Thiel preservation hardly effects relative dissipation, regarding the presented ramp tests and stress relaxation.

Some of the results for human fresh and preserved liver are comparable to values published in literature. For example, from stress-strain curves of tensile tests on fresh human parenchyma, published by Kemper et al. [2010], a stiffness of about 50 kPa for 5% strain was extracted (for a strain rate of 0.01 s^{-1}), matching our results for $E_{\text{I}} = 60$ kPa very well. Furthermore, for higher strains of 15%, a stiffness of about 120 kPa was extracted from the curves reported by Kemper et al. [2010], which is lower than resulting $E_{\text{II}} = 150 - 340$ kPa of the current study. The difference in stiffness might stem from the fact that tissues were tested less than 48 h *post mortem* by Kemper et al. [2010]. According to Dunford et al. [2018], liver stiffness might vary slightly (but not significantly) with storage time. Furthermore, different strain rates were used in Kemper et al. [2010] and the current study. No results that are comparable to E_{III} could be found in literature.

Concerning the obtained loss tangent for human fresh liver, $\tan\delta = 0.21 - 0.26$ matches values measured on canine liver parenchyma by Kiss et al. [2004] very well ($\tan\delta = 0.25$). Results for human liver reported by Lim et al. [2009] were higher (around 0.6). However, the dynamic indentation experiments by Lim et al. [2009] were conducted on the surface of a whole intact organ, which includes contributions from the liver capsule and, possibly, from large blood vessels.

Regarding storage and loss modulus, canine results of Kiss et al. [2004] were nearly 4 times lower than the current results for human tissue. This difference could be due to the fact that moduli of Kiss et al. [2004] were measured in compression.

To our knowledge, tensile tests have not been conducted on Thiel preserved human hepatic tissue previously. Based on optical coherence elastography, Ling et al. [2016] reported the Young's modulus of porcine Thiel embalmed liver to be around 350 kPa which is quite similar to the average stiffness $E_{\text{II}} = 388$ kPa found in the current study for human Thiel embalmed tissue. Ling et al. [2016] found that Thiel preservation increased the stiffness of porcine liver by about 65%, corresponding well to our data, in that E_{II} of preserved human liver was 57% stiffer than unpreserved liver. Concerning viscoelastic properties, no studies reporting E', E'', and $\tan\delta$ of Thiel preserved liver tissue were found in literature.

Comparison of fresh human and Thiel preserved liver When comparing the resulting mechanical properties of fresh and Thiel preserved human hepatic parenchyma, the preserved tissue was significantly stiffer than the fresh tissue, concerning initial loading E_{I} and unloading E_{III}. Formaldehyde, which is contained in the Thiel solution in small concentrations, is known to promote protein cross-linking between, as well as within collagen molecules, thus increasing tissue stiffness [Fishbein et al., 2007]. Con-

ventional preservation methods, using much higher formaldehyde concentrations than Thiel solutions, yield an even higher increase in stiffness [Ling et al., 2016]. Besides formaldehyde, the Thiel fluid also introduces various salts which bind water, previously contained in the tissue. Tissue dehydration during Thiel preservation might lead to an additional stiffening effect, as was reported by Kerdok et al. [2006] and Nicolle and Palierne [2010] who compared fresh and dehydrated unpreserved liver. Regarding high strain stiffness E_{II}, in our study the difference between fresh and preserved tissue was statistically not significant. These findings are consistent with Lee et al. [1989], who investigated the effect of formaldehyde preservation on bovine pericardium in tension, finding no significant difference between high strain moduli of fresh and preserved tissue. Concerning the initial stiffness, results of Lee et al. [1989] for preserved tissue were also significantly higher than for fresh tissue.

Regarding viscoelastic properties, Thiel preservation seemed to decrease damping in terms of $\tan\delta$ by around 40% compared to fresh tissue. A similar observation was made by Lee et al. [1989] for fresh and formaldehyde preserved bovine pericardium, finding that relaxation was less pronounced after fixation. Possibly, the higher degree of cross-linking prohibited extensive relaxation behaviour in the Thiel preserved liver tissue. Furthermore, fixation-related dehydration could have influenced the viscoelastic tissue properties by preventing the movement of water through the tissue.

Despite the above described discrepancies between fresh and Thiel preserved human liver, our results showed that the Thiel method still maintains mechanical properties relatively well. This is an important finding, especially when considering how drastically mechanical properties of formalin preserved cadavers are altered. Conventional formalin embalming results in extreme hardening of soft tissues and is not suitable for surgical training [Hayashi et al., 2016].

Comparison of fresh human and porcine liver When comparing fresh human and fresh porcine hepatic tissue, significant differences ($p < 0.0125$) were found regarding elastic moduli in all three regarded stretch ranges (E_{I}, E_{II}, and E_{III}), with porcine fresh tissue being stiffer than human fresh tissue. The reason for this could be due to histological differences between the tissues: porcine liver parenchyma exhibits higher contents of collagen, especially in connective tissue septa, surrounding the individual lobules. These septa are found in porcine, but not in human hepatic tissue [Kamimura et al., 2009]. Kemper et al. [2010] also found that porcine tissue was stiffer than human tissue in tensile loading, attributing this effect to the correlation between stiffness and collagen content. Experiments have shown that fibrotic liver is stiffer compared to healthy tissue [Yeh et al., 2001]. With increasing severity of liver fibrosis, tissue scarring leads to excessive accumulation of collagen in the tissue, indicating that hepatic tissue stiffness is indeed proportional to collagen content [Mazza et al., 2007].

Concerning the viscoelastic properties E', E'', and $\tan\delta$, no significant differences between fresh human and porcine tissue were found.

Comparison of fresh human and bovine liver While the collagen content differs between human and porcine hepatic tissue, results of histological analysis show that human and bovine hepatic tissue do exhibit similar amounts of collagen [Neuman and Logan, 1950, Aycock and Seyer, 1989]. Therefore, it is not surprising that stiffness concerning high strains (E_{II}) and unloading (E_{III}) was similar for bovine and human fresh liver; collagen being the major structural protein in hepatic tissue and mainly

responsible for resistance to high strains.

Damping behaviour in terms of loss tangent $\tan\delta$ was more than twice as high for human fresh tissue, compared to bovine tissue. The loss tangent of fluid filled porous media is proportional to the fluid volume fraction and the porosity of the solid component [Bear and Corapcioglu, 1984]. Thus, the difference of $\tan\delta$ between human and bovine liver tissue could be explained by variations in the parenchymal fluid network. Liver lobules are the functional units of parenchyma, consisting of the portal triad (hepatic artery branch, portal vein branch, and bile duct), the central vein, and — in the area in-between — hepatocytes and sinusoids. The sinusoids form a network of specialised capillaries, which transport blood from the portal triad to the central vein. Endothelial lining, perforated by pores called fenestrae, is present in the sinusoids [Braet and Wisse, 2002]. The size and density of the sinusoids determines the volume fraction of free fluid in the parenchyma, while the extent of fenestration influences the porosity of the "solid" space surrounding the sinusoids. Differences in sinusoid architecture between species have been observed [Wood, 1962, Higashi et al., 2002]. Human liver parenchyma exhibits larger and more densely arranged fenestrae in the sinusoid endothelial lamina than bovine tissue [Horn et al., 1986, Higashi et al., 2002, Wisse et al., 2008]. Concerning differences in sinusoidal volume fraction, Debbaut et al. [2012] reported $14.3 \pm 2.8\%$ for human liver, while Gröhn and Lindberg [1985] found lower values of $13.2 \pm 0.7\%$ for bovine liver. Furthermore, light microscopy images of stained liver sections by Madhan and Raju [2014] indicate that human liver sinusoids might be larger than those of bovine parenchyma. Human and bovine liver were both treated according to the same experimental protocol by Madhan and Raju [2014], meaning that both specimen were fresh before they were prepared for imaging. However, it should be noted that factors influencing sinusoidal shape and distribution, such as age, lifestyle, and health status [Brunt et al., 2014, Wake and Sato, 2015], were unknown for the donor liver imaged in Madhan and Raju [2014]. For a more detailed interpretation, further research is necessary, regarding the inter-species differences in terms of sinusoidal morphology.

In conclusion, the higher loss tangent of human liver compared to bovine liver, could be explained by larger and more numerous fenestrae and a higher sinusoidal volume fraction in human tissue.

4.5 Limitations

Following limitations of this study should be pointed out:

- The biggest limitation is that only one organ was tested for the preserved and unpreserved human tissues, respectively. Therefore, possible variations between individuals were not accounted for. When Untaroiu et al. [2015] tested two human donor livers in tension, they found no significant difference between donors, regarding failure stress and failure strain. However, these results were based on only two livers. Increasing the number of tested organs would surely be beneficial in future studies, however availability of human livers for biomechanical studies is very limited.

- The unpreserved human liver was harvested from a donor body, stored at 6° C for 5 days after death before testing. Thus, tissue degradation may have already taken place to a certain degree. This could lead to confounding differences

in mechanical properties between the fresh animal tissues and the fresh human tissue, which may actually be attributed to *post mortem* tissue changes. Furthermore, Thiel preservation was also initiated on body donors less than 5 days after death, with bodies also being cold-stored prior to embalming. However, results published by Duong et al. [2015] indicate that refrigerated storage of whole livers for up to one week does not alter the tensile material properties. Liver contains hardly any elastin, as opposed to other internal organs, such as the kidney or spleen [Neuman and Logan, 1950]. Elastin degradation is the main reason for early changes in mechanical properties during storage. Thus, liver mechanical properties seem unaffected by cold storage in the first week, unlike other elastin-rich organs [Tamura et al., 2002, Nguyen et al., 2012, Duong et al., 2015].

- The fresh human liver was examined macroscopically before tesing and there was no known history of liver-related pathologies of the donor. However, additional histological analysis would have been beneficial to exclude possible inflammation or steatosis of the tissue.

4.6 Conclusions

Uniaxial tensile tests were conducted on fresh human, Thiel preserved human, and fresh animal hepatic parenchyma tissue, for comparing mechanical properties in terms elasticity and viscoelasticity. The results confirmed non-linear and viscoelastic behaviour. Thiel preservation seemed to be associated with increased stiffness and a reduction of damping behaviour in terms of loss tangent, due to increased protein cross-linking and dehydration during preservation. Porcine tissue was stiffer, compared to human fresh tissue, possibly due to histological differences in collagen content. Viscoelastic properties, however, were statistically the same for porcine and human fresh tissue. Bovine and human tissue, being alike concerning collagen content, exhibited similar stiffness for high strains and unloading. The loss tangent of human fresh tissue was higher than bovine tissue, which could be explained by histological differences concerning the hepatic sinusoid morphology.

In conclusion, amongst the examined substitutes for fresh human parenchyma, the different mechanical properties were best matched by different tissues. Despite some disparity regarding elasticity, the viscoelasticity of Thiel preserved human liver was comparable to fresh human liver. In light of the current results, Thiel preservation seems recommendable for the study of human anatomy and surgical training. For applications that require accurate elastic properties, possibly in the context of testing new medical devices, bovine liver should be used instead. Keeping this in mind, the appropriate substitute tissue should always be chosen depending on its application.

4.7 Ethical approval

The study was approved by the Committee of Scientific Integrity and Ethics of the Karl Landsteiner University (1058/2019).

4.8 Acknowledgements

The research was funded by the NFB Science Call Dissertations 2017 (SC17-016), and the Austrian Center for Medical Innovation and Technology (funded in the framework of COMET by BMVIT, BMDW, the Federal State of Lower Austria and Standortagentur Tirol). The authors acknowledge TU Wien University Library for financial support through its Open Access Funding Program.

The authors wish to sincerely thank those who donated their bodies to science so that anatomical research could be performed. Results from such research can potentially improve patient care and increase mankind's overall knowledge. Therefore, these donors and their families deserve our highest gratitude.

Chapter 5

Microstructural material design

From the manuscript:

Material design of soft biological tissue replicas using viscoelastic micromechanical modelling

S.-J. Estermann, D. H. Pahr, A. Reisinger

Currently under review: *J. Mech. Behav. Biomed. Mater.*

Abstract

Anatomical models for research and education are often made of artificial materials that attempt to mimic biological tissues in terms of their mechanical properties. Recent developments in additive manufacturing allow tuning mechanical properties with microstructural designs.

We propose a strategy for designing material microstructures to mimic soft tissue viscoelastic behaviour, based on a micromechanical Mori-Tanaka model. The model was applied to predict homogenised viscoelastic properties of materials, exhibiting a matrix-inclusion microstructure with varying inclusion volume fractions. The input properties were thereby obtained from compression relaxation tests on silicone elastomers. Validation of the model was done with experimental results for composite samples. Finally, different combinations of silicones were compared to mechanical properties of soft tissues (hepatic, myocardial, adipose, cervical, and prostate tissue), found in literature, in order to design microstructures for replicating these tissues in terms of viscoelasticity.

The viscoelastic Mori-Tanaka model showed good agreement with the corresponding experimental results for low inclusion volume fractions, while high fractions lead to underestimation of the complex modulus by the model. Predictions for the loss tangent were reasonably accurate, even for higher inclusion volume fractions. Based on the model, designs for 3D printed microstructures can be extracted in order to replicate the viscoelastic properties of soft tissues.

Keywords: soft tissues; micromechanical model; viscoelasticity; Mori-Tanaka model;

homogenisation; silicone elastomer; stress relaxation

5.1 Introduction

Medical education and research require accurate models of human anatomical features in terms of mechanical properties and morphology. Some models consist of biological alternatives to fresh human tissue, such as animal tissue or preserved human cadavers, while other models are made of artificial materials, due to practical reasons and ethical considerations. Most biological tissues exhibit viscoelastic behaviour and complex microstructures, making it challenging to obtain realistic mechanical properties when using artificial materials. According to Caldiran et al. [2019], viscoelastic cues play a significant role in tactile perception. Therefore, it is important to match the viscoelastic properties of the artificial material and tissue if the aim is to produce realistically feeling models.

3D printing, or additive manufacturing, has gained traction in the field of anatomical model production, addressing some issues of conventional models. For instance, additive manufacturing allows the production of highly standardised models, as well as patient-specific models based on medical imaging data. Early 3D printed models were often made of hard, rigid materials with unrealistic mechanical properties [Starosolski et al., 2014, Anderson et al., 2016]. However, new developments, allowing multi-material printing, yield interesting composite materials whose overall mechanical properties can be influenced by adapting their microstructure, e.g. by combining different materials with fibres or spherical inclusions [Wang et al., 2016, Tarantino et al., 2019, Ezzaraa et al., 2020]. Faced with so many possibilities, it has become important to design the microstructure of the printed material according to its mechanical requirements.

Modeling the mechanical behaviour of structures as a whole, including the underlying microstructure, leads to huge computational costs. Thus, numerical and analytical strategies have been developed, in the context of continuum micromechanics, for homogenising mechanical properties by "replacing" the heterogenous composite with an equivalent homogenous material. Most numerical approaches utilise finite element analysis, especially concerning periodic microstructures [Suquet, 1987, Yvonnet, 2019]. Early analytical models include the Voigt [Voigt, 1887] and Reuss [Reuss, 1929] rule of mixtures. Later, based on the Eshelby inclusion problem [Eshelby, 1957], the self-consistent scheme [Hill, 1965a] and Mori-Tanaka approach [Mori and Tanaka, 1973], were introduced. The advantage of these analytical models is that they require very little computational time.

The Mori-Tanaka mean-field method, applied to the Eshelby inclusion problem, is commonly used for homogenising mechanical properties of composite materials, exhibiting matrix-inclusion morphologies [Mori and Tanaka, 1973, Benveniste, 1987]. Information on the individual phases—considering volume fraction, mechanical properties, and morphology—yields effective mechanical properties of the composite. Previously, Mori-Tanaka models have been used in the field of biomechanics for elastic [Hellmich et al., 2004, Fritsch and Hellmich, 2007], poroelastic [Hellmich et al., 2009, Morin and Hellmich, 2014], and viscoelastic [Eberhardsteiner et al., 2012] properties. Viscoelastic homogenisation thereby relies on the Laplace-Carson transform for extending the framework from elastic to viscoelastic properties [Scheiner and Hellmich, 2009, El Kouri et al., 2015, Nguyen et al., 2016]. This is referred to as elastic-

viscoelastic correspondence principle [Brinson and Lin, 1998]. Recently, the Mori-Tanaka model has also been used for estimating the homogenised elastic properties of multi-material 3D printed composites, without incorporating viscoelastic considerations [Sano et al., 2018, Kong et al., 2019, Ezzaraa et al., 2020]. Concerning viscoelastic properties of 3D printed materials, Andreasen et al. [2014] suggested using the correspondence principle, applied to a finite element model, to optimise the structural morphology of a two-phase composite for increased damping. Pathan et al. [2017] proposed a numerical viscoelastic homogenisation approach of fibre reinforced polymers, based on the correspondence principle.

The above mentioned modelling strategies for designing 3D printed microstructures, either neglect viscoelastic properties or involve numerical calculations. Even when the correspondence principle is applied within analytical frameworks, complex numerical calculations are typically required for the inversion of the Laplace-Carson transform [Lévesque et al., 2007, Scheiner and Hellmich, 2009, El Kouri et al., 2015, Nguyen et al., 2016]. Computational speed, however, is important when designing additive manufacturing materials for soft tissue models, especially if different tissues are to be combined in one model. Research by Xu et al. [2020] illustrates how viscoelastic properties of 3D printed materials can be tuned, using microstructural designs based on an analytical experimental model, however in the context of relatively hard materials.

In this study, we propose using the Mori-Tanaka model and the correspondence principle as a tool for designing materials that replicate viscoelastic properties of soft biological tissues. The conceptualised composite materials could be potentially produced by recent methods in additive manufacturing. Viscoelasticity is described by frequency dependant material properties (complex modulus, storage modulus, loss modulus, and loss tangent); thereby avoiding inversion of the Laplace-Carson transform. Specifically, the aim is to qualify a microstructure with matrix-inclusion morphology, made from two silicone elastomers, as surrogate material for selected soft tissues in terms of viscoelastic properties. Due to the analytical nature and simplicity of the viscoelastic Mori-Tanaka model (vMTM), effective properties can be estimated extremely fast without time-consuming numerical computation. The validation of the model is done by compression testing silicone composite samples, produced by casting.

5.2 Materials & methods

A viscoelastic micromechanical model, based on the Mori-Tanaka method, was used for homogenising the viscoelastic properties of soft, tissue mimicking, composite materials. The considered composites consisted of a soft silicone matrix, containing randomly distributed spherical inclusions with varying volume fractions. Different viscoelastic soft silicone elastomers were used as input materials for the matrix and inclusion phases of the vMTM, yielding composite materials with tuneable effective properties. Viscoelastic properties of the individual silicone phases were found by conducting compression relaxation tests on two soft silicones, as well as taken from previous studies for two additional silicones. Furthermore, the model was validated with compression relaxation tests on composite samples. Finally, the resulting effective viscoelastic properties of the vMTM were compared to values reported for soft biological tissues in order to find the ideal microstructure for mimicking these tissues. Figure 5.1 gives an overview of the methods used in this study.

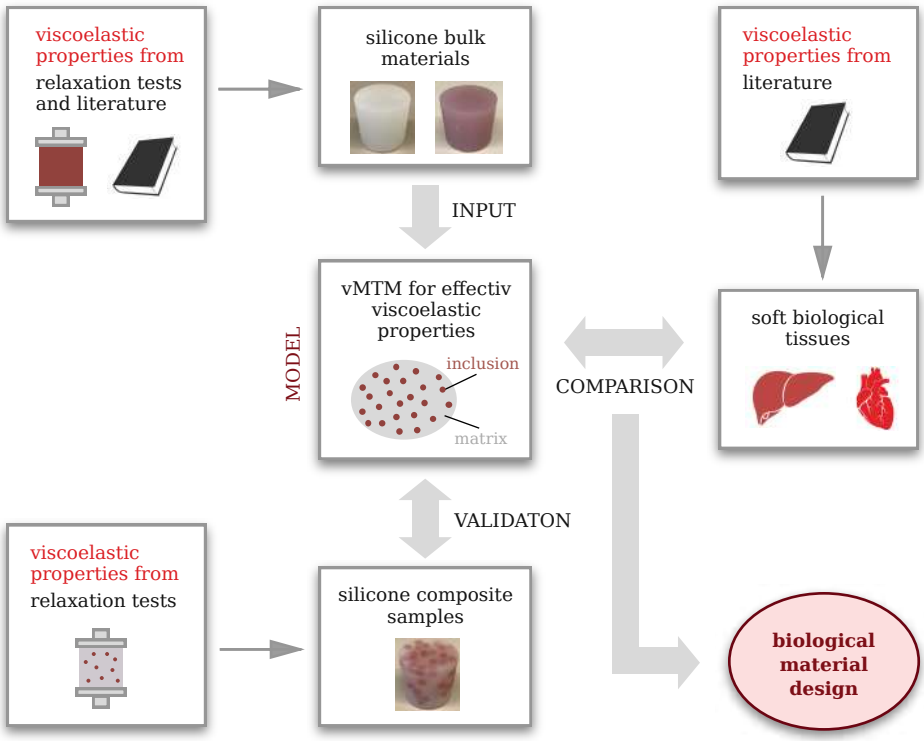

Figure 5.1: The viscoelastic Mori-Tanaka model (vMTM) is fed with input properties of silicone bulk materials from relaxation testing and literature; to validate the model, results are compared to experimentally tested composite samples; the resulting homogenised viscoelastic properties, predicted by the model, are compared to viscoelastic properties of biological tissues.

5.2.1 Micromechanical model

The *Mori-Tanaka model* is a common mean-field approach, oftentimes used for the homogenisation of linear elastic properties [Mori and Tanaka, 1973, Benveniste, 1987]. Due to the correspondence principle, a straightforward extension to linear viscoelastic properties is possible [Hashin, 1965, Fung, 1965, Brinson and Lin, 1998]. In the following, the Mori-Tanaka model for homogenising *elastic* properties is first explained, and then extended to *viscoelastic* properties.

As depicted in Figure 5.2, a heterogeneous composite material is considered, which consists of an isotropic matrix phase m and a phase of embedded isotropic spherical inclusions i. Homogenisation strategies aim at finding equivalent homogenous material properties which cause the same mechanical behaviour as the heterogenous material would, when observed on a macroscopic level.

Starting with linear elastic phases r, the 4th order stiffness tensor $\mathbb{C}_r$ relates the 2nd order tensors of average stress $\boldsymbol{\sigma}_r$ and average strain $\boldsymbol{\varepsilon}_r$ on the matrix and inclusion level with

$$\boldsymbol{\sigma}_r = \mathbb{C}_r : \boldsymbol{\varepsilon}_r \,. \tag{5.1}$$

Considering the assumption of mean field approaches that the strain and stress fields within each phase are constant, the average stress $\boldsymbol{\Sigma}$ and average strain $\mathbf{E}$ are related via the effective stiffness tensor $\mathbb{C}_{\text{eff}}$ on the composite level by

$$\boldsymbol{\Sigma} = \sum_r f_r \boldsymbol{\sigma}_r = \mathbb{C}_{\text{eff}} : \mathbf{E} \,, \tag{5.2}$$

with f_r being the volume fraction of the phases.

In the context of mean-field micromechanical models, the average strain fields $\boldsymbol{\varepsilon}_r$ of each phase r can be expressed in terms of the average macroscopic strain $\mathbf{E}$, using the 4th order concentration tensor $\mathbb{A}_r$ associated with the individual phase [Hill, 1963], as

$$\boldsymbol{\varepsilon}_r = \mathbb{A}_r : \mathbf{E} \,. \tag{5.3}$$

After inserting Eq. 5.3 into Eq. 5.1 and subsequently into Eq. 5.2, the homogenised stiffness tensor can be written as

$$\mathbb{C}_{\text{eff}} = \sum_r f_r \mathbb{C}_r : \mathbb{A}_r \,. \tag{5.4}$$

The derivation of $\mathbb{A}_r$ of phase r results in

$$\mathbb{A}_r = [\mathbb{I} + \mathbb{P}_{r,0} : (\mathbb{C}_r - \mathbb{C}_0)]^{-1} : \left\{ \sum_s f_s [\mathbb{I} + \mathbb{P}_{s,0} : (\mathbb{C}_s - \mathbb{C}_0)]^{-1} \right\}^{-1} \tag{5.5}$$

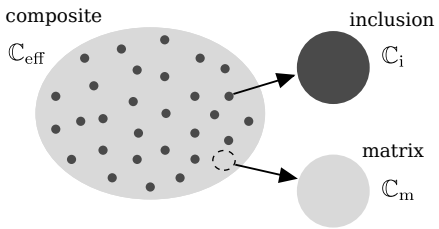

Figure 5.2: Schematic representation of the microstructure for micromechanical modelling.

[Hill, 1965b, Laws, 1975, Hellmich et al., 2004], with s being the index variable standing for the different phases and $\mathbb{I}$ being the fourth order unity tensor. The Hill tensor $\mathbb{P}_{r,0}$ describes the interaction between phase r embedded in a fictitious unbounded homogenous matrix with stiffness $\mathbb{C}_0$, and depends only on the characteristic shape of r and the stiffness $\mathbb{C}_0$. It should be noted that $\mathbb{P}_{r,0}$ is only defined for ellipsoidal inhomogeneities, including extreme cases of ellipsoids, such as fibres and spheres. The Mori-Tanaka method ($\mathbb{C}_0 = \mathbb{C}_\mathrm{m}$) [Mori and Tanaka, 1973, Benveniste, 1987] is applicable when the microstructure consists of two or more material phases, where one phase can be identified as the matrix and the others as embedded inclusions, perfectly bonded to the surrounding matrix. In the case of two phases (matrix m and inclusion i), the homogenised stiffness tensor for the Mori-Tanaka method, after inserting Eq. 5.5 into Eq. 5.4, results in

$$\mathbb{C}_\mathrm{eff} = \left\{ f_\mathrm{m}\mathbb{C}_\mathrm{m} + f_\mathrm{i}\mathbb{C}_\mathrm{i} : [\mathbb{I} + \mathbb{P}_\mathrm{i,m} : (\mathbb{C}_\mathrm{i} - \mathbb{C}_\mathrm{m})]^{-1} \right\} : \left\{ f_\mathrm{m}\mathbb{I} + f_\mathrm{i}[\mathbb{I} + \mathbb{P}_\mathrm{i,m} : (\mathbb{C}_\mathrm{i} - \mathbb{C}_\mathrm{m})]^{-1} \right\}^{-1}, \tag{5.6}$$

with inclusion volume fraction f_i and matrix volume fraction f_m being connected via $f_\mathrm{m} = 1 - f_\mathrm{i}$. For spherical inclusions in an isotropic matrix, $\mathbb{P}_\mathrm{i,m}$ can be expressed analytically, as will be shown later for an isotropic viscoelastic matrix.

The elastic-viscoelastic *correspondence principle* allows using relations, given above for elastic properties, in an equivalent manner for the time- or frequency-dependent properties of a viscoelastic material [Hashin, 1965]. The fourth order static stiffness tensors $\mathbb{C}_r$ of the elastic phases is transformed via Laplace-Carson transform to the frequency domain, yielding $\mathbb{C}_r^\mathrm{LC}(\omega)$, in the case of viscoelastic phases [Hashin, 1965, Fung, 1965, Brinson and Lin, 1998]. For harmonic excitation, the Laplace-Carson transformed stiffness tensor $\mathbb{C}_r^\mathrm{LC}(\omega)$ can be written in terms of the Laplace transformed stiffness tensor $\mathbb{C}_r^\mathrm{L}(\omega)$ as

$$\mathbb{C}_r^\mathrm{LC}(\omega) = i\omega\mathbb{C}_r^\mathrm{L}(\omega) = \mathbb{C}_r^*(\omega)\,, \tag{5.7}$$

yielding $\mathbb{C}_r^*(\omega)$, the complex frequency-dependent stiffness tensor whose components consist of complex material properties [Lakes, 1998, Tschoegl et al., 2002, Andreasen et al., 2014].

Replacing static $\mathbb{C}_\mathrm{m}$ and $\mathbb{C}_\mathrm{i}$ with complex stiffness tensors $\mathbb{C}_\mathrm{m}^*(\omega)$ and $\mathbb{C}_\mathrm{i}^*(\omega)$ in Eq. 5.6 yields the effective complex stiffness tensor of the homogenised material for the viscoelastic Mori-Tanaka model (vMTM)

$$\begin{aligned}\mathbb{C}_\mathrm{eff}^*(\omega) = \left\{ f_\mathrm{m}\mathbb{C}_\mathrm{m}^*(\omega) + f_\mathrm{i}\mathbb{C}_\mathrm{i}^*(\omega) : [\mathbb{I} + \mathbb{P}_\mathrm{i,m} : (\mathbb{C}_\mathrm{i}^*(\omega) - \mathbb{C}_\mathrm{m}^*(\omega))]^{-1} \right\} : \\ \left\{ f_\mathrm{m}\mathbb{I} + f_\mathrm{i}[\mathbb{I} + \mathbb{P}_\mathrm{i,m} : (\mathbb{C}_\mathrm{i}^*(\omega) - \mathbb{C}_\mathrm{m}^*(\omega))]^{-1} \right\}^{-1}.\end{aligned} \tag{5.8}$$

For a given volume fraction f_i of spherical inclusions i in an isotropic matrix m, with volume fraction $f_\mathrm{m} = 1 - f_\mathrm{i}$, the 4th order Hill tensor $\mathbb{P}_\mathrm{i,m}$ has the analytical solution [Eshelby, 1957, Parnell, 2016]

$$\mathbb{P}_\mathrm{i,m} = \frac{1}{3k_\mathrm{m}^* + 4\mu_\mathrm{m}^*}\mathbb{J} + \frac{3k_\mathrm{m}^* + 6\mu_\mathrm{m}^*}{5\mu_\mathrm{m}^*(3k_\mathrm{m}^* + 4\mu_\mathrm{m}^*)}\mathbb{K}\,, \tag{5.9}$$

with $k_\mathrm{m}^* = k_\mathrm{m}^*(\omega)$ and $\mu_\mathrm{m}^* = \mu_\mathrm{m}^*(\omega)$ being the complex frequency-dependent bulk and shear moduli of the linear viscoelastic matrix, and $\mathbb{J}$ ($J_{ijkl} = \frac{1}{3}\delta_{ij}\delta_{kl}$ with Kronecker

delta δ_{ij}) and $\mathbb{K} = \mathbb{I} - \mathbb{J}$ the volumetric and deviatoric part of the 4th order unity tensor.

To finally calculate the effective complex stiffness tensor $\mathbb{C}^*_{\text{eff}}(\omega)$, based on the vMTM (according to Eq. 5.8), the complex stiffness tensors of the phase bulk materials, $\mathbb{C}^*_{\text{r}}(\omega)$ (for $r = \text{i, m}$), are required.

For isotropic linear viscoelastic phases, the complex stiffness tensors $\mathbb{C}^*_r(\omega)$ can be written in an analogous form to isotropic elastic materials [Scheiner and Hellmich, 2009]:

$$\mathbb{C}^*_r(\omega) = 3k^*_r(\omega)\mathbb{J} + 2\mu^*_r(\omega)\mathbb{K}\,, \tag{5.10}$$

with complex and frequency-dependent bulk and shear modulus $k^*_r(\omega)$ and $\mu^*_r(\omega)$. Using relations

$$k^*_r(\omega) = \frac{E^*_r(\omega)}{3(1-2\nu^*_r(\omega))} \tag{5.11}$$

and

$$\mu^*_r(\omega) = \frac{E^*_r(\omega)}{2(1+\nu^*_r(\omega))} \tag{5.12}$$

[Tschoegl et al., 2002], the complex stiffness tensor of the phases (Eq. 5.10) can be expressed, depending on their complex tensile modulus $E^*_r(\omega)$ and viscoelastic Poisson's ratio $\nu^*_r(\omega)$. In the following section, it will be explained how $E^*_r(\omega)$ was measured experimentally. The viscoelastic Poisson's ratio of the individual isotropic silicone phases was assumed to be independent of frequency [Obaid et al., 2017] with $\nu^*_r(\omega) = \nu_r = 0.49$ [Sparks et al., 2015, Müller et al., 2019]. As a consequence, the main viscous contribution stems from shear relaxation, as opposed to the bulk response [Holzapfel and Gasser, 2001, Pritz, 2009], which is supported experimentally for rubbers [Wada et al., 1962, Theocaris, 1969, Pritz, 2007]. Subsequently, the obtained phase tensors were inserted into Eq. 5.8 with varying volume fractions as matrix phase $\mathbb{C}^*_{\text{m}}(\omega)$ and inclusion phase $\mathbb{C}^*_{\text{i}}(\omega)$, yielding the homogenized complex tensor $\mathbb{C}^*_{\text{eff}}(\omega)$ of the vMTM.

An equivalent way of writing an isotropic stiffness tensor, explicitly as a matrix in Kelvin notation, yields

$$\mathbb{C}^*(\omega) = \frac{E^*}{(1+\nu^*)(1-2\nu^*)} \begin{pmatrix} 1-\nu^* & \nu^* & \nu^* & 0 & 0 & 0 \\ \nu^* & 1-\nu^* & \nu^* & 0 & 0 & 0 \\ \nu^* & \nu^* & 1-\nu^* & 0 & 0 & 0 \\ 0 & 0 & 0 & 1-2\nu^* & 0 & 0 \\ 0 & 0 & 0 & 0 & 1-2\nu^* & 0 \\ 0 & 0 & 0 & 0 & 0 & 1-2\nu^* \end{pmatrix}. \tag{5.13}$$

Comparing the homogenised isotropic stiffness tensor $\mathbb{C}^*_{\text{eff}}(\omega)$ from the vMTM to Eq. 5.13, yields an analytical solution for the effective complex modulus $E^*_{\text{eff}}(\omega)$ of an isotropic matrix with isotropic spherical inclusions:

$$
\begin{aligned}
E^*_{\text{eff}} = &\Big[9\mu^*_{\text{m}}\Big(f_{\text{i}}k^*_{\text{i}}(3k^*_{\text{m}}+4\mu^*_{\text{m}})+f_{\text{m}}k^*_{\text{m}}(3k^*_{\text{i}}+4\mu^*_{\text{m}})\Big)\\
&\Big(5f_{\text{i}}(3k^*_{\text{m}}+4\mu^*_{\text{m}})\mu^*_{\text{i}}+f_{\text{m}}(9k^*_{\text{m}}\mu^*_{\text{m}}+8{\mu^*_{\text{m}}}^2+6k^*_{\text{m}}\mu^*_{\text{i}}+12\mu^*_{\text{m}}\mu^*_{\text{i}})\Big)\Big]/\\
&\Big[5{f_{\text{i}}}^2\mu^*_{\text{m}}(3k^*_{\text{m}}+4\mu^*_{\text{m}})^2(3k^*_{\text{i}}+\mu^*_{\text{i}})+\\
&f^2_{\text{m}}(3k^*_{\text{m}}+\mu^*_{\text{m}})(3k^*_{\text{i}}+4\mu^*_{\text{m}})(9k^*_{\text{m}}\mu^*_{\text{m}}+8{\mu^*_{\text{m}}}^2+6k^*_{\text{m}}\mu^*_{\text{i}}+12\mu^*_{\text{m}}\mu^*_{\text{i}})+\\
&f_{\text{m}}f_{\text{i}}(3k^*_{\text{m}}+4\mu^*_{\text{m}})\Big(3k^*_{\text{m}}(24\mu^*_{\text{m}}k^*_{\text{i}}+6\mu^*_{\text{i}}k^*_{\text{i}}+23{\mu^*_{\text{m}}}^2+2\mu^*_{\text{i}}\mu^*_{\text{m}})+\\
&\mu^*_{\text{m}}(8{\mu^*_{\text{m}}}^2+32\mu^*_{\text{i}}\mu^*_{\text{m}}+24k^*_{\text{i}}\mu^*_{\text{m}}+51\mu^*_{\text{i}}k^*_{\text{i}})\Big)\Big].
\end{aligned}
\tag{5.14}
$$

Extracting the real and imaginary parts of $E^*_{\text{eff}}(\omega) = E'_{\text{eff}}(\omega)+iE''_{\text{eff}}(\omega)$, finally yields storage and loss moduli $E'_{\text{eff}}(\omega)$ and $E''_{\text{eff}}(\omega)$, as well as loss tangent $\tan\delta_{\text{eff}}(\omega) = \frac{E''_{\text{eff}}(\omega)}{E'_{\text{eff}}(\omega)}$.

5.2.2 Mechanical testing

With the viscoelastic homogenisation model at hand, combinations of soft bulk materials (arranged in matrix-inclusion morphology) can be determined that best mimic certain soft biological tissues. In the following, two sets of mechanical tests were conducted: First, the bulk viscoelastic material properties of silicone elastomers were determined to serve as input for the vMTM. Second, composite samples, made from two silicone phases, were tested and compared to the vMTM predictions to validate the model (see Figure 5.1).

Silicone samples

Two types of samples were produced in this study, using two soft silicones which have been previously shown to exhibit viscoelastic behaviour [Estermann et al., 2020a]. First, bulk material samples were produced to experimentally determine bulk viscoelastic properties of the respective silicones. The silicones were both two-component room-temperature-vulcanising silicones: one with a nominal Shore A hardness of 13 (ZA13 Mould WT45, Polymerschmiede GmbH, Mönchengladbach, Germany), referred to as ZA13, and the other with a nominal Shore 00 hardness of 10 (Ecoflex 00-10, Smooth-On Inc., Macungie, Pennsylvania), referred to as EF10. The silicones were prepared according to the recommendations of the manufacturers, in a 1:1 ratio of their two components, and cast in cylindrical 3D printed moulds (diameter $D_0 = 42$ mm and height $H_0 = 42$ mm). Before casting, liquid EF10 was placed in a vacuum desiccator for removing air bubbles. ZA13 was dyed red for better distinction and not degassed, due to the fact that ZA13 was later-on used without degassing for the spherical inclusions in the composite samples.

Second, composite samples with matrix-inclusion morphology were produced to validate the vMTM model experimentally. The composite samples consisted of ZA13 spheres (radius $r = 3$ mm) embedded in a matrix of EF10, constituting cylindrical samples (diameter $D_0 = 42$ mm and height $H_0 = 42$ mm). In order to yield effective material properties, representative of the composite, the characteristic sample size (42 mm) must be at least 2–5 times larger than the characteristic size of the inclusions ($2r = 6$mm) [Drugan and Willis, 1996].

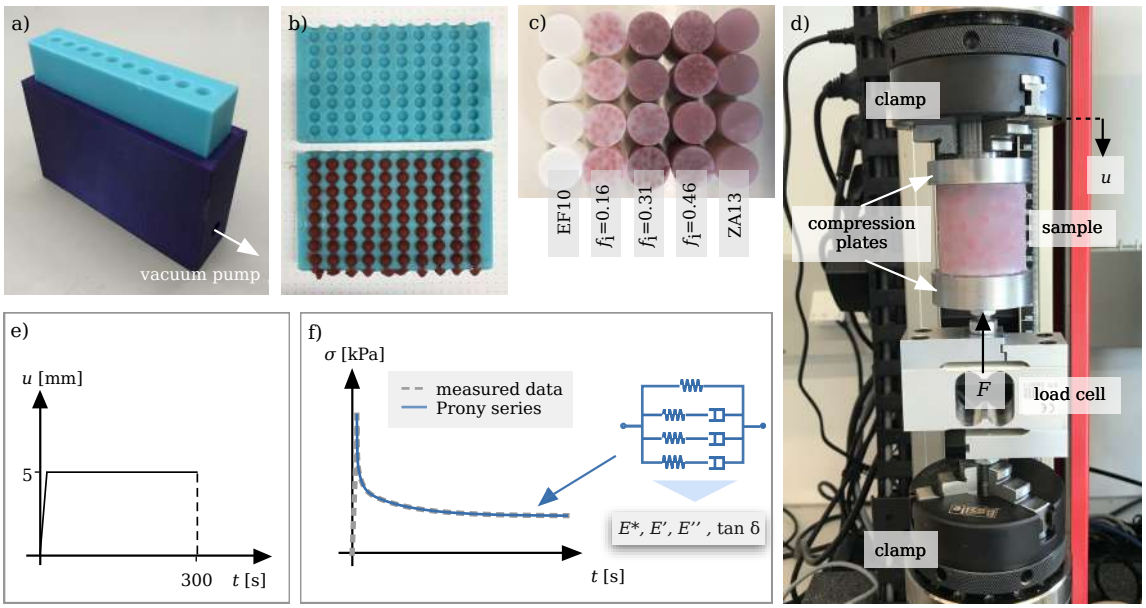

Figure 5.3: Overview of mechanical testing: (a) 3D printed mould for producing silicone spheres. (b) Silicone spheres of ZA13 silicone, ready to be removed from mould. (c) Cylindrical samples of bulk material EF10 and ZA13, and composite samples of EF10 matrix with varying volume fraction f_i of ZA13 inclusions. (d) Mechanical test setup with a composite sample tested in compression. (e) Testing procedure for measuring stress relaxation by exposing the sample to a constant displacement of 5 mm for 300 s. (f) Analysis of the relaxation data, based on the generalised Maxwell model, yielding complex modulus E^*, storage modulus E', loss modulus E'', and loss tangent $\tan\delta$.

.

The spheres were cast in the 3D printed device depicted in Figure 5.3a: liquid ZA13 was poured into the top part of the mould, while a vacuum pump, connected to the bottom part, drew the material into the mould. Upon hardening (24 h), the top part of the mould was removed and opened, revealing connected silicone spheres (Figure 5.3b). After separating the spheres from each other, they were mixed into the liquid matrix material (EF10), cast into the cylindrical moulds, and left to harden for 24 h before testing. Samples with different numbers of ZA13 spheres per sample, $n = \{80, 160, 240\}$, were produced. The inclusion volume fractions f_i were calculated according to

$$f_\mathrm{i} = \frac{4r^3 n}{3(D_0/2)^2 H_0}\,, \tag{5.15}$$

yielding average volume fractions $f_\mathrm{i} = 0.16$ for $n = 80$, $f_\mathrm{i} = 0.31$ for $n = 160$, and $f_\mathrm{i} = 0.46$ for $n = 240$ (with $r = 3$ mm), based on measured D_0 and H_0. Casting single spheres of ZA13 into EF10 revealed strong adhesion between the two silicones, justifying the mean field model's assumption of perfect bonding between the phases.

Four samples, depicted in Figure 5.3c, were tested for each type of material.

Furthermore, the viscoelastic properties of two types of soft, highly viscous silicone elastomers, found in literature, were included in the model. First, Sylgard 184, a commercial silicone elastomer, was chosen due to its broad application in biomedical engineering, including in microfluidics [Peterson et al., 2005, Pitts et al., 2013, Johnston et al., 2014], microelectronics [Blau et al., 2011, Kim et al., 2011], and mechanobiology [Teixeira et al., 2009, Hopf et al., 2016]. Furthermore, Sylgard 184 has also been used as a tissue mimicking material in terms of mechanical properties, for instance in the context of vascular modelling [Brown et al., 2005, Colombo et al., 2010]. Viscoelastic results for Sylgard 184 were extracted from Bartolini et al. [2018] who conducted dynamic cyclic nanoindentation.

Second, Elastomer-HV22, a non-commercial experimental elastomer, was selected. Hu et al. [2020] investigated and developed Elastomer-HV22, aiming at finding an extremely soft, yet elastic, elastomer for replicating human muscle. Originally published by Goff et al. [2016], the experimental elastomer is based on the main constituent of the commercial Exsil elastomer (Gelest Inc, Morrisville, Pennsylvania); however, adapted to eliminate typical covalent cross-links. Viscoelastic properties of Elastomer-HV22 were reported by Hu et al. [2020] who applied oscillatory shear testing.

Stress relaxation tests

Stress relaxation is one of the many methods, used for evaluating linear viscoelastic properties of materials. The decline in stress is measured in a sample, exposed to displacement that is held constant over a period of time. Evaluating this relaxation data using a Prony series approach, the viscoelastic material parameters of the sample can be extracted. In detail, a universal mechanical testing machine (ZwickiLine Z2.5, ZwickRoell GmbH & Co. KG, Ulm, Germany) with custom-made compression plates (radius 50 mm), and an extra load cell (S2M/100N, Hottinger Baldwin Messtechnik GmbH, Darmstadt, Germany) which was connected to a universal data acquisition module (QuantumX MX840B, Hottinger Baldwin Messtechnik GmbH, Darmstadt, Germany), were used for testing (see Figure 5.3d). First, the sample was placed on the bottom compression plate, with lubricating silicone oil applied to both platens to reduce friction. Then, the top compression plate was lowered until a small compressive

force (of around 0.15 N) was recorded, signifying contact with the sample. As depicted in Figure 5.3e, a machine displacement $u = 5$ mm was applied within 0.4 s and held for 300 s. Force F and machine displacement u were both recorded at a rate of 10 Hz.

Compression testing can be influenced by adverse effects, such as barreling of the sample and unclear boundary conditions, caused by friction between the sample and the platens. Selecting an adequate ratio of sample height H_0 to diameter D_0, as well as applying lubrication between the sample and platens can ameliorate these issues. According to Kim et al. [2018], a ratio $H_0/D_0 = 1.0$ should be chosen for rubber materials in compression testing to obtain nearly friction-free conditions. Furthermore, strain at the holding phase was small ($\varepsilon_0 = 0.12$) so as to remain in the linear region for silicone [Hattab et al., 2020].

Concerning data analysis, uniaxial (in direction of the sample axis) engineering strain $\varepsilon = u/H_0$ and stress $\sigma = F/A_0$ were calculated, with initial sample height H_0 and initial sample cross section A_0. For extracting linear viscoelastic properties, step-loading was assumed. The relaxation function, which relates stress $\sigma(t)$ and constant strain ε_0 during the holding phase, was approximated with a three-element Prony series [Findley et al., 1989], yielding

$$\sigma(t)_{\text{Prony}} = \left(E_0 - \sum_{i=1}^{3} E_i (1 - e^{-\frac{t}{\tau_i}}) \right) \varepsilon_0 \,. \tag{5.16}$$

The Prony series approach corresponds to the generalised Maxwell rheological model (see Figure 5.3f), with E_0 being the initial elastic modulus at the beginning of the holding phase, and E_i and τ_i being the elastic moduli and characteristic relaxation times of each series element i. Three elements were shown by Estermann et al. [2020a] to adequately describe the relaxation behaviour of the considered silicones. Using a non-linear least squares method with parameters limited to positive values, Eq. 5.16 was fit to the experimentally obtained stress data, yielding the Prony series parameters (E_0, E_i, τ_i).

In order to calculate the frequency-dependent storage and loss moduli, $E'(\omega)$ and $E''(\omega)$, the constitute equation (Eq. 5.16) was transformed via Laplace transform to the frequency domain and split into real and imaginary part, yielding [Brinson and Lin, 1998, Gutierrez-Lemini, 2014]

$$E'(\omega) = E_0 + \sum_{i=1}^{3} \left(\frac{E_i \omega^2 \tau_i^2}{1 + \omega^2 \tau_i^2} - E_i \right) \tag{5.17}$$

and

$$E''(\omega) = \sum_{i=1}^{3} \frac{E_i \omega \tau_i}{1 + \omega^2 \tau_i^2} \,. \tag{5.18}$$

Finally, loss tangent $\tan\delta(\omega) = \frac{E''(\omega)}{E'(\omega)}$ and the absolute value of the complex modulus $|E^*(\omega)| = \sqrt{E'(\omega)^2 + E''(\omega)^2}$ were calculated.

In the following section, all results are reported for a frequency of 1 Hz (i.e. $\omega = 2\pi$ rad/s). The reason behind the selected frequency is that 1 Hz is typically used for assessing tactile properties [Caldiran et al., 2018]; a crucial aspect when dealing with materials that should *feel* similar to biological tissues.

As described above, compression relaxation tests were conducted on bulk samples of EF10 and ZA13 for extracting their compressive complex moduli E^* and inserted as matrix (EF10) and inclusion (ZA13) phase into the vMTM, yielding effective storage modulus E'_{eff}, loss modulus E''_{eff}, absolute value of the complex modulus $|E^*_{\text{eff}}|$, and loss tangent $\tan\delta_{\text{eff}}$. The viscoelastic properties stemming from the vMTM were then validated with corresponding results of experimentally tested composite samples. Finally, the effective viscoelastic properties, calculated for combinations of different soft silicones (EF10, ZA13, Sylgard 184, and Elastomer-HV22) were compared to viscoelastic properties found in literature for soft biological tissues.

5.3 Results

The viscoelastic Mori-Tanaka model was used for estimating the effective viscoelastic properties of composite materials, consisting of different viscoelastic silicone elastomers (EF10, ZA13, Sylgard 184 and Elastomer-HV22). In order to validate the model experimentally, composite samples made of EF10 and ZA13 were tested and compared to the model predictions. Finally, the viscoelastic properties of the composites were compared to previously published properties of soft biological tissues in order to find tissue-mimicking combinations of silicones.

5.3.1 Experimental validation of the model

Figure 5.4 depicts the model results for a material, consisting of a EF10 matrix with spherical ZA13 inclusions for different volume fractions. Comparison of the model results with the experimental results shows that for small inclusion volume fractions ($f_{\text{i}} = 0.16$) the model predictions were quite accurate. For higher inclusion volume fractions ($f_{\text{i}} = 0.31$ and $f_{\text{i}} = 0.46$) the model predictions seemed to underestimate complex modulus $|E^*|$ and storage modulus E', while loss tangent $\tan\delta$ was still predicted accurately. The model line (in Figure 5.4a for $|E^*|$ and $\tan\delta$ and in Figure 5.4b for E' and E''), did, however, follow a similar trend as the experimental values.

5.3.2 Tissue-mimicking composite materials

After assessing the validity of the vMTM experimentally, using EF10 and ZA13 composite samples (see previous section 5.3.1), two additional, very soft and highly viscoelastic, silicone elastomers were used as input for the model. For this, the viscoelastic properties of Sylgard 184 [Bartolini et al., 2018] and Elastomer-HV22 [Hu et al., 2020] were taken from literature (see Table 5.1) and introduced into the vMTM as spherical inclusion phase.

Bartolini et al. [2018] tested the polydimethylsiloxane Sylgard 184 (Dow Corning Inc., Midland, Michigan) with oscillatory nanoindentation, yielding a mean storage modulus of $E' = 31$ kPa and loss modulus of around $E'' = 5$ kPa (at 1 Hz). The elastomer base and curing agent were mixed in a relatively high weight ratio of 50:1 and degassed in vacuum by Bartolini et al. [2018].

Concerning Elastomer-HV22, the oscillatory shear storage modulus and loss tangent were reported by Hu et al. [2020] and converted to tensile storage modulus E' (using Eq. 5.12). At a frequency of 1 Hz, resulting storage modulus was approximately $E' = 104$ and loss tangent $\tan\delta = 0.2$.

Table 5.1: Overview of viscoelastic properties of soft biological tissues and silicone elastomers at the frequency of 1 Hz, written as mean value and standard deviation.

Material	**Method**	**Storage modulus [kPa]**	**Loss modulus [kPa]**	**Complex modulus [kPa]**	**Loss tangent [-]**	**Reference**
Human liver	Relaxation tension	177.1 ± 78.6	43.1 ± 24.6	n.a.	0.23 ± 0.03	[Estermann et al., 2021a]
Porcine liver	Relaxation tension	118.8 ± 62.0	16.7 ± 10.5	n.a.	0.15 ± 0.09	[Estermann et al., 2020b]
Bovine liver	Relaxation tension	115.2 ± 28.2	9.4 ± 3.2	n.a.	0.08 ± 0.02	[Estermann et al., 2020b]
Human prostate tissue	Oscillatory compression	33 ± 3	11 ± 2	n.a.	n.a.	[Qiu et al., 2017]
Porcine adipose tissue	Oscillatory compression	1.8 ± 0.8	0.4 ± 0.2	n.a.	n.a.	[Comley and Fleck, 2009]
Porcine myocardium	Oscillatory compression	20 ± 5	3.6 ± 1	n.a.	0.17 ± 0.1	[Ramadan et al., 2017]
Human cervical tissue	Oscillatory compression	n.a.	n.a.	45 ± 7	0.28 ± 0.01	[Kiss et al., 2006]
EF10	Relaxation compression	51.98 ± 3.2	3.02 ± 1.2	52.1 ± 1.7	0.06 ± 0.02	current
ZA13	Relaxation compression	401.3 ± 12.6	13.8 ± 2.3	401.7 ± 11.2	0.03 ± 0.01	current
Sylgard 184	Oscillatory nanoindentation	31	5	n.a.	n.a.	[Bartolini et al., 2018]
Elastomer-HV22	Oscillatory shear	104*	n.a.	n.a.	0.2	[Hu et al., 2020]

* The storage modulus was calculated based on the reported shear storage modulus with Eq. 5.12.

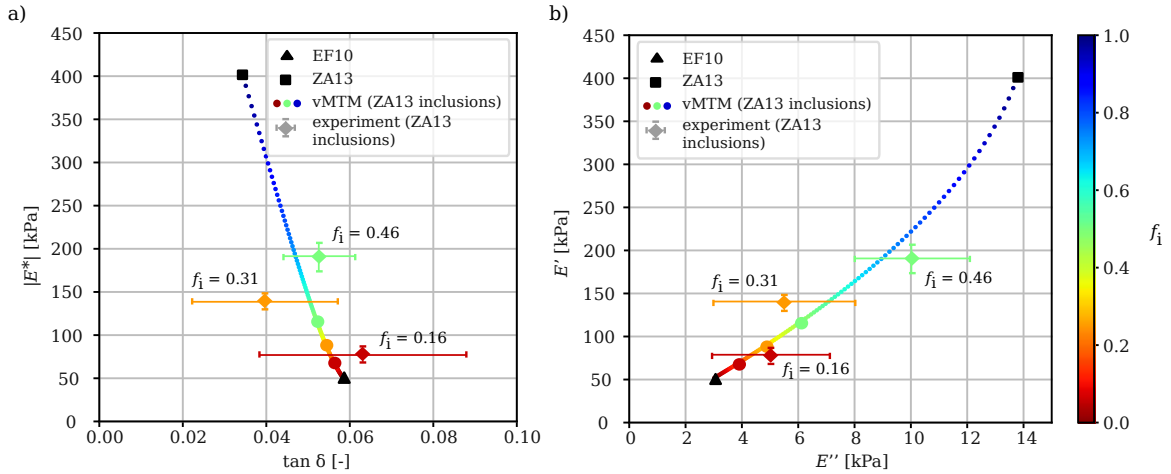

Figure 5.4: Viscoelastic properties of the bulk silicones EF10 and ZA13 (black triangles and black squares) and composite samples (red, orange, and green diamond symbols for different inclusion volume fractions f_i of ZA13 in EF10 matrix), based on the experiments; and results of the viscoelastic Mori-Tanaka model (vMTM) for corresponding matrix-inclusionin materials (rainbow coloured circles for varying f_i). Circles and diamonds of the same colour represent the same inclusion volume fraction. (a) Absolute value of the complex modulus $|E^*|$ plotted against loss tangent $\tan\delta$ (frequency 1 Hz). (b) Storage modulus E' plotted against loss modulus E'' (frequency 1 Hz).

The viscoelastic properties of various soft biological tissues are listed in Table 5.1. Values for biological tissues that were not explicitly given in the cited publications had to be calculated based on the reported values. Missing standard deviations were calculated using Gaussian propagation of uncertainty for uncorrelated variables [Ku, 1966].

Figure 5.5 depicts resulting effective properties, predicted by the vMTM, for spherical inclusions of different silicone elastomers with various volume fractions f_i in a matrix of EF10 (Figure 5.5a and c) and in a matrix of ZA13 (Figure 5.5b and d). Furthermore, viscoelastic properties of soft biological tissues are also indicated in Figure 5.5 to allow straightforward comparison with the silicone composites.

Figures 5.5a–d demonstrate that the bulk material of EF10 and ZA13 alone, do not match the viscoelastic properties of soft biological tissues very well. However, according to the model, a combination of the the two (with EF10 being the matrix and ZA13 the spherical inclusions) yielded effective properties close to bovine and porcine liver parenchyma for $f_i = 0.5 - 0.6$. Compared to the softest silicone, tested experimentally in this study (EF10), adipose and myocardial tissues were even softer (concerning $|E^*|$ and E'). Prostate and cervical tissue exhibited similar values of $|E^*|$ and E' as EF10 with higher viscous contributions ($\tan\delta$ and E''). All considered biological tissues tended to exhibit higher values of $\tan\delta$, compared to the EF10 and ZA13 composites. Introducing, two further silicones, whose viscoelastic properties were found in literature (Sylgard 184 [Bartolini et al., 2018] and Elastomer-HV22 [Hu et al., 2020]), enabled simulating more viscous composites in terms of $\tan\delta$ and E''.

The results show that effective viscoelastic properties are adaptable, depending on the chosen constitutive materials and volume fractions.

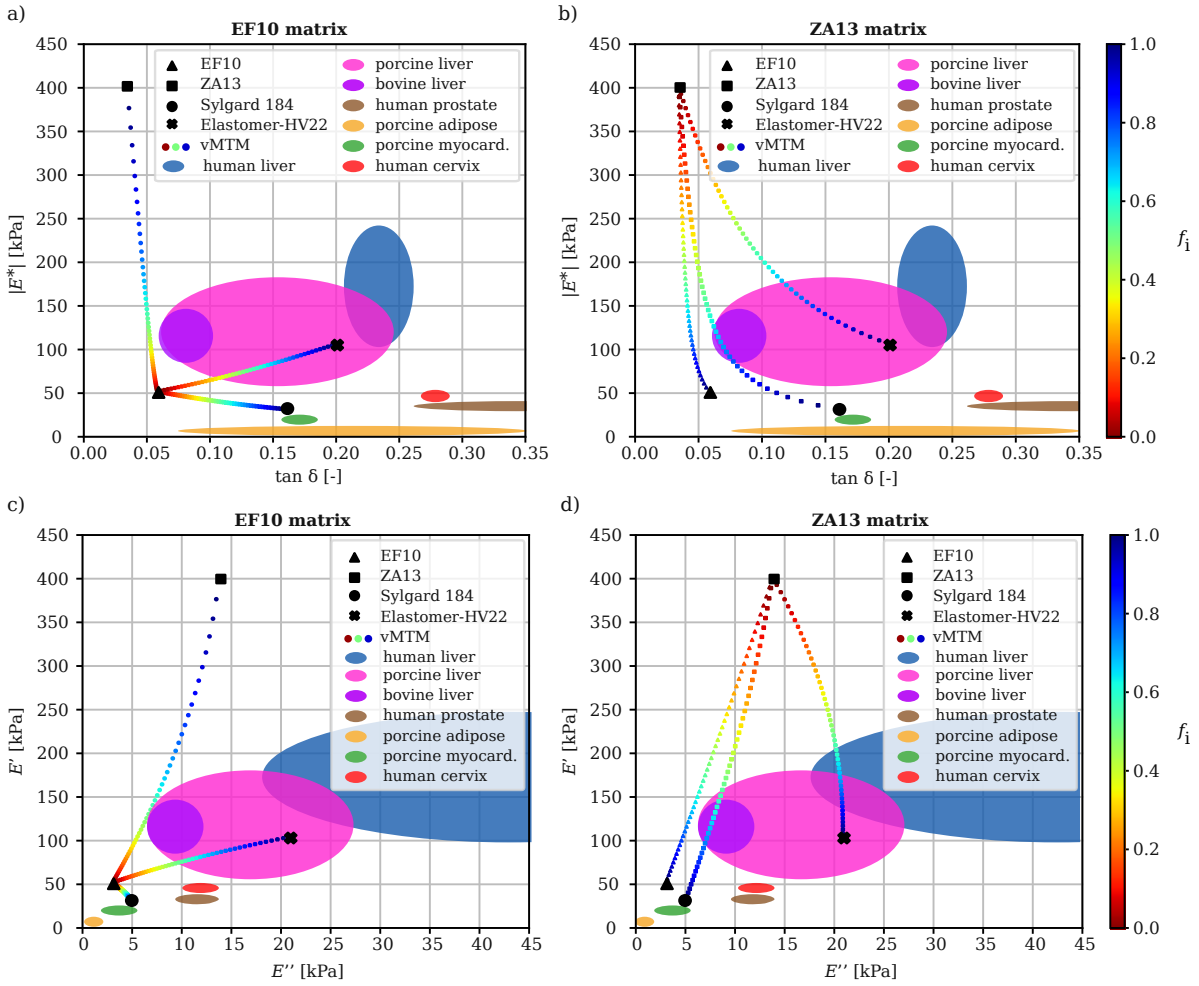

Figure 5.5: Effective properties, according to the vMTM, for different combinations of silicone elastomers and viscoelastic properties of soft biological tissues (at a frequency of 1 Hz): (a) Absolute value of the complex modulus $|E^*|$ and loss tangent $\tan\delta$ for EF10 matrix with spherical inclusions. (b) Absolute value of the complex modulus $|E^*|$ and loss tangent $\tan\delta$ for ZA13 matrix with spherical inclusions. (c) Storage modulus E' and loss modulus E'' for EF10 matrix with spherical inclusions. (d) Storage modulus E' and loss modulus E'' for ZA13 matrix with spherical inclusions.

5.4 Discussion

In this study, we aimed at defining tissue-mimicking microstructures by using the vMTM for homogenising viscoelastic properties of soft silicone composites of matrix-inclusion morphology. Viscoelastic input properties for the vMTM were found by compression relaxation testing of two silicones (EF10 and ZA13), as well as by using viscoelastic properties reported in literature (Sylgard 184 and Elastomer-HV22). Model validation was done by comparing vMTM results for composites (EF10 matrix with ZA13 inclusions) with corresponding experimentally tested composite samples. The model predictions indicate how materials should be designed to achieve effective viscoelastic properties, similar to soft biological tissues.

5.4.1 Experimental results — bulk materials

Viscoelastic results, found for the tested bulk silicone elastomers in this study, were partially comparable to previously published results. For instance, concerning EF10, the storage modulus E'— representing the elastic part of the complex modulus—was similar to results published by Vaicekauskaite et al. [2020] for the Young's modulus (around 50 kPa). Regarding macroindentation of EF10, an average loss tangent $\tan\delta = 0.28$ was reported in an earlier study [Estermann et al., 2020a], which is much higher than current results (approximately $\tan\delta = 0.09$). However, variations amongst silicone batches were likely the reason for this difference. It was observed that EF10, purchased for the earlier study [Estermann et al., 2020a] in 2019, exhibited a more sticky surface, lighter colour, and was palpably softer than the EF10 of the current study (purchased in late 2020). Concerning ZA13, the loss tangent found via macroindentation of $0.03 - 0.06$ [Estermann et al., 2020a] was similar to the current study ($\tan\delta = 0.02 - 0.04$).

5.4.2 Experimental validation of the model

Regarding the experimentally tested composite samples, obtained viscoelastic properties matched the model predictions well for inclusion volume fraction $f_\mathrm{i} = 0.16$. For higher volume fractions ($f_\mathrm{i} = 0.31$ and $f_\mathrm{i} = 0.46$), the micromechanical model underestimated $|E^*|$ and E'. This trend is consistent with literature, concerning linear elastic properties. In the case of stiff spherical inclusions reinforcing a softer matrix, the Mori-Tanaka model predictions seem to underestimate stiffness for volume fractions higher than 0.2 [Christensen et al., 1992, Segurado and Llorca, 2002, Böhm, 2015]. The model is only based on volume fractions and (visco-)elastic stiffness tensors of the phases, and assumes that the shape of the inclusions stays the same during deformation. According to Kwon and Dharan [1995], factors, such as inclusion size, shape, phase continuity, and distance between inclusions, are not negligible for larger inclusion volume fractions.

The viscous part of the complex modulus, the loss modulus E'', was underestimated by the model only for the highest tested volume fraction $f_\mathrm{i} = 0.46$. Fairly good agreement between the vMTM and the experiment was observed for $\tan\delta$ for all tested volume fractions, indicating that $\tan\delta$ might be less influenced by changes in volume fractions. This finding is consistent with Liu et al. [2021], who concluded that changes in particle volume fraction predominantly effect the complex modulus while the loss tangent is more susceptible to changes in interface between inclusions and matrix.

5.4.3 Comparison of silicone composites with biological tissues

The tested silicones, EF10 and ZA13, as bulk materials alone do not match any of the examined biological tissues. However, a combination of ZA13 spherical inclusions in a matrix of EF10 with an inclusion volume fraction of 0.5–0.6 (according to the vMTM) matches bovine and porcine liver best. Other soft silicones, found in literature, were introduced to the model and their bulk properties alone were suitable for mimicking porcine myocardial tissue (Sylgard 184) and porcine liver (Elastomer-HV22). According to the model, a combination of Sylgard 184 as inclusions in a stiffer matrix of ZA13 would intersect with properties for porcine liver. In order to recreate viscoelastic properties of human liver, cervical and prostate tissue, a combination of materials, exhibiting even higher $\tan\delta$ than the considered silicones, is required. Porcine adipose tissue is so soft that it would be recommendable to attempt adding voids to the matrix of EF10 to potentially further decrease its complex modulus.

The current results indicate that replicating viscoelastic properties of soft biological tissues is feasible with appropriate microstructural combinations of different silicones. One of the silicone phases should thereby exhibit dampening to an even higher extent than the considered silicones, especially for tissues with very high values of $\tan\delta$ (e.g. prostate and cervical tissue).

5.5 Limitations

Following limitations of this study should be considered:

- For evaluating the relaxation data, ideal step loading was assumed and the finite time, needed for reaching the holding displacement, was neglected. More sophisticated models, that include the effect of the rise time, could be applied for extracting the viscoelastic properties based on the experimental data [Oyen, 2005].
- The viscoelastic Poisson's ratio $\nu^*(\omega)$ of the matrix and inclusion phases introduced into the vMTM, was assumed to be constant. Generally, $\nu^*(\omega)$ is complex and frequency-dependant and very difficult to measure experimentally [Hilton, 2001, Tschoegl et al., 2002]. However, even if the Poisson's ratios of the individual phases were assumed constant, this does not mean that the Poisson's ratio of the homogenised composite is necessarily also constant, due to interactions between the different phases [Charpin and Sanahuja, 2017]. Thus, no assumptions on the viscoelastic Poisson's ratio of the composite were made.
- Concerning the experimental validation of the model, only three different inclusion volume fractions were tested ($f_\mathrm{i} = \{0.16, 0.31, 0.46\}$). For an even more rigorous vMTM validation, additional volume fractions should be tested experimentally. It would, however, be convenient if composite samples were to be produced via 3D printing in future to avoid the laborious sample production using moulds.

5.6 Conclusions

Material design for soft tissue replicas is facilitated with the here presented vMTM, allowing fast estimation of composite viscoelasticity. The considered composite mate-

rials consisted of heterogenous materials, exhibiting matrix-inclusion-type morphologies. Specifically for liver and myocardial tissue, combinations of different silicone elastomers were found, based on the vMTM, to match their viscoelastic properties for the production of anatomical models. Results from validating the vMTM with tested composite samples, revealed that the model was accurate for low inclusion volume fractions. While complex modulus and storage modulus were underestimated for higher inclusion volume fractions, the loss modulus exhibited good agreement between vMTM and experiment for all volume fractions.

5.7 Acknowledgements

The research was funded by the Science Call Dissertations 2017 (Gesellschaft für Forschungsförderung Niederösterreich, SC17-016), and the Austrian Center for Medical Innovation and Technology (funded in the framework of COMET by BMVIT, BMDW, the Federal State of Lower Austria and Standortagentur Tirol). The authors acknowledge TU Wien University Library for financial support through its Open Access Funding Programme.

Chapter 6

Conclusion

6.1 Conclusions of the original contributions

The previous Chapters 2–5 contained the original research that was published in peer reviewed journals in the course of this dissertation. In the following, the main findings of the original contributions are summarised.

- Chapter 2 provides a convenient method for assessing tactile properties of liver tissue and respective tissue mimicking materials. Structural properties, extracted from macroindentation, of the different materials were compared with each other, using the newly introduced *tactile similarity error*. It was shown that viscoelastic properties are important for characterising soft tissue tactility, as opposed to simply describing elastic properties alone. It was also shown that most of the tested artificial materials were highly elastic with insufficient viscous contribution. The only tested 3D printed soft polymer exhibited high viscoelastic damping, due to its microstructure, but was far too stiff to resemble liver. Regarding the tactile similarity error, which takes viscoelastic as well as elastic and hardness properties into account, one of the super-soft silicone elastomers was most similar to liver (Ecoflex 00-30 SmoothOn Inc.). Thus, a material was found which is suitable for producing liver anatomical models. However, even for this material, the tactile similarity error was still relatively high, owing to the low viscoelastic damping of the elastomer. [Estermann et al., 2020a]

- Chapter 3 characterises linear viscoelastic behaviour of animal liver tissue with newly developed tensile testing methods. The fairly simple method of stress relaxation is compared to the gold standard in viscoelastic testing, dynamic cyclic testing. It was shown that, even in light of the assumptions made for evaluating the stress relaxation data (step displacement, discrete 3-element generalised Maxwell model), viscoelastic properties found with both methods were similar. However, this is only the case if tests are conducted at the same level of strain, due to non-linear elastic characteristics, exhibited by liver tissue for strains exceeding approximately 3%. Furthermore, this non-linear stress-stretch behaviour, stemming from ramp loading and unloading, of liver was modelled with a pseudoelastic Veronda-Westmann model, providing material constants that could be useful in the context of computational modelling of liver tissue. [Estermann et al., 2020b]

- Chapter 4 applies methods, developed on animal liver in Chapter 3 for characterising liver pseudohyperelasticity and viscoelasticity, to human liver. Samples extracted from fresh healthy human liver and Thiel preserved human liver were tested. The results showed that Thiel preservation significantly increases tissue stiffness and loss tangent, likely due to increased protein cross-linking and dehydration during preservation. Porcine liver, which has a higher collagen content compared to fresh human liver, was stiffer with similar viscoelastic properties. Bovine liver has a similar collagen content to fresh human tissue and therefore stiffness was similar. Nevertheless, viscoelastic properties of bovine liver were significantly different to fresh human liver, which can be explained by microstructural morphological differences. In conclusion, when selecting a biological substitutes for fresh human liver, it must be kept in mind which mechanical properties are important for the application. Even though some differences were found regarding elasticity and loss tangent, Thiel preservation still seems recommendable for the practice of surgical training (which is not possible using conventional formalin preservation). Based on the current results, bovine liver is more suitable for applications, requiring accurate elastic properties (for instance for developing new medical devices). [Estermann et al., 2021a]

- Chapter 5 proposes a strategy for using micromechanical modelling as a design tool for tissue mimicking microstructures. The utilized Mori-Tanaka model was capable of predicting homogenised viscoelastic properties, such as complex modulus and loss tangent, of composite materials, exhibiting a matrix-inclusion morphology. Based on the model, combinations of soft silicone elastomers were found that simulate selected soft biological tissues (hepatic, myocardial, adipose, cervical, and prostate tissue), whose viscoelastic properties were found in literature and in Chapters 3–4. Furthermore, the viscoelastic Mori-Tanaka model was also validated experimentally, showing good agreement of model and experiment for low inclusion volume fractions. The proposed micromechanical model is a fast and efficient method for selecting tissue mimicking matrix-inclusion composites and could be used in designing 3D printed microstructures. [Estermann et al., 2021b]

6.2 Future outlook

In future research, it would be interesting to apply the experimental methods, developed in this dissertation, to other soft tissues. The establishment of a database of tissue mechanical properties, alongside viscoelastic properties of artificial materials, all measured with the same experimental methods, would be beneficial for selecting materials for whole-body anatomical models.

For accurately matching tissues with artificial materials, composite materials can be used as opposed to the bulk materials alone, allowing fine-tuning of the desired properties. The composite microstructure can thereby be designed, using the presented viscoelastic Mori-Tanaka model. In future, the micromechanical model can be extend to cover microstructures additional to the current matrix-inclusion morphology, for instance by using self-consistent schemes, when no distinct matrix phase is identifiable. Furthermore the Mori-Tanaka model, utilized here for spherical inclusions, can be adapted to reflect fibrous inclusions or ellipsoidal inclusions of various aspect rations,

thus also considering transverse isotropy.

Concerning the production of anatomical models, made of microstructure materials, and also for the validation of the micromechanical models, further developments in the field of soft material additive manufacturing are necessary. A system capable of 3D printing soft silicone elastomers, based on paste extrusion, is currently under development in our research group.

Bibliography

J. Aboudi, S. M. Arnold, B. A. Bednarcyk, J. Aboudi, S. M. Arnold, and B. A. Bednarcyk. Chapter 3 - fundamentals of the mechanics of multiphase materials. In *Micromechanics of Composite Materials*, pages 87–145. Butterworth-Heinemann, Oxford, 2013.

V. Abraira and D. Ginty. The sensory neurons of touch. *Neuron*, 79(4):618 – 639, 2013. ISSN 0896-6273. doi: 10.1016/j.neuron.2013.07.051.

F. Adams, T. Qiu, A. Mark, B. Fritz, L. Kramer, D. Schlager, U. Wetterauer, A. Miernik, and P. Fischer. Soft 3d-printed phantom of the human kidney with collecting system. *Annals of Biomedical Engineering*, 45(4):963–972, Apr. 2017. ISSN 1573-9686.

B. Ahn, Y. Kim, C. K. Oh, and J. Kim. Robotic palpation and mechanical property characterization for abnormal tissue localization. *Med. Biol. Eng. Comput.*, 50(9): 961–971, Sept. 2012. ISSN 1741-0444. doi: 10.1007/s11517-012-0936-2.

R. Akhtar, M. J. Sherratt, J. K. Cruickshank, and B. Derby. Characterizing the elastic properties of tissues. *Mater. Today (Kidlington)*, 14(3):96–105, Mar. 2011. ISSN 1873-4103. doi: 10.1016/s1369-7021(11)70059-1.

V. V. Alli, J. Yang, J. Xu, A. T. Bates, A. D. Pryor, M. A. Talamini, and D. A. Telem. Nineteen-year trends in incidence and indications for laparoscopic cholecystectomy: the ny state experience. *Surgical Endoscopy*, 31(4):1651–1658, 2017. ISSN 1432-2218.

J. R. Anderson, W. L. Thompson, A. K. Alkattan, O. Diaz, R. Klucznik, Y. J. Zhang, G. W. Britz, R. G. Grossman, and C. Karmonik. Three-dimensional printing of anatomically accurate, patient specific intracranial aneurysm models. *J. NeuroIntervent. Surg.*, 8(5):517, May 2016.

C. S. Andreasen, E. Andreassen, J. S. Jensen, and O. Sigmund. On the realization of the bulk modulus bounds for two-phase viscoelastic composites. *J. Mech. Phys. Solids*, 63:228–241, Feb. 2014. ISSN 0022-5096. doi: 10.1016/j.jmps.2013.09.007.

P. R. Armijo, S. Pagkratis, E. Boilesen, T. Tanner, and D. Oleynikov. Growth in robotic-assisted procedures is from conversion of laparoscopic procedures and not from open surgeons' conversion: a study of trends and costs. *Surg. Endosc.*, 32: 2106–2113, Apr 2018.

R. S. Aycock and J. M. Seyer. Collagens of normal and cirrhotic human liver. *Connect. Tissue Res.*, 23:19–31, 1989. doi: 10.3109/03008208909103901.

M. Ayyildiz, R. Aktas, and C. Basdogan. Effect of solution and post-mortem time on mechanical and histological properties of liver during cold preservation. *Biorheology*, 51, June 2014. doi: 10.3233/bir-14007.

S. L. Barnes, A. Lyshchik, M. K. Washington, J. C. Gore, and M. I. Miga. Development of a mechanical testing assay for fibrotic murine liver. *Med. Phys.*, 34(11):4439–4450, Nov. 2007. ISSN 0094-2405. doi: 10.1118/1.2795665.

L. Bartolini, D. Iannuzzi, and G. Mattei. Comparison of frequency and strain-rate domain mechanical characterization. *Sci. Rep.*, 8(1):13697, Sept. 2018. doi: 10.1038/s41598-018-31737-3.

J. Bear and M. Corapcioglu, editors. *Fundamentals of Transport Phenomena in Porous Media*. Springer, Dordrecht, 1984. doi: 10.1007/978-94-009-6175-3.

Y. Benveniste. A new approach to the application of mori-tanaka's theory in composite materials. *Mech. Mater.*, 6(2):147–157, 1987. ISSN 0167-6636. doi: 10.1016/0167-6636(87)90005-6.

A. Blau, A. Murr, S. Wolff, E. Sernagor, P. Medini, G. Iurilli, C. Ziegler, and F. Benfenati. Flexible, all-polymer microelectrode arrays for the capture of cardiac and neuronal signals. *Biomaterials*, 32(7):1778–1786, 2011. ISSN 0142-9612.

H. Böhm. *A Short Introduction to Basic Aspects of Continuum Micromechanics*. ILSB Report 206, 2015.

F. Braet and E. Wisse. Structural and functional aspects of liver sinusoidal endothelial cell fenestrae: A review. *Comp. Hepatol.*, 1:1, Sept. 2002.

L. C. Brinson and W. S. Lin. Comparison of micromechanics methods for effective properties of multiphase viscoelastic composites. *Compos. Struct.*, 41(3):353–367, 1998. ISSN 0263-8223. doi: 10.1016/s0263-8223(98)00019-1.

J. D. Brown, J. Rosen, Y. S. Kim, L. Chang, M. N. Sinanan, and B. Hannaford. In-vivo and in-situ compressive properties of porcine abdominal soft tissues. *Stud. Health Technol. Inform.*, 94:26–32, 2003.

X. Q. Brown, K. Ookawa, and J. Y. Wong. Evaluation of polydimethylsiloxane scaffolds with physiologically-relevant elastic moduli: interplay of substrate mechanics and surface chemistry effects on vascular smooth muscle cell response. *Biomaterials*, 26 (16):3123–3129, 2005. ISSN 0142-9612. doi: 10.1016/j.biomaterials.2004.08.009.

A. Brunon, K. Bruyère-Garnier, and M. Coret. Mechanical characterization of liver capsule through uniaxial quasi-static tensile tests until failure. *J. Biomech.*, 43(11): 2221–2227, Aug. 2010. ISSN 0021-9290. doi: 10.1016/j.jbiomech.2010.03.038.

E. M. Brunt, A. S. H. Gouw, S. G. Hubscher, D. G. Tiniakos, P. Bedossa, A. D. Burt, F. Callea, A. D. Clouston, H. P. Dienes, Z. D. Goodman, E. A. Roberts, T. Roskams, L. Terracciano, M. S. Torbenson, and I. R. Wanless. Pathology of the liver sinusoids. *Histopathology*, 64(7):907–920, June 2014. doi: 10.1111/his.12364.

S. Budday, G. Sommer, G. Holzapfel, P. Steinmann, and E. Kuhl. Viscoelastic parameter identification of human brain tissue. *J. Mech. Behav. Biomed. Mater.*, 74:463 – 476, 2017. doi: 10.1016/j.jmbbm.2017.07.014.

B. Cai, R. Kanagasuntheram, B. Bay, J. Lee, and C. Yen. The effects of a functional threedimensional (3d) printed knee joint simulator in improving anatomical spatial knowledge. *Anat. Sci. Educ.*, 12(6), Dec. 2018. doi: 10.1002/ase.1847.

O. Caldiran, H. Z. Tan, and C. Basdogan. An investigation of haptic perception of viscoelastic materials in the frequency domain. In *2018 IEEE Haptics Symposium (HAPTICS)*, pages 222–228, 2018. doi: 10.1109/haptics.2018.8357180.

O. Caldiran, H. Z. Tan, and C. Basdogan. Visuo-haptic discrimination of viscoelastic materials. *IEEE Transactions on Haptics*, 12(4):438–450, 2019. ISSN 2329-4051. doi: 10.1109/toh.2019.2924212.

A. Capilnasiu, L. Bilston, R. Sinkus, and D. Nordsletten. Nonlinear viscoelastic constitutive model for bovine liver tissue. *Biomech. Model. Mechanobiol.*, 2020. doi: 10.1007/s10237-020-01297-5.

W. C. Carson, G. J. Gerling, T. L. Krupski, C. G. Kowalik, J. C. Harper, and C. A. Moskaluk. Material characterization of ex vivo prostate tissue via spherical indentation in the clinic. *Med. Eng. Phys.*, 33(3):302–309, Apr. 2011. doi: 10.1016/j.medengphy.2010.10.013.

G. Chagnon, J. Ohayon, J.-L. Martiel, D. Favier, Y. Payan, and J. Ohayon. Chapter 1 - hyperelasticity modeling for incompressible passive biological tissues. In *Biomechanics of Living Organs*, volume 1, pages 3–30. Academic Press, Oxford, 2017.

L. Charpin and J. Sanahuja. Creep and relaxation poissons ratio: Back to the foundations of linear viscoelasticity. application to concrete. *International Journal of Solids and Structures*, 110-111:2–14, 2017. ISSN 0020-7683.

S. Chatelin, J. Oudry, N. Perichon, L. Sandrin, P. Allemann, L. Soler, and R. Willinger. In vivo liver tissue mechanical properties by transient elastography: comparison with dynamic mechanical analysis. *Biorheology*, 48:75–88, Jan. 2011. doi: 10.3233/bir-2011-0584.

E. J. Chen, J. Novakofski, W. K. Jenkins, and W. D. O'Brien. Young's modulus measurements of soft tissues with application to elasticity imaging. *IEEE Trans. Ultrason. Ferroelectr. Freq. Control*, 43(1):191–194, 1996. doi: 10.1109/58.484478.

R. Chen, P. Rodrigues Armijo, C. Krause, K.-C. Siu, D. Oleynikov, and S. A. G. E. S. R. T. Force. A comprehensive review of robotic surgery curriculum and training for residents, fellows, and postgraduate surgical education. *Surgical Endoscopy*, 34 (1):361–367, 2020. doi: 10.1007/s00464-019-06775-1.

X. Chen, N. Masano, T. Teppei, J. Xin, A. Satoko, A. Koyu, K. Atsushi, and U. Masaru. Identification of physical properties of swine liver for surgical simulation using a dynamic deformation model. *System Integration (SII), 2011 IEEE/SICE International Symposium on*, pages 655–660, Dec. 2011. doi: 10.1109/sii.2011.6147526.

Z. Chen, T. Scheffer, H. Seibert, and S. Diebels. Macroindentation of a soft polymer: Identification of hyperelasticity and validation by uni/biaxial tensile tests. *Mech. Mater.*, 64a:111–127, Sept. 2013. doi: 10.1016/j.mechmat.2013.05.003.

L. Cherkasskiy, J. P. Caffrey, A. F. Szewczyk, E. Cory, J. D. Bomar, C. L. Farnsworth, M. Jeffords, D. R. Wenger, R. L. Sah, and V. V. Upasani. Patient-specific 3d models aid planning for triplane proximal femoral osteotomy in slipped capital femoral epiphysis. *J. Child.'s Orthop.*, 11(2):147–153, Feb. 2017. doi: 10.1302/1863-2548-11-170277.

C. L. Cheung, T. Looi, T. S. Lendvay, J. M. Drake, and W. A. Farhat. Use of 3-dimensional printing technology and silicone modeling in surgical simulation: Development and face validation in pediatric laparoscopic pyeloplasty. *Journal of Surgical Education*, 71(5):762 – 767, 2014. doi: 10.1016/j.jsurg.2014.03.001.

M. Christensen, H. Schantz, and J. Shapiro. On the range of validity of the mori-tanaka method. *J. Mech. Phys. Solids*, 40:69–73, Dec. 1992.

C. Chui, E. Kobayashi, X. Chen, T. Hisada, and I. Sakuma. Combined compression and elongation experiments and non-linear modelling of liver tissue for surgical simulation. *Med. Biol. Eng. Comput.*, 42(6):787–798, Nov. 2004. doi: 10.1007/bf02345212.

A. Colombo, H. Zahedmanesh, D. M. Toner, P. A. Cahill, and C. Lally. A method to develop mock arteries suitable for cell seeding and in-vitro cell culture experiments. *J. Mech. Behav. Biomed. Mater.*, 3(6):470–477, 2010. ISSN 1751-6161. doi: 10.1016/j.jmbbm.2010.04.003.

K. Comley and N. Fleck. The mechanical response of porcine adipose tissue. *ASME J. Biomech. Eng.*, pages 1–30, 2009.

J. M. Crawford and C. Lui. *Robbins and Cotrans Pathological Basis of Disease*, chapter Liver and Biliary Tract. Saunders Elsevier, Philadelphia, 2010.

J. Dargahi and S. Najarian. Human tactile perception as a standard for artificial tactile sensing–a review. *Int. J. Med. Robot.*, 1:23–35, Nov. 2004. doi: 10.1581/mrcas.2004.010109.

C. Debbaut, J. Vierendeels, C. Casteleyn, P. Cornillie, V. Denis, P. Simoens, L. Hoorebeke, D. Monbaliu, and P. Segers. Perfusion characteristics of the human hepatic microcirculation based on three-dimensional reconstructions and computational fluid dynamic analysis. *J. Biomech. Eng.*, 134:011003, Jan. 2012. doi: 10.1115/1.4005545.

R. J. DeWall, S. Bharat, T. Varghese, M. E. Hanson, R. M. Agni, and M. A. Kliewer. Characterizing the compression-dependent viscoelastic properties of human hepatic pathologies using dynamic compression testing. *Phys. Med. Biol.*, 57(8):2273–2286, Mar. 2012. doi: 10.1088/0031-9155/57/8/2273.

W. J. Drugan and J. R. Willis. A micromechanics-based nonlocal constitutive equation and estimates of representative volume element size for elastic composites. *J. Mech. Phys. Solids*, 44(4):497–524, 1996. ISSN 0022-5096. doi: 10.1016/0022-5096(96)00007-5.

K. M. Dunford, T. LeRoith, and A. R. Kemper. Effects of postmortem time and storage fluid on the material properties of bovine liver parenchyma in tension. *J. Mech. Behav. Biomed. Mater.*, 87:240–255, 2018. doi: 10.1016/j.jmbbm.2018.05.043.

M. T. Duong, N. H. Nguyen, T. N. Tran, R. H. Tolba, and M. Staat. Influence of refrigerated storage on tensile mechanical properties of porcine liver and spleen. *Int. Biomech.*, 2(1):79–88, Jan. 2015. doi: 10.1080/23335432.2015.1049295.

L. Eberhardsteiner, C. Hellmich, and S. Scheiner. Layered water in crystal interfaces as source for bone viscoelasticity: Arguments from a multiscale approach. *Comput. Methods Biomech. Biomed. Engin.*, 17, May 2012. doi: 10.2316/p.2012.764-173.

R. Eisma, M. Gueorguieva, E. Immel, R. Toomey, G. Mcleod, R. Soames, and A. Melzer. Liver displacement during ventilation in thiel embalmed human cadavers - a possible model for research and training in minimally invasive therapies. *Minim. Invasiv Ther.*, 22, Mar. 2013. doi: 10.3109/13645706.2013.769451.

M. El Kouri, A. Bakkali, and L. Azrar. Mathematical modeling of the overall time-dependent behavior of non-ageing viscoelastic reinforced composites. *Appl. Math. Modell.*, 40, Nov. 2015. doi: 10.1016/j.apm.2015.11.031.

J. D. Eshelby. The determination of the elastic field of an ellipsoidal inclusion, and related problems. *Proc. R. Soc. A*, 241(1226):376–396, Aug. 1957. doi: 10.1098/rspa.1957.0133. URL `https://doi.org/10.1098/rspa.1957.0133`.

D. M. Espino, D. E. T. Shepherd, and D. W. L. Hukins. Viscoelastic properties of bovine knee joint articular cartilage: dependency on thickness and loading frequency. *BMC Musculoskelet. Disord.*, 15:205–205, June 2014. doi: 10.1186/1471-2474-15-205.

S.-J. Estermann, D. H. Pahr, and A. Reisinger. Quantifying tactile properties of liver tissue, silicone elastomers, and a 3D printed polymer for manufacturing realistic organ models. *J. Mech. Behav. Biomed. Mater.*, 104:103630, Apr. 2020a. doi: 10.1016/j.jmbbm.2020.103630.

S.-J. Estermann, D. H. Pahr, and A. Reisinger. Hyperelastic and viscoelastic characterisation of hepatic tissue under uniaxial tension in time and frequency domain. *J. Mech. Behav. Biomed. Mater.*, 112:104038, 2020b. doi: 10.1016/j.jmbbm.2020.104038.

S.-J. Estermann, S. Förster-Streffleur, L. Hirtler, J. Streicher, D. H. Pahr, and A. Reisinger. Comparison of thiel preserved, fresh human, and animal liver tissue in terms of mechanical properties. *Ann. Anat.*, 236C:151717, 2021a. doi: 10.1016/j.aanat.2021.151717.

S.-J. Estermann, D. H. Pahr, and A. Reisinger. Material design of soft biological tissue replicas using viscoelastic micromechanical modelling. *under review in J. Mech. Behav. Biomed. Mater.*, 2021b.

J. Eurell and B. Frappier. *Dellmanns Textbook of Veterinary Histology.* Blackwell Publishing, Ames, 2006.

D. W. Evans, E. C. Moran, P. M. Baptista, S. Soker, and J. L. Sparks. Scale-dependent mechanical properties of native and decellularized liver tissue. *Biomech. Model. Mechanobiol.*, 12(3):569–580, June 2013.

I. Ezzaraa, N. Ayrilmis, M. K. Kuzman, S. Belhouideg, and J. Bengourram. Study of the effects of microstructure on the mechanical properties of 3d printed wood/pla composite materials by a micromechanical approach. In *2020 IEEE 2nd International Conference on Electronics, Control, Optimization and Computer Science (ICECOCS)*, pages 1–5, 2020. doi: 10.1109/icecocs50124.2020.9314564.

G. Fallenstein, V. Hulce, and J. Melvin. Dynamic mechanical properties of human brain tissue. *J. Biomech.*, 2(3):217 – 226, 1969. doi: 10.1016/0021-9290(69)90079-7.

G. Falvo D'Urso Labate, F. Baino, M. Terzini, A. Audenino, C. Vitale-Brovarone, P. Segers, R. Quarto, and G. Catapano. Bone structural similarity score: A multiparametric tool to match properties of biomimetic bone substitutes with their target tissues. *Journal of Applied Biomaterials and Fundamental Materials*, 14:e277–e289, May 2016.

C. Fang and P. S. Sidhu. Ultrasound-based liver elastography: current results and future perspectives. *Abdom. Radiol.*, 45(11):3463–3472, 2020. doi: 10.1007/s00261-020-02717-x.

G. Fessel, K. Frey, A. Schweizer, M. Calcagni, O. Ullrich, and J. G. Snedeker. Suitability of thiel embalmed tendons for biomechanical investigation. *Ann. Anat.*, 193 (3):237–241, May 2011. doi: 10.1016/j.aanat.2011.03.007.

W. N. Findley, J. S. Lai, and K. Onaran. *Creep and Relaxation of Nonlinear Viscoelastic Materials*. Dover Publications, Inc., New York, 1989. ISBN 0-486-66016-8.

A. C. Fischer-Cripps. The hertzian contact surface. *J. Mater. Sci.*, 34(1):129–137, 1999.

K. W. Fishbein, Y. A. Gluzband, M. Kaku, H. Ambia-Sobhan, S. A. Shapses, M. Yamauchi, and R. G. Spencer. Effects of formalin fixation and collagen cross-linking on t2 and magnetization transfer in bovine nasal cartilage. *Magn. Reson. Med.*, 57 (6):1000–1011, June 2007. doi: 10.1002/mrm.21216.

A. Fritsch and C. Hellmich. 'universal' microstructural patterns in cortical and trabecular, extracellular and extravascular bone materials: micromechanics-based prediction of anisotropic elasticity. *J. Theor. Biol.*, 244:597–620, Feb 2007.

Y. Fu and C. Chui. Modelling and simulation of porcine liver tissue indentation using finite element method and uniaxial stressstrain data. *J. Biomech.*, 47(10):2430 – 2435, 2014. ISSN 0021-9290. doi: 10.1016/j.jbiomech.2014.04.009.

Y. C. Fung. *Foundations of Solid Mechanics*. Prentice-Hall Inc, Englewood Cliffs, New Jersey, 1965. doi: 10.1115/1.3625018.

Y. C. Fung. Elasticity of soft tissues in simple elongation. *Am. J. Physiol.*, 213(6): 1532–1544, Dec. 1967. doi: 10.1152/ajplegacy.1967.213.6.1532.

Y. C. Fung. *Biomechanics: Mechanical Properties of Living Tissues*. Springer Science+Business Media New York, 2 edition, 1993. doi: 10.1007/978-1-4757-2257-4.

Y. C. Fung, K. Fronek, and P. Patitucci. Pseudoelasticity of arteries and the choice of its mathematical expression. *Am. J. Physiol.*, 237:H620–31, Nov 1979.

Z. Gao and J. P. Desai. Estimating zero-strain states of very soft tissue under gravity loading using digital image correlation. *Medical Image Analysis*, 14(2):126–137, Apr. 2010. ISSN 1361-8415.

Z. Gao, K. Lister, and J. P. Desai. Constitutive modeling of liver tissue: Experiment and theory. *Ann. Biomed. Eng.*, 38(2):505–516, Feb. 2010. doi: 10.1007/s10439-009-9812-0.

U. Giger, I. Frésard, A. Häfliger, M. Bergmann, and L. Krähenbühl. Laparoscopic training on thiel human cadavers: A model to teach advanced laparoscopic procedures. *Surg. Endosc.*, 22:901–6, May 2008.

J. Goff, S. Sulaiman, B. Arkles, and J. P. Lewicki. Soft materials with recoverable shape factors from extreme distortion states. *Adv. Mater.*, 28(12):2393–2398, Mar. 2016. ISSN 0935-9648. doi: 10.1002/adma.201503320.

Y. Gröhn and L.-A. Lindberg. Ultrastructural changes of the liver in spontaneously ketotic cows. *Journal of Comparative Pathology*, 95(3):443–452, 1985. doi: 10.1016/0021-9975(85)90049-0.

D. Gutierrez-Lemini. *Engineering Viscoelasticity*. Springer, New York, Jan. 2014. doi: 10.1007/978-1-4614-8139-3.

J. L. Habicht, C. Kiessling, and A. Winkelmann. Bodies for anatomy education in medical schools: An overview of the sources of cadavers worldwide. *Academic medicine : journal of the Association of American Medical Colleges*, 93(29561275):1293–1300, Sept. 2018. doi: 10.1097/acm.0000000000002227.

E. C. Halperin. The poor, the black, and the marginalized as the source of cadavers in united states anatomical education. *Clin. Anat.*, 20(5):489–495, July 2007. doi: 10.1002/ca.20445.

Z. Hashin. Viscoelastic behavior of heterogeneous media. *J. Appl. Mech.*, 32:630–636, 1965. doi: 10.1115/1.3627270.

Z. Hashin. Complex moduli of viscoelastic composites–i. general theory and application to particulate composites. *Int. J. Solids Struct.*, 6(5):539–552, 1970. ISSN 0020-7683. doi: 10.1016/0020-7683(70)90029-6.

S. Hata, H. Imamura, T. Aoki, T. Hashimoto, M. Akahane, K. Hasegawa, Y. Bekku, Y. Sugawara, M. Makuuchi, and N. Kokudo. Value of visual inspection, bimanual palpation, and intraoperative ultrasonography during hepatic resection for liver metastases of colorectal carcinoma. *World J. Surg.*, 35(12):2779–2787, Dec 2011. doi: 10.1007/s00268-011-1264-7.

G. Hattab, T. Ahlfeld, A. Klimova, A. Koepp, M. Schuerer, and S. Speidel. Uniaxial compression testing and cauchy stress modeling to design anatomical silicone replicas. *Scientific Reports*, 10(1):11849, 2020. ISSN 2045-2322.

S. Hayashi, M. Naito, S. Kawata, N. Qu, N. Hatayama, S. Hirai, and M. Itoh. History and future of human cadaver preservation for surgical training: from formalin to saturated salt solution method. *Anat. Sci. Int.*, 91:1–7, Jan 2016.

C. Hellmich, J.-F. Barthélémy, and L. Dormieux. Mineral-collagen interactions in elasticity of bone ultrastructure - a continuum micromechanics approach. *Eur. J. Mech. A. Solids*, 23(5):783–810, 2004. ISSN 0997-7538. doi: 10.1016/j.euromechsol.2004.05.004.

C. Hellmich, D. Celundova, and F.-J. Ulm. Multiporoelasticity of hierarchically structured materials: Micromechanical foundations and application to bone. *J. Eng. Mech.*, 135(5):382–394, May 2009. doi: 10.1061/(asce)em.1943-7889.0000001.

H. Hertz. über die berührung fester elastischer krper. *Journal fr die reine und angewandte Mathematik*, 92:156–171, 1882. doi: 10.1515/crll.1882.92.156.

N. Higashi, H. Ueda, O. Yamada, S. Oikawa, M. Koiwa, P. Tangkawattana, and K. Takehana. Micromorphological characteristics of hepatic sinusoidal endothelial cells and their basal laminae in five different animal species. *Okajimas Folia Anat. Jpn.*, 79:135–42, Dec 2002. doi: 10.2535/ofaj.79.135.

P. Hildebrand, M. Kleemann, U. Roblick, L. Mirow, H.-P. Bruch, and C. Bürk. Development of a perfused ex vivo tumor-mimic model for the training of laparoscopic radiofrequency ablation. *Surg. Endosc.*, 21(10):1745–1749, Oct. 2007. doi: 10.1007/s00464-007-9216-x.

R. Hill. Elastic properties of reinforced solids: Some theoretical principles. *J. Mech. Phys. Sol.*, 11:357–372, 1963. doi: 10.1016/0022-5096(63)90036-x.

R. Hill. A self-consistent mechanics of composite materials. *Journal of the Mechanics and Physics of Solids*, 13(4):213–222, 1965a. ISSN 0022-5096.

R. Hill. Continuum micro-mechanics of elastoplastic polycrystals. *J. Mech. Phys. Solids*, 13(2):89–101, 1965b. ISSN 0022-5096.

H. H. Hilton. Implications and constraints of time-independent poisson ratios in linear isotropic and anisotropic viscoelasticity. *J. Elast.*, 63(3):221–251, 2001.

E. Hohmann, N. Keough, V. Glatt, K. Tetsworth, R. Putz, and A. Imhoff. The mechanical properties of fresh versus fresh/frozen and preserved (thiel and formalin) long head of biceps tendons: A cadaveric investigation. *Ann. Anat.*, 221:186–191, 2019. doi: 10.1016/j.aanat.2018.05.002.

M. Hollenstein, A. Nava, D. Valtorta, J. Snedeker, and E. Mazza. Mechanical characterization of the liver capsule and parenchyma. In M. Harders and G. Szekely, editors, *Lecture Notes in Computer Science*, volume 4072, pages 150–158, Berlin, Heidelberg, July 2006. Springer.

G. A. Holzapfel. *Nonlinear Solid Mechanics*. John Wiley and Sons, New York, 2000.

G. A. Holzapfel and T. C. Gasser. A viscoelastic model for fiber-reinforced composites at finite strains: Continuum basis, computational aspects and applications. *Comput. Methods Appl. Mech. Eng.*, 190(34):4379–4403, May 2001. ISSN 0045-7825.

F. Hölzle, E.-P. Franz, J. Lehmbrock, S. Weihe, C. Teistra, H. Deppe, and K.-D. Wolff. Thiel embalming technique: a valuable method for teaching oral surgery and implantology. *Clin. Implant Dent. Relat. Res.*, 14(1):121–126, 2012. doi: 10.1111/j.1708-8208.2009.00230.x.

R. Hopf, L. Bernardi, J. Menze, M. Zndel, E. Mazza, and A. E. Ehret. Experimental and theoretical analyses of the age-dependent large-strain behavior of sylgard 184 (10:1) silicone elastomer. *Journal of the Mechanical Behavior of Biomedical Materials*, 60:425–437, 2016. ISSN 1751-6161.

T. Horn, J. H. Henriksen, and P. Christoffersen. The sinusoidal lining cells in "normal" human liver. a scanning electron microscopic investigation. *Liver*, 6:98–110, Apr 1986. doi: 10.1111/j.1600-0676.1986.tb00275.x.

P. Hu, J. Madsen, Q. Huang, and A. L. Skov. Elastomers without covalent crosslinking: Concatenated rings giving rise to elasticity. *ACS Macro Lett.*, 9:1458–1463, Oct. 2020. doi: 10.1021/acsmacrolett.0c00635.

H. M. Ismail, C. G. Pretty, M. K. Signal, M. Haggers, C. Zhou, and J. G. Chase. Mechanical behaviour of tissue mimicking breast phantom materials. *Biomed. Phys. Engin. Express*, 3(4):045010, 2017. doi: 10.1088/2057-1976/aa7992.

R. L. Izzo, R. P. O'Hara, V. Iyer, R. Hansen, K. M. Meess, S. V. Setlur Nagesh, S. Rudin, A. H. Siddiqui, M. Springer, and C. N. Ionita. 3d printed cardiac phantom for procedural planning of a transcatheter native mitral valve replacement. In *Proc. of SPIE Vol. 9789*, volume 9789, page 978908, 04 2016. doi: 10.1117/12.2216952.

D. Jalocha, A. Constantinescu, and R. Neviere. Revisiting the identification of generalized maxwell models from experimental results. *International Journal of Solids and Structures*, 67-68:169–181, Aug. 2015. ISSN 0020-7683.

Y. Jing, Y. Lingtao, L. Wang, L. Hongyang, and Q. An. Study on mechanical characterization of liver tissue based on haptic devices for virtual surgical simulation. *J. Mech. Med. Biol.*, 16(8):1640016, Oct. 2016. doi: 10.1142/s0219519416400169.

I. D. Johnston, D. K. McCluskey, C. K. L. Tan, and M. C. Tracey. Mechanical characterization of bulk sylgard 184 for microfluidics and microengineering. *J. Micromech. Microeng.*, 24(3):035017, 2014. ISSN 1361-6439. doi: 10.1088/0960-1317/24/3/035017.

D. Jones and M. Whitaker. Anatomy's use of unclaimed bodies: Reasons against continued dependence on an ethically dubious practice. *Clin. Anat.*, 25:246–54, July 2011. doi: 10.1002/ca.21223.

K. Jungermann. Zonation of metabolism and gene expression in liver. *Histochem. Cell Biol.*, 103(2):81–91, 1995. doi: 10.1007/bf01454004.

K. Kamimura, T. Suda, W. Xu, G. Zhang, and D. Liu. Image-guided, lobe-specific hydrodynamic gene delivery to swine liver. *Mol. Ther.*, 17(3):491–499, 2009. doi: 10.1038/mt.2008.294.

J. Kanta. Elastin in the liver. *Frontiers in Physiology*, 7:491, 2016. doi: 10.3389/fphys.2016.00491.

A. Karimi and A. Shojaei. An experimental study to measure the mechanical properties of the human liver. *Dig. Dis.*, 36:150–155, 2018.

P. Kelly. *Solid Mechanics Part I: An Introduction to Solid Mechancis*, chapter Viscoelasticity, pages 325–329. The University of Auckland, 2015. URL `http://homepages.engineering.auckland.ac.nz`.

A. R. Kemper, A. C. Santago, J. D. Stitzel, J. L. Sparks, and S. M. Duma. Biomechanical response of human liver in tensile loading. *Ann. Adv. Automot. Med.*, 54: 15–26, Jan. 2010.

A. E. Kerdok, M. P. Ottensmeyer, and R. D. Howe. Effects of perfusion on the viscoelastic characteristics of liver. *J. Biomech.*, 39(12):2221–2231, Jan. 2006. doi: 10.1016/j.jbiomech.2005.07.005.

S. Kim, M. Kim, H. Shin, and K.-Y. Rhee. Measurement of a nearly friction-free stress-strain curve of silicone rubber up to a large strain in compression testing. *Exp. Mech.*, 58(9):1479–1484, 2018. ISSN 1741-2765. doi: 10.1007/s11340-018-0426-z.

S. H. Kim, J.-H. Moon, J. H. Kim, S. M. Jeong, and S.-H. Lee. Flexible, stretchable and implantable pdms encapsulated cable for implantable medical device. *Biomed. Eng. Lett.*, 1(3):199, 2011. ISSN 2093-9868. doi: 10.1007/s13534-011-0033-8.

M. Z. Kiss, T. Varghese, and T. J. Hall. Viscoelastic characterization of in vitro canine tissue. *Phys. Med. Biol.*, 49(18):4207–4218, Sept. 2004. doi: 10.1088/0031-9155/49/18/002.

M. Z. Kiss, M. A. Hobson, T. Varghese, J. Harter, M. A. Kliewer, E. M. Hartenbach, and J. A. Zagzebski. Frequency-dependent complex modulus of the uterus: preliminary results. *Physics in Medicine and Biology*, 51(15):3683–3695, 2006. doi: 10.1088/0031-9155/51/15/006.

R. Klatzky, D. Pawluk, and A. Peer. Haptic perception of material properties and implications for applications. *Proc. IEEE*, 101:2081–2092, Sept. 2013. doi: 10.1109/JPROC.2013.2248691.

Y. Kobayashi, M. Tsukune, T. Miyashita, and M. G. Fujie. Simple empirical model for identifying rheological properties of soft biological tissues. *Phys. Rev. E*, 95:022418, Feb 2017.

C. Kohlhauser and C. Hellmich. Ultrasonic contact pulse transmission for elastic wave velocity and stiffness determination: Influence of specimen geometry and porosity. *Eng. Struct.*, 47:115–133, Feb. 2013. doi: 10.1016/j.engstruct.2012.10.027.

L. Kong, M. Ostadhassan, S. Zamiran, B. Liu, C. Li, and G. G. Marino. Geomechanical upscaling methods: Comparison and verification via 3d printing. *Energies*, 12(3), 2019. ISSN 1996-1073. doi: 10.3390/en12030382.

H. H. Ku. Notes on the use of propagation of error formulas. *J. Res. Nat. Bur. Stand. Sec. C: Eng. Inst.*, 70C(4):263, 1966. doi: 10.6028/jres.070C.025.

J. Kwon, J. Ock, and N. Kim. Mimicking the mechanical properties of aortic tissue with pattern-embedded 3d printing for a realistic phantom. *Materials*, 13(33182404): 5042, Nov. 2020. doi: 10.3390/ma13215042.

P. Kwon and C. K. H. Dharan. Effective moduli of high volume fraction particulate composites. *Acta Metall. Mater.*, 43(3):1141–1147, 1995. doi: 10.1016/0956-7151(94)00326-d.

A. Laird, G. D. Stewart, S. Hou, B. Tang, M. E. McLornan, A. C. P. Riddick, and S. A. McNeill. A novel bovine model for training urological surgeons in laparoscopic radical nephrectomy. *J. Endourol.*, 25(8):1377–1383, Aug. 2011. doi: 10.1089/end.2011.0060.

R. Lakes. *Viscoelastic Solids*. Boca Raton: CRC Press, New York, 1998. doi: 10.1201/9781315121369.

M. J. Lamela, P. Fernàndez, A. Ramos, A. Fernàndez-Canteli, and E. Tanaka. Dynamic compressive properties of articular cartilages in the porcine temporomandibular joint. *J. Mech. Behav. Biomed. Mater.*, 23:62–70, July 2013. doi: 10.1016/j.jmbbm.2013.04.006.

W. W. Lautt. *Hepatic Circulation: Physiology and Pathophysiology*. Morgan & Claypool Life Sciences San Rafael (CA), 2009.

N. Laws. On interfacial discontinuities in elastic composites. *J. Elast.*, 5(3):227–235, 1975. ISSN 1573-2681.

J. M. Lee, S. A. Haberer, and D. R. Boughner. The bovine pericardial xenograft: I. effect of fixation in aldehydes without constraint on the tensile viscoelastic properties of bovine pericardium. *J. Biomed. Mater. Res.*, 23(5):457–475, May 1989. doi: 10.1002/jbm.820230502.

A. Leibinger, A. E. Forte, Z. Tan, M. J. Oldfield, F. Beyrau, D. Dini, and F. Rodriguez y Baena. Soft tissue phantoms for realistic needle insertion: A comparative study. *Ann. Biomed. Eng.*, 44(8):2442–2452, Aug. 2016. doi: 10.1007/s10439-015-1523-0.

M. Lévesque, M. Gilchrist, N. Bouleau, K. Derrien, and D. Baptiste. Numerical inversion of the laplace-carson transform applied to homogenization of randomly reinforced linear viscoelastic media. *Comput. Mech.*, 40:771–789, Sept. 2007. doi: 10.1007/s00466-006-0138-6.

L. Li, A. Maccabi, A. Abiri, Y.-Y. Juo, W. Zhang, Y.-J. Chang, G. N. Saddik, L. Jin, W. S. Grundfest, E. P. Dutson, J. D. Eldredge, P. Benharash, and R. N. Candler. Characterization of perfused and sectioned liver tissue in a full indentation cycle using a visco-hyperelastic model. *J. Mech. Behav. Biomed. Mater.*, 90:591–603, Feb. 2019. doi: 10.1016/j.jmbbm.2018.11.006.

Y.-J. Lim, D. Deo, T. P. Singh, D. B. Jones, and S. De. In situ measurement and modeling of biomechanical response of human cadaveric soft tissues for physics-based surgical simulation. *Surg. Endosc.*, 23(6):1298–1307, June 2009. doi: 10.1007/s00464-008-0154-z.

G. Limbert, editor. *Skin Biophysics: From Experimental Characterisation to Advanced Modelling*. Springer, Cham, Switzerland, 2019. doi: doi:10.1007/978-3-030-13279-8.

Y. Ling, C. Li, K. Feng, R. Duncan, R. Eisma, Z. Huang, and G. Nabi. Effects of fixation and preservation on tissue elastic properties measured by quantitative optical coherence elastography (oce). *J. Biomech.*, 49(7):1009–1015, May 2016. doi: 10.1016/j.jbiomech.2016.02.013.

S. Liu, Y. Cheng, B. Liang, H. Cheng, B. Luo, and K. Zhang. Sequential homogenization in laplace domain for viscoelastic properties of composites with functionally graded interphase. *Compos. Struct.*, 260:113266, 2021. doi: 10.1016/j.compstruct.2020.113266.

W. Liu, X. Zheng, R. Wu, Y. Jin, S. Kong, J. Li, J. Lu, H. Yang, X. Xu, Y. Lv, and X. Zhang. Novel laparoscopic training system with continuously perfused ex-vivo porcine liver for hepatobiliary surgery. *Surg. Endosc.*, 32(2):743–750, 2018. doi: 10.1007/s00464-017-5731-6.

Z. Liu and L. Bilston. On the viscoelastic character of liver tissue: Experiments and modelling of the linear behaviour. *Biorheology*, 37:191–201, Feb. 2000.

Z. Liu and L. Bilston. Large deformation shear properties of liver tissue. *Biorheology*, 39:735–42, Feb. 2002.

J. S. Lowe and P. G. Anderson. *Stevens & Lowe's Human Histology*. Mosby, Philadelphia, 2015.

M. N. Lozoya. *Development of a tissue-mimicking brain phantom for neurosurgical preoperative planning and training*. PhD thesis, Graduate School of Clemson University, 2016.

Y.-C. Lu and C. Untaroiu. Effect of storage methods on indentation-based material properties of abdominal organs. *Proc. Inst. Mech. Eng. H J. Eng. Med.*, 227:293–301, Nov. 2012. doi: 10.1177/0954411912468558.

Y.-C. Lu, A. R. Kemper, and C. D. Untaroiu. Effect of storage on tensile material properties of bovine liver. *J. Mech. Behav. Biomed. Mater.*, 29:339–349, Jan. 2014. doi: 10.1016/j.jmbbm.2013.09.022.

K. Madhan and S. Raju. Comparative histology of human and cow, goat and sheep liver. *J. Surg. Acad.*, 4:10–13, Jan. 2014.

E. L. Madsen, M. A. Hobson, H. Shi, T. Varghese, and G. R. Frank. Tissue-mimicking agar/gelatin materials for use in heterogeneous elastography phantoms. *Physics in medicine and biology*, 50 23:5597–618, 2005.

J. Maier, M. Weiherer, M. Huber, and C. Palm. Imitating human soft tissue on basis of a dual-material 3d print using a support-filled metamaterial to provide bimanual haptic for a hand surgery training system. *Quantitative imaging in medicine and surgery*, 9(30788244):30–42, Jan. 2019. doi: 10.21037/qims.2018.09.17.

S. J. Manoogian, J. A. Bisplinghoff, C. McNally, A. R. Kemper, A. C. Santago, and S. M. Duma. Effect of strain rate on the tensile material properties of human placenta. *J. Biomech. Eng.*, 131(9):091008–091006, Aug. 2009. doi: 10.1115/1.3194694.

S. Marchesseau, S. Chatelin, and H. Delingette. Chapter 11 - nonlinear biomechanical model of the liver. In Y. Payan and J. Ohayon, editors, *Biomechanics of Living Organs*, volume 1, pages 243–265. Academic Press, Oxford, Jan. 2017.

D. Marquardt. An algorithm for least-squares estimation of nonlinear parameters. *SIAM J. Appl. Math.*, 11(2):431–441, 1963. doi: 10.1137/0111030.

P. A. L. S. Martins, R. Natal Jorge, and A. Ferreira. A comparative study of several material models for prediction of hyperelastic properties: Application to silicone-rubber and soft tissues. *Strain*, 42(3):135–147, 2006. doi: 10.1111/j.1475-1305.2006.00257.x.

G. Mattei and A. Ahluwalia. Sample, testing and analysis variables affecting liver mechanical properties: A review. *Acta Biomater.*, 45:60–71, Nov. 2016. doi: 10.1016/j.actbio.2016.08.055.

J. M. Mattice, A. G. Lau, M. L. Oyen, and R. W. Kent. Spherical indentation load-relaxation of soft biological tissues. *J. Mater. Res.*, 21, Aug. 2006. doi: 10.1557/jmr.2006.0243.

E. Mazza, A. Nava, D. Hahnloser, W. Jochum, and M. Bajka. The mechanical response of human liver and its relation to histology: An in vivo study. *Med. Image Anal.*, 11(6):663–672, 2007. doi: 10.1016/j.media.2007.06.010.

K. Miller and K. Chinzei. Constitutive modelling of brain tissue: Experiment and theory. *Journal of Biomechanics*, 30(11):1115–1121, 1997. doi: 10.1016/s0021-9290(97)00092-4.

M. Mooney. A theory of large elastic deformation. *J. Appl. Phys.*, 11(9):582–592, Sept. 1940. doi: 10.1063/1.1712836.

T. Mori and K. Tanaka. Average stress in matrix and average elastic energy of materials with misfitting inclusions. *Acta Metall.*, 21(5):571–574, 1973. ISSN 0001-6160. doi: 10.1016/0001-6160(73)90064-3.

C. Morin and C. Hellmich. A multiscale poromicromechanical approach to wave propagation and attenuation in bone. *Ultrasonics*, 54, Dec. 2014. doi: 10.1016/j.ultras.2013.12.005.

P. Mukherjee, K. Cheng, S. Flanagan, and S. Greenberg. Utility of 3d printed temporal bones in pre-surgical planning for complex bonebridge cases. *European Archives of Oto-Rhino-Laryngology*, 274(8):3021–3028, 05 2017. doi: 10.1007/s00405-017-4618-4.

A. Müller, M. Wapler, and U. Wallrabe. A quick and accurate method to determine the poissons ratio and the coefficient of thermal expansion of pdms. *Soft Matter*, 15:779–784, 2019. doi: 10.1039/c8sm02105h.

W. Nafo and A. Al-Mayah. Measuring the hyperelastic response of porcine liver tissues in-vitro using controlled cavitation rheology. *Exp. Mech.*, 61(2):445–458, 2021.

R. E. Neuman and M. A. Logan. The determination of collagen and elastin in tissues. *J. Biol. Chem.*, 186(2):549–56, 1950.

N. H. Nguyen, M. T. Duong, T. N. Tran, P. T. Pham, O. Grottke, R. Tolba, and M. Staat. Influence of a freeze-thaw cycle on the stress-stretch curves of tissues of porcine abdominal organs. *J. Biomech.*, 45(14):2382–2386, Sept. 2012. doi: 10.1016/j.jbiomech.2012.07.008.

S.-T. Nguyen, M.-Q. Thai, M.-N. Vu, and Q.-D. To. A homogenization approach for effective viscoelastic properties of porous media. *Mech. Mater.*, 100:175–185, 2016. doi: 10.1016/j.mechmat.2016.06.015.

L. Nicholson, R. Adams, and C. Maher. Manual discrimination capability when only viscosity is varied in viscoelastic stiffness stimuli. *Journal of manipulative and physiological therapeutics*, 26:365–73, 07 2003. doi: 10.1016/S0161-4754(03)00070-8.

S. Nicolle and J.-F. Palierne. Dehydration effect on the mechanical behaviour of biological soft tissues: Observations on kidney tissues. *J. Mech. Behav. Biomed. Mater.*, 3(8):630–635, 2010. doi: 10.1016/j.jmbbm.2010.07.010.

S. Nicolle, P. Vezin, and J.-F. Palierne. A strain-hardening bi-power law for the nonlinear behaviour of biological soft tissues. *J. Biomech.*, 43(5):927–932, Mar. 2010. doi: 10.1016/j.jbiomech.2009.11.002.

N. Obaid, M. T. Kortschot, and M. Sain. Understanding the stress relaxation behavior of polymers reinforced with short elastic fibers. *Materials (Basel, Switzerland)*, 10, Apr 2017. doi: 10.3390/ma10050472.

C. S. O'Bryan, T. Bhattacharjee, S. Hart, C. P. Kabb, K. D. Schulze, I. Chilakala, B. S. Sumerlin, W. G. Sawyer, and T. E. Angelini. Self-assembled micro-organogels for 3d printing silicone structures. *Sci. Adv.*, 3(5):e1602800, May 2017. doi: 10.1126/sciadv.1602800.

S. Ocal, M. Umut Ozcan, I. Basdogan, and C. Basdogan. Effect of preservation period on the viscoelastic material properties of soft tissues with implications for liver transplantation. *J. Biomech. Eng.*, 132:101007, Oct. 2010. doi: 10.1115/1.4002489.

W. C. Oliver and G. M. Pharr. An improved technique for determining hardness and elastic modulus using load and displacement sensing indentation experiments. *J. Mater. Res.*, 7(6):1564–1583, 1992. doi: 10.1557/jmr.1992.1564.

M. P. Ottensmeyer, A. E. Kerdok, R. D. Howe, and S. L. Dawson. The effects of testing environment on the viscoelastic properties of soft tissues. In *Medical Simulation*, pages 9–18, Berlin, Heidelberg, 2004. Springer.

N. Ottone, C. A. Vargas, R. Fuentes, and M. Sol. Walter thiel's embalming method. review of solutions and applications in different fields of biomedical research. *Int. J. Morphol.*, 34:1442–1454, Dec. 2016. doi: 10.4067/s0717-95022016000400044.

M. Oyen. Spherical indentation creep following ramp loading. *J. Mater. Res.*, 20, Aug. 2005. doi: 10.1557/jmr.2005.0259.

J. Palacio-Torralba, S. Hammer, D. W. Good, S. Alan McNeill, G. D. Stewart, R. L. Reuben, and Y. Chen. Quantitative diagnostics of soft tissue through viscoelastic characterization using time-based instrumented palpation. *J. Mech. Behav. Biomed. Mater.*, 41:149–160, Jan. 2015. doi: 10.1016/j.jmbbm.2014.09.027.

L. Panait, A. Rafiq, V. Tomulescu, C. Boanca, I. Popescu, A. Carbonell, and R. C. Merrell. Telementoring versus on-site mentoring in virtual reality-based surgical training. *Surg. Endosc.*, 20(1):113–118, 2006. ISSN 1432-2218.

W. J. Parnell. The eshelby, hill, moment and concentration tensors for ellipsoidal inhomogeneities in the newtonian potential problem and linear elastostatics. *J. Elast.*, 125(2):231–294, 2016. ISSN 1573-2681. doi: 10.1007/s10659-016-9573-6.

M. V. Pathan, V. L. Tagarielli, and S. Patsias. Numerical predictions of the anisotropic viscoelastic response of uni-directional fibre composites. *Composites Part A: Applied Science and Manufacturing*, 93:18–32, Feb. 2017. ISSN 1359-835X.

F. Pervin, W. W. Chen, and T. Weerasooriya. Dynamic compressive response of bovine liver tissues. *J. Mech. Behav. Biomed. Mater.*, 4:76–84, Jan 2011. doi: 10.1016/j.jmbbm.2010.09.007.

S. L. Peterson, A. McDonald, P. L. Gourley, and D. Y. Sasaki. Poly(dimethylsiloxane) thin films as biocompatible coatings for microfluidic devices: Cell culture and flow studies with glial cells. *J. Biomed. Mater. Res.*, 72A(1):10–18, Jan. 2005. ISSN 1549-3296. doi: 10.1002/jbm.a.30166.

K. L. Pitts, S. Abu-Mallouh, and M. Fenech. Contact angle study of blood dilutions on common microchip materials. *J. Mech. Behav. Biomed. Mater.*, 17:333–336, 2013. ISSN 1751-6161. doi: 10.1016/j.jmbbm.2012.07.007.

T. Pritz. The poisson's loss factor of solid viscoelastic materials. *J. Sound Vib.*, 306 (3):790–802, 2007. doi: 10.1016/j.jsv.2007.06.016.

T. Pritz. Relation of bulk to shear loss factor of solid viscoelastic materials. *J. Sound Vib.*, 324(3):514–519, 2009. doi: 10.1016/j.jsv.2009.02.003.

K. Pusch, T. J. Hinton, and A. W. Feinberg. Large volume syringe pump extruder for desktop 3d printers. *HardwareX*, 3:49–61, Apr. 2018. doi: 10.1016/j.ohx.2018.02.001.

K. Qiu, Z. Zhao, G. Haghiashtiani, S.-Z. Guo, M. He, R. Su, Z. Zhu, D. B. Bhuiyan, P. Murugan, F. Meng, S. H. Park, C.-C. Chu, B. M. Ogle, D. A. Saltzman, B. R. Konety, R. M. Sweet, and M. C. McAlpine. 3d printed organ models with physical properties of tissue and integrated sensors. *Adv. Mater. Technol.*, page e1700235, 2017. doi: 10.1002/admt.201700235.

K. Qiu, G. Haghiashtiani, and M. C. McAlpine. 3d printed organ models for surgical applications. *Annual review of analytical chemistry (Palo Alto, Calif.)*, 11(1):287–306, June 2018. doi: 10.1146/annurev-anchem-061417-125935.

S. Ramadan, N. Paul, and H. E. Naguib. Standardized static and dynamic evaluation of myocardial tissue properties. *Biomed. Mater.*, 12(2):025013, 2017. ISSN 1748-605X. doi: 10.1088/1748-605x/aa57a5.

B. Reitinger, A. Bornik, R. Beichel, and D. Schmalstieg. Liver surgery planning using virtual reality. *IEEE Comput. Graphics Appl.*, 26:36–47, Dec. 2006. doi: 10.1109/mcg.2006.131.

F. Rengier, A. Mehndiratta, H. von Tengg-Kobligk, C. M. Zechmann, R. Unterhinninghofen, H.-U. Kauczor, and F. L. Giesel. 3d printing based on imaging data: review of medical applications. *International Journal of Computer Assisted Radiology and Surgery*, 5(4):335–341, Jul 2010. doi: 10.1007/s11548-010-0476-x.

A. Reuss. Berechnung der Fließgrenze von Mischkristallen auf Grund der Plastizitätsbedingung für Einkristalle. *Z. angew. Math. Mech.*, 9(1):49–58, Jan. 1929. ISSN 0044-2267. doi: 10.1002/zamm.19290090104.

R. S. Rivlin and E. K. Rideal. Large elastic deformations of isotropic materials iv. further developments of the general theory. *Philos. Trans. R. Soc. Lond. Ser. A Math. Phys. Sci.*, 241(835):379–397, Oct. 1948. doi: 10.1098/rsta.1948.0024.

E. Roan and K. Vemaganti. The nonlinear material properties of liver tissue determined from no-slip uniaxial compression experiments. *J. Biomech. Eng.*, 129:450–6, July 2007.

E. Roan and K. Vemaganti. Strain rate-dependent viscohyperelastic constitutive modeling of bovine liver tissue. *Med. Biol. Eng. Comput*, 49(4):497–506, 2011. doi: 10.1007/s11517-010-0702-2.

D. Roylance. *Engineering Viscoelasticity*. Massachusetts Institute of Technology: MIT OpenCourseWare, 2001. URL `https://ocw.mit.edu/`.

F. v. Rundstedt, J. M. Scovell, S. Agrawal, J. Zaneveld, and R. E. Link. Utility of patientspecific silicone renal models for planning and rehearsal of complex tumour resections prior to robotassisted laparoscopic partial nephrectomy. *BJU International*, 119(4):598–604, 2017. ISSN 1464-410X.

M. Salmi, K.-S. Paloheimo, J. Tuomi, J. Wolff, and A. Mkitie. Accuracy of medical models made by additive manufacturing (rapid manufacturing). *J. Craniomaxillofac. Surg.*, 41(7):603–609, 2013. doi: 10.1016/j.jcms.2012.11.041.

E. Samur, M. Sedef, C. Basdogan, L. Avtan, and O. Duzgun. A robotic indenter for minimally invasive measurement and characterization of soft tissue response. *Med. Image Anal.*, 11(4):361–373, Aug. 2007. ISSN 1361-8415.

L. Sandrin, B. Fourquet, J.-M. Hasquenoph, S. Yon, C. Fournier, F. Mal, C. Christidis, M. Ziol, B. Poulet, F. Kazemi, M. Beaugrand, and R. Palau. Transient elastography: a new noninvasive method for assessment of hepatic fibrosis. *Ultrasound Med. Biol.*, 29:1705–13, Dec 2003. doi: 10.1016/j.ultrasmedbio.2003.07.001.

Y. Sano, R. Matsuzaki, M. Ueda, A. Todoroki, and Y. Hirano. 3d printing of discontinuous and continuous fibre composites using stereolithography. *Addit. Manuf.*, 24: 521–527, 2018. ISSN 2214-8604. doi: 10.1016/j.addma.2018.10.033.

A. C. Santago, A. R. Kemper, C. McNally, J. Sparks, and S. M. Duma. The effect of temperature on the mechanical properties of bovine liver. *Biomed. Sci. Instrum.*, 45:376–381, Jan. 2009.

D. Sasse, U. M. Spornitz, and I. P. Maly. Liver architecture. *Enzyme*, 46:8–32, 1992. doi: 10.1159/000468776.

S. Scheiner and C. Hellmich. Continuum microviscoelasticity model for aging basic creep of early-age concrete. *J. Eng. Mech.*, 135(4):307–323, Apr. 2009. doi: 10.1061/(asce)0733-9399(2009)135:4(307).

J. Segurado and J. Llorca. A numerical approximation to the elastic properties of sphere-reinforced composites. *J. Mech. Phys. Solids*, 50(10):2107–2121, 2002. ISSN 0022-5096. doi: 10.1016/s0022-5096(02)00021-2.

O. A. Shergold, N. A. Fleck, and D. Radford. The uniaxial stress versus strain response of pig skin and silicone rubber at low and high strain rates. *Int. J. Impact Eng.*, 32 (9):1384–1402, Sept. 2006. doi: 10.1016/j.ijimpeng.2004.11.010.

J. Snedeker, P. Niederer, F. Schmidlin, M. Farshad, C. Demetropoulos, J. Lee, and K. Yang. Strain-rate dependent material properties of the porcine and human kidney capsule. *J. Biomech.*, 38:1011–1021, May 2005. doi: 10.1016/j.jbiomech.2004.05.036.

J. L. Sparks, N. A. Vavalle, K. E. Kasting, B. Long, M. L. Tanaka, P. A. Sanger, K. Schnell, and T. A. Conner-Kerr. Use of silicone materials to simulate tissue biomechanics as related to deep tissue injury. *Adv. Skin Wound Care*, 28:59–68, Feb 2015. doi: 10.1097/01.asw.0000460127.47415.6e.

Z. A. Starosolski, J. H. Kan, S. D. Rosenfeld, R. Krishnamurthy, and A. Annapragada. Application of 3-d printing (rapid prototyping) for creating physical models of pediatric orthopedic disorders. *Pediatr. Radiol.*, 44(2):216–221, 2014.

P. Suquet. *Elements of homogenization for inelastic solid mechanics*, chapter Elements of homogenization for inelastic solid mechanics, pages 194–278. Springer-Verlag, Berlin, Jan. 1987.

Á. Takács, I. J. Rudas, and T. Haidegger. Surface deformation and reaction force estimation of liver tissue based on a novel nonlinear mass-spring-damper viscoelastic model. *Med. Biol. Eng. Comput.*, 54(10):1553–1562, Oct. 2016. doi: 10.1007/s11517-015-1434-0.

Á. Takács, P. Galambos, I. J. Rudas, and T. Haidegger. A novel methodology for usability assesment of rheological soft tissue models. In *2017 IEEE 15th International Symposium on Applied Machine Intelligence and Informatics (SAMI)*, pages 000271–000278, 2017. doi: 10.1109/sami.2017.7880316.

A. Tamura, K. Omori, K. Miki, J. B. Lee, K. H. Yang, and A. I. King. Material characterization of porcine abdominal organs. *Stapp Car Crash J.*, 46:55–69, Nov. 2002.

K. Tan, S. Cheng, L. Jug, and L. Bilston. Characterising soft tissues under large amplitude oscillatory shear and combined loading. *J. Biomech.*, 46(6):1060–1066, Mar. 2013. doi: 10.1016/j.jbiomech.2013.01.028.

B. Tang, G. B. Hanna, and A. Cuschieri. Analysis of errors enacted by surgical trainees during skills training courses. *Surgery*, 138(1):14–20, July 2005. doi: 10.1016/j.surg.2005.02.014.

M. G. Tarantino, O. Zerhouni, and K. Danas. Random 3d-printed isotropic composites with high volume fraction of pore-like polydisperse inclusions and near-optimal elastic stiffness. *Acta Mater.*, 175:331–340, 2019. ISSN 1359-6454. doi: 10.1016/j.actamat.2019.06.020.

L. Taylor, A. Lerner, D. Rubens, and K. Parker. A kelvin-voigt fractional derivative model for viscoelastic characterization of liver tissue. In *Proceedings of IMECE2002 ASME International Mechanical Engineering Congress & Exposition*, volume 53, Jan. 2002. doi: 10.1115/imece2002-32605.

A. I. Teixeira, S. Ilkhanizadeh, J. A. Wigenius, J. K. Duckworth, O. Ingans, and O. Hermanson. The promotion of neuronal maturation on soft substrates. *Biomaterials*, 30(27):4567–4572, 2009. ISSN 0142-9612.

A. Tejo-Otero, P. Lustig-Gainza, F. Fenollosa-Artés, A. Valls, L. Krauel, and I. Buj-Corral. 3d printed soft surgical planning prototype for a biliary tract rhabdomyosarcoma. *J. Mech. Behav. Biomed. Mater.*, 109:103844, May 2020. doi: 10.1016/j.jmbbm.2020.103844.

P. S. Theocaris. Interrelation between dynamic moduli and compliances in polymers. *Kolloid-Zeitschrift und Zeitschrift fr Polymere*, 235(1):1182–1188, 1969. doi: 10.1007/bf01542525.

W. Thiel. Die Konservierung ganzer Leichen in natürlichen Farben. *Ann. Anat.*, 174 (3):185–195, June 1992. doi: 10.1016/s0940-9602(11)80346-8.

W. Thiel. Ergänzung für die konservierung ganzer leichen nach w. thiel. *Ann. Anat.*, 184(3):267–269, 2002. doi: 10.1016/s0940-9602(02)80121-2.

L. R. G. Treloar. The elasticity of a network of long-chain molecules–ii. *Trans. Faraday Soc.*, 39(0):241–246, 1943. doi: 10.5254/1.3546653.

N. W. Tschoegl, W. G. Knauss, and I. Emri. Poisson's ratio in linear viscoelasticity - a critical review. *Mech. Time Depend. Mater.*, 6(1):3–51, 2002.

T. Tsujita, K. Sase, A. Konno, M. Nakayama, C. Xiaoshuai, K. Abe, and M. Uchiyama. Design and evaluation of an encountered-type haptic interface using mr fluid for surgical simulators. *Advanced Robotics*, 27:525–540, Apr. 2013.

H. Uehara. A study on the mechanical properties of the kidney, liver, and spleen, by means of tensile stress test with variable strain velocity. *Journal of Kyoto Prefectural University of Medicine*, 104(1):439–451, 1995.

S. Umale, C. Deck, N. Bourdet, P. Dhumane, L. Soler, J. Marescaux, and R. Willinger. Experimental mechanical characterization of abdominal organs: liver, kidney & spleen. *J. Mech. Behav. Biomed. Mater.*, 17:22–33, Jan. 2013. doi: 10.1016/j.jmbbm.2012.07.010.

C. D. Untaroiu, Y.-C. Lu, S. K. Siripurapu, and A. R. Kemper. Modeling the biomechanical and injury response of human liver parenchyma under tensile loading. *J. Mech. Behav. Biomed. Mater.*, 41:280–291, Jan. 2015. doi: 10.1016/j.jmbbm.2014.07.006.

T. Usami, T. Fujioka, A. Yoshida, H. Miyaue, T. Yasuoka, Y. Uchikura, K. Takagi, Y. Matsubara, T. Matsumoto, K. Matsubara, and T. Sugiyama. Assessment of laparoscopic training for gynecological malignancies using thielembalmed human cadavers. *Mol. Clin. Oncol.*, 9, Sept. 2018. doi: 10.3892/mco.2018.1715.

J. Vaicekauskaite, P. Mazurek, S. Vudayagiri, and A. L. Skov. Mapping the mechanical and electrical properties of commercial silicone elastomer formulations for stretchable transducers. *J. Mater. Chem. C*, 8:1273–1279, 2020. doi: 10.1039/C9TC05072H.

D. R. Veronda and R. A. Westmann. Mechanical characterization of skin–finite deformations. *J. Biomech.*, 3(1):111–124, Jan. 1970. doi: 10.1016/0021-9290(70)90055-2.

W. Voigt. Theoretische Studien über die Elasticitätsverhältnisse der Krystalle. *Abh. KGL. Ges. Wiss. Göttingen, Math. Kl.*, 34:3–51, 1887.

M. Vukicevic, D. S. Puperi, K. Jane Grande-Allen, and S. H. Little. 3d printed modeling of the mitral valve for catheter-based structural interventions. *Ann. Biomed. Eng.*, 45(2):508–519, Feb. 2017.

Y. Wada, R. Ito, and H. Ochiai. Comparison between mechanical relaxations associated with volume and shear deformations in styrene-butadiene rubber. *J. Phys. Soc. Jpn.*, 17(1):213–218, 1962. doi: 10.1143/jpsj.17.213.

K. Wake and T. Sato. the sinusoid in the liver: Lessons learned from the original definition by charles sedgwick minot (1900). *Anat. Rec.*, 298(12):2071–2080, Dec. 2015. doi: 10.1002/ar.23263.

K. Wang, Y. Zhao, Y.-H. Chang, Z. Qian, C. Zhang, B. Wang, M. A. Vannan, and M.-J. Wang. Controlling the mechanical behavior of dual-material 3d printed metamaterials for patient-specific tissue-mimicking phantoms. *Mater. Des.*, 90:704–712, Jan. 2016. ISSN 0264-1275. doi: 10.1016/j.matdes.2015.11.022.

Y. Wang, B. L. Tai, H. Yu, and A. J. Shih. Silicone-based tissue-mimicking phantom for needle insertion simulation. *J. Med. Devices*, 8(2), Mar. 2014. doi: 10.1115/1.4026508.

C. Wex, A. Stoll, M. Fröhlich, S. Arndt, and H. Lippert. How preservation time changes the linear viscoelastic properties of porcine liver. *Biorheology*, 50:115–31, July 2013. doi: 10.3233/BIR-130632.

C. Wex, A. Stoll, M. Fröhlich, S. Arndt, and H. Lippert. Mechanics of fresh, frozen-thawed and heated porcine liver tissue. *Int. J. Hyperthermia*, 30(4):271–283, June 2014. doi: 10.3109/02656736.2014.924161.

A. G. Wilcox, K. G. Buchan, and D. M. Espino. Frequency and diameter dependent viscoelastic properties of mitral valve chordae tendineae. *J. Mech. Behav. Biomed. Mater.*, 30:186–195, Feb. 2014. doi: 10.1016/j.jmbbm.2013.11.013.

E. Wisse, F. Jacobs, B. Topal, P. Frederik, and B. De Geest. The size of endothelial fenestrae in human liver sinusoids: implications for hepatocyte-directed gene transfer. *Gene Therapy*, 15(17):1193–1199, 2008. doi: 10.1038/gt.2008.60.

R. L. Wood. Evidence of species differences in the ultrastructure of the hepatic sinusoid. *Zeitschrift fr Zellforschung und Mikroskopische Anatomie*, 58(5):679–692, 1962. doi: 10.1007/bf00410656.

G. Wu, M. Gotthardt, and M. Gollasch. Assessment of nanoindentation in stiffness measurement of soft biomaterials: kidney, liver, spleen and uterus. *Scientific Reports*, 10:18784, Nov. 2020.

Z. Xu, C. S. Ha, R. Kadam, J. Lindahl, S. Kim, H. F. Wu, V. Kunc, and X. Zheng. Additive manufacturing of two-phase lightweight, stiff and high damping carbon fiber reinforced polymer microlattices. *Addit. Manuf.*, 32:101106, 2020. doi: 10.1016/j.addma.2020.101106.

Z. Ye, A. Dun, H. Jiang, C. Nie, S. Zhao, T. Wang, and J. Zhai. The role of 3d printed models in the teaching of human anatomy: a systematic review and meta-analysis. *BMC Med. Educ.*, 20(1):335, 2020. doi: 10.1186/s12909-020-02242-x.

W.-C. Yeh, Y.-M. Jeng, H.-C. Hsu, P.-L. Kuo, M.-L. Li, P. Yang, C.-M. Lee, and P.-C. Li. Young's modulus measurements of human liver and correlation with pathological findings. In *Proceedings of the IEEE Ultrasonics Symposium*, volume 2, pages 1233–1236, 2001. doi: 10.1109/ultsym.2001.991942.

O. H. Yeoh. Some forms of the strain energy function for rubber. *Rubber Chem. Technol.*, 66(5):754–771, Nov. 1993. doi: 10.5254/1.3538343.

N. Yoganandan, F. A. Pintar, T. A. Gennarelli, and M. R. Maltese. Patterns of abdominal injuries in frontal and side impacts. *Annu. Proc. Assoc. Adv. Automot. Med.*, 44(11558081):17–36, 2000.

M. Yokoyama, L. Mailaender, H. Raestrup, and G. Buess. Training system for laparoscopic fundoplication. *Minim. Invasiv Ther.*, 12(3-4):143–150, Jan. 2003. doi: 10.1080/13645700310007706.

S.-J. Yoo, T. Spray, E. Austin, T.-J. Yun, and G. Arsdell. Hands-on surgical training of congenital heart surgery using 3d print models. *J. Thorac. Cardiovas. Surg.*, 153, Feb. 2017.

Y. C. Yoon, J. S. Lee, S. U. Park, J. H. Kwon, T. H. Hong, and D. G. Kim. Quantitative assessment of liver fibrosis using shore durometer. *Ann. Surg. Treat. Res.*, 93(6): 300–304, 2017. doi: 10.4174/astr.2017.93.6.300.

H. Yoshida, N. Taniai, M. Yoshioka, A. Hirakata, Y. Kawano, T. Shimizu, J. Ueda, H. Takata, Y. Nakamura, and Y. Mamada. Current status of laparoscopic hepatectomy. *J. Nippon Med. Sch.*, 86(4):201–206, 2019.

J. Yvonnet. *Computational Homogenization of Heterogeneous Materials with Finite Elements*. 258. Springer-Verlag, Cham, 2019. doi: 10.1007/978-3-030-18383-7.

A. Zaoui. Continuum micromechanics: Survey. *J. Eng. Mech.*, 128(8):808–816, Aug. 2002. doi: 10.1061/(asce)0733-9399(2002)128:8(808).

N. N. Zein, I. A. Hanouneh, P. D. Bishop, M. Samaan, B. Eghtesad, C. Quintini, C. Miller, L. Yerian, and R. Klatte. Three-dimensional print of a liver for preoperative planning in living donor liver transplantation. *Liver Transpl.*, 19(12):1304–1310, 2013. doi: 10.1002/lt.23729.

M. Zhang, B. Castaneda, Z. Wu, P. Nigwekar, J. V. Joseph, D. J. Rubens, and K. J. Parker. Congruence of imaging estimators and mechanical measurements of viscoelastic properties of soft tissues. *Ultrasound Med. Biol.*, 33(10):1617–1631, 2007. doi: 10.1016/j.ultrasmedbio.2007.04.012.

M. Zhang, P. Nigwekar, B. Castaneda, K. Hoyt, J. V. Joseph, A. di Sant'Agnese, E. M. Messing, J. G. Strang, D. J. Rubens, and K. J. Parker. Quantitative characterization of viscoelastic properties of human prostate correlated with histology. *Ultrasound Med. Biol.*, 34(7):1033–1042, 2008. doi: 10.1016/j.ultrasmedbio.2007.11.024.

S. Zhang. *An Atlas of Histology*. Sprinnger-Verlag, New York, 1999. doi: 10.1007/978-0-387-21760-4.

X. Zhang, X. Gao, P. Zhang, Y. Guo, H. Lin, X. Diao, Y. Liu, C. Dong, Y. Hu, S. Chen, and X. Chen. Dynamic mechanical analysis to assess viscoelasticity of liver tissue in a rat model of nonalcoholic fatty liver disease. *Med. Eng. Phys.*, 44: 79–86, 2017. doi: 10.1016/j.medengphy.2017.02.014.

J. Zhao, C. Cao, G. Li, L. Chao, H. Ding, Y. Yao, L. Song, and X. Jin. Study on the similarity of biomechanical behavior between gelatin and porcine liver. *Biomed. Res. Int.*, 2020(32908907):7021636–7021636, Aug. 2020. doi: 10.1155/2020/7021636.

Y. Zhu, Y. Zheng, Y.-y. Shen, X. Chen, X.-y. Zhang, H.-m. Lin, Y.-r. Guo, T.-f. Wang, and S.-p. Chen. Analyzing and modeling rheological behavior of liver fibrosis in rats using shear viscoelastic moduli. *Journal of Zhejiang University. Science. B*, 15(4): 375–381, Oct. 2013. doi: 10.1631/jzus.b1300121.